Design and Chemical Synthesis
of Fluorescent Bicolor Indicators
for the Detection of Neutrinoless
Double Beta Decay of ^{136}Xe

BORJA APARICIO GIL

DOCTORAL THESIS

DONOSTIA/SAN SEBASTIÁN 2022

eman ta zabal zazu

Universidad
del País Vasco

Euskal Herriko
Unibertsitatea

ABBREVIATIONS AND ACRONYMS

$\beta\beta 0\nu$	Neutrinoless Double Beta Decay
$\beta\beta 2\nu$	Double Beta Decay
$T_{1/2}^{0\nu}$	Lifetime
AcOEt	Ethyl acetate
AFM	Atomic Force Microscopy
COSY	Correlation Spectroscopy
CHCl$_3$	Chloroform
d	Doublet (NMR)
DavePhos	2-Dicyclohexylphosphino-2′-(N,N-dimethylamino)biphenyl
DCM	Dichloromethane
DIPEA	N,N-diisopropylethylamine
DFT	Density Functional Theory
DMF	N,N-Dimethylformamide
DMSO	Dimethyl Sulfoxide
eq.	Equivalent(s)
EtOH	Ethanol
Et$_3$N	Triethylamine
ERG	Electron Releasing Group
EWG	Electron Withdrawing Group
FS	Fluorescence Spectroscopy
FTIR	Fourier Transform Infrared Spectroscopy
h	Hours

Hex	Hexane
HRMS	High Resolution Mass Spectra
HSQC	Heteronuclear Single Quantum Coherence
Hz	Hertz
ISC	Intersystem Crossing
IUPAC	International Union of Pure and Applied Chemistry
J	Coupling constant
LUMO	Lowest Unoccupied Molecular Orbital
m	Multiplet (NMR)
MS	Mass Spectrometry
MeOH	Methanol
MeCN	Acetonitrile
min	Minute
mL	Mililitre
mp	Melting point
MW	Microwave
NMR	Nuclear Magnetic Resonance
Pd(dba)$_2$	Bis(dibenzylideneacetone)palladium(0)
Pd$_2$(dba)$_3$	Tris(dibenzylideneacetone)dipalladium(0)
r.t.	Room temperature
s	Second(s)
s	Singlet (NMR)
t	Triplet (NMR)
TEA	Triethylamine

THF	Tetrahydrofuran
TLC	Thin Layer Chromatography
TMS	Trimethylsilyl
UV	Ultraviolet
UV-Vis	Ultraviolet-visible
yr.	Year(s)

INDEX

CHAPTER I

INTRODUCTION

1.1.- NUCLEAR PROCESSES

In 1934, Enrico Fermi explained the β-decay.[1] This nuclear reaction consists of the emission of a fast electron (or positron) from a nucleus. Thus, a neutron can be decay to a proton, with the concomitant emission of an electron and an antineutrino is a β^- decay:

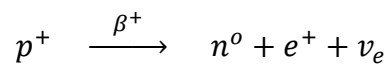$$n^o \xrightarrow{\quad \beta^- \quad} p^+ + e^- + \bar{\nu}_e$$
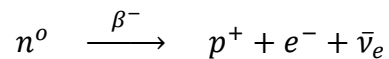
Similarly, a proton can be transformed into a neutron with the emission of a positron and a neutrino:

$$p^+ \xrightarrow{\quad \beta^+ \quad} n^o + e^+ + \nu_e$$

One year later, Maria Goeppert-Mayer calculated and applied the probability of simultaneous emission of two electrons and two neutrinos from two neutrons present in the same nucleus.[2] Double beta decay ($\beta\beta2\nu$) is a very unusual radioactive process in which a nucleus (Z, A), with Z protons and mass number A, decays to a final nucleus (Z+2, A) emitting two electrons and two neutrinos. For this process to occur, the initial species has to be less bound than the final nucleus. Furthermore, whereas in beta decay, the Z+1 nucleus is stronger than Z+2 and, for this reason, only occurs a single decay, in double beta decay processes, Z+2 and Z nuclei are more strongly bound than Z+1. Despite its rarity, there are 11 nuclei susceptible to this decay (i.e. ^{48}Ca, ^{76}Ge, ^{82}Se, ^{130}Te, ^{136}Xe, or ^{238}U).[3]

[1] Fermi, E. I. *Zeitschrift für Phys.* **1934**, *88*, 161–177.
[2] Goeppert-Mayer, M. *Phys. Rev.* **1935**, *48*, 512–516.
[3] Barabash, A. S. *Nucl. Phys. A* **2015**, *935*, 52–64.

Figure 1.- Some of the elements susceptible to double beta decay.

Two modes can be distinguished for double beta decay:

The regular two-neutrino double-beta decay mode (*ββ2ν*): This process involves two synchronized beta decays to yield two electronic antineutrinos ν_e and a nucleus with two additioned protons:

$$(Z, A) \rightarrow (Z + 2, A) + 2e^- + 2\bar{\nu}_e$$
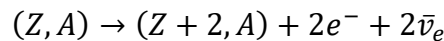
It has been repeatedly observed in numerous isotopes with typical lifetimes in the order of 10^{18} -10^{21} years.

The neutrinoless double-beta decay mode (*ββ0ν*):

$$(Z, A) \rightarrow (Z + 2, A) + 2e^-$$
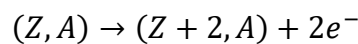
This is the most interesting mode for double beta decay processes, proposed by Wendell H. Fury in 1939.[4] This process violates the total lepton number conservation so that is only possible if neutrinos, in contrast to all the other known fermions, are Majorana particles,[5] namely, particles identical to their antiparticles.

The empirical demonstration of neutrinoless double beta decay would change the view about the standard model of matter, having deep implications in particle physics and cosmology, helping to understand the leptogenesis[6] and giving a potential explanation for

[4] Furry, W. H. *Phys. Rev.* **1939**, *56*, 1184–1193.
[5] Majorana, E. *Nuovo Cim.* **1937**, *14*, 171-184.
[6] Sakharov, D. *Sov. Phys. - Uspekhi* **1991**, *34*, 392–393.

the cosmic asymmetry between matter and antimatter.[7] Moreover, the really low mass of the neutrino, in comparison with other leptons, could be explained by Majorana neutrinos and the "see-saw" mechanism.[8]

Ever since, the aim of particle physicists working in this field was to find signs and evidence of the existence of neutrinoless double beta decay, $\beta\beta0\nu$, in various isotopes, without a conclusive result. One issue concerning the detection of $\beta\beta0\nu$ is its half-life or lifetime $T_{1/2}^{0\nu}$. Nowadays, it has already known that nucleus of the isotope ^{136}Xe is the best to obtain the lowest limit on the lifetime of $\beta\beta0\nu$ processes, for which $T_{1/2}^{0\nu} > 10^{26}$ yr.[9] For some time now, the goal is to improve the sensitivity to $T_{1/2}^{0\nu}$, gaining as far as two orders of magnitude.[10] The way to reach the objective is doing experiments with very large exposure, measured in ton-years, and an actually great ability to minimize or, even better, to suppress background signals from false events. The most common background is the $\beta\beta2\nu$. As far as the energy of the emitted electrons is concerned, the energy for $\beta\beta2\nu$ process is lower than the neutrinoless mode, so the use of a detector with excellent energy resolution would be desirable. In the endpoint of energy (Q), the $\beta\beta2\nu$ process is almost absolutely suppressed by kinematics and the contamination of the decay to the $\beta\beta0\nu$ signal turns out to be very small if the detector has good energy resolution.[11]

---

[7] Fukugita, M.; Yanagida, T. *Phys. Lett. B* **1986**, *174*, 45–47.

[8] a) Gell-Mann, M.; Pierre Ramond, S.; Slansky, R. In *Conf. Proc.*; **1979**; Vol. *C790927*, pp 315–321. b) Yanagida, T. In *Conf. Proc.*; **1979**; Vol. *C7902131*, pp 95–99. c) Mohapatra, R. N.; Senjanović, G. *Phys. Rev. Lett.* **1980**, *44*, 912–915.

[9] Gando, A.; Gando, Y.; Hachiya, T.; Hayashi, A.; Hayashida, S. and KamLAND-Zen Collaboration. *Phys. Rev. Lett.* **2016**, *117*, 082503.

[10] Gomez-Cadenas, J. J. **2019**. ArXiv ID: 1906.01743

[11] Elliott, S. R.; Vogel, P. *Annu. Rev. Nucl. Part. Sci.* **2002**, *52*, 115–151.
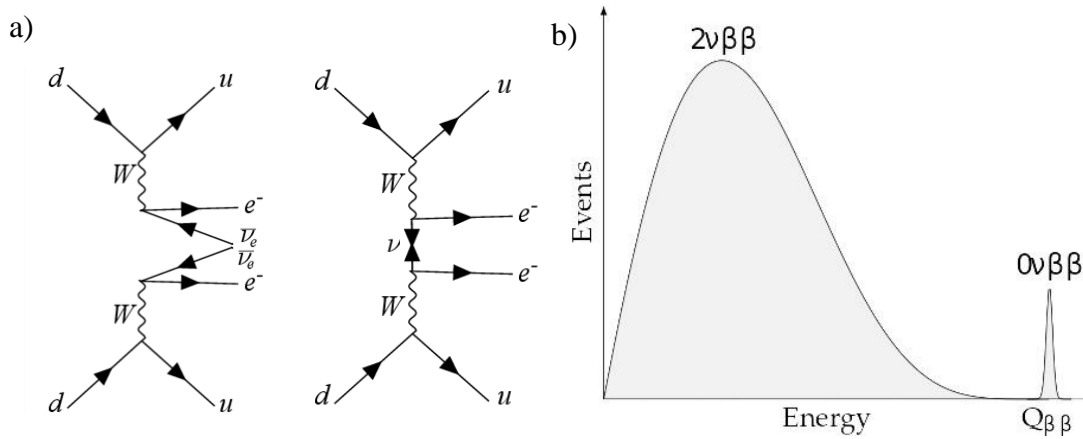
Figure 2.- Feynman diagram of the a) 2-neutrino mode double-beta decay and 0-neutrino mode (2νββ). b) Model of b energy spectrum of the two modes. A spread curve for *2νββ* on the left and a clear peak for the *0νββ* on the right.

The two neutrino mode (*ββ2ν*) has been measured for 12 isotopes to date and falls within the Standard Model of particles.[12] The corresponding Feynman diagram for such process is shown in Figure 2.a. The total energy in the decay is the difference in masses between the mother and the daughter isotope, for example, the masses of ^{136}Xe and ^{136}Ba, respectively. The total energy is distributed between four particles in the case of the two-neutrino mode, two electrons and two neutrinos. For this reason, if the energy of the two electrons is summed, a continuous spectrum is obtained. In the case of the neutrinoless mode (*ββ0ν,* Figure 2.b), all the energy goes to the two electrons, therefore the signal is monochromatic and located exactly at Qββ. This value is simply the aforementioned difference of masses. Figure 2.b shows schematically the contributions of both processes to the energy spectrum of the two electrons.

One of the best way to discern the correct signal between *ββ2ν* processes is the detection of the daughter atom. That atom is located two steps ahead in the periodic table relative to the initial species. In the case of ^{136}Xe, the decay will be ^{136}Xe → ^{136}Ba^{2+} + 2e^{-} + (2$\bar{\nu}_e$), giving a barium cation as the most likely outcome from xenon gas. In isolated xenon gas, no known radioactive process will produce a cation of barium as a result, in coincidence with two electrons. So, if the ^{136}Xe is the candidate, Ba^{2+} is the only cation without any other species, the next step would be the use of a highly sensitive Ba^{2+} detection technique

---

[12] Renner, J.; Díaz López, G.; Ferrario, P.; Hernando Morata, J. A.; Kekic, M. and NEXT Collaboration. *J. High Energ. Phys* **2019**, *2019*, 1–13.

in order to simplify the detection of *ββ0ν*. Using barium as target to demonstrate the neutrinoless double beta decay from ^{136}Xe isotope was proposed by Moe in 1991,[13] which has led to an increase in research in this field over the last 20 years.[14]

Recently the nEXO collaboration[15] has used the counting of individual barium atoms in a solid xenon matrix by scanning a focused laser through a sapphire window. This is a promising step for barium tagging in liquid xenon.

In 2015, a Ba^{2+} fluorescent sensor that could be combined within a high-pressure gas xenon Time Projection Chamber (TPC) was proposed by Prof. David Nygren.[16] This idea is the basis for the NEXT Collaboration. In this chamber, when a beta decay event occurs, one Xe atom will lose two neutrons in the form of electrons and the corresponding Ba^{2+} cation will be formed.

The basic design of the NEXT detector is as follows: first, an electromagnetic field is applied to both sides of the detector. In this way, the electrons will travel towards the positively charged area (anode) of the detector. Once the electrons have been mapped and their energy and drift properly checked, it is possible to anticipate the trajectory of the more weighted and slower Ba^{2+} cation and therefore its arrival on the cathode, on which there is a monolayer of fluorescent sensors able to capture the daughter cation. If the emission spectra of the sensor are different for the free and coordinated states, it is possible to detect the cation with an adequate signal over background noise.[17]

---

[13] Moe, M. K. *Phys. Rev. C* **1991**, *44*, R931.

[14] a) Danilov, M.; DeVoe, R.; Dolgolenko, A.; Giannini, G.; Gratta, G.; Picchi, P.; Piepke, A.; Pietropaolo, F.; Vogel, P.; Vuilleumier, J. L.; Wang, Y. F.; Zeldovich, O. *Phys. Lett. Sect. B Nucl. Elem. Part. High-Energy Phys.* **2000**, *480*, 12–18. b) Sinclair, D. Sinclair, D.; Rollin, E.; Smith, J.; Mommers, A.; Ackeran, N.; Aharmin, B.; Auger, M.; Barbeau, P. S.; Benitez-Medina, C.; Breidenbach, M.; Burenkov, A.; Cook, S.; Coppens, A.; Daniels, T.; de Devoe, R.; Dobi, A.; Dolinski, M. J.; Donato, K.; Fairbank, W.; Farine, J.; Giroux, G.; Gornea, G.; Graham, K.; Gratta, G.; Green, M.; Hagemann, C.; Hall, C.; Hall, K.; Hallman, D.; Hargrove, C.; Herrin, S.; Kaufman, L. K.; Leonard, D. S.; Leport, F.; MacKay, D.; MacLennan, R.; Mong, B.; Díez, M.; Müller, R.; Neilson, R.; Niner, E.; Odian, A.; O'Sullivan, K.; Ouellet, C.; Piepke, A.; Pocar, A.; Prescott, C. Y.; Pushkin, K.; Rowson, P. C.; Slutsky, S.; Stekhanov, V.; Twelker, K.; Voskanian, N.; Vuilleumier, J. L.; Wichoski, U.; Wodin, J.; Yang, L.; Yen, Y. R. *J. Phys. Conf. Ser.* **2011**, *309*, 1–8. c) Mong, B.; Cook, S.; Walton, T.; Chambers, C.; Craycraft, A. and NEXO Collaboration. *Phys. Rev. A - At. Mol. Opt. Phys.* **2015**, *91*, 022505.

[15] Chambers, C.; Walton, T.; Fairbank, D.; Craycraft, A.; Yahne, D. R. and nEXO Collaboration. *Nature* **2019**, *569*, 203–207.

[16] Nygren, D. R., *J. Phys. Conf. Ser.* **2015**, *650*, 012002.

[17] a) Martín-Albo, J.; Muñoz Vidal, J.; Ferrario, P.; Nebot-Guinot, M.; Gómez-Cadenas, J. J. and NEXT Collaboration. *J. High Energ. Phys.* **2016**, *2016*, 1–30. b) Álvarez, V.; Borges, F. I. G. M.; Cárcel, S.; Carmona, J. M.; Castel, J.; Catalá, J. M. and NEXT Collaboration. *J. Instrum.* **2012**, *7*. c) Ferrario, P.; Benlloch-Rodríguez, J. M.; Díaz López, G.; Hernando Morata, J. A.; Kekic, M. and NEXT Collaboration. *J. High Energ. Phys.* **2019**, *2019*, 1–20.
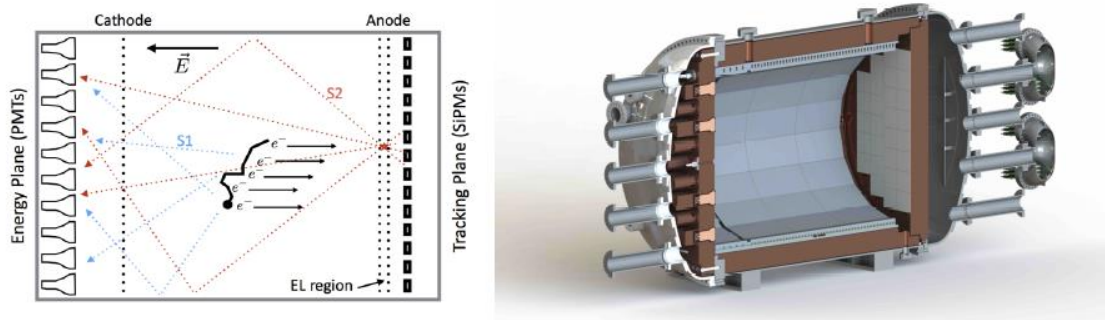
Figure 3.- On the left, schematic diagram of chamber operation. On the right, rendering of the TPC.

Figure 4.- NEXT Sensor in Canfranc Underground Laboratory (LSC).

The TPC device is a widely used detector in particle physics. In the recent years, its use has grown significantly for the experiments that search dark matter or neutrinoless double beta decay. The main advantage of using gaseous TPCs instead of liquid chambers is the ability to obtain a three-dimension image of particle tracks (Topological signal). This represents a useful tool to discriminate the signal expected from the background.[17, 18]

In this respect, the topological signal of a *ββ0ν* decay consists of two electrons originating from the same spot, while the background comes from the high energy gamma photons of the radioactive environment and detector components. The difference between both sources can be seen in the final spectra (*vide infra*).[17c]

---

[18] Gomez-Cadenas, J. J.; Martin-Albo, J.; Mezzetto, M.; Monrabal, F.; Sorel, M. *Riv. Nuovo Cim.* **2011**, *35*, 29–98.
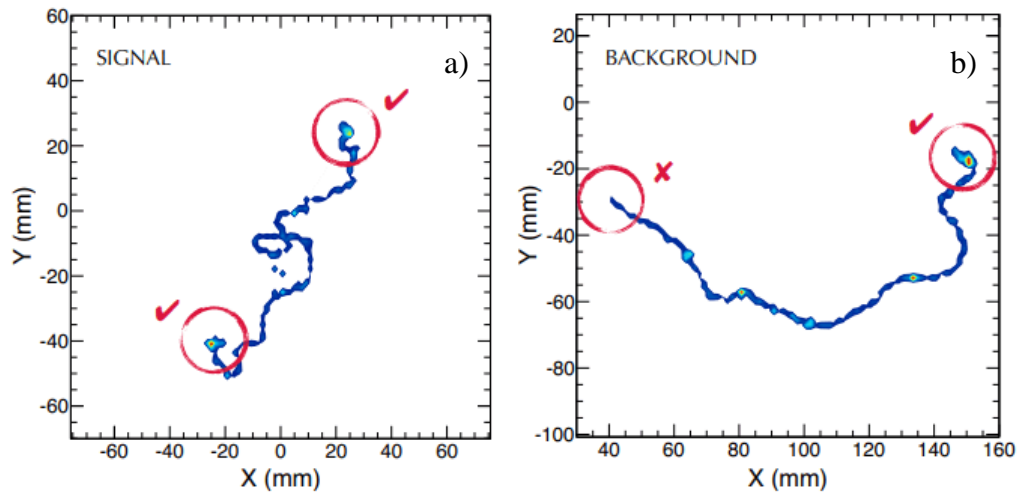
Figure 5.- Monte Carlo simulation of signal and background events in 136Xe gas at 15 bar.[17c]

As can be seen in Figure 5, a signal from a double beta decay process (left) has two endpoints (blobs) joined by a uniform energy thread. In contrast, the background signal (right) has only one blob.

To date, all efforts to demonstrate neutrinoless double beta decay have been aimed at detecting electron traces. Recently, the NEXT collaboration has published a paper on the NEXT-White experiment.[19] In this work the authors demonstrate, for the first time, the sensibility of electronic tracking in an experimental way, since it can distinguish between events with a single blob and others with two blobs.

---

[19] Novella, P.; Sorel, M.; Usón, A.; Almazán, H; Aparicio, B. and NEXT Collaboration; *Phys. Rev. C* **2022**, *105*, 55501.
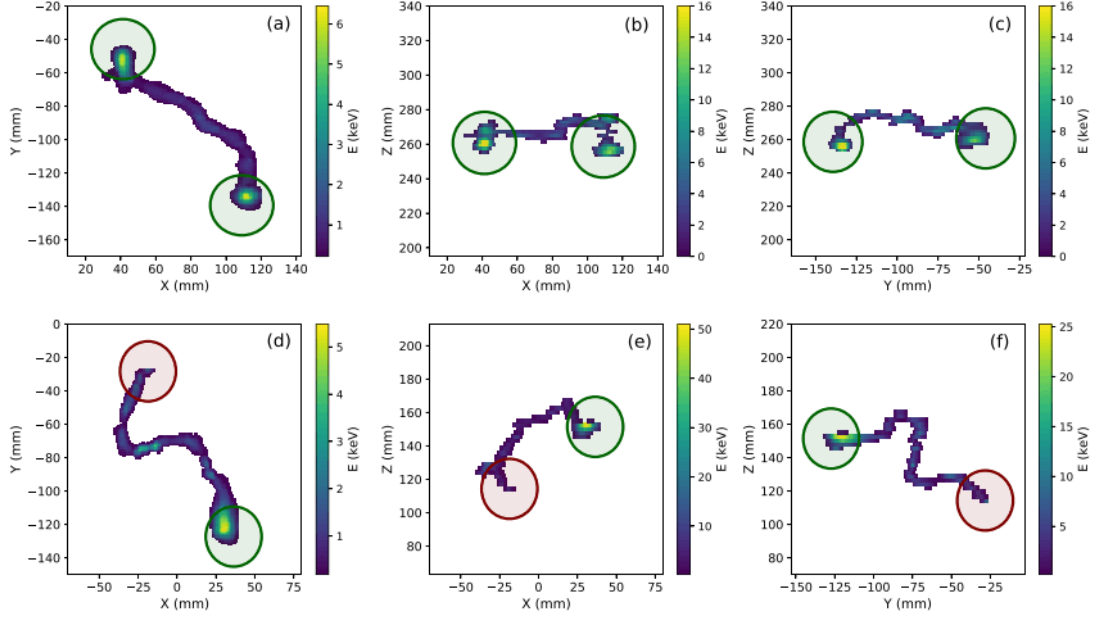
Figure 6.- Electronic tracking measured in NEXT-White Experiment. Figures a), b) and c) show XY, XZ and YZ projection of 3D double electron track. Figures d), e) and f) show the projections in single electron case.[19]

Within the field of double-beta decay experiments of the ^{136}Xe isotope, we can highlight several experiments. Some of them and the main difference with respect to NEXT are mentioned below:

- nEXO: It is the most direct competitor of NEXT. It searches exclusively *ββ0ν*, and uses the same technology (Time Projection Chamber, TPC).[20] They were also the first to use barium tagging.[21] In the case of nEXO, it works with liquid Xenon. (LXe). The main advantage of using LXe is that there are more Xenon atoms in less space, which improves the statistics of the experiment. In addition, working at low temperatures improves the sensitivity of the photodetectors. On the other hand, the cons are that it has a topological signal (which allows rejecting up to 95-97% of the background) and has a worse energy resolution: 2.3% FWHM in Qßß vs. 0.8% of NEXT. This collaboration has also reported works is solid xenon matrix.[22]

[20] Albert, J. B.; Anton, G.; Badhrees, I.; Barbeau, P. S.; Bayerlein, R. and EXO Collaboration, *Phys. Rev. Lett.* **2018**, *120* (7), 072701.

[21] Mong, B.; Cook, S.; Walton, T.; Chambers, C.; Craycraft, A. and nEXO Collaboration, *Phys. Rev. A* **2015**, *91* (2), 022505.

[22] Chambers, C.; Walton, T.; Fairbank, D.; Craycraft, A.; Yahne, D. R. and nEXO Collaboration. *Nature* **2019**, *569*, 203–207.
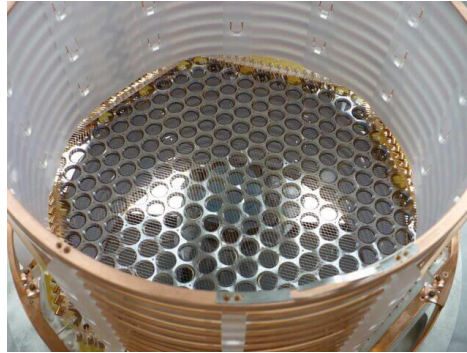
Figure 7.- Photograph of nEXO detector.

- DARWIN: It also uses LXe-TPC technology, but with natural Xenon (not enriched) because their primary scientific goal is searching for Dark Matter. Therefore it only has the natural abundance of ^{136}Xe (9%). This project has reported a better energy resolution than that obtained by nEXO (1.8%).[23] (Figure 8.a)

- KamLAND-Zen: This collaboration works with LXe but it is not TPC, so it is not a direct technological competitor with NEXT. However, the best limit for the lifetime of a *ββ0ν* isotope was obtained by them, corresponding to $T_{1/2}^{0\nu} >$ 1.07·10^{26} yr for the decay of ^{136}Xe.[24] (Figure 8.b)

- PandaX: It is the project most similar to NEXT. This group uses enriched xenon gas. The reported topological signal is good but their energy resolution is worse (3%) than that of NEXT.[25] (Figure 8.c)
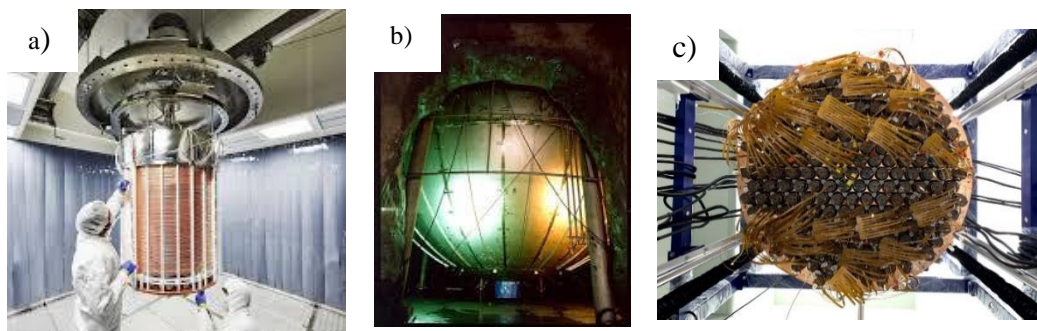

Figure 8.- Photographs of a) DARWIN detector, b) KamLAND-Zen detector, c) PandaX detector.

[23] Aalbers, J.; Agostini, F.; Alfonsi, M.; Amaro, F. D.; Amsler, C. and DARWIN Collaboration, *J. Cosmol. Astropart. Phys.* **2016**, *2016* (11), 017–017.

[24] Gando, A.; Gando, Y.; Hachiya, T.; Hayashi, A.; Hayashida, S. and KamLAND-Zen Collaboration, *Phys. Rev. Lett.* **2016**, *117* (8), 082503.

[25] Wang, S. *Nucl. Instrum. Methods Phys. Res. A* **2020**, *958*, 162439.

Despite this preference for this xenon isotope, there are other experiments using other isotopes, such as CUORE,[26] which works with ^{130}Te, or GERDA,[27] which searches for neutrinoless double beta decay with the ^{76}Ge isotope.
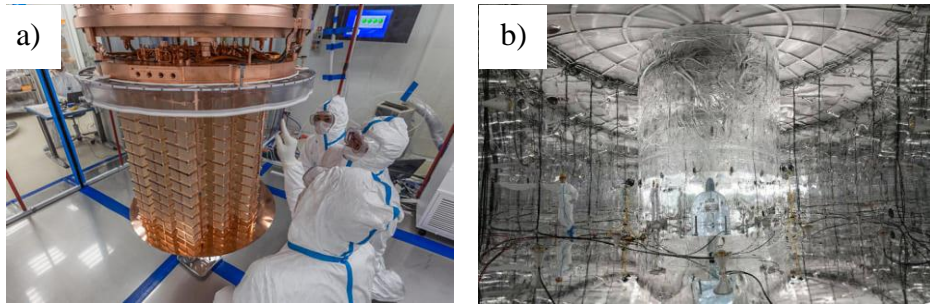
Figure 9.- CUORE detector (a). GERDA detector (b).

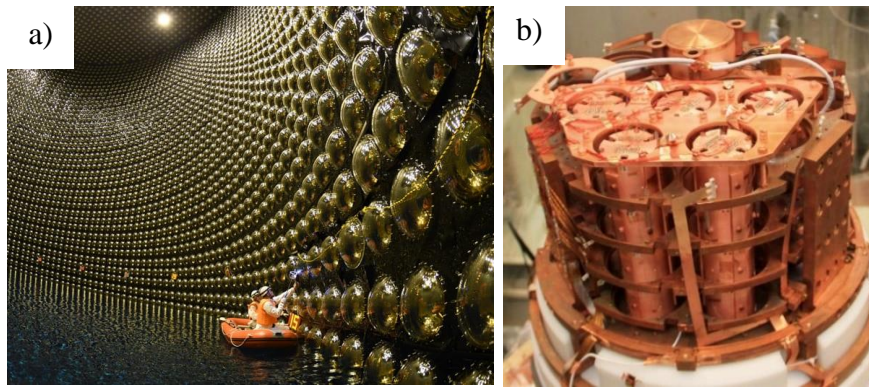***Figure 10.-*** Other Neutrinoless double beta decay detectors. a) SuperKamiokande and b) CUPID.

---

[26] Alduino, C.; Alessandria, F.; Alfonso, K.; Andreotti, E.; Arnaboldi, C. and CUORE Collaboration, *Phys. Rev. Lett.* **2018**, *10*, 132501.

[27] Agostini, M.; Bakalyarov, A. M.; Balata, M.; Barabanov, I.; Baudis, L. and GERDA Collaboration, *Phys. Rev. Lett.* **2018**, *120*, 132503.

1.2.- CHEMICAL SENSORS

As mentioned in the previous section, one of the traces that would be left by neutrinoless double beta decay is a daughter cation. Therefore, another way to detect this process would consist of detecting the corresponding positively charged species. To this end, the use of a chemical sensor would be a suitable tool.

This analytical tool has been (and it is being) applied to many technological fields, such as food industry (poisons), security (explosives, drugs), quality tests and, other scientific areas that require compounds or materials with the ability to detect a very wide variety of analytes under different conditions. These analytes include small organic molecules,[28] cations,[29] anions,[30] biological macromolecules (peptides[31] or oligonucleotides[32]) and larger species such as, whole cells and microorganisms.[33] A couple of examples of sensor systems with millions of uses per day in the world are blood glucose-meters and pregnancy tests.

To successfully design a chemical sensor it is necessary to consider the following five factors:

- The <u>analyte</u> (or target)
- The <u>recognition part</u> of the sensor and how it is going to interact with the sample.
- The <u>translator</u> moiety, which shows a visual or measurable response when the detector is interacting with the analyte.
- The working <u>environment</u> (organic solvent, aqueous solution, cell media, gas phase…).
- <u>Other experimental parameters</u> as concentration, temperature, pressure…

[28] a) Chaudhuri, S.; DIScenza, D. J.; Smith, B.; Yocum, R.; Levine, M. *New J. Chem.* **2017**, *41*, 14431–14437. b) Beyeh, N. K.; Jo, H. H.; Kolesnichenko, I.; Pan, F.; Kalenius, E.; Anslyn, E. v.; Ras, R. H. A.; Rissanen, K. *J. Org. Chem.* **2017**, *82*, 5198–5203.

[29] Harding Lepage, P.; Peytavi, R.; Bergeron, M. G.; Leclerc, M. *Anal. Chem.* **2011**, *83*, 8086–8092.

[30] Chi, X.; Peters, G. M.; Hammel, F.; Brockman, C.; Sessler, J. L. *J. Am. Chem. Soc.* **2017**, *139*, 9124–9127.

[31] Zhang, R.; Sung, S. H. P.; Feng, G.; Zhang, C. J.; Kenry; Tang, B. Z.; Liu, B. *Anal. Chem.* **2018**, *90*, 1154–1160.

[32] a) Ruehl, C. L.; Lim, A. H. M.; Kench, T.; Mann, D. J.; Vilar, R. *Chem. – A Eur. J.* **2019**, *25*, 9691–9700. b) Pont, I.; González-García, J.; Inclán, M.; Reynolds, M.; Delgado-Pinar, E.; Albelda, M. T.; Vilar, R.; García-España, E. *Chem. - A Eur. J.* **2018**, *24*, 10850–10858.

[33] a) Gade, A. M.; Meadows, M. K.; Ellington, A. D.; Anslyn, E. V. *Org. Biomol. Chem.* **2017**, *15*, 9866–9874. b) Disney, M. D.; Zheng, J.; Swager, T. M.; Seeberger, P. H. *J. Am. Chem. Soc.* **2004**, *126*, 13343–13346. c) Fang, Y.; Ramasamy, R. *Biosensors* **2015**, *5*, 537–561.

All of these factors are essential but, maybe, the first three have the key to achieve great values in two important parameters: selectivity and sensitivity.

Selectivity is an analytical parameter that indicates the ability of the sensor to distinguish a particular analyte against other species (interferences). Sensitivity is determined by the response versus concentration of the analyte; greater responses at low concentrations will provide better values of sensitivity. In terms of analytical parameters, best sensors will posses good selectivity, high levels of sensitivity for low concentrations of analyte and the ability to apply the sensor in multiple environmental conditions.[34]

The aspects related to each of the previously indicated components of a chemical sensor are shown below:

1.2.1.- The analyte

The first question to be answered when designing a chemosensor is: *"What needs to be detected?"*. The nature of the target will dictate all the design. For atomic species and small molecules (anions, cations, or neutral species) the detector and, specifically, the recognition moiety, will normally catch and cover all the analyte. For this reason, this part of the structure will be larger than the ones usually employed in detectors for macromolecules or large species as peptides or cells.

1.2.2.- The recognition part

Once the analyte is known, the next step is to evaluate how that analyte can be recognized (coordinated, bonded, etc.); this is, to choose an efficient and selective binding group. This association analyte-chemosensor can occur via covalent or non-covalent interactions. The last one is the most commonly used, due to its reversibility. Instead, covalent binding molecules are single-use sensors.

Some of non-covalent interactions could be Van der Waals forces, hydrogen bond, $\pi-\pi$ stacking (in the case of aromatic systems) or ion-π electrostatic interactions. It is possible that combinations of these interactions appears in the same compound.

---

[34] *IUPAC Compendium of Chemical Terminology*; IUPAC, 2009.

Electrostatic interaction is defined as the attraction of two contrarily charged (or partially charged) species. In gas phase, these interactions are so strong, due to the absence of any interaction with the solvent.

In most of the examples reported in the literature, the chemical structure of the sensor rely on the presence of heteroatoms, due to its Lewis base character. In many cases, these atoms are nitrogen atoms. For example, works such as those published by Zang & Han[35] in 2017 or Woodruff & O'Halloran[36] in 2019 use nitrogen heterocycles and aliphatic amines as centers to capture metal cations, such as cadmium or zinc (Figure 11).
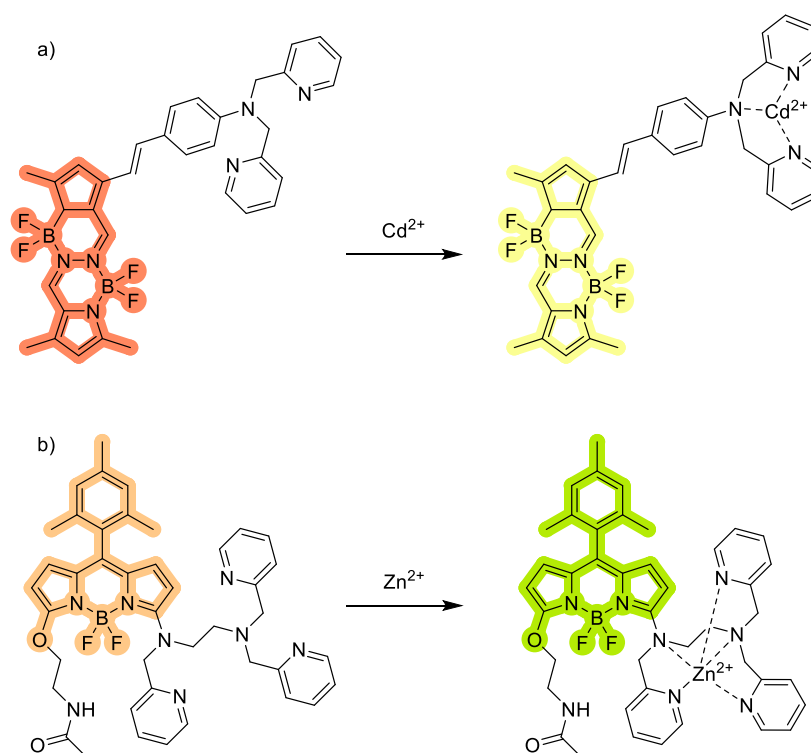

Figure 11.- Fluorescence bicolor sensors to capture a) cadmium[35] and b) zinc.[36]

In addition, it is worth mentioning that these sensors are bicolor. This feature is vital for the design of our sensor. The importance of this behavior is explained in the next subsection ("*1.2.3.- Translator Moiety*"). In the following discussion we present other bicolor sensors.

[35] Cheng, D.; Liu, X.; Xie, Y.; Lv, H.; Wang, Z.; Yang, H.; Han, A.; Yang, X.; Zang, L. A. *Sensors,* **2017**, *17*, 2517.

[36] Garwin, S. A.; Kelley, M. S.; Sue, A. C.; Que, E. L.; Schatz, G. C.; Woodruff, T. K.; O'Halloran, T. v. *J. Am. Chem. Soc.* **2019**, *141*, 16696–16705.

Thus, both examples gathered in Figure 12 correspond to bicolor sensors for Zn^{2+} possessing 2,2'-pyridine and 2-(pyridyn-2-yl)thiazole scaffolds.
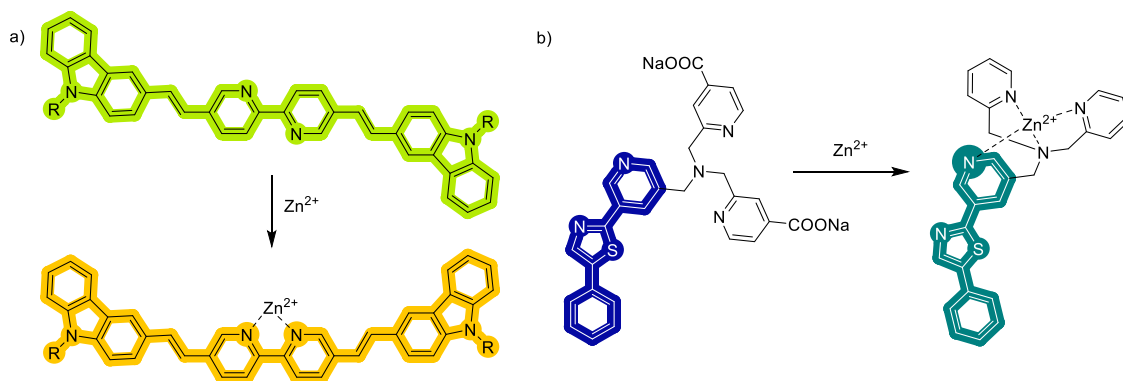

Figure 12.- Structures of zinc bicolor dyes based on metal-nitrogen interaction. Developed by a) Zhao & Ajayaghosh sensor[37] and b) Rosenberg & Fahrni.[38]

On the other hand, sensors incorporating coordinating groups with other heteroatoms, such as oxygen or sulfur, are also described in the literature. Short polyethylene thiaglycol chains or similar are described in several works as in the case of Zeng and collaborators[39] (Figure 13).
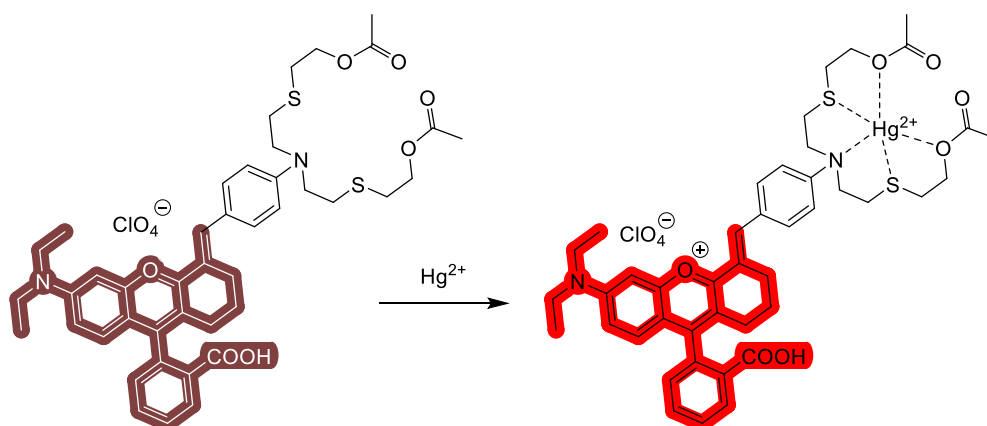

Figure 13.- Structure of mercury bicolor dye based on different heteroatoms.

---

[37] Divya, K. P.; Sreejith, S.; Ashokkumar, P.; Yuzhan, K.; Peng, Q.; Maji, S. K.; Tong, Y.; Yu, H.; Zhao, Y.; Ramamurthy, P.; Ajayaghosh, A. *Chem. Sci.* **2014**, *5*, 3469–3474.

[38] Bourassa, D.; Elitt, C. M.; McCallum, A. M.; Sumalekshmy, S.; McRae, R. L.; Morgan, M. T.; Siegel, N.; Perry, J. W.; Rosenberg, P. A.; Fahrni, C. J. *ACS Sens.* **2018**, *3*, 458–467.

[39] Jiao, X.; Liu, C.; He, S.; Zhao, L.; Zeng, X. *Dyes Pigm.* **2019**, *160*, 86–92.

In this work, it can be seen how the sensor structure has two aliphatic appendages with oxygen and sulfur atoms that use their lone electron pairs to capture the metal cation.

If these aliphatic chains close into a cycle, the resulting structure is a crown ether. The main adventage of these coordinating groups is that the system is preorganized, thus allowing to minimize the entropic penalty associated with coordination. The main issue of these cyclic systems is that the restriction of conformational freedom makes these moieties less tolerant to structural changes, although this can reflect in a higher selectivity.

The crown ethers, described and developed by Charles Pedersen in 1967,[40] are macrocyclic compounds that consist of a ring containing several ether groups.

The number of -CH_2CH_2O- units can give rise to macrocycles up to 18, 21, 24… atoms. Furthermore, it is also possible to introduce other heteroatoms as nitrogen or sulfur.[41]

This particular family of ethers has been widely used in alkaline and alkaline earth metals sensors.[42] In this case, it is important to know the size of the crown ether and choose the correct one depending upon the ionic radius of the cation (Figure 14).

---

[40] Pedersen, C.P. *J. Am. Chem. Soc.*, **1967**, *89*, 7017–7036.

[41] Gokel, G. W.; Leevy, W. M.; Weber, M. E. *Chem. Rev.* **2004**, *104*, 2723−2750.

[42] a) Sazonov, P. K.; Minacheva, L. K.; Churakov, A. v.; Sergienko, V. S.; Artamkina, G. A.; Oprunenko, Y. F.; Beletskaya, I. P. *J. Chem. Soc. Dalt. Trans.* **2008**, 5, 843–850. b) Hou, C.; Urbanec, A. M.; Cao, H. *Tetrahedron Lett.* **2011**, *52*, 4903–4905. c) Kimura, K.; Mizutani, R.; Yokoyama, M.; Arakawa, R. **2000**, 7, 5448–5454. d) Yang, L.; Liao, D.; Wu, A.; Yan, H. *Tetrahedron Lett.* **2017**, *58*, 889–891.
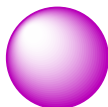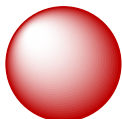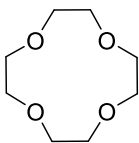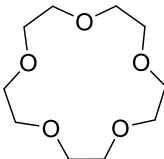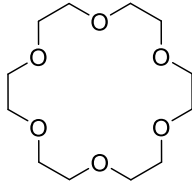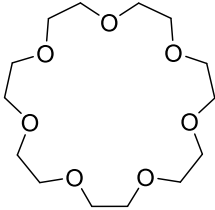
Li⁺	Na⁺	K⁺	Rb⁺	Cs⁺

Pauling Ionic Radius

0.78 Å	0.97 Å	1.33 Å	1.48 Å	1.67 Å

Be^{2+}	Mg^{2+}	Ca^{2+}	Sr^{2+}	Ba^{2+}
0.31 Å	0.65 Å	0.99 Å	1.13 Å	1.35 Å

12-crown-4	15-crown-5	18-crown-6	21-crown-7
1.20 - 1.50 Å	1.70 - 2.20 Å	2.60 - 3.20 Å	3.40 - 4.30 Å

Figure 14.- Comparison of ionic radii (r_i) of different metals and average inner diameters (d_i) of several crown ethers. Notice that for an adequate binding, the condition $r_i \approx (d_i / 2)$ must be fulfilled.

1.2.3.- The translator moiety

This part is determined by the technique to be used to measure the chelation or non-chelation of the analyte by any of the parts described above.

The measurement usually consist of the change of one or more properties of the sensor, such as changes in colour (Absorption-based detection), changes in Raman spectral signals, changes in the mass of the final complex or, as in the case of this work, changes in emission spectra. For this kind of detectors, a photophysical active component is required to show the measurable changes when the analyte is coordinated or bound. The changes of the luminescence activity may occur through an increment (or descent) of emission intensity, the quantum yield, a change in the wavelength of the emission maximum or, in special cases, the ratios of fluorescence-phosphorescence active components.

The nature of this luminescence can be fluorescence or phosphorescence. Both processes are based on the release of a photon from the molecule when it relaxes from an excited estate, going back to the ground state configuration. Nevertheless, there are some differences between them. In fluorescence, the electron promoted to an excited state doesn't change its spin, remaining paired with the electron of the fundamental state (Singlet state, $<s^2> = 0$).This is an allowed relaxation (singlet to singlet), for this reason, its lifetime has values between 10^{-9} and 10^{-6} s. On the other hand, in phosphorescence, the excited electron becomes its spin parallel to its couple (Triplet excited state, $<s^2> = 2\hbar$), doing a formally forbidden relaxation (triplet to singlet) (Figure 15). The phosphorescence average lifetime may range from 10^{-4} to 10^2 s. The well-known Jablonski diagram, shown in Figure 16, graphically summarizes these electronic transitions.[43]
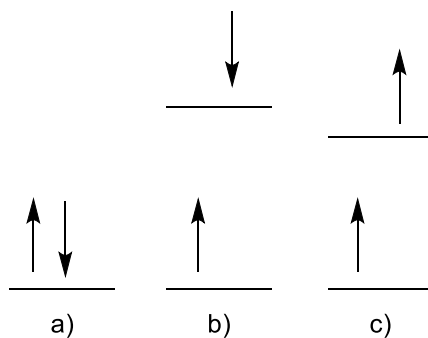

Figure 15.- Electronic spin states. a) Ground singlet state. b) Excited singlet state. c) Excited triplet state.

[43] a) Hanlan, J.; Skoog, D. A.; West, D. M. *Principles of Instrumental Analysis*; **1973**; Vol. 18. b) Lakowicz, J. R. *Principles of Fluorescence Spectroscopy, 3rd Edition*; **2006**.
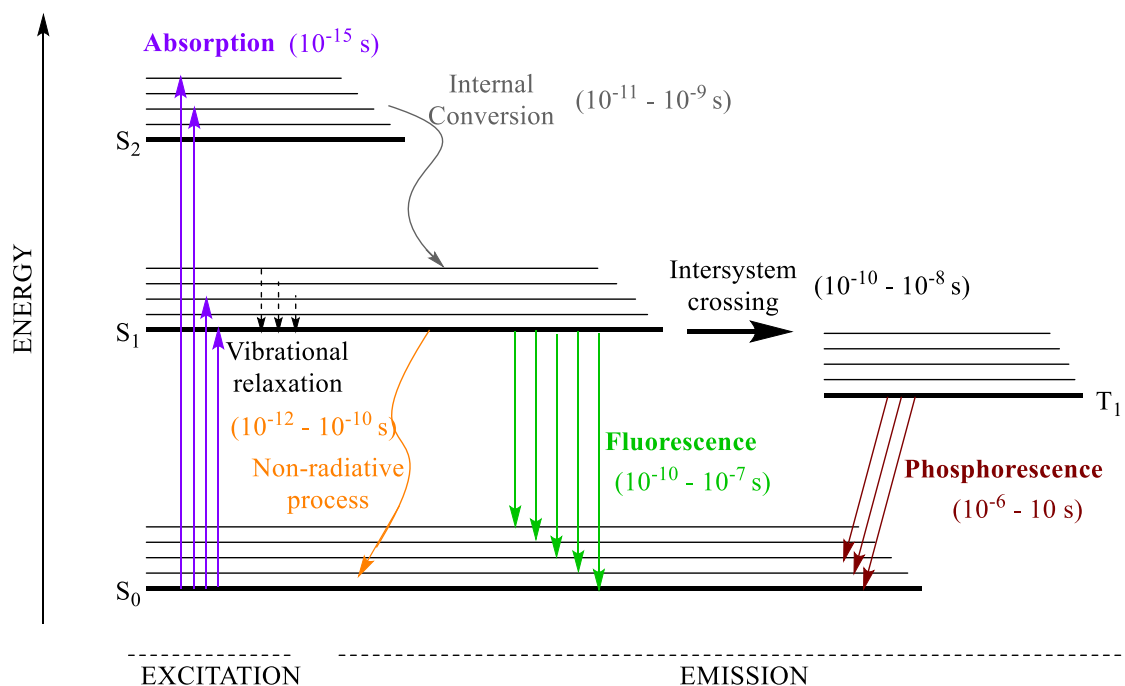
Figure 16.- Jablonski diagram showing fluorescence and phosphorescence emissions, as well as non-radioative $S_1 \rightarrow S_0$ processes. Notice that a fluorescence emission requires a change in geometry from the excited state. Similarly, a phosphorescence emission only can occur via an intersystem crossing of the $S_1 \rightarrow T_1$.

As can be seen in Figure 16, when a molecule is irradiated, it absorbs a photon and goes from the ground state S_0 to the excited state S_2. Usually, the molecule returns to S_0 via a non-radiative transition in which no photon is emitted and, therefore, there is not luminescence. Otherwise, the molecule can suffer a vibrational relaxation and an internal conversion. In the first one, the molecule be placed on a lower vibrational level within the same electronic state. In the internal conversion, the molecule, which is placed in a singlet electronic state, may also go to a lower energy electronic state ($S_2 \rightarrow S_1$) with the same spin multiplicity (singlet). Once the molecule is the new electronic state, its relaxation from S_1 to S_0 is a radiative decay and a photon is released. This decay is called *Fluorescence* and the energy loss before fluorescence is the physical principle according to which Michael Kasha stablished his rule in 1950: "*Luminescence only occurs with appreciable yield from the lowest excited state of a given multiplicity*".[44] Not only fluorescence is possible but also the molecule can change the excited state, from Singlet S_1 to Triplet T_1, through a spin-forbidden transition, a non-radiative process called intersystem crossing (ISC). Although this ISC is forbidden, spin-orbit coupling can

---

[44] *IUPAC Compendium of Chemical Terminology*; IUPAC, 2009.

circumvent restriction thus giving rise to a radiative phosphorescent signal. A consequence of being a forbidden transition is that the lifetimes are longer than those associated with fluorescence (from ms to s).[45] This permits the obtention of time resolved signals, with in turn adds new possibilities to techniques based on luminescence phenomena.

It is important to note that the NEXT experiment is looking for an extremely unusual event. This means that the measurement has to be very clean and, for this reason, it is important to achieve a practically non-existent background. Some research groups are working in the development of an Off-On sensor [46] such as that gathered in Figure 17.
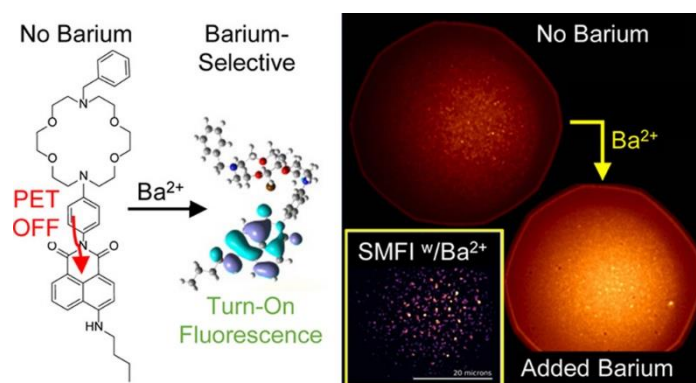
Figure 17.- Schematic image of the Off-On sensor described by Thapa et al.[49] (Reprinted with permission from Ref. 49, Copyright 2021, ACS).

This means that the sensor has practically no fluorescence emission when irradiated in the free state and, once it captures the barium cation, its emission is triggered. This can be very useful for other uses. However, in a process as atypical as double beta decay, a large number of molecules with weak fluorescence can generate, by accumulation, a signal that can cover the emission when the event happens.

The easiest way to avoid this serious drawback is to build a sensor that emits at two wavelengths; one when it is in its free state and one when cation capture occurs. The greater the difference between the two wavelengths, the better the result as the resolution of both curves is higher. The bicolor behavior shown by the molecules may be due to different fluorescence processes. These are based on the electronic structure and how it is affected when the analyte binds to the sensor. Four main types can be distinguished:

---

[45] Engel, T. *Quantum Chemistry & Spectroscopy*, Third Ed.; Pearson, **2013**.

[46] a) Nygren, D. R.; Woodruff, K et al. *Sci.* **2019**, *9*, 1–13. b) Thapa, P., Byrnes, N. et al., *ACS Sens.* **2021**, *6*, 1, 192–202.

Intramolecular Charge Transfer (ICT): [47]

It is based on the polarization of the electronic structure due to its modification between the free and the chelated states. In these systems, an Electron Releasing Group (ERG) yields part of that electron density to an Electron Withdrawing Group (EWG). Depending on the proximity of the boundary orbitals of the EWG and ERG to those of the metal cation, two situations can occur.

When the ERG is closer to the metal cation than the EWG, the ERG $\rightarrow$ M^{n+} interaction will compete with the ERG $\rightarrow$ EWG donation, increasing the ν'_{em} frequency associated with the $S_1 \rightarrow S_0$ fluorescence transition. Because of this, a hypsochromic shift in the emission wavelength will be observed. In the opposite case, a bathochromic shift will be observed, in which the EWG is the closest moiety to the metal cation (Figure 18).
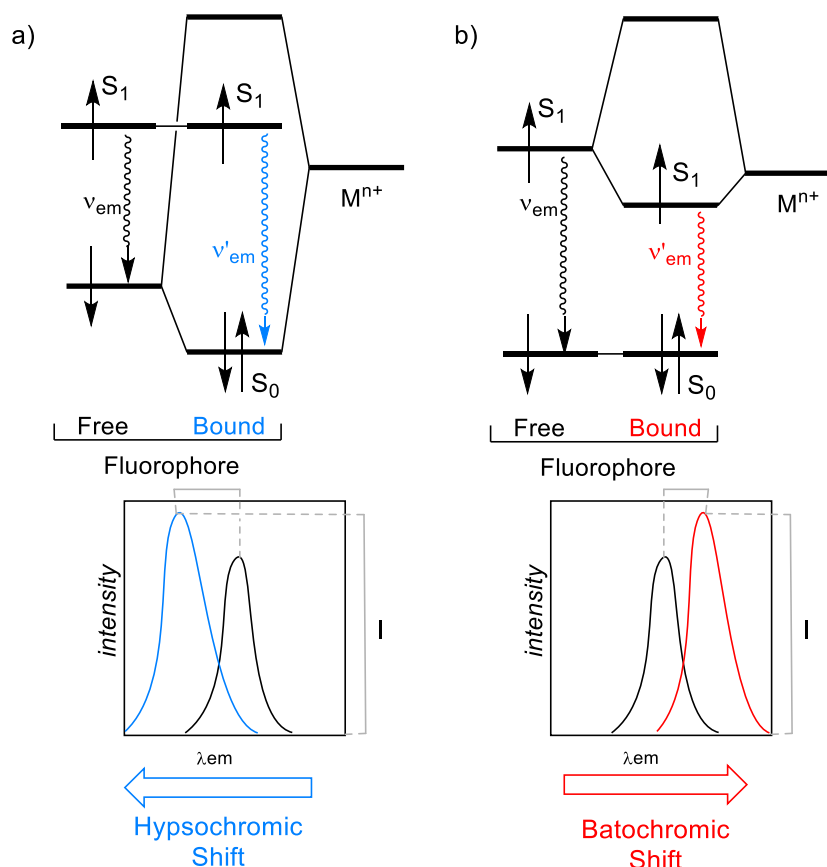
Figure 18.- Schematic figures for Intramolecular Charge Transfer (ICT). a) Frontier Orbital energy levels when ERG is closer to the metal (up) and its effect on fluorescence emission (down). b) Frontier Orbital energy levels when EWG is closer to the metal (up) and its effect on fluorescence emission (down).

[47] a) Freixa, Z.; Rivilla, I.; Monrabal, F.; Gómez-Cadenas, J. J.; Cossío, F. P. *Phys. Chem. Chem. Phys.* **2021**, *23*, 15440–15457. b) Misra, R.; Bhattacharyya, S. P. *Intramolecular Charge Transfer : Theory and Applications*; Wiley-VCH, 2018.

<u>Excimers</u>[48]

Excimers are molecular associates that exist only in excited electronic states. The term stems from the union of "excited" and "dimer". As it can be deduced, this mechanism occurs through the formation of a dimer (homo- or hetero dimer) that is more stable in the excited state S1. Therefore, an excimer originates from the interaction between a fluorophore in the excited state with one in the ground state. If the boundary orbitals of both fluorophores are analyzed, it can be seen how the HOMO-LUMO gap is reduced, generating a red shift (Figure 19).
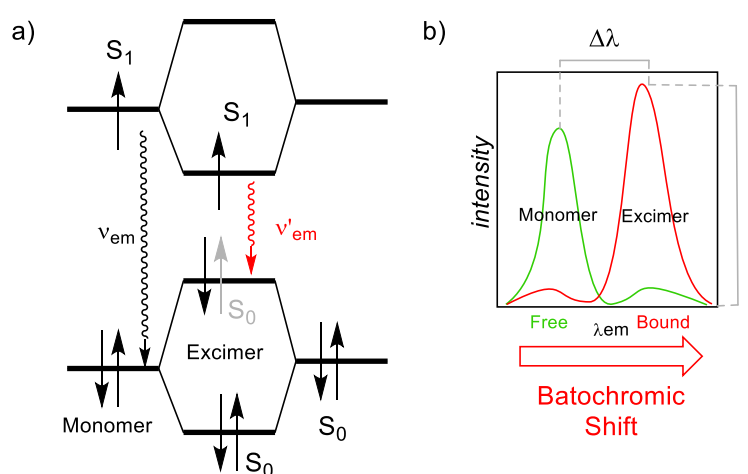
Figure 19.- a) Frontier Molecular Orbitals for monomer and excimer. b) Red shift expected after the formation of excimer.

<u>Förster Resonance Energy Transfer (FRET):</u>[49]

This mechanism is based on the interaction of two fluorophores or two parts of the same fluorophore, an acceptor (A) and a donor (D). Specifically, it is a non-radiative transfer from an excited fluorophore or donor group to an acceptor fluorophore in the ground state. The release of a photon through a fluorescence process by D is absorbed by A, passing to the excited state and carrying out another fluorescence process in A. For this mechanism, a series of conditions must be fulfilled:

---

[48] a) Förster, T. *Angew. Chem. Int. Ed.* **1969**, *8*, 333–343. b) Hoche, J.; Schmitt, H. C.; Humeniuk, A.; Fischer, I.; Mitrić, R.; Röhr, M. I. S. *Phys. Chem. Chem. Phys.* **2017**, *19*, 25002–25015. c) Freixa, Z.; Rivilla, I.; Monrabal, F.; Gómez-Cadenas, J. J.; Cossío, F. P. *Phys. Chem. Chem. Phys.* **2021**, *23*, 15440–15457.

[49] a) Kaur, A.; Kaur, P.; Ahuja, S. *Anal. Methods* **2020**, *12*, 5532–5550. b) Pietraszewska-Bogiel, A.; Gadella, T. W. J. *J. Microsc.* **2011**, *241*, 111–118. c) Freixa, Z.; Rivilla, I.; Monrabal, F.; Gómez-Cadenas, J. J.; Cossío, F. P. *Phys. Chem. Chem. Phys.* **2021**, *23*, 15440–15457.

- Both fluorophores or parts of these must have different excitation wavelengths.
- The emission region of D and the excitation region of A must overlap. Thus, the energy emitted by D, could excite A.
- In the space, both parts must be at a maximum of 10 nm apart.
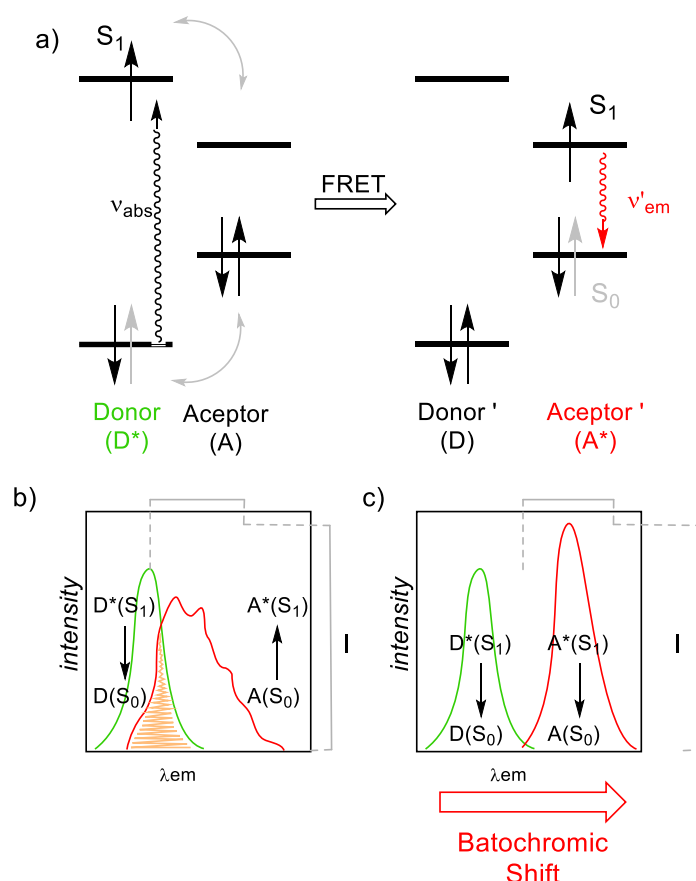
Figure 20.- a) Orbitals energy level diagram in FRET process. b) Overlap of emission spectrum of donor and excitation spectrum of acceptor (in orange). c) Expected bathocromic shift between emission spectra of D and A.

It is worth mentioning the similarity of this mechanism with PET (Photoinduced Electron Transfer).[50] However, the energy released in FRET by the relaxation of D in S_1 is responsible for the excitation of A in S_0. In the case of PET, the electron that is excited in D to the S_1 level of A is transferred. For this reason, D would be left with a positive charge and A with a negative charge. Moreover, since the ground state S_0 of A has its two electrons, that extra electron causes a quenching of the signal, instead of a shift. The last difference is based on the distance between A and D. In the case of transferring an

---

[50] Lakowicz, J. R. *Principles of Fluorescence Spectroscopy*; Springer, 2006.

electron, this distance must be one nm or lower, much smaller than the 10 nm maximum distance allowed in the case of FRET (Figure 21).
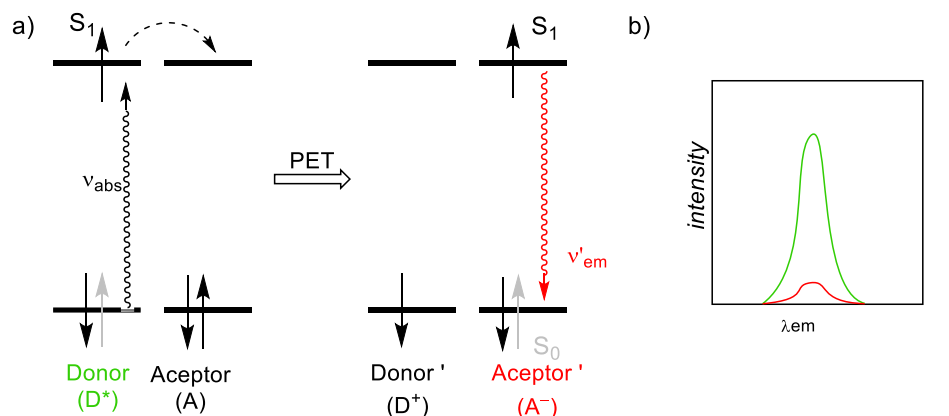
Figure 21.- Schematic orbitals diagram in PET processes. b) Quenching diagram in emission spectra.

Two-component fluorophores:[47a]

These luminescence sensors incorporate a fluorescent compound which, through a single bond rotation process, can connect or disconnect different components. This is caused by the interaction of the metal with the different parts of the molecule, usually with the π-system of aromatic rings. Thus, the conjugation of the π-orbitals of the compound varies depending on the presence or absence of the metal. This causes a change in the emission wavelength (Figure 22).

a)

b)
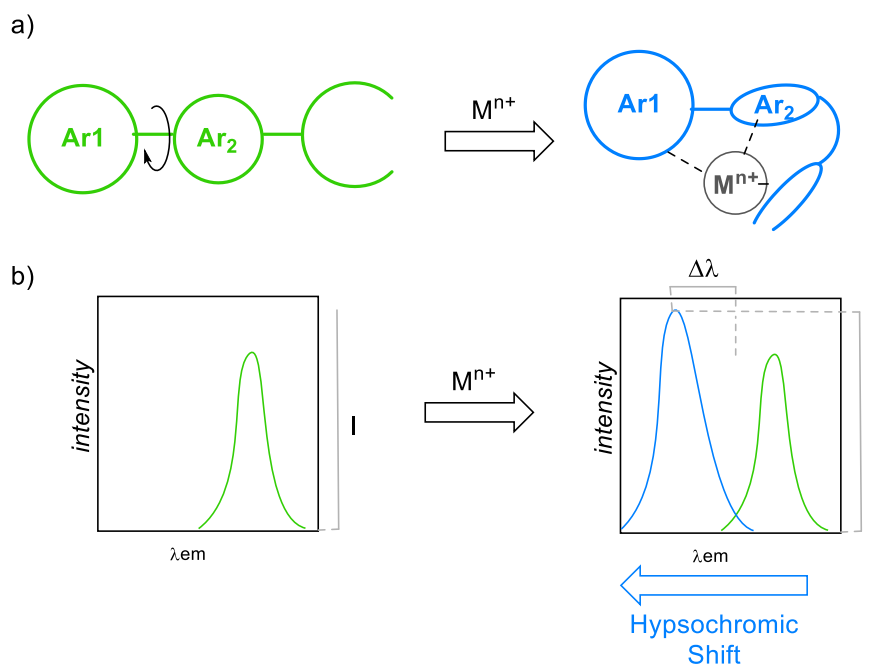
Figure 22.- a) Schematic structures for two component fluorophores in presence and in absence of metal. b) Expected emission spectra for both species.

1.2.4.- The working environment

It is known that the emission spectra of the fluorescent sensors can vary depending upon temperature, pH or other conditions in the medium. As it can be deduced from Section 1.1, in our case the sensor must operate ultimately in gas phase, due to the characteristics of the final NEXT device. However, in this work we will study the sensors in solution (Chapter II) and then we will study the necessary modifications required to anchor it to different surfaces (Chapter III).

1.3.- SURFACE CHEMISTRY

Surface chemistry is a research field in which more and more research has been carried out in recent decades. Recent examples are the antigen and antibody tests for the detection of COVID-19.[51] Scientific areas such as medicine or dentistry are benefiting from the use of nanoparticles or nanodiamonds on which antibiotics can be supported, for instance.[52]

It is important to know the chief features of surface to worked with. Depending on the functional groups present in the material, a molecule must be synthesized accordingly.[53]

Another option is to work on flat surfaces, such as gold, silver or graphene, for example. Not only a molecule can be deposited on them, but chemical reactions, such as the Ullmann reaction, can also take place.[54]

Due to the design of the NEXT experiment, carrying it out in a TPC involves anchoring the molecule on a surface. This anchoring can be accomplished by electrostatic forces or the formation of covalent bonds. The first type of bond is easier to achieve, although it is weaker than covalent linkage. Therefore, it is important to understand the nature and conditions of the experiment to use the most convenient type of interaction.

In both cases, it is necessary to use a functional group suitable for the surface on which the molecule is to be deposited. In order to functionalize the surface, several methods have been described for this deposition. Depending on the surface, pre-treatment with O_2-plasma,[55] treatment with acids or bases, etc. is required. The second step, namely the deposition of the molecule can be done by spraying,[56] immersion of the surface in a

---

[51] a) Feng, M.; Chen, J.; Xun, J.; Dai, R.; Zhao, W.; Lu, H.; Xu, J.; Chen, L.; Sui, G.; Cheng, X.; Sui, G.; Cheng, X. *ACS Sens* **2020**, *5* (8), 2331–2337. b) Liu, G.; Rusling, J. F. *ACS Sens* **2021**, *6* (3), 593–612.

[52] a) Li, Y.; Leung, P.; Yao, L.; Song, Q. W. *J. Hosp. Infect.* **2006**, *62*, 58–63. b) Prokopovich, P.; Köbrick, M.; Brousseau, E.; Perni, S. *J. Biomed. Mater. Res. B Appl. Biomater.* **2015**, *103*, 273–281. c) Lee, D. K.; Kim, S. V.; Limansubroto, A. N.; Yen, A.; Soundia, A.; Wang, C. Y.; Shi, W.; Hong, C.; Tetradis, S.; Kim, Y.; Park, N. H.; Kang, M. K.; Ho, D. *ACS Nano* **2015**, *9*, 11490–11501. d) Qin, J. X.; Yang, X. G.; Lv, C. F.; Li, Y. Z.; Liu, K. K.; Zang, J. H.; Yang, X.; Dong, L.; Shan, C. X. *Mater. Des.* **2021**, *210*, 110091.

[53] a) Hoffmann, K.; Resch-Genger, U.; Mix, R.; Friedrich, J. F. *J. Fluoresc.* **2006**, *16*, 441–448. b) Zhu, G.; Liu, Y.; Sweeney, S.; Chen, S. *Encyclopedia of Interfacial Chemistry: Surface Science and Electrochemistry* **2018**, 711–724. c) Chusuei, C. C. *Encyclopedia of Interfacial Chemistry: Surface Science and Electrochemistry* **2018**, 628–636.

[54] a) Sarasola, A.; Barragán, A.; Vitali, L. *J Am Chem Soc* **2018**, *140*, 15631–15634. b) Barragán, A.; Sarasola, A.; Vitali, L. *Angew. Chem. Int. Ed.* **2020**, *59*, 15599–15602. c) Tenorio, M.; Moreno, C.; Febrer, P.; Castro-Esteban, J.; Ordejón, P.; Peña, D.; Pruneda, M.; Mugarza, A.; Tenorio, M.; Moreno, C.; Febrer, P.; Ordejón, P.; Pruneda, M.; Mugarza, A.; Castro-Esteban, J.; Peña, D. *Adv. Mater.* **2022**, *34*, 2110099. d) Domínguez-Celorrio, A.; Garcia-Fernandez, C.; Quiroga, S.; Koval, P.; Langlais, V.; Peña, D.; Sánchez-Portal, D.; Serrate, D.; Lobo-Checa, J. *Nanoscale* **2022**, *14*, 8069–8077. e) Eisenhut, F.; Kühne, T.; García, F.; Fernández, S.; Guitián, E.; Pérez, D.; Trinquier, G.; Cuniberti, G.; Joachim, C.; Peña, D.; Moresco, F. *ACS Nano* **2020**, *14*, 1011–1017.

[55] Hoffmann, K.; Resch-Genger, U.; Mix, R.; Friedrich, J. F. *J. Fluoresc.* **2006**, *16*, 441–448.

[56] Mateus, C.; Costil, S.; Bolot, R.; Coddet, C. *Surf. Coat. Technol.* **2005**, *191*, 108–118.

solution[57] or spin-coating. This latter method consists of depositing a drop on the surface and distributing it using centrifugal force,[58] other methods are also available. This part of the project will be further explained in Chapter III.

---

[57] Qu, M.; Zhang, B.; Song, S.; Chen, L.; Zhang, J.; Cao, X. *Adv. Funct. Mater.* **2007**, *17*, 593–596.

[58] a) Sahu, N.; Parija, B.; Panigrahi, S. *Indian J. of Phys.* **2009**, *83*, 493–502. b) Ogi, T.; Modesto-Lopez, L. B.; Iskandar, F.; Okuyama, K. *Colloids Surf. A Physicochem. Eng. Asp.* **2007**, *297*, 71–78.

CHAPTER II
DESIGN, SYNTHESIS AND PHOTOPHYSICAL PROPERTIES OF FLUORESCENT BICOLOR INDICATOR (FBI) MOLECULES

2.1.- OBJECTIVES

According to what was developed in the introduction, the main objective of this chapter is the development of a Ba^{2+} sensor, which must exhibit bicolor behavior. Furthermore, it has to be as sensitive and selective as possible to barium cations with report to other possible competitors.

Once a sensor, which has these requirements, is developed, various modifications will be studied. The possible improvements of these modifications will also be evaluated. Finally, a photophysical study will be carried out to characterize each of the parameters of interest of the synthesized compounds.

2.2.- DESIGN AND SYNTHESIS OF BARIUM SENSORS

As it has been described in the introduction, in the first approach, we tried to chelate Ba^{2+} using two nitrogen atoms as chelating site. Furthermore, in other works of our research group,[59] this kind of molecules has been used as fluorescent probes to synthesize a new family of platinum complexes to be applied in chemotherapy.

The first reaction to synthesize this kind of compounds was a double addition, obtaining a imidazopyridine (Scheme 1). As it will see later on, the main scaffold of the main compounds obtained this Thesis.
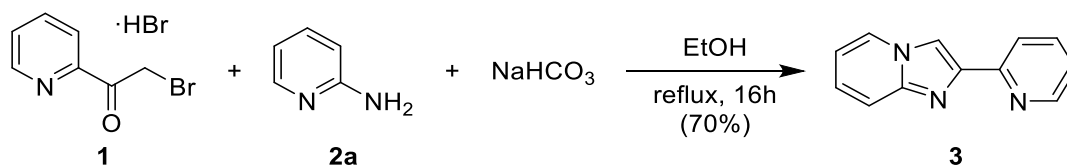
Scheme 1.- Synthesis of compound **3**.

---

[59] Odriozola Gimeno, M. Proteins and DNA as Sources of Catalytic and Biological Activities: from *Huisgenases* to Chemotherapy. Ph.D. Thesis, University of Basque Country, 2019

Once compound **3** was obtained, the next step was to generate the [8 + 2] cycloaddition adduct, a reaction previously developed in our research group.[60] For this purpose, imidazopyridine **3** was reacted with the benzyne precursor **4a** at 180 ℃ and 250 W for 15 minutes, using microwave irradiation (Scheme 2).

Scheme 2.- Synthesis of compound **5**.

Compounds **3** was measured at room temperature by UV-Vis Spectroscopy in the absence and in the presence of barium perchlorate, using acetonitrile as solvent, at $5 \cdot 10^{-5}$ M. It shows a signal quenching, slightly decreasing in intensity, although the maxima did not change. However, no change was observed when fluorescence experiments were carried out. In this case, compound **3** shows the same behavior both alone and in the presence of perchlorate, as it shown in Figure 23.

Figure 23.- a) Absorbance spectra for compounds **3** and **3·Ba²⁺** (1eq), $5 \cdot 10^{-5}$ M in MeCN, r.t. b) Fluorescence spectra for compounds **3** and **3·Ba²⁺** (1eq), $5 \cdot 10^{-5}$ M in MeCN, r.t., $\lambda_{exc} = 250$ nm.

[60] Aginagalde, M.; Vara, Y.; Arrieta, A.; Zangi, R.; Cebolla, V. L.; Delgado-Camón, A.; Cossío, F. P. *J. Org. Chem.* **2010**, *75*, 2776–2784.

In the case of compound **5**, the absorbance plots are coincident. The same occurs in the fluorescence spectra, where the maxima are shifted towards the visible region of the spectrum (with respect to compound **3**, see Figure 24).
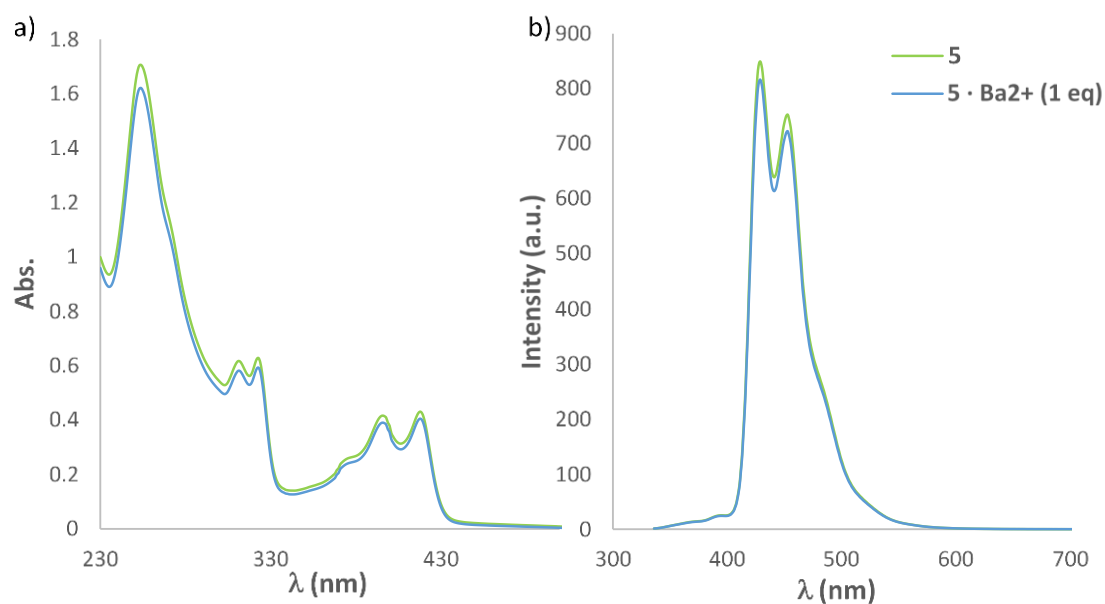

Figure 24.- a) Absorbance spectra for compound **5** and **5·Ba²⁺** (1eq), $5 \cdot 10^{-5}$ M in MeCN, r.t. b) Fluorescence spectra for compound **5** and **5·Ba²⁺** (1eq), $5 \cdot 10^{-5}$ M in MeCN, r.t., $\lambda_{exc} = 254$ nm.

Our preliminary idea was to generate BaL or BaL$_2$ systems, where L was either compound **3** or compound **5**. The predicted structures as monomers or as dimers are shown in Figure 25.
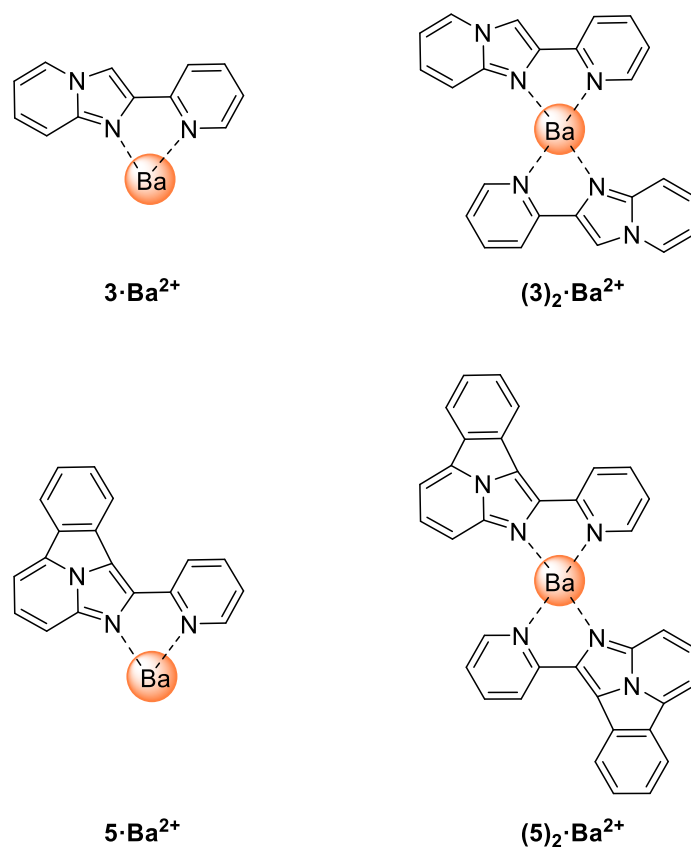
Figure 25.- Expected structures for compounds **3** and **5** in presence of Ba²⁺.

After the development and study of compounds **3** and **5,** it can be concluded that the fluorescence behavior of these sensors does not change significantly. Analyzing these spectra, it might seem that barium does not bind to the fluorophore. However, the interaction between two nitrogen atoms and a metal cation has been observed in numerous works, as it is shown in the introduction of this Thesis. However, the way in which the presence of this cation affects the molecule in this case does not generate a change in the electronic structure of the compounds and, therefore, no changes in the fluorescence mechanism are observed.

2.3.- DESIGN AND SYNTHESIS OF FLUORESCENT BICOLOR INDICATORS (FBI)

In view of the results obtained in this first approach, it was decided to change our strategy. In this new synthetic route, it was decided to incorporate a preorganized aza-crown ether (*vide supra*) as a chelating agent.

As mentioned in Chapter I, crown ethers are a very useful moiety for detecting alkali and alkali-earth metals. Therefore, we synthesized the double addition product, changing the pyridine in position C2 by a *p*-chlorophenyl group, on which the crown ether coupling reaction could be carried out Scheme 3.
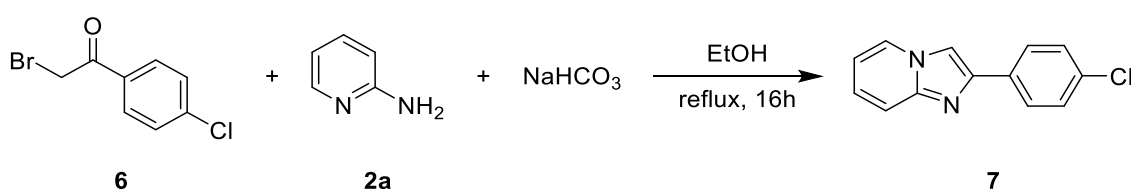

Scheme 3.- Synthesis of starting material **7**.

Once compound **7** was obtained in good yield, the coupling reaction of the crown ether was carried out under different conditions, as it is reported in Table 1 and in Scheme 4. In a first attempt, compound **7** was dissolved in THF and cooled at -12 ºC. A cold solution of 1-aza-12-crown-4-ether **8a** in THF was added slowly and the mixture was stirred for 5 min. Then, potassium carbonate was added and the reaction was stirred for 2 h at room temperature (r.t.). After this time, it was acidified with HCl 0.1 N and washed with brine. After analysis of the ^{1}H-NMR of the resulting product, it was observed that the unaltered starting material has been recovered (Table 1, Entry 1).

After this negative result, the reaction was repeated for 6 h at r.t. However, the result was the same: the recovery of starting material (Table 1, Entry 2).

In addition, different sizes of crown ether were tested, under the same conditions, to evaluate the possible influence of the crown ether size on reactivity. In all cases, the reaction did not proceed and the imidazopyridine **7** was recovered (Table 1, Entries 3 and 4). Finally, the reaction mixture was heated at 110 ºC for 12 h. Unfortunatelly, it did not yield the desired product (Table 1, Entry 5). After observing that neither the time nor the size of the crown ether, nor the temperature seem to be the determinants in the reaction, we proceeded to change the base. In this case, sodium hydride was used (Table 1, Entry

6). Once again, the recovery of the SM was observed. After all these attempts and a literature review,[61] the coupling strategy switched to palladium catalysis (Table 1, Entry 7). For this purpose, Pd(dba)$_2$ was used together with a phosphine ligand such as DavePhos and sodium tertbutoxide as a base. To these three species, in a sealed vial under argon atmosphere, crown ether **8c**, haloderivative **7** and toluene were added. The reaction mixture was stirred for 24h at 100ºC. After several attempts, all of them failed in coupling to the crown ether.


7   **8a-c**
              8a: n=1
              8b: n=2
              8c: n=3
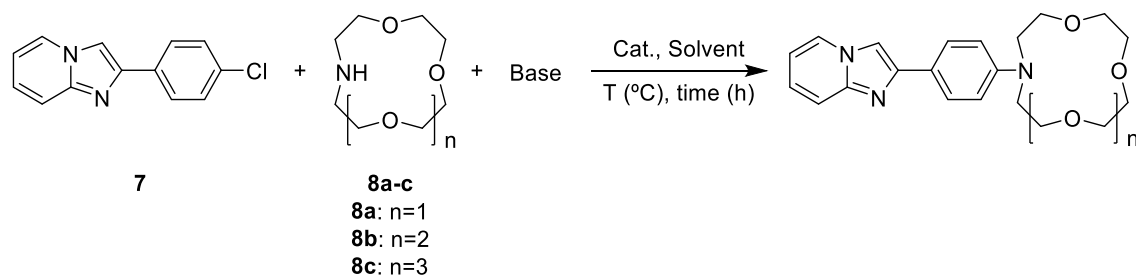
Scheme 4.- Coupling reactions of crown ether to compound **7**.

Entry	8	Base	Cat.	Solvent	T (ºC)	t (h)	Yield
1	a	K$_2$CO$_3$	–	THF	-12 to r.t.	2	–
2	a	K$_2$CO$_3$	–	THF	-12 to r.t.	6	–
3	b	K$_2$CO$_3$	–	THF	-12 to r.t.	6	–
4	c	K$_2$CO$_3$	–	THF	-12 to r.t.	6	–
5	a	K$_2$CO$_3$	–	THF	75	2	–
6	b	NaH	–	THF$_{anh}$	0 to r.t.	24	–
7	c	^{t}BuONa	Pd(dba)$_2$[*] DavePhos[**]	Toluene	110	24	–

Table 1.- Conditions and results for the reaction of Scheme 4. [*] Pd(dba)$_2$: Bis(dibenzylideneacetone) palladium(0). [**] DavePhos: 2-Dicyclohexylphosphino-2′-(N,N-dimethylamino)biphenyl.

[61] a) Sibert, J. W.; Seyer, D. J.; Hundt, G. R. *J. Supramol. Chem.* **2002**, *2*, 335–342. b) Urgaonkar, S.; Verkade, J. G. *Tetrahedron* **2004**, *60*, 11837–11842.

Many authors described the use of bromine derivates to carry out the coupling of crown ether via palladium-catalyzed amination.[62] Since this is a better leaving group, it was decided to attempt the coupling in this way. For this purpose, bromo acetophenone was used in the first approach (Scheme 5).
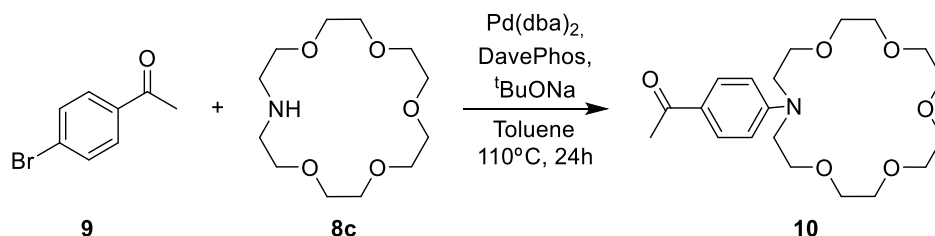
Scheme 5.- Proof of coupling with a bromine derivate.

With this methodology, the desired product **10** was obtained succesfully. This was easily verified by NMR (Figure 26 and Figure 27), where the signals of crown ether change completely, together with the disappearance of the NH signal of **8c** (Figure 26a). Furthermore, the *para* system was also affected, with the doublet in meta-position with respect to the Br atom going from 7.64 ppm to 6.67 ppm because of the electron releasing amino group.
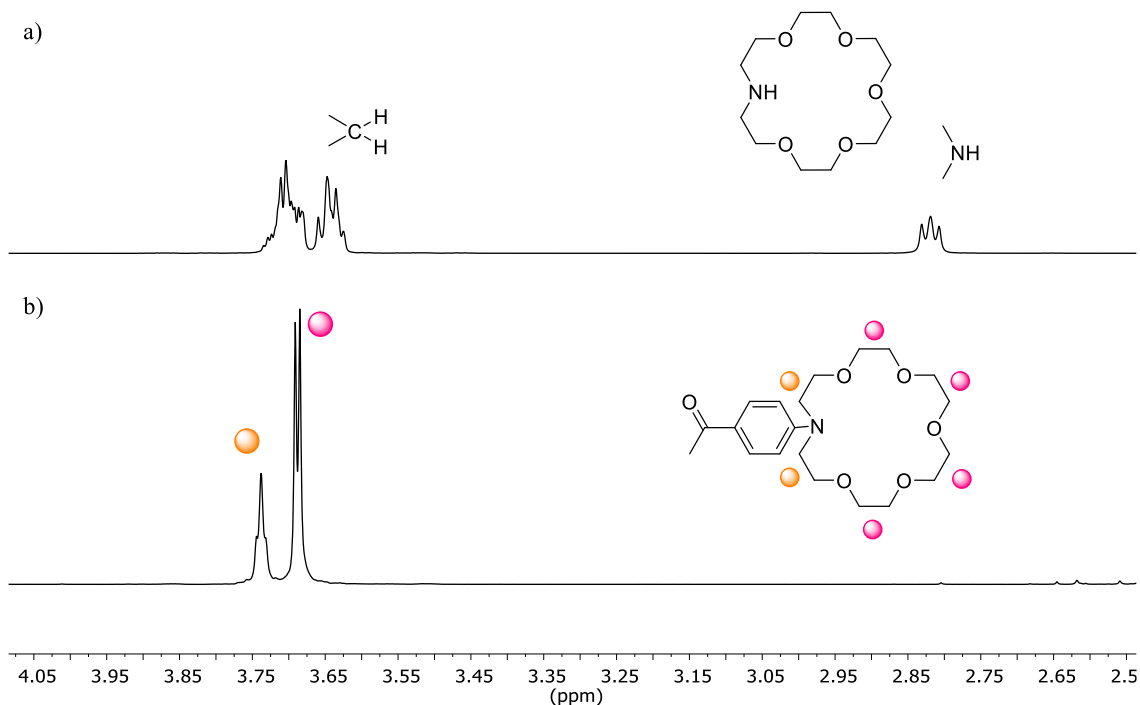
Figure 26.- Changes in crown ether region of the NMR spectra. CDCl$_3$, r.t. ^{1}H-NMR for 1-Aza-18-crown-6 ether **8c** (a) and for product **10** (b).

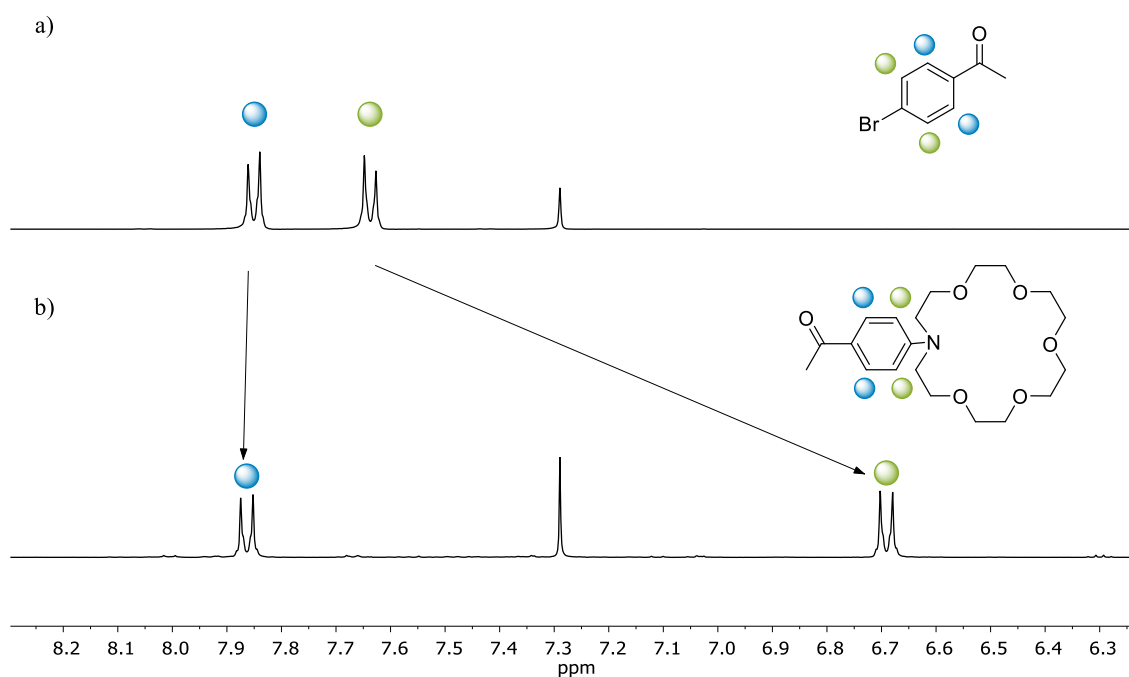[62] Zhang, X. X.; Buchwald, S. L. *J. Org. Chem.* **2000**, *65*, 8027–8031.

Figure 27. - Shift caused by crown ether coupling in *para* system in NMR. CDCl₃, r.t. a) Aromatic region of the ¹H-NMR spectrum for starting material **9**. b) Aromatic region of the ¹H-NMR spectrum for compound **10**.

Furthermore, the absorption and the fluorescence spectra of compound **10** were studied. In UV-Vis, it could be observed that the absorbance spectrum of compound **10** did not change in the presence of barium perchlorate. However, upon recording the corresponding fluorescence spectra, a hypsochromic shift was observed when molecule **10** chelated the metal salt. The maximum for the compound in the absence of barium is 468 nm. When the barium is trapped, three maxima appear at 374, 428 and 451 nm (Figure 28).
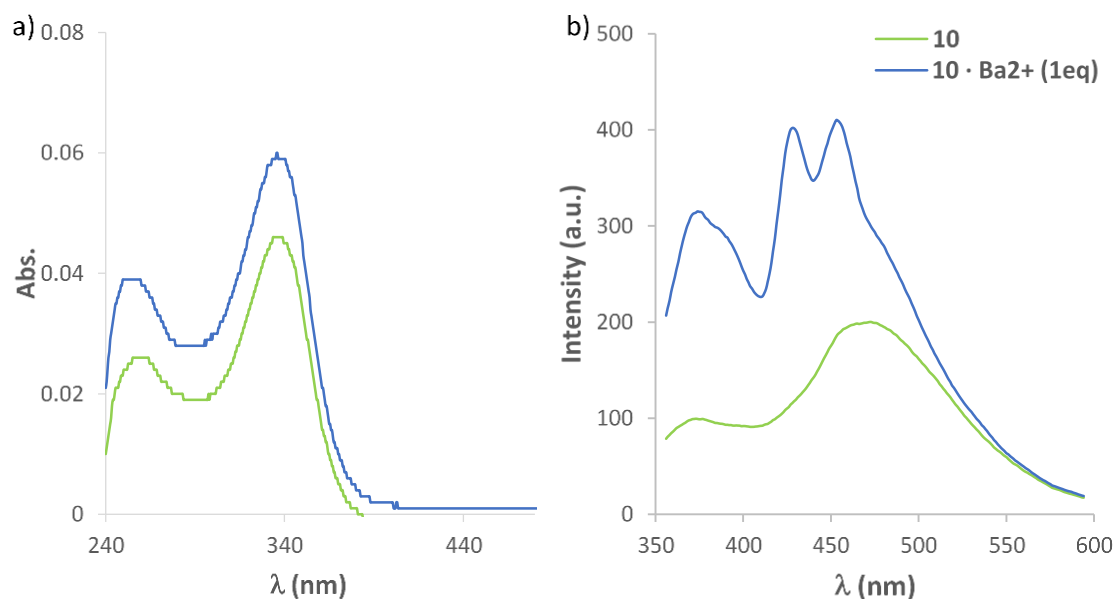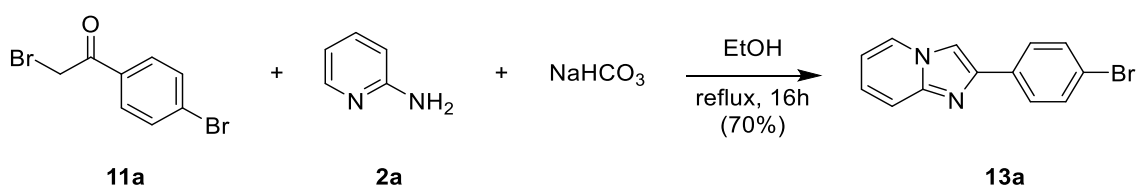
Figure 28.- a) Absorbance spectra for compound **10** and **10·Ba²⁺** (1eq), $5 \cdot 10^{-5}$ M in MeCN, r.t. b) Fluorescence spectra for compound **10** and **10·Ba²⁺** (1eq), $5 \cdot 10^{-5}$ M in MeCN, r.t., λ_{exc} = 256 nm.

Therefore, after verifying that bromine seemed to hold the solution, compound **13a**, 2-(4-bromophenyl)imidazo[1,2*a*]pyridine, the brominated equivalent of **7,** was synthesized.

Scheme 6.- Synthesis of imidazopyridine **13a**.

Once the double addition product **13a** was obtained, it was used in the aza-crown-ether coupling reaction. In this case, unlike the attempts with the chlorinated derivative, the product obtained was the desired one. As it can be seen in Figure 29 the corresponding signals to *para* system suffer the same shift after aza-crown ether coupling.
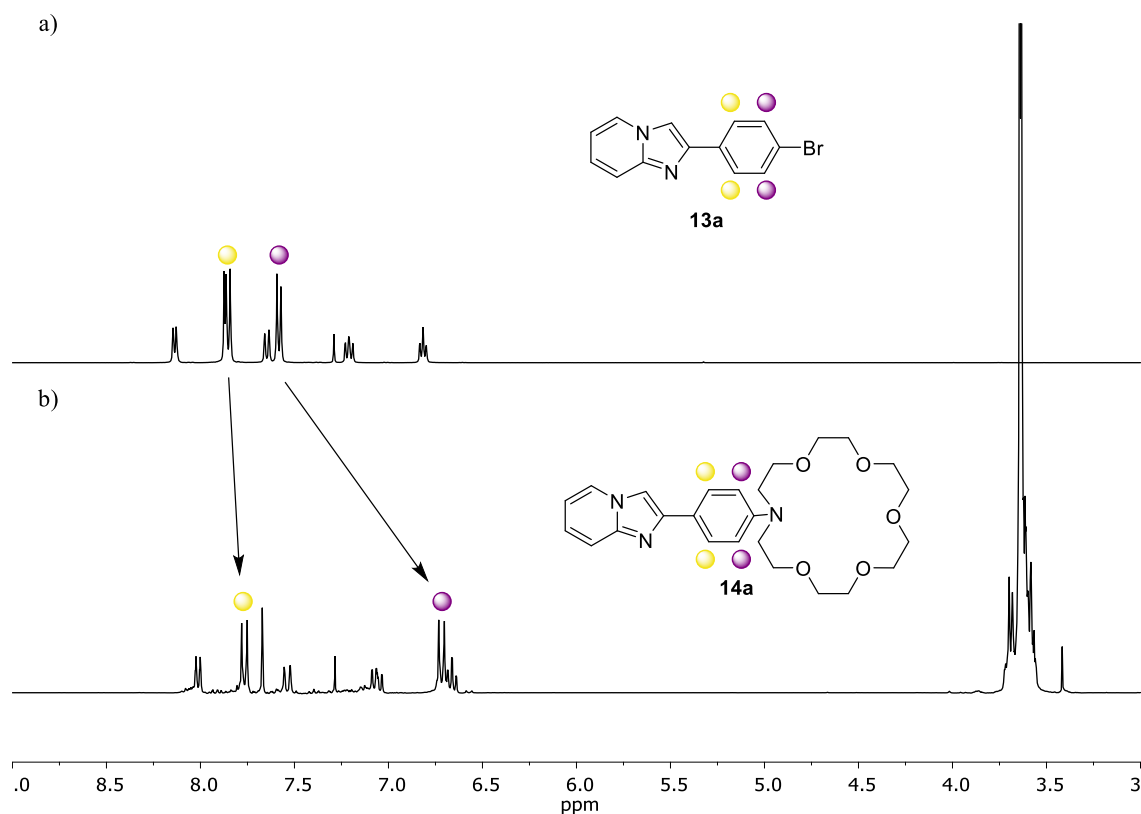
39
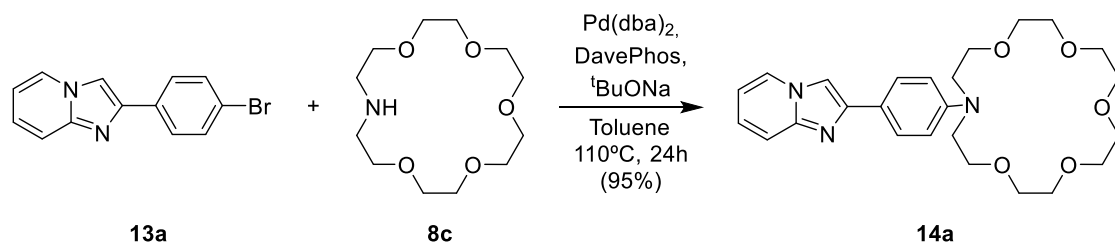
Scheme 7.- Synthesis of compound **14a**.

Figure 29.- Shift caused by crown ether coupling in *para* system in NMR. CDCl₃, r.t. a) Aromatic region of the ¹H-NMR spectrum for starting material **13a**. b) Aromatic region of the ¹H-NMR spectrum for compound **14a**.

After obtaining compound **14a**, their photophysical properties were studied. For this purpose, a solution in acetonitrile of compound **14a**, with a concentration $5 \cdot 10^{-5}$ M, was prepared. The spectra recorded for absorbance and fluorescence are shown in Figure 30. The absorbance spectrum shows maxima at 259, 282 and 342 nm. However, once the barium is chelated, the spectrum is totally different, with a clear maximum at 252 nm. On the other hand, in the fluorescence spectrum, the hypsochromic shift of 122 nm can be observed, since the maximum shown by **14a** in the absence of barium (458 nm) is shifted to 366 nm in **14a·Ba²⁺**.
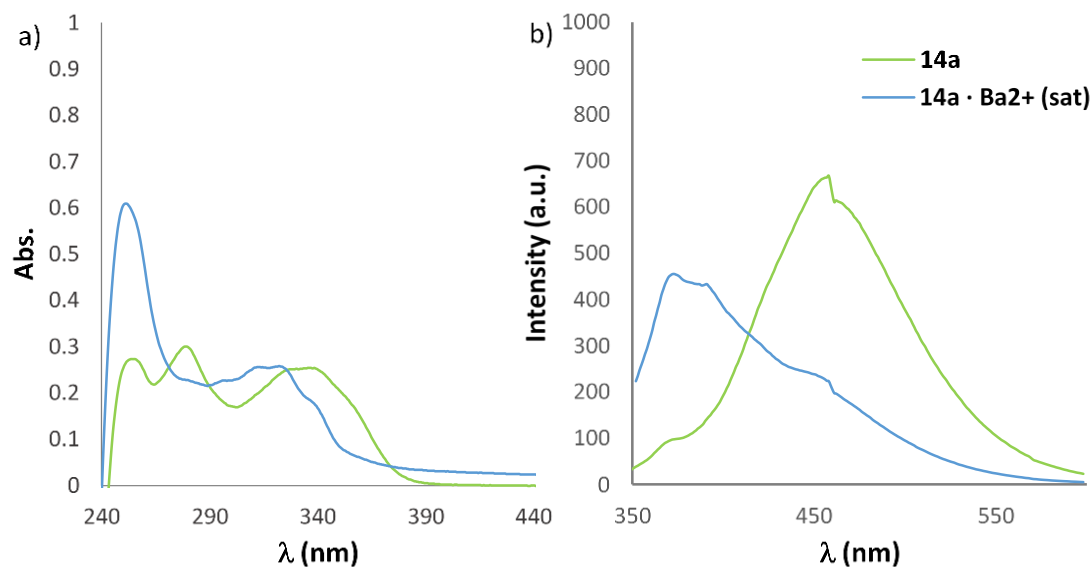
Figure 30. a) Absorbance spectra for compound **14a** and **14a·Ba²⁺** (1eq), $5 \cdot 10^{-5}$ M in MeCN, r.t. b) Fluorescence spectra for compound **14a** and **14·Ba²⁺** (1eq), $5 \cdot 10^{-5}$ M in MeCN, r.t., λ_{exc} = 278 nm.

This result was considered very promising, since the desired bicolor behavior could be observed. However, the need to have a background signal practically null, made this compound not the most suitable for this purpose. As it can be observed in the fluorescence spectra shown of Figure 30.b, under the emission maximum of the chelated compound **14a·Ba²⁺** (366 nm), the intensity of the free species **14a** is not negligible.

In order to increase the intensity of the emission signals, the next step in the fluorophore synthesis was the [8 + 2] cycloaddition under microwave irradiation.[63] For this reason, cycloaddition between adduct **13a** and benzyne precursor **4a** was first carried out under microwave irradiation (Scheme 8).
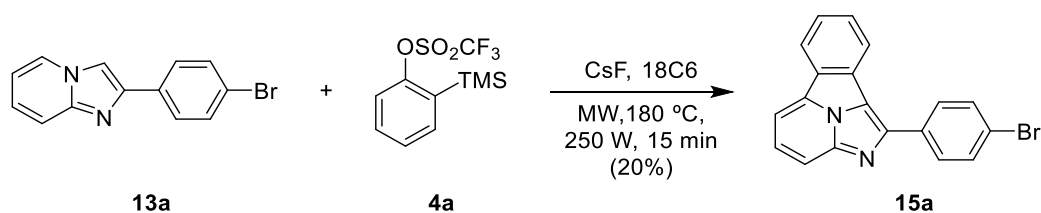
Scheme 8. Synthesis of intermediate **15a**.

---

[63] Aginagalde, M.; Vara, Y.; Arrieta, A.; Zangi, R.; Cebolla, V. L.; Delgado-Camón, A.; Cossío, F. P. *J. Org. Chem.* **2010**, *75*, 2776–2784.

Finally, the coupling amination reaction was carried out by means of the methodology described above. After 24 h of reaction and a purification by column, the final product **16a** was obtained with a yield of 40% (Scheme 9).
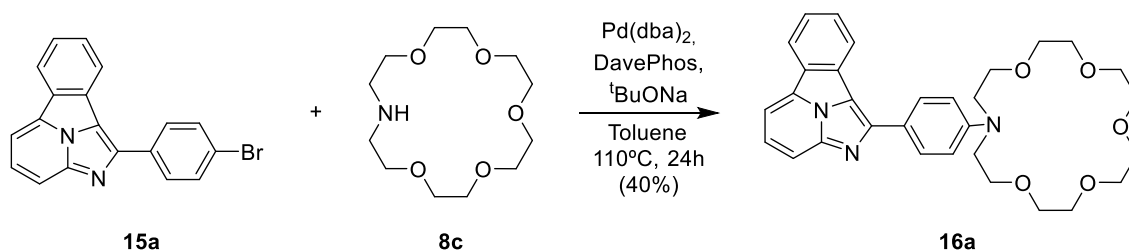
***Scheme 9.**- Synthesis of FBI molecule **16a**.*

Then, the photophysical properties were studied in a very preliminary way. Only two solutions were prepared for this purpose. One, containing the free ligand and another one with a stoichiometric solution of compound **16a** and barium perchlorate. Both solutions were prepared in acetonitrile at a concentration of $5 \cdot 10^{-5}$ M and measured at room temperature.

First, the UV-Vis absorbance spectra of both the free species and the chelated molecule with Ba were measured. In this case, in contrast with compound **10**, for example, the spectra of **16a** and **16a·Ba^{2+}** show significant differences to each other, suggesting that the chelation with barium could leads to a change in the three-dimensional structure and electronic properties of the fluorophore. In the following figure, the absorbance spectra of molecule **16a** in the free state and with one equivalent of Ba^{2+} are shown.

Figure 31.- Compounds **16a** and **16a·Ba^{2+}** in MeCN showing bicolor emission upon irradiation at 365 nm.

Furthermore, Figure 32.b, a change in the fluorescence spectrum is also observed where one equivalent of barium salt is added. The compound undergoes a hypsochromic shift from green to blue. Furthermore, the signal of the **16a·Ba^{2+}** complex clearly increases in intensity with respect to the **16a** signal.
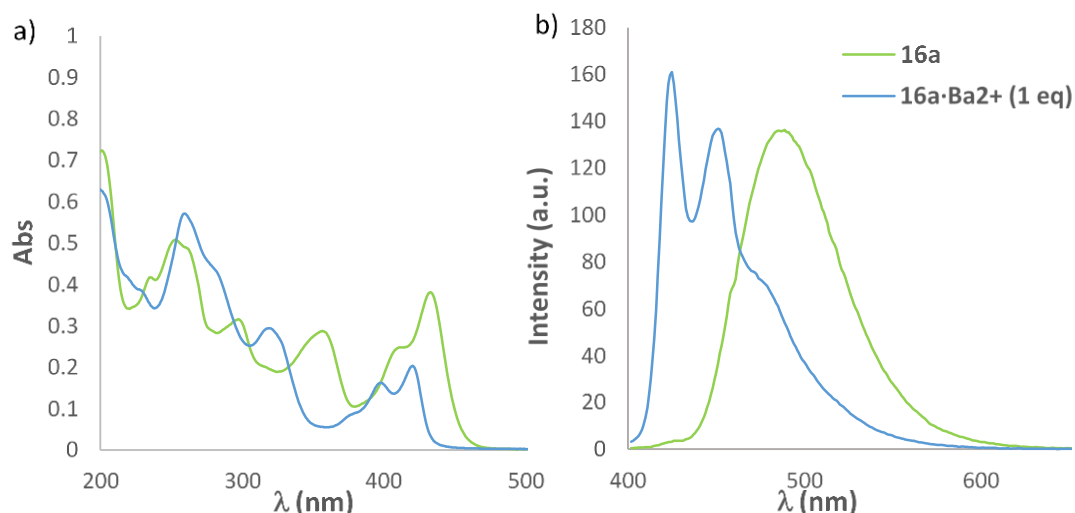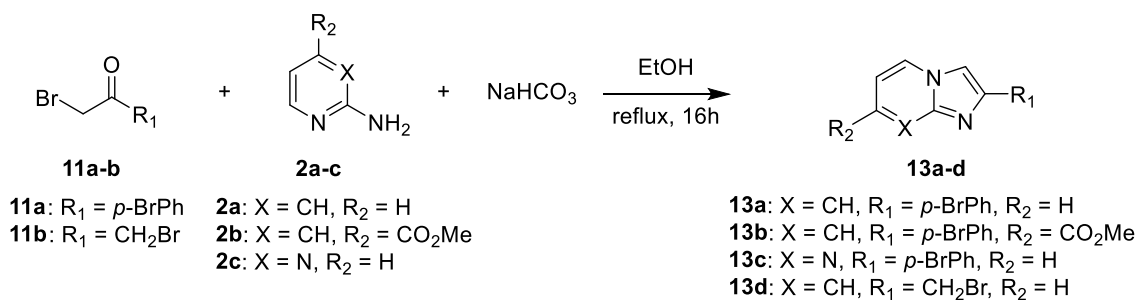
Figure 32. - a) Absorbance spectra for compound **16** and **16·Ba^{2+}** (1 eq), $5 \cdot 10^{-5}$ M in MeCN, r.t. b) Fluorescence spectra for compound **16** and **16·Ba^{2+}** (1 eq), $5 \cdot 10^{-5}$ M in MeCN, r.t., λ_{exc} = 252nm.

2.4.- MODIFICATIONS OF THE HETEROCYCLIC FLUOROPHORE

In order to study the influence of different substituent in the photophysical behavior, following the promising results shown by compound **16a**, it was decided to make slight modifications to the fluorophore skeleton. For this purpose, the previously described synthetic route.

11a-b	**2a-c**
11a: R$_1$ = *p*-BrPh	**2a**: X = CH, R$_2$ = H
11b: R$_1$ = CH$_2$Br	**2b**: X = CH, R$_2$ = CO$_2$Me
	2c: X = N, R$_2$ = H

13a-d
13a: X = CH, R$_1$ = *p*-BrPh, R$_2$ = H
13b: X = CH, R$_1$ = *p*-BrPh, R$_2$ = CO$_2$Me
13c: X = N, R$_1$ = *p*-BrPh, R$_2$ = H
13d: X = CH, R$_1$ = CH$_2$Br, R$_2$ = H
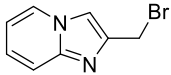
Scheme 10. - Synthesis of different imidazopyridines **17**.
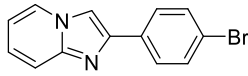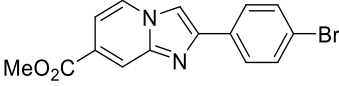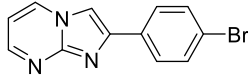
Entry	Ketone	Pyridine	Product	Yield (%)
1	11a	2a	**13a**	70
2	11a	2b	**13b**	68
3	11a	2c	**13c**	61
4	11b	2a	**13d**	21

***Table 2.**- Data for the synthesis of imidazopyridines **13**.*

*NOTE: Compound **13a** (Table 2, Entry 1), the synthesis of which has already been detailed with in section 2.3, is listed in the table as a reminder. This is because it will be used again along with the rest of the compound family in this section.*

The next step, was the necessary double addition reactions for the desired scope. First, the formation of an imidazo pyridine, which had a carboxylate group, was carried out (Table 2, Entry 2). The presence of this methyl ester, in addition to providing one more conjugated bond, which can generate a hypsochromic shift, in fluorescence, with respect to compound **16a**, can be a good starting point to use it as a linker on a surface.

The design of the following compound consisted of introducing one more nitrogen atom into the fused heterocycle (Table 2, Entry 3). This is due to previous experiments in the group[63] where it was observed that varying the number of heteroatoms could be of interest.
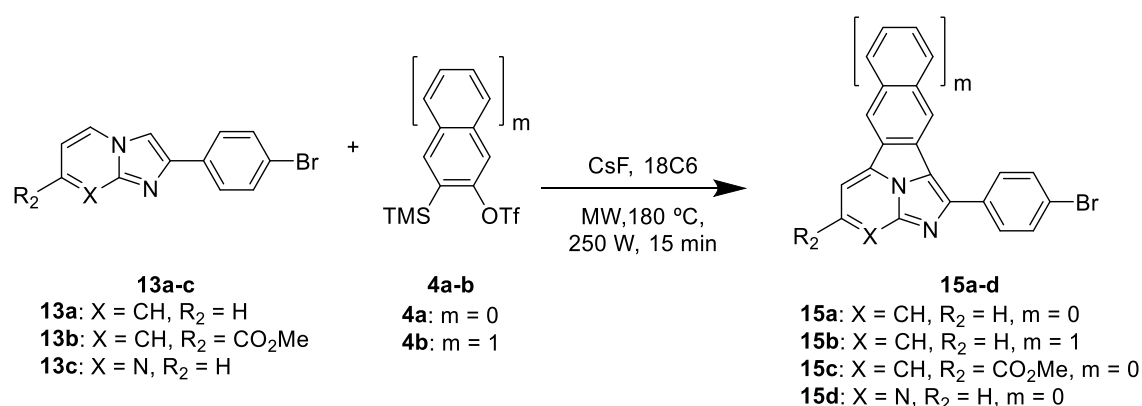
Finally, the formation of the last imidazopyridine in which the phenyl was replaced by a methylene group (Table 2, Entry 4) was carried out. The presence of this methylene group may be important in disconnecting the macrocycle from the aromatic scaffold. This type of bonding has been seen in the literature for the use of crown ethers.

---

[63] Aginagalde, M.; Vara, Y.; Arrieta, A.; Zangi, R.; Cebolla, V. L.; Delgado-Camón, A.; Cossío, F. P. *J. Org. Chem.* **2010**, *75*, 2776–2784.

Once the family of compounds **13** was obtained, two possible routes were followed to reach the FBI molecules.

Scheme 11.- Synthesis of FBI molecules. In blue, microwave-assisted method (*Route A*). In red, full palladium-catalyzed method (*Route B*).

Route A started with a cycloaddition using a benzyne precursor and carrying out the reaction under microwave irradiation. After the formation of the [8 + 2] product, the coupling of the crown ether was addressed. This reaction was done by palladium catalysis and a phosphine ligand. After this coupling, products FBI **16a-d** were obtained.

In contrast, *Route B* started with a C(sp^2)-N(sp^3) coupling catalyzed by palladium. The conditions, in this case, were the same as those used in *Route A*. Finally, once the aza-crown ether was coupled, palladium catalysis and 1,2-dibromobenzene were used again to obtain cycloadducts **16a-d**.

The microwave route allowed to obtain [8+2] cycloadducts in a very short period of time (15 min). However, the scale that can be used as starting material is small (up to 150 mg). On the other hand, the conversion of the reaction as well as its yield are low.

In the case of *Route B*, the first step has great yields and works up to the gram scale. In addition, it is possible to proceed to the next stage after precipitation of intermediates **14a-c** without further purification.

The second step of *Route B*, namely the cycloaddition at positions 3 and 5 of the corresponding imidazopyridine **14** remains the limiting step. This is due to the high energy barrier associated with the $[\pi^2s + \pi^8s]$/aromatization process.[63]

13a-c
13a: X = CH, R$_2$ = H
13b: X = CH, R$_2$ = CO$_2$Me
13c: X = N, R$_2$ = H

4a-b
4a: m = 0
4b: m = 1

15a-d
15a: X = CH, R$_2$ = H, m = 0
15b: X = CH, R$_2$ = H, m = 1
15c: X = CH, R$_2$ = CO$_2$Me, m = 0
15d: X = N, R$_2$ = H, m = 0

Scheme 12.- Synthesis of compounds **15a-d**.

Entry	Imidazopyridine	Benzyne precursor	Product	Yield (%)
1	13a	4a	15a	20
2	13a	4b	15b	17
3	13b	4a	15c	18
4	13c	4a	15d	17

Table 3.- Route A, Step 1. Microwave reaction. Reaction conditions and results.

Using the same starting material (**13a**), the [8 + 2] cycloaddition was carried out with phenyl (**4a**) and naphthyl groups (**4b**) (Table 3, Entries 1 and 2). The case of phenyl, which will give rise to the final molecule **16a** has already been studied in section 2.3. First, the [8 + 2] cycloaddition of a naphthyl group, without changing the starting

[63] Aginagalde, M.; Vara, Y.; Arrieta, A.; Zangi, R.; Cebolla, V. L.; Delgado-Camón, A.; Cossío, F. P. *J. Org. Chem.* **2010**, *75*, 2776–2784.

imidazopyridine, was considered. This, a priori, should result in a hypsochromic shift due to the increase of conjugated bonds in the system. Therefore, compound **13a** was reacted with the aryne precursor **4b**. For this purpose, the microwave irradiation conditions described in the previous section were used, yielding cycloadduct **15b**.

This latter compound was reacted with the benzyne precursor **4a**, resulting in compound **15c** (Table 3, entry 3). Microwave irradiation was used for this purpose, under the same conditions previously described. Finally, microwave reaction for substrate **13c** with *in situ* generated benzyne was performed, yielding the synthetic intermediate **15d** (Table 3, Entry 4).

15a-d
15a: X = CH, R$_2$ = H, m = 0
15b: X = CH, R$_2$ = H, m = 1
15c: X = CH, R$_2$ = CO$_2$Me, m = 0
15d: X = N, R$_2$ = H, m = 0

8c
8c: n=3

16a-d
16a: X = CH, R$_2$ = H, m = 0
16b: X = CH, R$_2$ = H, m = 1
16c: X = CH, R$_2$ = CO$_2$Me, m = 0
16d: X = N, R$_2$ = H, m = 0
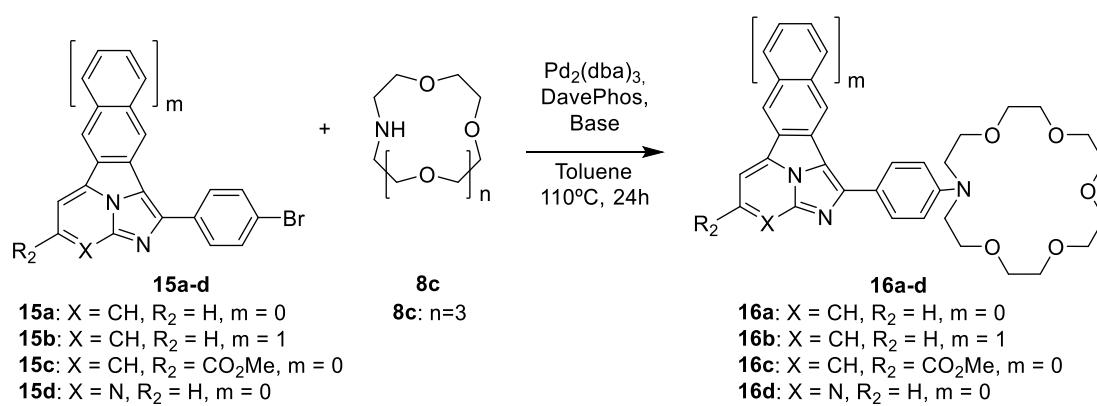
Scheme 13.- Synthesis of compounds **16a-d**.

Entry	SM	Base	FBI	Yield (%)
1	15a	^{t}BuONa	16a	13
2	15b	^{t}BuONa	16b	6
3	15c	Cs$_2$CO$_3$	16c	7
4	15d	^{t}BuONa	16d	-

Table 4.- Route A, Step 2. Aza-crown-ether coupling. Reaction conditions and results.

The coupling of the macrocycle to the adducts obtained after formal [8 + 2] cycloaddition, did not give satisfactory results. The products formed were as desired, although the yields were very low. In addition, compound **16d** could not be obtained in this way. For this reason, the steps were reversed (*Route B*). First, the coupling of the crown ether was carried out, followed by the [8 + 2] cycloaddition.
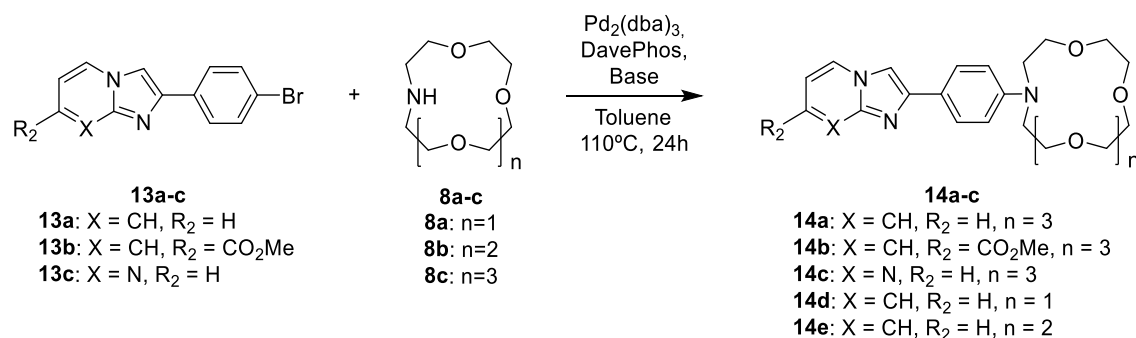
Scheme 14.- Synthesis of compounds **14a-e**.

Entry	Imidazopyridine	Base	Product	Yield (%)
1	13a	^{t}BuONa	14a	95
2	13b	Cs$_2$CO$_3$	14b	47
3	13c	^{t}BuONa	14c	30

Table 5.- *Route B, Step 1.* Aza-crown-ether coupling. Reaction conditions and results.

In this case, as shown in Table 5, the $C(sp^3)$ - $N(sp^2)$ coupling yielded, in spite of being the same methodology, much higher yields than those shown in Table 4, route A step 2. It should be noted that, when using compound **13b** (Table 5, Entry 2), which has a methyl ester group, it was necessary to change the base. When we used ^{t}BuONa, not only the coupling was not produced, but also the methyl signal disappeared in NMR. It was therefore necessary to avoid such a strong base as tertbutoxide and to use cesium carbonate instead.
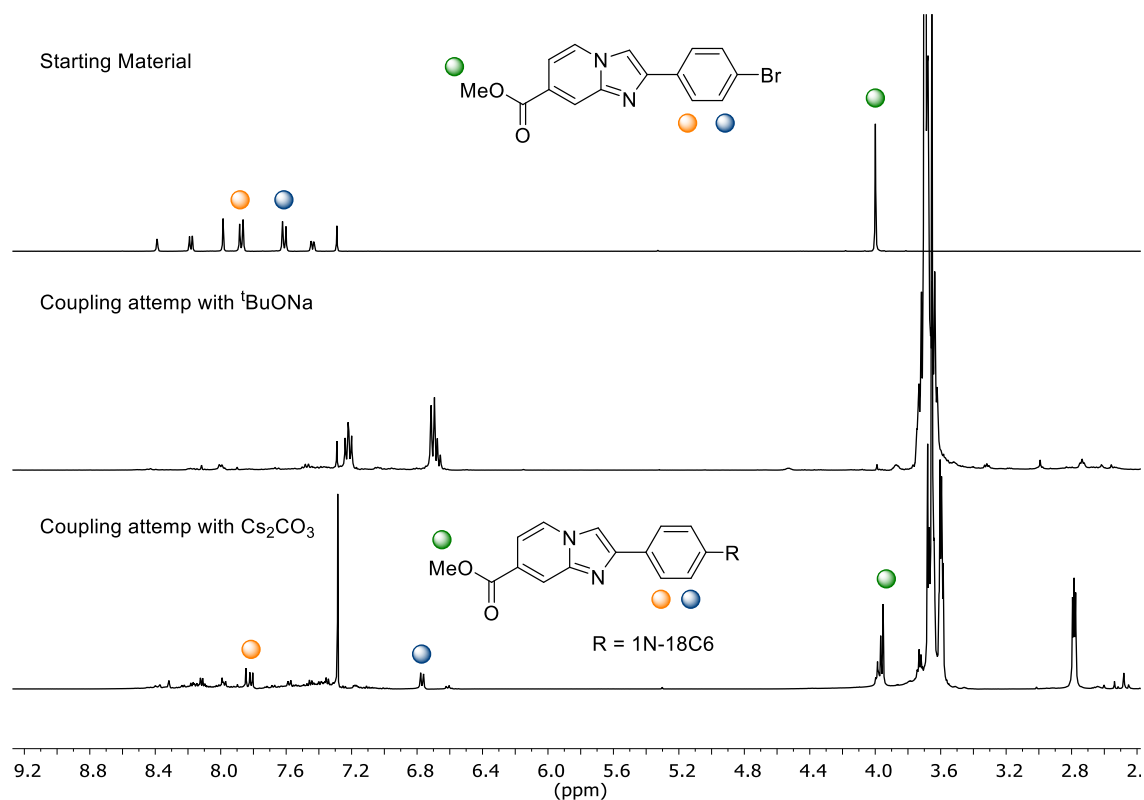
Figure 33. - Comparison between the use of the base in the coupling of the crown ether on **13b** (Table 5, Entry 2).

However, in the above spectra it can be seen gathered in Figure 33 how the reaction crude (Table 5, Entry 2) is much less clean. In addition, the aromatic zone does not appear to have a high amount of the desired compound. The coupling of the crown ether to other substrates is cleaner and sometimes in very high yields. In the case of compound **14b**, these problems may be due to a decarboxylation process catalyzed by palladium.[64]

---

[64] a) You, S. L.; Dai, L. X. *Angew. Chem. Int. Ed.* **2006**, *45*, 5246–5248. b) Leth, L. A.; Glaus, F.; Meazza, M.; Fu, L.; Thøgersen, M. K.; Bitsch, E. A.; Jørgensen, K. A. *Angew. Chem. Int. Ed.* **2016**, *55*, 15272–15276. c) Fields, W. H.; Chruma, J. J. *Org. Lett.* **2010**, *12*, 316–319. d) Hu, P.; Zhang, M.; Jie, X.; Su, W. *Angew. Chem. Int. Ed.* **2012**, *51*, 227–231. e) Wang, C.; Pahadi, N.; Tunge, J. A. *Tetrahedron* **2009**, *65*, 5102–5109.
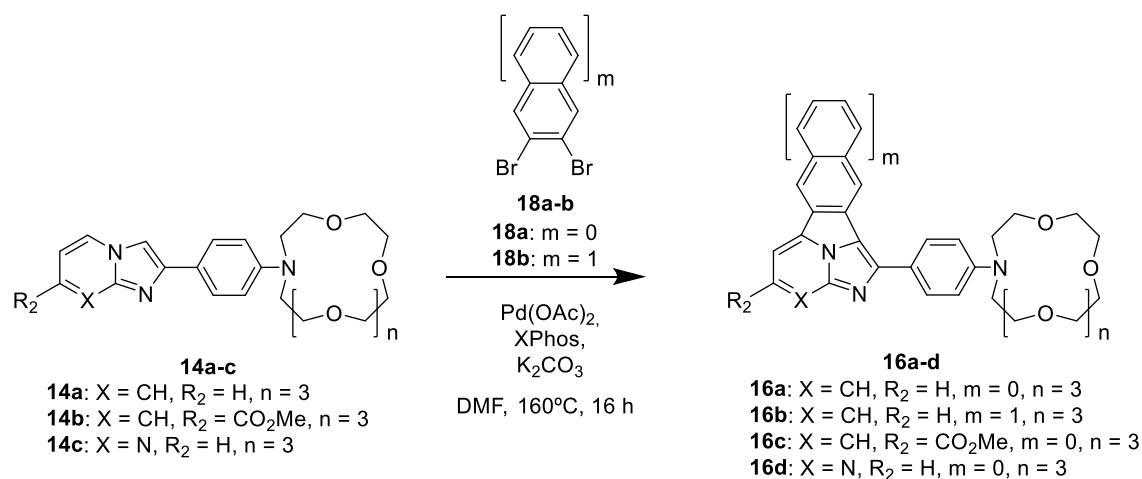
Scheme 15.- Synthesis of compounds **16a-d**.

Entry	SM	1,2-dibromoarene	FBI	Yield (%)
1	14a	18a	16a	47
2	14a	18b	16b	38
3	14b	18a	16c	32
4	14c	18a	16d	22

Table 6.- *Route B, Step 2.* Reaction conditions and results.

Finally, after obtaining compounds **14a-c**, cycloadditions with the halogenated derivative and palladium catalysis were approached. Compounds **14a-c** were filtered through a celite pad, concentrated under vaccum, redissolved in a minimal amount of chloroform and impurities were precipitated with hexane. The methyl ester compound **14b** was purified before the last step of the synthesis. As can be seen in Entries 1 and 2 of Table 6, phenyl seems to work better in this type of cycloadditions than its naphthyl counterpart. In Entry 3, Table 6, it can be appreciated how the presence of the ester also affects the reactivity of the system, decreasing by 15% with respect to compound **16a**. Finally, the pyrimidinic compound **16d**, presents the lowest yield of all. This may demonstrate the sensitivity of the system (in terms of reactivity) to changes in its structure. Nevertheless, a comparison of Table 4 and Table 6, shown below in Table 7, shows an increase in yields.

Entry	Product	Yield (%) / *Route A*	Yield (%) / *Route B*
1	16a	13	47
2	16b	6	38
3	16c	7	32
4	16d	-	22

Table 7.- Comparison of the yields of *Routes A* and *B*.

After the synthesis of these compounds, the behavior of all of them in solution, with and without barium, was evaluated. For this purpose, $5 \cdot 10^{-5}$ M solutions were prepared in acetonitrile, in the same way as in the previous section for the product FBI **16a**. As it can be seen in Figure 35, the UV-Vis spectrum of compound **16b**, in this case, does not show large variations when an equivalent of the barium salt is added.

On the other hand, as it can be observed in the right part of the Figure 35, the fluorescence spectra maintain the two-color behavior presented by compound **16a**. With the addition of the extra aromatic ring with respect to the previous product, the signal is shifted towards higher values of wavelength, as expected, since the number of conjugated double bonds increases. However, the shift is much smaller. In the case of compound **16a**, this displacement was approximately 75 nm. In the indicator **16b**, in contrast, it is reduced to 45 nm, shifting from 510 nm to 465 nm when barium is chelated.
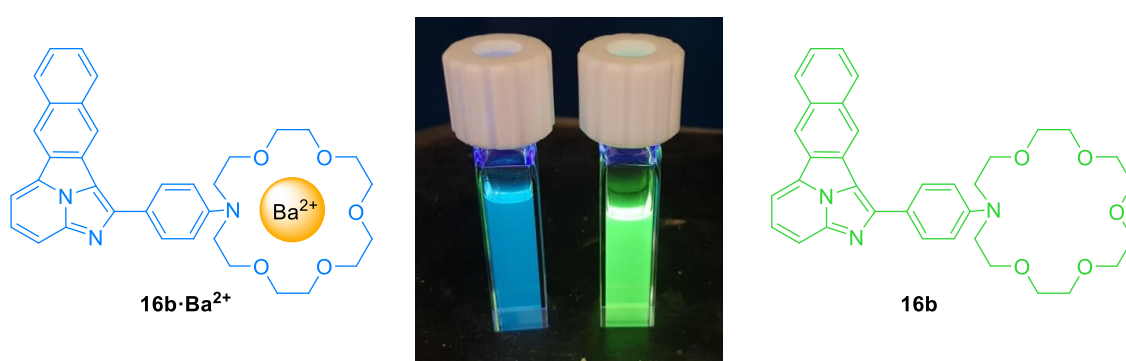
Figure 34.- Photograph and the corresponding structures of **16b** and **16b·Ba^{2+}** in acetonitrile showing bicolor emission upon irradiation at 365 nm.
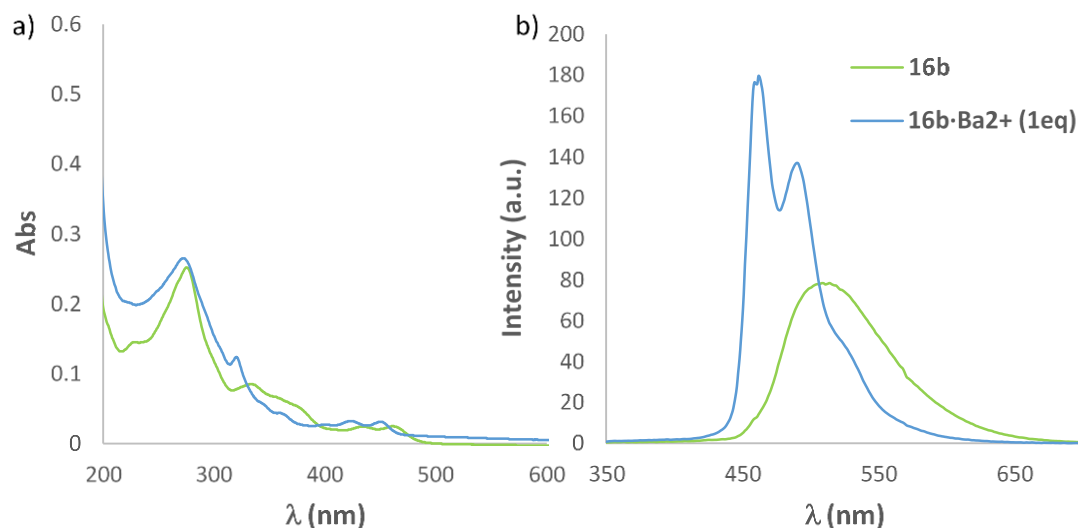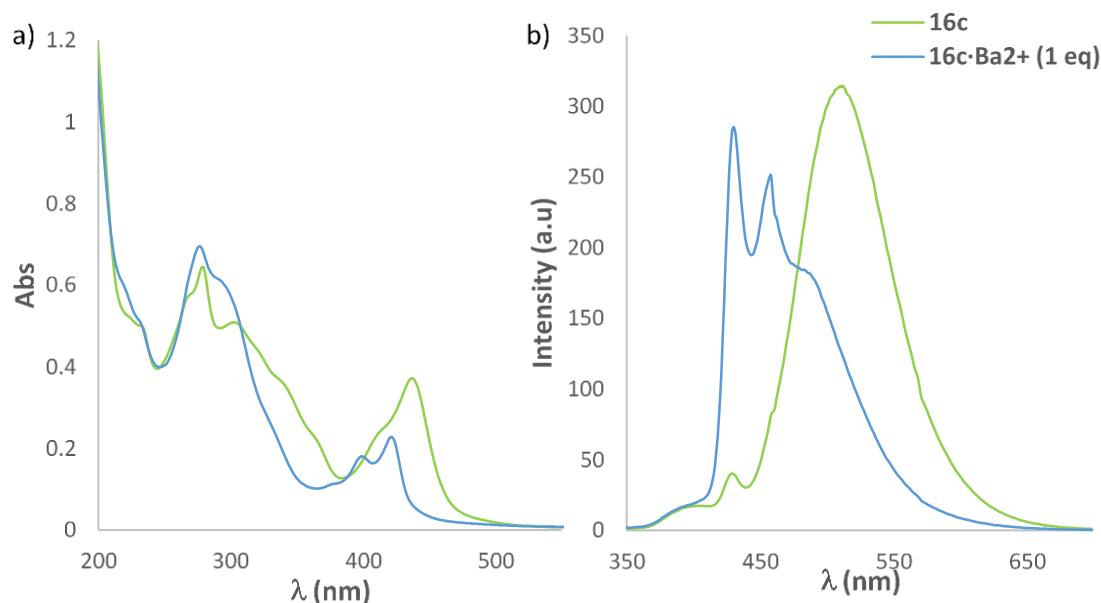
Figure 35.- a) Absorbance spectra for compound **16b** and **16b·Ba^{2+}** (1 eq), 5·10^{-5} M in MeCN, r.t. b) Fluorescence spectra for compound **16b** and **16b·Ba^{2+}** (1 eq), 5·10^{-5} M in MeCN, r.t, λ_{exc} = 252nm.

Compound **16c**, like our first candidate, **16a**, shows some variation in absorbance when a barium equivalent is added. In the case of fluorescence spectroscopy, compound **16c** shows a slightly higher shift than compound **16a**. Compound **16c** shows a maximum at 514 nm when it is in its free state. On the other hand, when the barium cation is trapped, this maximum decreases to 428 nm. However, a small maximum appears in the same wavelength region as the chelated species. This decreases considerably the value of the discrimination factor. (See section *2.6.- Photophysical studies of FBI compounds*).
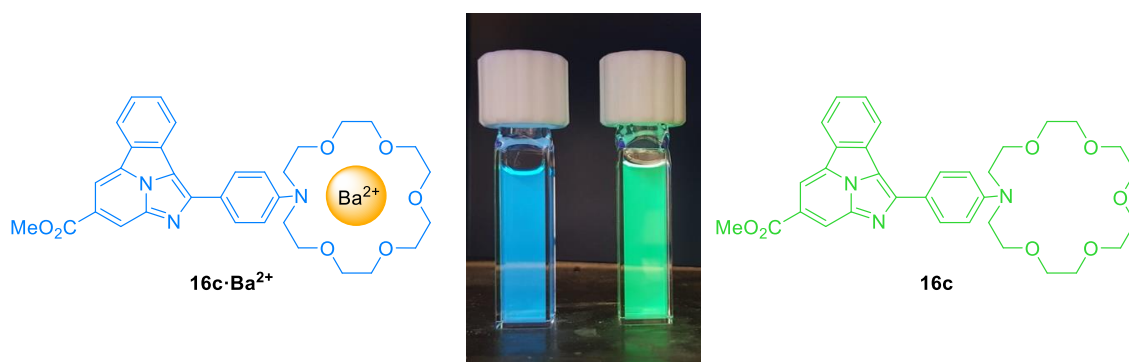
Figure 36.- Photograph and corresponding structures of **16c** and **16c·Ba^{2+}** in acetonitrile showing bicolor emission upon irradiation at 365 nm
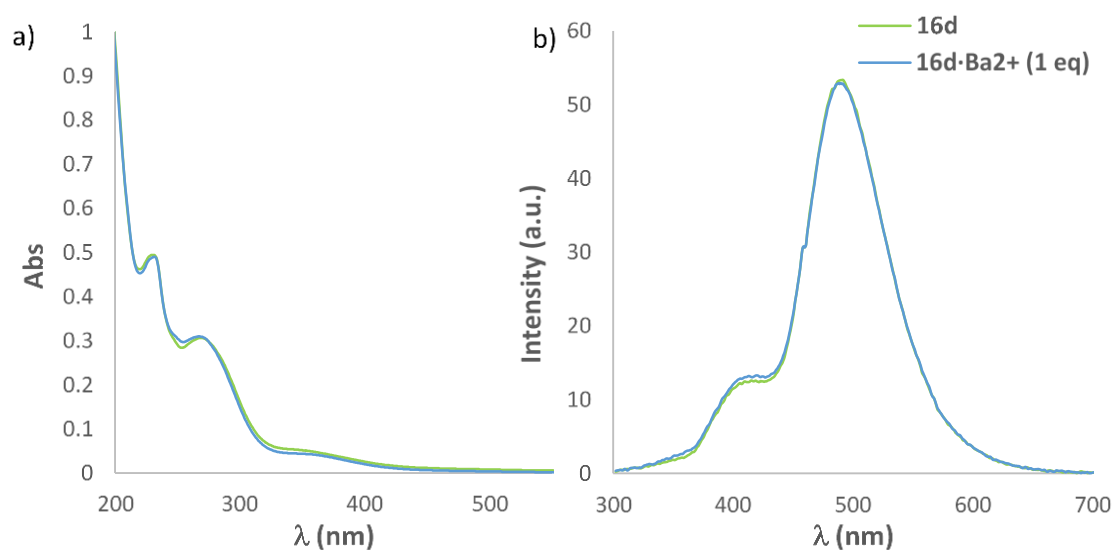
Figure 37. - a) Absorbance spectra for compound **16c** and **16c·Ba²⁺** (1 eq), $5 \cdot 10^{-5}$ M in MeCN, r.t. b) Fluorescence spectra for compound **16** and **16c·Ba²⁺** (1 eq), $5 \cdot 10^{-5}$ M in MeCN, r.t., $\lambda_{exc} = 252$nm.

When measuring the behavior of **16d** in solution, with and without barium, the introduction of this extra nitrogen atom has not proved to be satisfactory for barium sensing purposes. As can be seen in Figure 39, it does not show any change in solution. In both absorbance and fluorescence spectra, no change is detected, neither in intensity nor in wavelength. This may be due to a preference of barium for the nitrogen atoms present in the fluorophore rather than for the crown ether. If so, its binding group would be different from that used in the other compounds and, therefore, its behavior in solution is not the same.

In this case, this behavior is quite similar to those shown for molecules **3** and **5**, discussed at the beginning of this chapter. Thus, because in this case there is a crown ether that has already been shown to function as a binding group, the fact that it behaves similarly to **3** and **5** reinforces the theory that these nitrogen atoms do participate in the chelation of barium (*vide infra*).

53

Figure 38.- Photograph and corresponding structures of **16d** and **16d·Ba²⁺** in acetonitrile showing bicolor emission upon irradiation at 365 nm.

Figure 39.- a) Absorbance spectra for compound **16d** and **16d·Ba²⁺** (1 eq), $5 \cdot 10^{-5}$ M in MeCN, r.t. b) Fluorescence spectra for compound **16d** and **16d·Ba²⁺** (1 eq), $5 \cdot 10^{-5}$ M in MeCN, r.t., λ_{exc} = 252nm.

After the first photophysical tests in solution of the behavior of the fluorophores, it can be concluded that **16a** is the most promising one. This conclusion is based on four main reasons:

- It exhibits large shift between the chelated species and the free ligand. Compound **16d** shows an opposite behavior.
- The hypsochromic shift of the chelated species is sufficient so that the emission bands do not overlap with those associated with the free species. Product **16b** shows a contrary behavior.
- The region where the emission maximum of the chelated species appears is close to background free, which is not observed in the case of adduct **16c**.
- It is the only compound that, once chelated, increases its emission intensity.

2.5.- STUDY OF THE DIFFERENT SIZES OF 1-AZA-CROWN-ETHER

At that point, the next step was to evaluate how the size of the crown ether affected the detection of Ba^{2+}. As mentioned earlier, crown ethers are commonly used for the chelation of alkali and alkaline earth metals. In our case, the sensor design has to be made as selective as possible for a Ba^{2+} cation. To this end, it is necessary to evaluate how the number of atoms in the catcher affects the analyte. If the crown ether is small, for example, two molecules may be required for each barium atom. Therefore, compounds **14a** (Scheme 16) and **16a** (Scheme 17) and its analogues with 1-aza-12-crown-4-ether and 1-aza-15-crown-5-ether were synthesized. The results obtained are gathered in Table 8 and Table 9
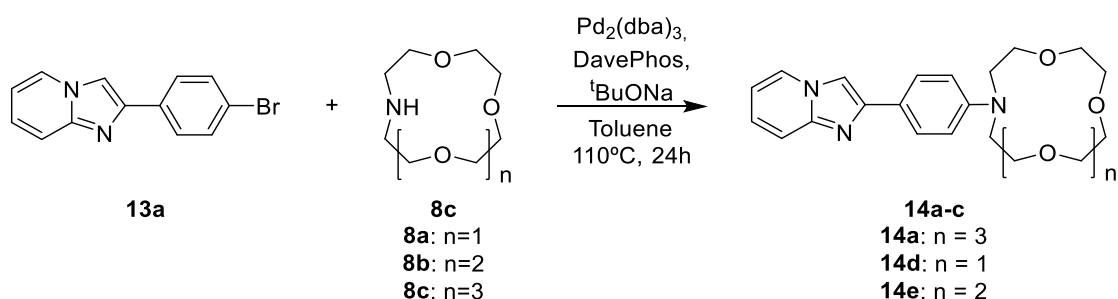
Scheme 16.- Coupling of different aza-crown-ethers.

Entry	Crown Ether	Product	Yield (%)	Structure
1	8a	14a	95	14a
2	8b	14d	87	14d
3	8c	14e	90	14e

Table 8.- Synthesis of compounds **14**.

The previous section has reflected how changes in the fluorophore affect the yields. However, in terms of reactivity, the size of the aza-crown-ethers does not present these issues. However, the highest yield is still for coupling of the crown ether **8a** (Table 8, Entry 1). However, both the smaller crown ether and the 5-heteroatom crown ether show excellent yields (Table 8, Entries 1 and 2).

14a-c
14a: n = 3
14d: n = 1
14e: n = 2

18a

Pd(OAc)$_2$,
XPhos,
K$_2$CO$_3$

DMF, 160ºC,
16 h

16a,e,f
16a: n = 3
16e: n = 1
16f: n = 2
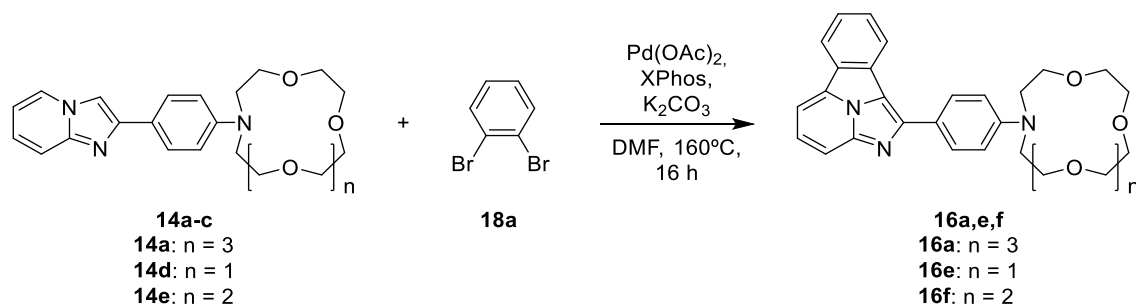
Scheme 17.- Synthesis of compounds **16a,e,f**.

Entry	Starting Material	Product	Yield (%)
1	14a	16a	47
2	14d	16e	40
3	14e	16f	40

Table 9.- Isolated yields for compounds **16a,e,f**.

The last stage of synthetic *Route B* (Scheme 17, Table 9), as in the previous case, was not significantly affected by the size of the macrocycle. Thus, the corresponding yields, although slightly lower compared to **16a**, are still acceptable.

Finally, as it was done with the rest of the FBI molecules **16**, the behavior in solution was measured and evaluated. For this purpose, the corresponding $5 \cdot 10^{-5}$ M solutions were prepared in acetonitrile as usual. As it can be easily seen in the Figure 41, the UV-Vis behavior of free **16e** is practically identical to the Ba^{2+}-bound species. A priori, this result may indicate that the heterocyclic compound and barium do not interact or interact slightly with the cation, with no noticiable conformational change. Analyzing the fluorescence spectra of **16e** and **16e·Ba^{2+}** (Figure 41.b), it appears that, in the presence of the perchloride salt, the signal is slightly quenched. This fact, suggest that there is a slight quenching induced by the interaction between the fluorophore and the cation, with no significant change in emission wavelength.

16e·Ba²⁺   **16e**

Figure 40.- Photograph and structures of **16e** and **16e·Ba²⁺** in acetonitrile showing bicolor emission upon irradiation at 365 nm.
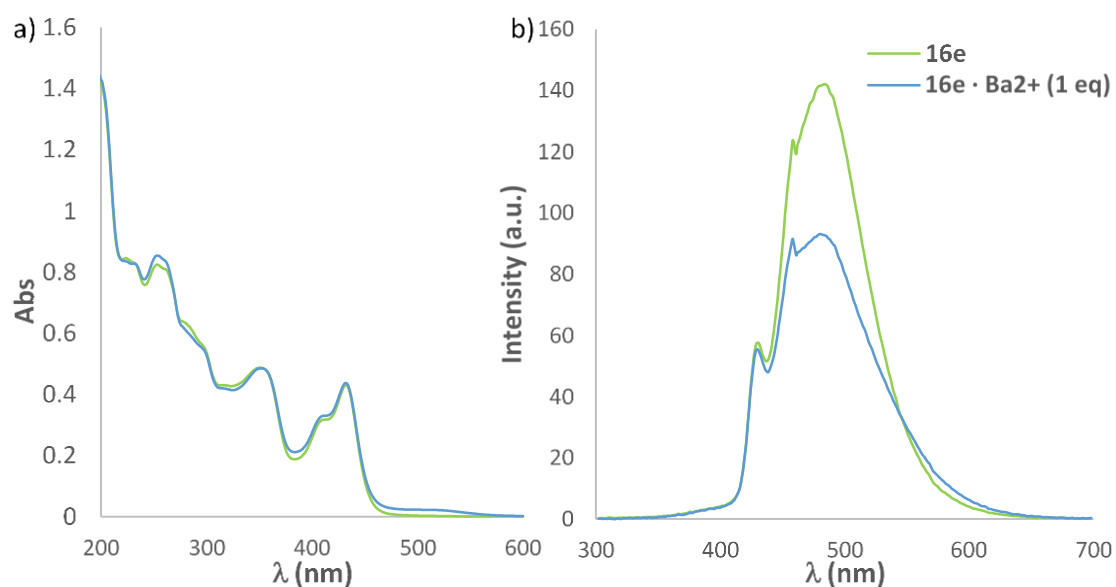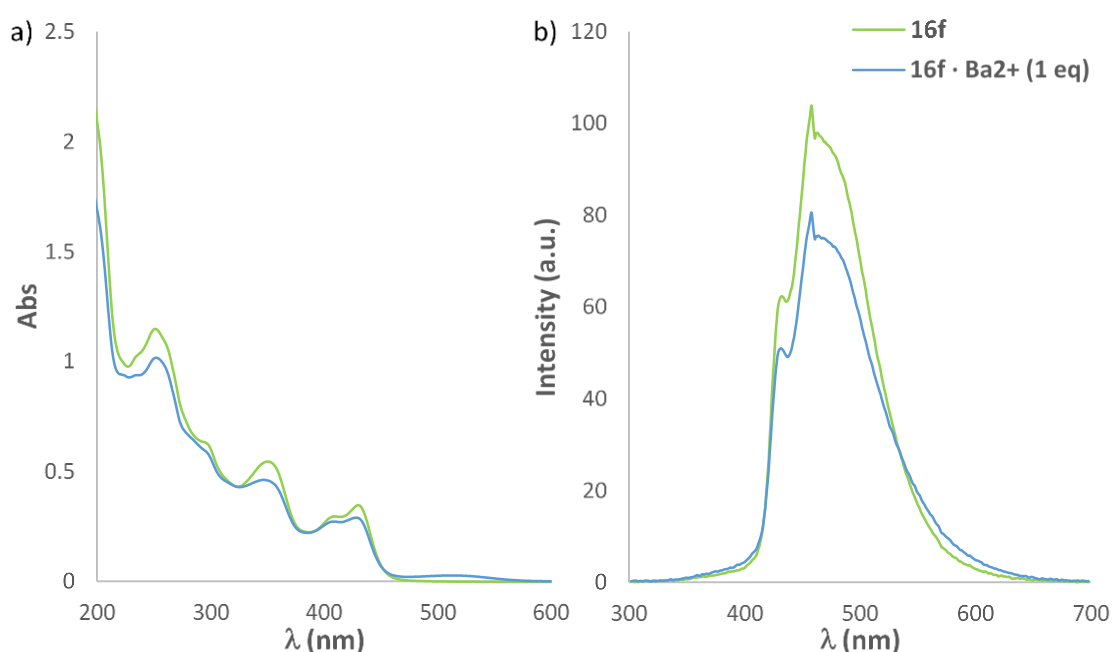

Figure 41.- a) Absorbance spectra for compound **16e** and **16e·Ba²⁺** (1 eq), $5 \cdot 10^{-5}$ M in MeCN, r.t. b) Fluorescence spectra for compound **16e** and **16e·Ba²⁺** (1 eq), $5 \cdot 10^{-5}$ M in MeCN, r.t., $\lambda_{exc} = 252$nm.

For the compound **16f**, the behavior in solution is similar to the last one. Figure 43, shown below, shows that there are no major changes between the free and chelated species. There is a slight variation in the intensity, but the absorption maxima being maintained at the same wavelength. The behavior presented by compound **16f** in the fluorescence spectra resembles that seen in compound **16e**.

Figure 42.- Photograph and structures of **16f** and **16f·Ba²⁺** in acetonitrile showing bicolor emission upon irradiation at 365 nm.

Figure 43.- *a)* Absorbance spectra for compound **16f** and **16f·Ba²⁺** (1 eq), $5\cdot10^{-5}$ M in MeCN, r.t. b) Fluorescence spectra for compound **16f** and **16f·Ba²⁺** (1 eq), $5\cdot10^{-5}$ M in MeCN, r.t., λ_{exc} = 252nm.

After the synthesis and preliminary analysis of compounds **16e** and **16f**, it was possible to confirm that the crown ether of 18 atoms (**8c**) is the one that presents the optimal size to observe a bicolor behavior. In the following section, the photophysical properties of the compounds **16** obtained so far will be measured and discussed in more detail. In this way it will be possible to determine more precisely which is the best compound for barium tagging experiments.

2.6.- PHOTOPHYSICAL STUDIES OF FBI COMPOUNDS

To study the photophysical properties of each compound, UV-Vis and Fluorescence Spectroscopy (FS) measurements were carried out. For this purpose, a series of solutions of the compound were used. The most common concentrations described in literature for photophysical studies are between 10^{-5} M and $5 \cdot 10^{-5}$ M.[65] From these measurements, the data of interest were obtained and calculated. These parameters are:

- Molar extinction coefficient, ε.
- Discrimination factor, f.
- Quantum yield, φ.
- Brightness, B.
- Minimum concentration at which we can work with that compound.
- Job´s Plot.
- Binding constant, k.

2.6.1.- Molar extinction coefficient, ε

First, absorbance measurements were performed. With the recorded spectra and the known concentration, the value of the molar extinction coefficient, ε, can be obtained for each molecule. For this purpose, the Lambert-Beer[66] equation is applied.

$$A = \varepsilon \cdot l \cdot c \qquad\qquad (1)$$

where A is the absorbance value (a.u.); ε is the molar extinction coefficient ($cm^{-1} \cdot M^{-1}$); l is the optical path length (in cm) and c is the concentration (M).

The UV-Vis spectra recorded for compound **16a** at different concentrations in Figure 44.

---

[65] a) Hirose, K. *J. Incl. Phenom.* **2001**, *39*, 193–209. b) Hu, S.; Wu, G.; Xu, C.; Dong, J.; Gao, Q. *J. Photochem. Photobiol. A Chem.* **2013**, *270*, 37–42.

[66] Atkins, P. W., de Paula J., K. J. Physical Chemistry, 8th Ed. *Oxford University Press, Oxford* **2006**.
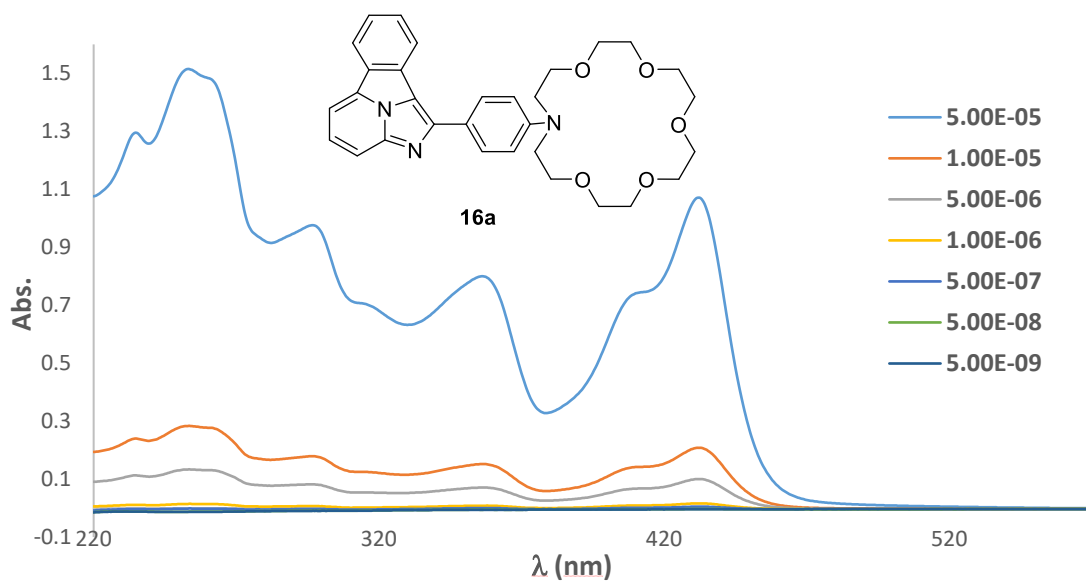
Figure 44.- Absorbance spectra for compound **16a** at different concentrations (M), MeCN, r.t.

Taking the values from the Figure 44, these values are plotted on a regression line. The linear fit of this line results in the coefficient we are looking for. This linear fit is made through the point (0,0), since it assumes an absorbance of 0 a.u. when the solution is 0 M. Thus, the slope **a** of this line corresponds to the value of ε, with **b** close to zero.

$$y = ax + b \qquad\qquad (2)$$

Substituting the absorbance values for *y* and the concentration values for *x*, the slope can be obtained. Using equation (1), the slope corresponds to the $l \cdot \varepsilon$ product. Since $l = 1$ cm, the slope is therefore the value of *ε*.
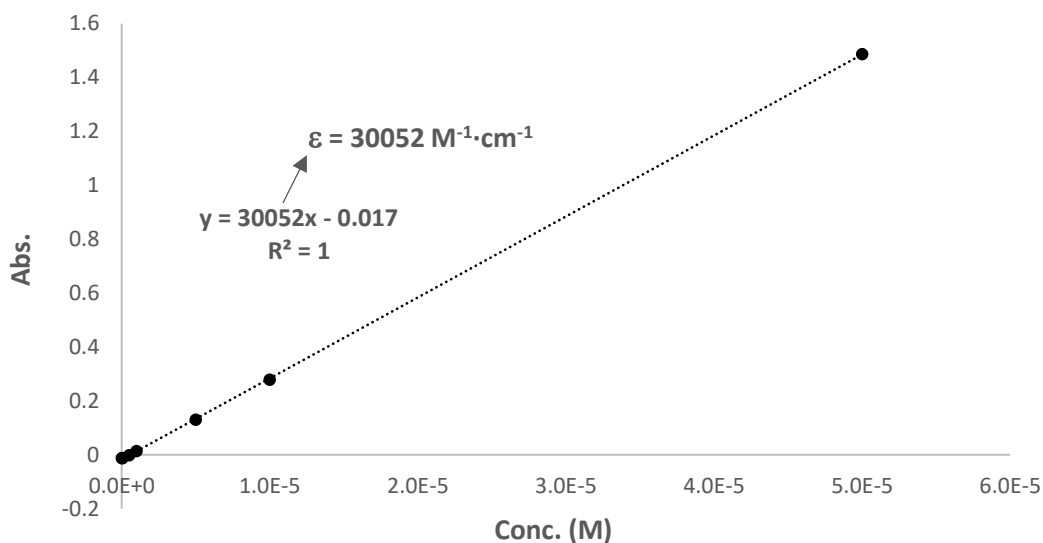
Figure 45.- Linear fit of the values obtained for compound **16a** at λ = 250 nm.

Thus, the values obtained for ε, $(cm^{-1} \cdot M^{-1})$ for the different compounds are shown in Table 10. From these data, it is also possible to set the working limit with these compounds. According to our results, $5 \cdot 10^{-7}$ M is the lowest working concentration since at concentrations lower than the above mentioned, the characteristic absorbance bands of compound **16a** are no longer visible.

Compound	ε without barium $(cm^{-1} \cdot M^{-1})$	ε with barium $(cm^{-1} \cdot M^{-1})$
16a	30052	22043
16b	22000	30250
16c	12586	12200
16d	8833	8500
16e	20048	20610
16f	22500	25406

Table 10.- ε values for FBI compounds **16a-f**.

2.6.2.- Job's Plot

When working on sensor design, one of the aspects to take into account is the stoichiometry of the binding process. It is important to know whether the molecule chelates a single or more barium cations. It may happen, however, that two molecules are

needed for a single cation or, on the contrary, that the same molecule captures several Ba^{2+} units.

The method known as Job's Plot is used to determine this stoichiometry. Two $5 \cdot 10^{-5}$ M stock solutions were prepared, one of FBI compound **16a** and the other of $Ba(ClO_4)_2$. From these solutions, eleven other solutions of 3 mL were prepared. The molar fraction of FBI varied from 0 to 1 and the remaining molar fraction corresponding to $Ba(ClO_4)_2$. Thus, in each solution there will be a molar fraction χ of FBI and a molar fraction $(1-\chi)$ of Ba^{2+}.
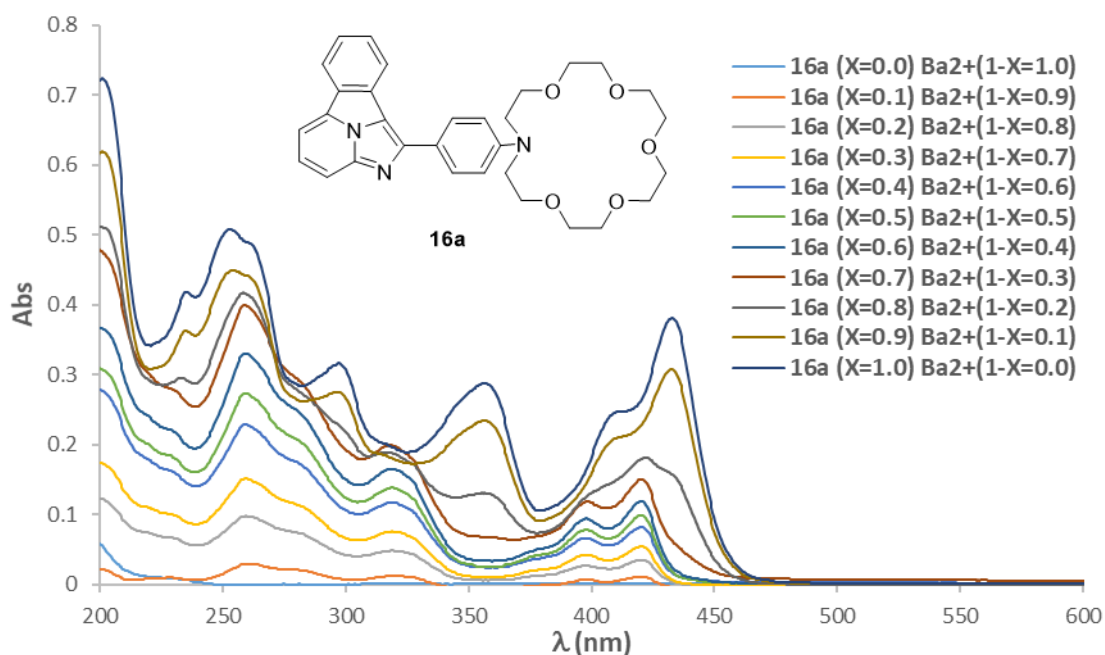
Figure 46.- Absorbance spectra for compound **16** Job´s Plot solutions, MeCN, r.t.

Once the different spectra were recorded for the aforementioned solutions, the maximum values at a given wavelength were taken. These maximum values were multiplied by the molar fraction of barium $(1-X)$ and plotted against the corresponding molar fraction of **16a** (Figure 47).
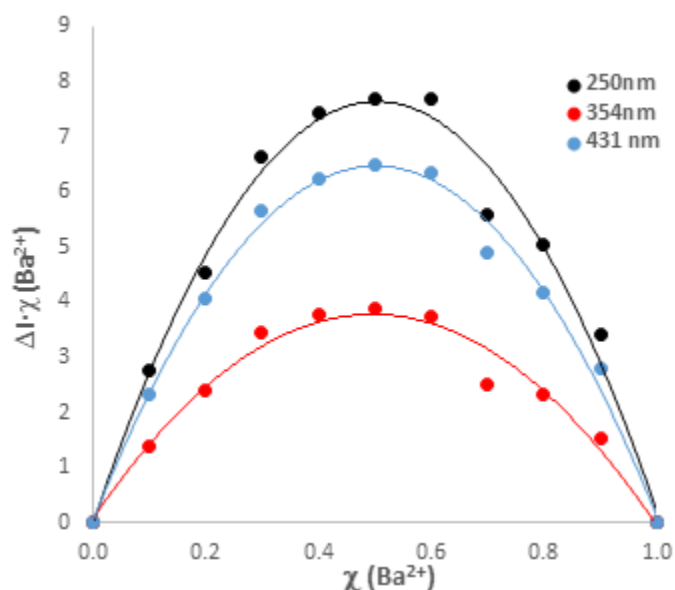
Figure 47.- Job´s Plot for compound **16a** at different wavelengths.

The thus obtained values are shown in Figure 47. Our results indicate that the polynomial fit is a parabola centered on the X-axis. The maximum of this parabola corresponds to the molar fraction of the barium salt with value 0.5. This means that the analyte:ligand ratio corresponds to a stoichiometry of 1:1. If the compound FBI were to trap two cations per molecule, the maximum would appear at a barium mole fraction of 0.33. Conversely, if two molecules **16** were needed to trap a single cation, the maximum would be shifted to the right (χ=0.67).
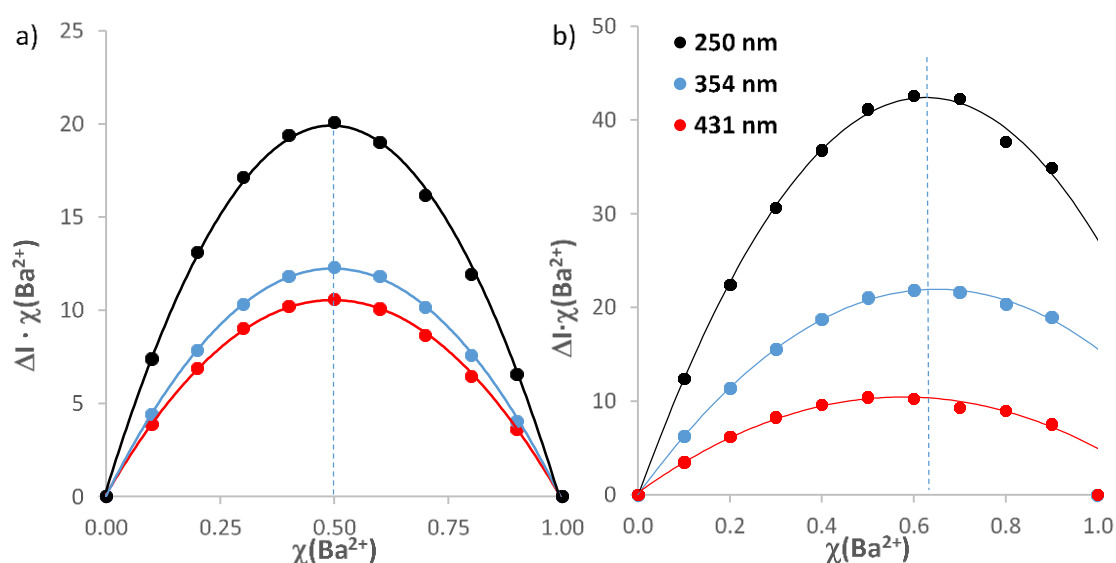
Figure 48.- a) Job's Plot for compound **16e**. b) Job's Plot for compound **16f**.

The Job's Plots for compounds **16e** (Figure 48, left) and **16f** (Figure 48, right) show that, in the latter case, the stoichiometry value, according to the Job's Plot would be a single Ba^{2+} for every two molecules. A similar result can be found in the literature (Figure 49).[67] In view of these results, one would expect that **16e** would also have the Job's plot curve in the 0.6 area. However, in this case, the maximum is at 0.5. Since the Job's Plot can be affected by several factors (for instance, the concentration limits or the binding contants),[68] it would be very useful to carry out a comprehensive theoretical study to understand the structural aspects associated with ligand-cation binding.
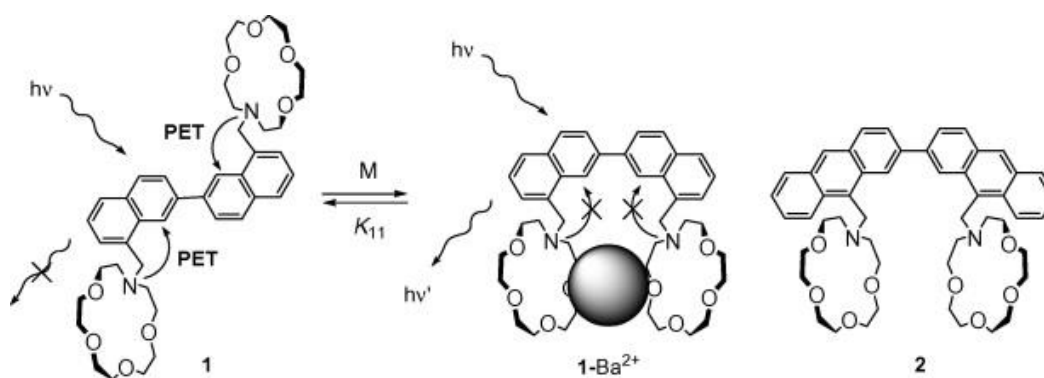
Figure 49. - Bianthracene-based fluorescence, naked-eye-detectable probe for barium ion.[67]

2.6.3.- Quantum Yields, ϕ_λ

The next parameter evaluated was the quantum yield. Quantum Yield[69] (ϕ_λ) is a photophysical parameter that describes the number of photons emitted relative to those absorbed. It is usually a value between zero and one, although it can be expressed as a percentage. Knowing this value provides a relevant knowledge about the efficiency of the fluorophore, in terms of fluorescence emission.

There are two ways to calculate these values. The most common method is to use a known standard such as quinine sulfate, rhodamine 6G or fluorescein. The alternative is to use an extra component of the fluorometer known as the "integrating sphere" (Figure 50 and Figure 51).

[67] Kondo, S. I., Takahashi, T., Takiguchi, Y., Unno, M. *Tetrahedron Lett.* **2011**, *52*, 453–457.

[68] Hibbert, D. B., Thordarson, P. *Chem. Commun*, **2016**, *52*, 12792.

[69] Freixa, Z.; Rivilla, I.; Monrabal, F.; Gómez-Cadenas, J. J.; Cossío, F. P. *Phys. Chem. Chem. Phys.* **2021**, *23*, 15440–15457.
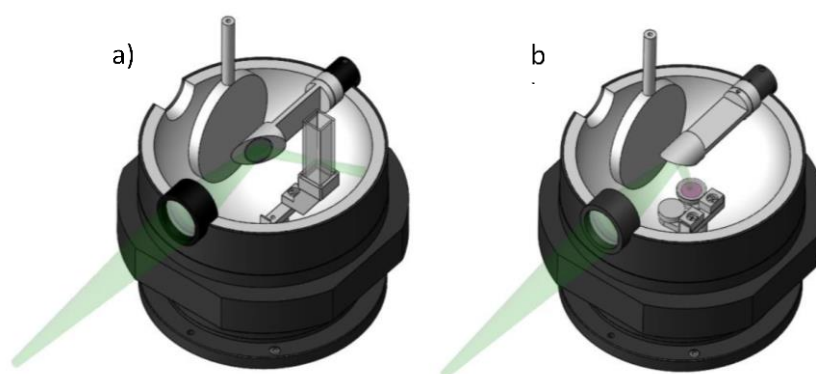
Figure 50.- Integrating Sphere set up for liquid samples (a) and for solid samples (b). [70]
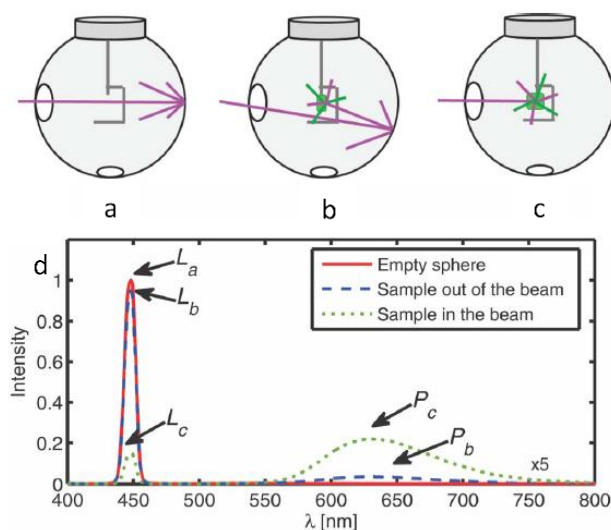
Figure 51.- a) Incidence of the light with the empty sphere. b) Incidence of the light on the sample in an indirect way. c) Incidence of the light beam in a direct way on the sample. d) Standard graph of these results.[71]

---

[70] Edimburgh Instrumets Ltd. *FLS1000 Series Reference Guide - Integrating Sphere*. **2017**.

[71] Leyre, S.; Coutino-Gonzalez, E.; Joos, J. J.; Ryckaert, J.; Meuret, Y.; Poelman, D.; Smet, P. F.; Durinck, G.; Hofkens, J.; Deconinck, G.; Hanselaer, P. *Rev. Sci. Instrum.* **2014**, *85*, 123115.

Among them, thus, quinine sulfate is usually the most commonly used standard for this kind of experiments. To make the calculation using a standard, the fluorescence spectra at a concentration of $5 \cdot 10^{-7}$ M must be recorded. The area under the curve is then integrated and compared with the value of the integral in the standard. In addition, if different solvents
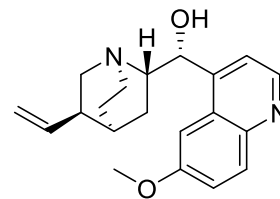
Figure 52. - Structure of Quinine

are used, a correction factor must be applied. For this purpose, the refractive indices of the different solvents are used. The formula to be applied in the calculation of QY is as follows:

$$\phi = \frac{I \cdot A_s \cdot n^2}{I_s \cdot A \cdot n_s^2} \, \phi_s \qquad (3)$$

where I is the area under the fluorescence curve, I_s the area under the fluorescence curve for the standard; A and A_s are the absorbance at the excitation wavelength and that of the standard, respectively; n the refractive index for the sample, in our case acetonitrile and n_s the refractive index of water, the solvent of the standard; and, finally, ϕ_s the tabulated value of the quantum yield of the standard.

Substituting the constant values[72] for all compounds, it would be:

$$\phi = \frac{I \cdot A_s \cdot 1.3442^2}{I_s \cdot A \cdot 1.33336^2} \cdot 0.546^* \qquad (4)$$

In which 0.546 is the quantum yield of quinine sulfate dihydrate in 0.5M H_2SO_4.

Using the above equation and substituting the experimental values obtained for the different FBI compounds **16a-f**, the quantum yields shown in Table 11 were obtained.

Compound	ε without barium ($cm^{-1} \cdot M^{-1}$)	ε with barium ($cm^{-1} \cdot M^{-1}$)	ϕ without barium	ϕ with barium
16a	30052	22043	0.67	0.45
16b	22000	30250	0.22	0.04
16c	12586	12200	0.29	0.25
16d	8833	8500	0.06	0.06
16e	20048	20610	0.42	0.41
16f	22500	25406	0.34	0.32

Table 11. - ε and ϕ_λ values for FBI compounds. ϕ_λ values calculated using quinine as standard.

---

[72] W. M. Haynes, *Handbook of Chemistry and Physics*, 96th ed.; Taylor & Francis, Boca Raton, FL, **2015**.

2.6.4.- Molecular Brightness, B_λ

Once the value of the molar extinction coefficient was obtained for each molecule as well as its quantum yield value, the brightness (B_λ) can be calculated. Brightness[73], by definition, is the product of the molar extinction coefficient (ε) and quantum yield (ϕ).

$$B_\lambda = \varepsilon \cdot \phi \qquad\qquad (5)$$

The brightness values are shown in Table 12, together with the ε and ϕ.

Compound	ε without barium $(cm^{-1} \cdot M^{-1})$	ε with barium $(cm^{-1} \cdot M^{-1})$	ϕ without barium	ϕ with barium	$B (\cdot 10^3)$ $(cm^{-1} \cdot M^{-1})$ without barium	$B (\cdot 10^3)$ $(cm^{-1} \cdot M^{-1})$ with barium
16a	30052	22043	0.67	0.45	20.13	9.92
16b	22000	30250	0.22	0.04	4.84	1.21
16c	12586	12200	0.29	0.25	3.65	3.05
16d	8833	8500	0.06	0.06	0.53	0.51
16e	20048	20610	0.42	0.41	8.42	8.45
16f	22500	25406	0.34	0.32	7.65	8.13

***Table 12.**-* ε, ϕ_λ, B_λ values for FBI compounds.

2.6.5.- Discrimination factor, f

In fluorescence, another value of interest is the discrimination factor, *f*. Mathematically it is calculated as follows: [74]

$$f_\lambda = \frac{I_\lambda(\mathbf{16} \cdot Ba^{2+}) - I_\lambda(\mathbf{16})}{I_\lambda(\mathbf{16})} \qquad\qquad (6)$$

Where thus, the greater the difference between the maximum in the band of the complex with barium and the molecule without barium, the higher the value of f. at wavelength λ.

---

[73] Piatkevich, K. D.; Verkhusha, V. V. *Guide to Red Fluorescent Proteins and Biosensors for Flow Cytometry*, Second Ed.; Elsevier Inc. **2011**

[74] Rivilla, I.; Aparicio, B.; Bueno, J. M.; Casanova, D.; Tonnelé, C.; Freixa, Z.; Herrero, P.; Rogero, C.; Miranda, J. I.; Martínez-Ojeda, R. M.; Monrabal, F.; Olave, B.; Schäfer, T.; Artal, P.; Nygren, D.; Cossío, F. P.; Gómez-Cadenas, J. J., *Nature* **2020**, *583*, 48–54.
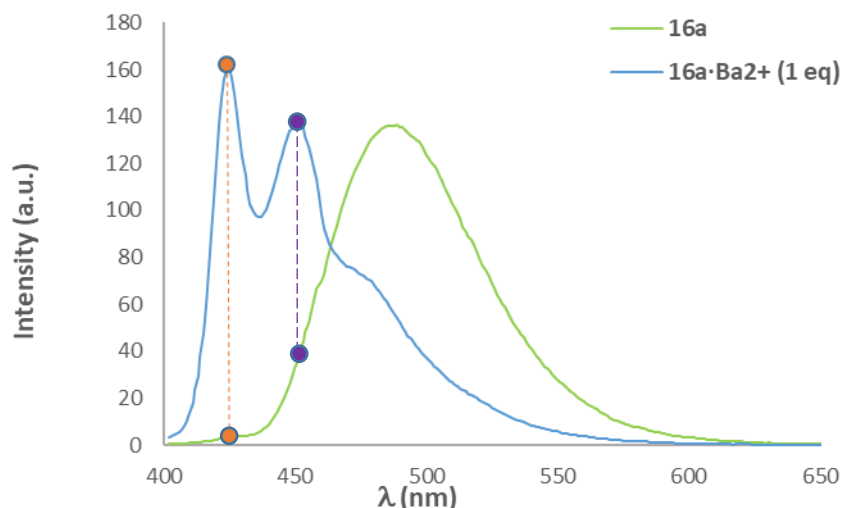
Figure 53.- Emission plots of **16a** and **16a·Ba2+** for the calculation of discrimination factor.

Figure 53 shows two dashed lines showing the maxima where we could calculate f. In the case of the orange line (428 nm), it can be seen that the contribution of **16a** is minimal. However, in the purple line (451 nm), the contribution of the unchelated compound accounts for almost one third of the signal. In this case the value of f will be quite small. Moreover, for the case of the maximum at 428 nm, the fact of having good separation with the emission maxima for **16a** and **16a·Ba²⁺**, allows the use of a green filter (*vide infra*). In this way, we can suppress the signal from a certain wavelength and thus enhance the clarity of the measurement.

Using Equation 6, the f_λ values for each of the FBI sensors are obtained (Table 13). Once again, compound **16a** is the best, by far, with a value of f, very distant from the rest.

Compound	λ (nm)	f_λ
16a	425	179.7
16b	458	4.9
16c	430	22.6
16d	488	n.d.
16e	485	0.07
16f	458	6.02

Table 13.- f values for compounds **16**.

2.6.6.- Binding constant, K_b

Another relevant parameter is the binding constant, which determines the affinity of the host and the guest. Given the equilibrium:

$$\textbf{16a-f} \quad + \quad Ba(ClO_4)_2 \quad \rightleftharpoons \quad \textbf{16a-f·Ba}^{2+} \quad + \quad 2\ ClO_4^-$$
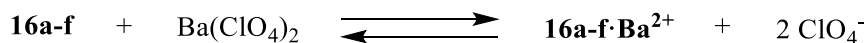
Scheme 18.- Guest-Host Scheme between FBI compounds and barium salt.

To calculate this constant, a $5 \cdot 10^{-5}$ M solution of compound **16a** in acetonitrile was prepared. Fractions of an equivalent of barium perchlorate were added to this solution. After each of these additions, the fluorescence spectrum was recorded. All these spectra are shown in Figure 54.
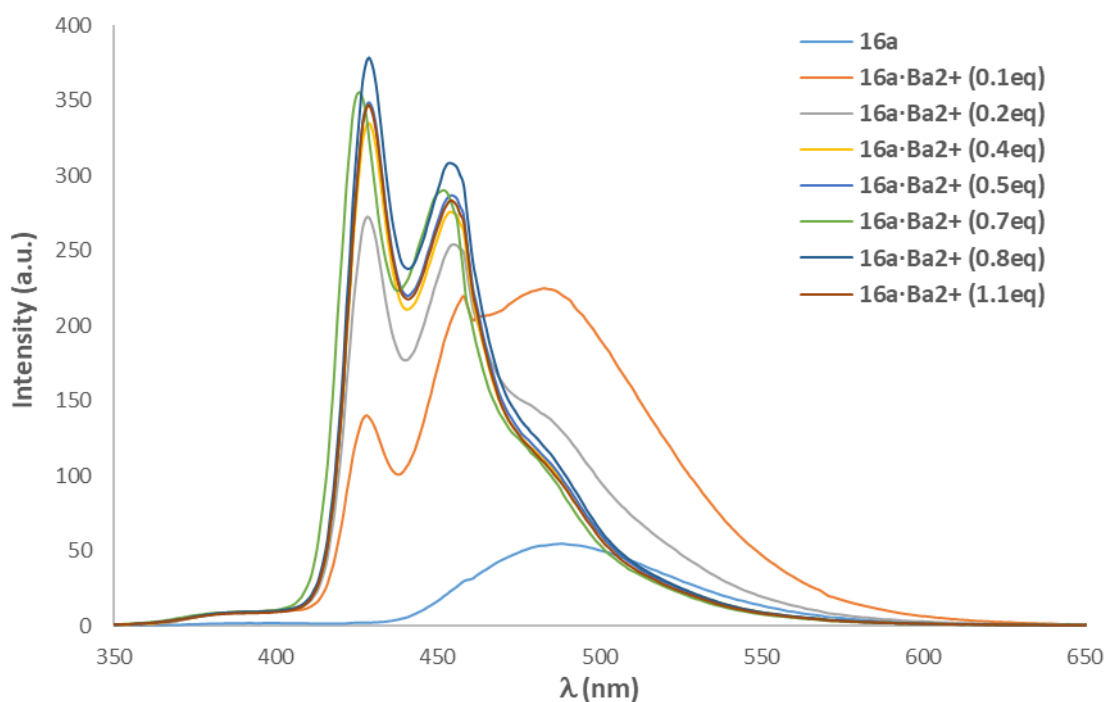
Figure 54.- Emission spectra for compound **16a** in presence of different equivalents of barium perchlorate. $5 \cdot 10^{-5}$ M, r.t., $\lambda_{exc} = 252$ nm.

Once spectra were recorded, the data processing was carried out. In this way, the mathematical process used for this purpose is known as Benesi-Hildebrand method.[75] According to this method, the following linear correlation of the inverse of I-I_0 with respect to $[Ba^{2+}]^{-1}$ must be obtained:

---

[75] Kuntz, I. D.; Gasparro, F. P.; Johnston, M. D.; Taylor, R. P. *J Am Chem Soc* **1968**, *90* (18), 4778–4781.

$$\frac{1}{I - I_0} = \frac{1}{I_f - I_0} + \frac{1}{k_b[Ba^{2+}](I_f - I_0)} \qquad\qquad (7)$$

Taking the maximum values I-I₀ of the different spectra, we can perform a linear fit using Equation 7. In this case, K_b corresponds to the division of the ordinate at the origin by the slope. The values for compounds **16a**, **16e** and **16f**, i.e. crown ether 6, 4 and 5, respectively, were compared. These values are gathered in Table 14. As it can be seen, the 18-atom crown ether is by far the best one in terms of its binding constant compared to compounds with smaller crown ethers.
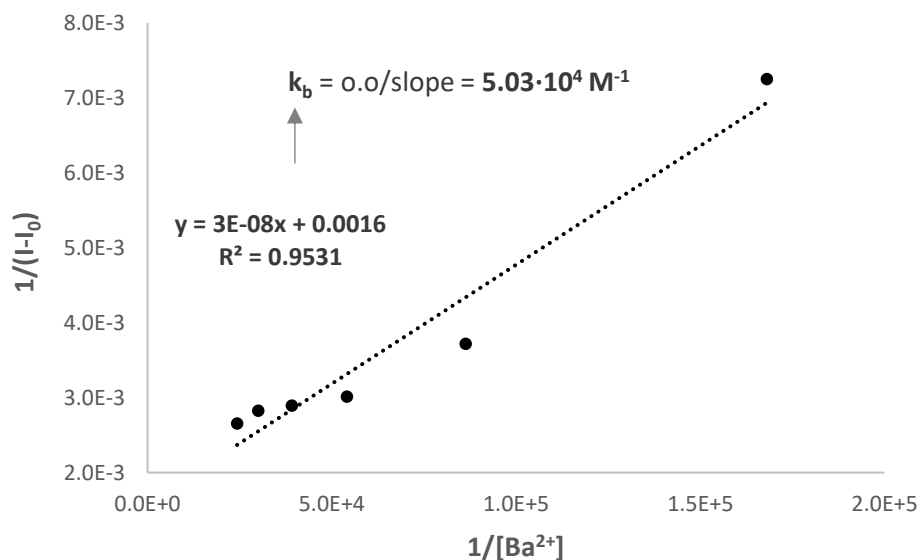
Figure 55.- Benesi Hilldebrand linear fit for compound **16a**.

Compound	n	k_b (M^{-1})
16a	3	$5.03 \cdot 10^4$
16e	1	$8.74 \cdot 10^1$
16f	2	$1.83 \cdot 10^2$
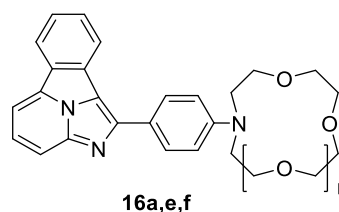
Table 14.- k_b values for compounds **16a**, **16e** and **16f**.

2.6.7.- Lifetime, τ1

Fluorescence, as already mentioned in the introduction, depends on two energetic states of the electron. The basic state (S0) and the excited state (S1). After excitation by absorption of a photon, in the case of fluorophores, there is a relaxation (in nanoseconds) associated with the emission of a photon. The time that the electron spends in S1 before relaxation is the lifetime of the fluorophore. Figure 56 shows the dependence of the fluorophore spectrum of **16a** with time.
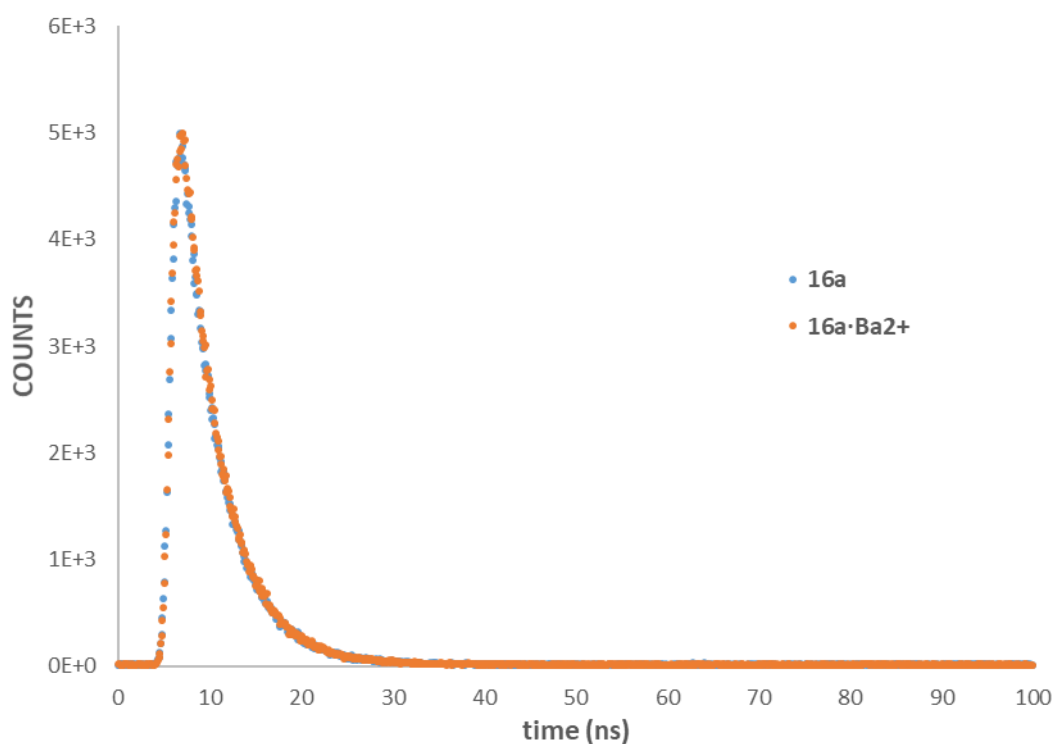
Figure 56.- Raw lifetime spectra of **16a** and **16a-Ba²⁺**.1·10⁻⁵ M in MeCN, r.t., light source: 485nm laser. Pulse: 100ns

In general, the decay of the fluorescence response R(t) with time can be adjusted up to four terms according to Equation 8

$$R(t) = \sum_{i=1}^{4} B_i e^{\left(-t/\tau_i\right)} \qquad (8)$$

71

Where B_i are the coefficients that reflects the contribution of each mode and τ_i are the corresponding lifetimes. In our experiments, we observed that the first relaxation mode was largely the most important one and therefore

$$R(t) \approx B_i e^{\left(-t/\tau_1\right)} \qquad (9)$$

Table 15 collects the τ_1 values obtained for **16a** in its free and bound (**16a·Ba^{2+}**) states. According to our results, both species have almost equal lifetimes at both 50ns and 100 ns. In addition, it can be seen that the species with barium has a ca. 1 ns longer lifetime than the free state. Fot this reason, in Figure 56 both lines are almost the same. In both cases, the contribution is 100%, since both lifetimes have a single component.

	Periodic Pulse (ns)	τ_1 (ns)	Rel. (%)	χ^2
16a	**50**	3,39	100	1,068
	100	3,40	100	1,077
16a·Ba^{2+}	**50**	4,29	100	1,097
	100	4,27	100	1,132

Table 15.- Lifetime values of **16a** and **16a·Ba^{2+}**, with their contribution percentage and χ^2 value of the fit, where χ^2 is a coefficient that represents how accurate the fit is. The adjustment is correct if this value is between 1 and 2.

2.6.8.- Absorption cross section, σ_λ

The cross section σ at a given wavelength λ is defined by Equation 10:

$$\sigma = \frac{ln10}{N_A} \times \varepsilon \times 1000 \qquad (10)$$

Where N_A is the Avogadro number and ε is the molar extinction coefficient (see Section 2.6.1). According to our results, the σ values range from ca. 0.3 Å^2 (**16d**, **16d·Ba^{2+}**) to 1.1 Å^2 (**16a**, **16b·Ba^{2+}**). These values are useful to design functional monolayers to optimize the absorption features of the fluorescent sensors.

Compound	without barium		with barium	
	ε (cm$^{-1}\cdot$M^{-1})	$\sigma\lambda$ (Å^2)	ε (cm$^{-1}\cdot$M^{-1})	$\sigma\lambda$ (Å^2)
16a	30052	1.15	22043	0.84
16b	22000	0.84	30250	1.16
16c	12586	0.48	12200	0.47
16d	8833	0.34	8500	0.33
16e	20048	0.77	20610	0.79
16f	22500	0.86	25406	0,97

Table 16.- $\sigma\lambda$ values for compounds **16a-f**.

2.6.9.- Selectivity with respect to other metals

As discussed in the introduction, the selectivity of a sensor is a crucial parameter within the NEXT Collaboration. Therefore, in this section, the behavior of compound **16a** in the presence of different alkali and alkaline-earth metals was evaluated (Figure 57).
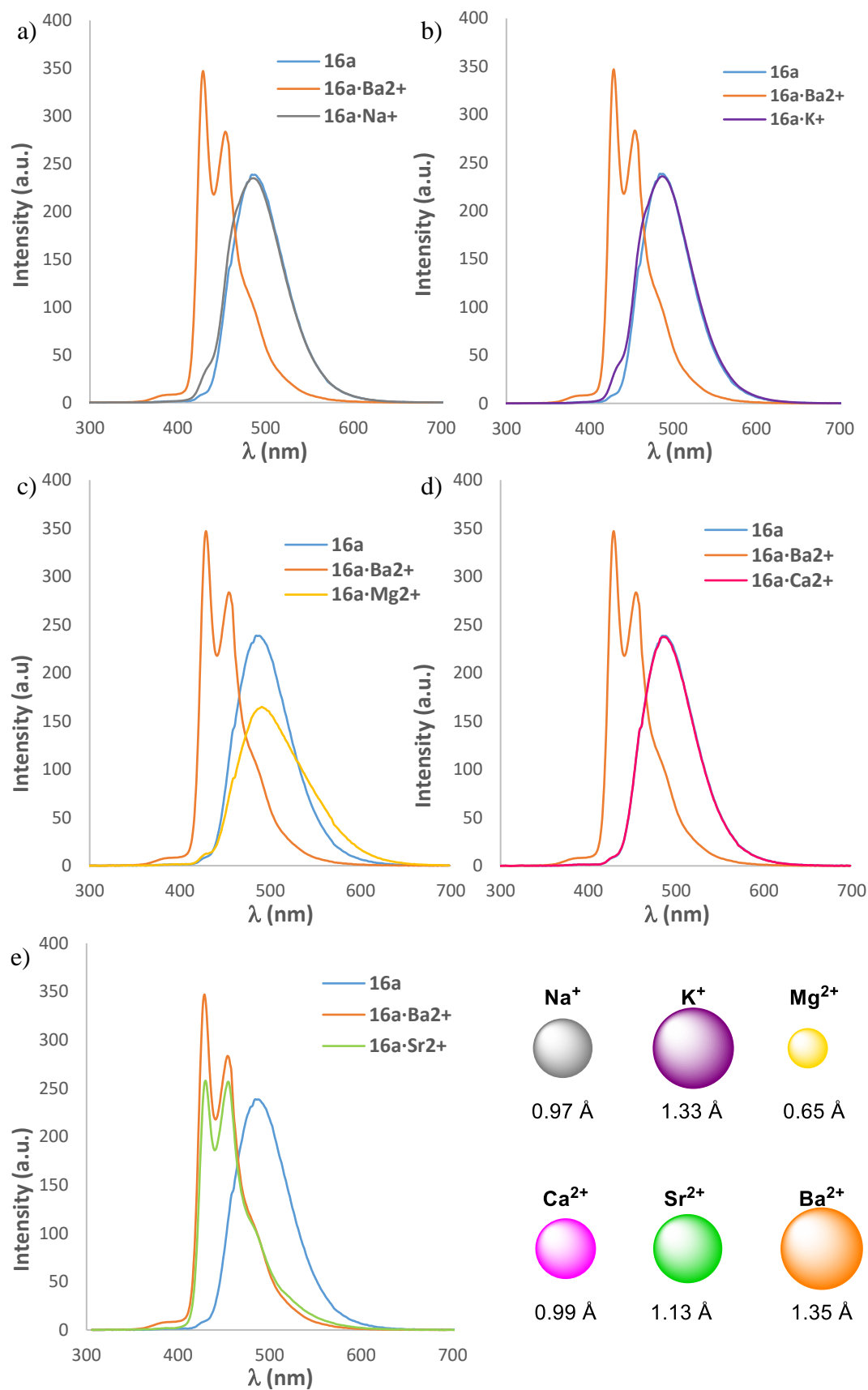
Figure 57.- Emission spectra for **16a** in presence of different metal salts: a) sodium perchlorate, b) potassium perchlorate, c) magnesium perchlorate, d) calcium perchlorate, e) strontium perchlorate. $5 \cdot 10^{-5}$ M in MeCN, r.t., $\lambda_{exc} = 325$ nm

Our results indicate that molecule **16a** is quite selective since it only exhibits bicolor behavior with barium and strontium (Figure 57.e). With metals such as sodium (a), potassium (b) and calcium (d), the emission signal does not change in wavelength or intensity. This, however, does not indicate that the compound does not interact with these metals. In the literature, a large number of papers can be found in which crown 6 ether is used as a host for these cations. Finally, in the case of magnesium (c), the emission signal exhibits a slight change in intensity and suffers a small widening.

2.7.- DFT STUDIES

The strong affinity of compound **16a** to chelate barium cations observed in the last section, was confirmed by electronic structure calculations at the Density Functional Theory (DFT). This theorical studies were performed by Prof. Fernando Cossío and PhD. David Casanova. The optimized structure for the coordinated species **16a·Ba^{2+}** reveals a large molecular torsion of the aza-crown ether with respect to the free **16a** compound (see the ω dihedral angle in Figure 58.b, calculation done at ωB97X-D/6-311++G(p,d)&Lanl2DZ level of theory), so that a molecular cavity is formed, when the metal cation creates a π-complex between the Ba2+ metallic centre and the phenyl group. The oxygen atoms of the aza-crown ether occupy five coordination positions with O·Ba contacts within the range of the diameter (2.6-3.2 Å). Interestingly, the aromatic ring bound to the crown ether is oriented towards the centre of the cavity, using its π-electrons to chelate the cation.
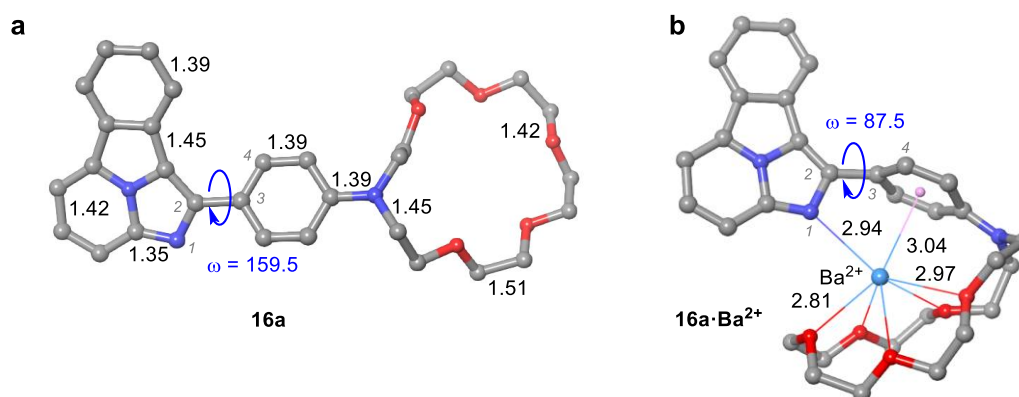
Figure 58.- DFT-derived gas-phase structures of **16a** (a) and **16a·Ba^{2+}** (b). Bond distances are given in Å. Dihedral angles ω formed by covalently bonded atoms 1–4 are given in degrees and in absolute values.

Frontier molecular orbitals (MO) of **16a** are delocalised over the entire fluorophore scaffold, with apparently no participation of the electrons of the aza-crown ether (Figure 59, computed at the ωB97X-D/6-311G(d,p)/LANDL2DZ level).

The lowest bright state of the unbound FBI molecule can be mainly characterised as the electronic transition between highest occupied MO (HOMO) and the lowest unoccupied MO (LUMO). Due to the loss of planarity when the metal is chelated, since the phenyl group rotates and breaks the π-coordination with the rest of the fluorophore, the electronic structure is heavily affected by the molecular distortion upon metal coordination in **16a·Ba^{2+}**. This torsion modifies HOMO and LUMO energy levels (Figure 59)

The decrease of the effective conjugation with respect to 7ca increases the symmetry allowed $\pi \rightarrow \pi *$ gap, thus resulting in the blue shift of the fluorescent emission (Figure 59). Therefore, these results support the viability of 7ca as an efficient Ba2+ indicator in both wet and dry conditions (see Supporting Information).
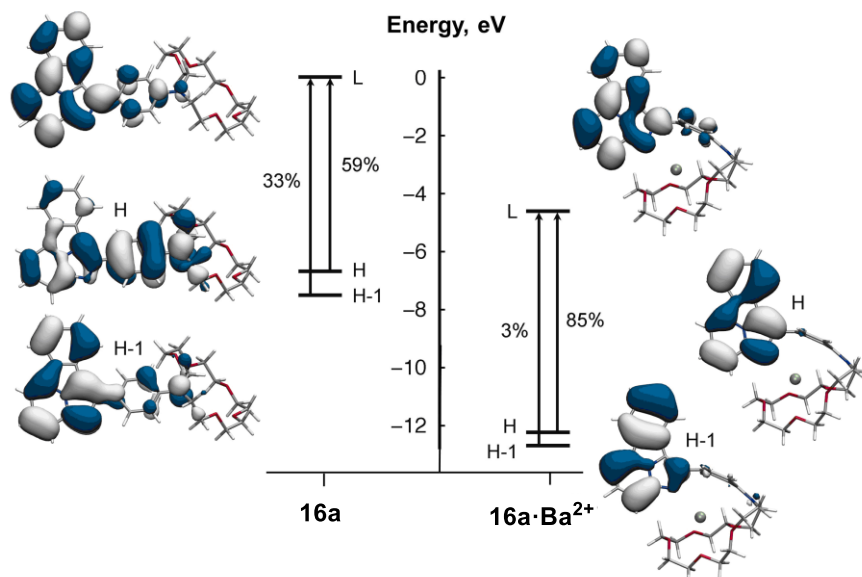
Figure 59.- Frontier molecular orbital energy diagram of **16a** (left) and **16a·Ba^{2+}** (right). Vertical arrows indicate the main contributions to the electronic transition to the lowest bright state.

2.8.- NMR STUDIES

By analyzing the NMR spectra for compound **16a** with different Ba^{2+} equivalents, it can be seen how the *para* system is affected as well as the crown ether. This indicates that both parts of the molecule play a crucial role in the interaction with the barium cation.

In Figure 60, it can be seen how one signal of the *para* system is slightly offset while the other is greatly shifted. This corroborates what was shown in the calculations about the torsion of the molecule when capturing barium. Furthermore, it can also be seen how up to an equivalent the shift is enormous, however, it stabilizes when the barium is in excess. This may also explain the 1:1 ratio seen in Job's Plot in Section 2.6.2. These results are fully agree with the computational studies, since the deshielding of the *para*-phenyl group (Figure 60) upon coordination with Ba^{2+} can be associated with the formation of a π-cation complex,[76] as well as binding of the aza-crown ether, reflected by deshielding of the protons corresponding to the methylene group contiguous to the nitrogen atom (see Figure 60)

---

[76] Dougherty, D. A. The Cation-π Interaction. *Acc. Chem. Res.* **2013**, *46*, 885–893.
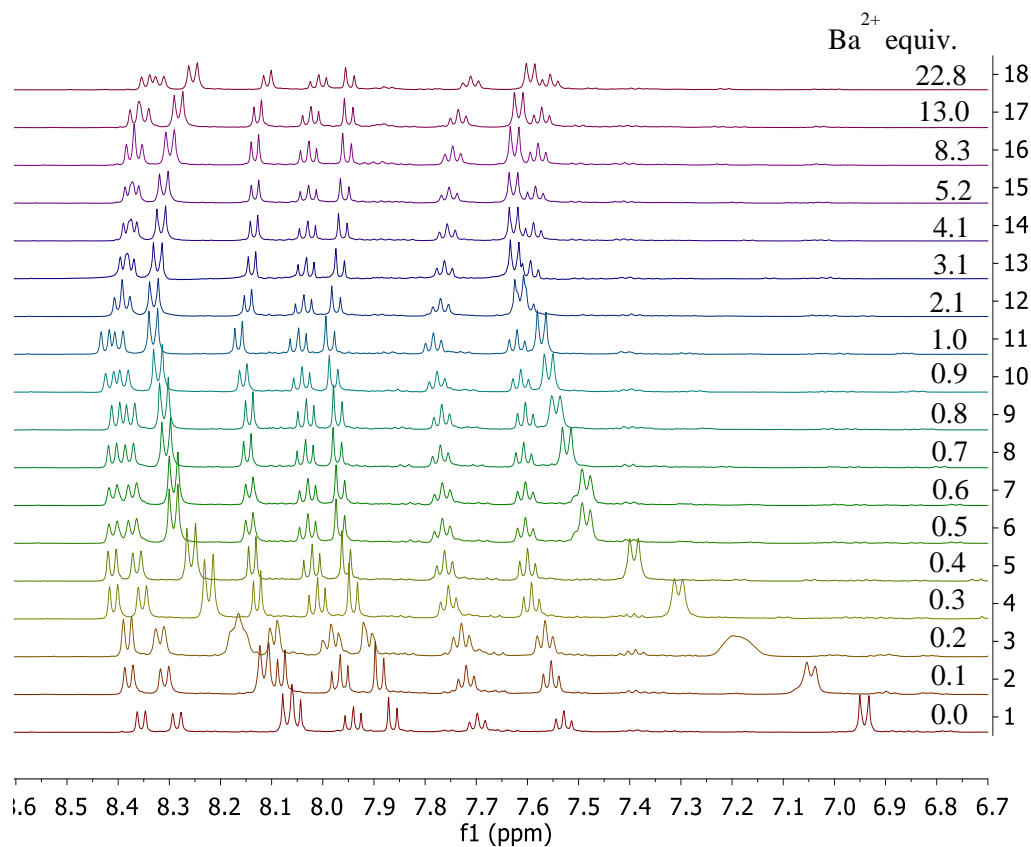
Figure 60.- Aromatic region of ¹H-NMR spectra for compound **16a** at different equivalents of barium perchlorate. MeOD, r.t.
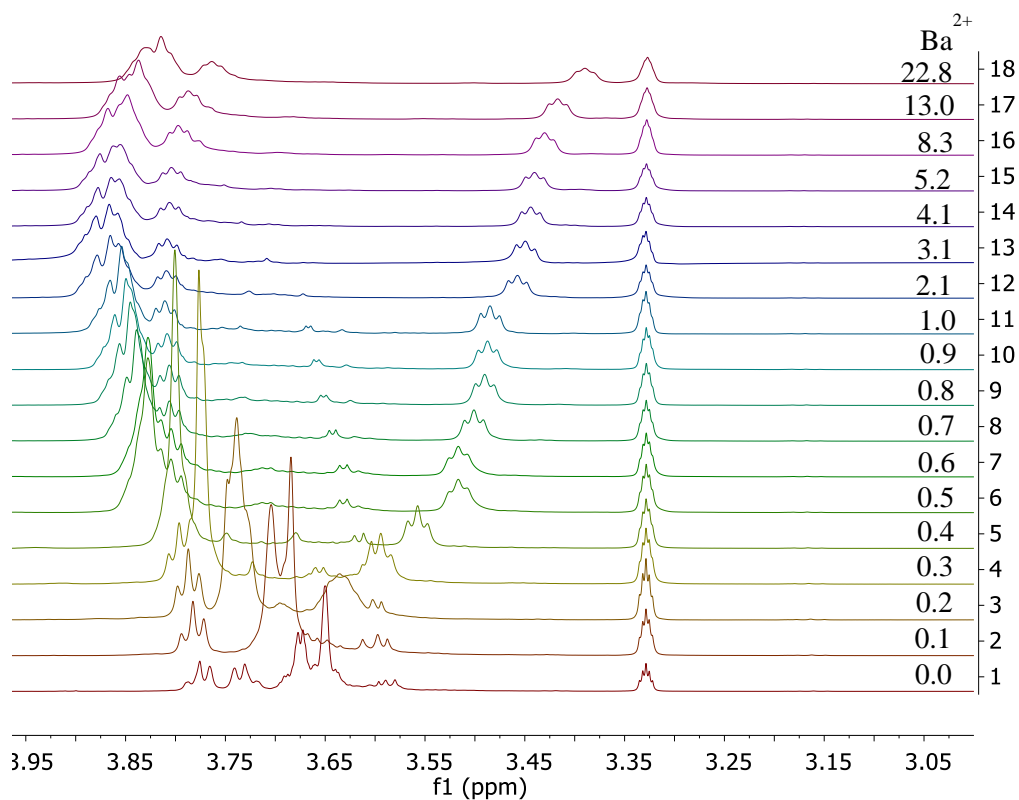
Figure 61.- Crown ether signals in ¹H-NMR for **16a** at different equivalents of barium perchlorate. MeOD, r.t.

2.9 DEVELOPMENT OF A NEW GENERATION OF FBI (FBI-G$_2$)

Despite having obtained good results in the design and chemical synthesis of the compounds explained throughout this chapter, the work of this thesis, at this point, bifurcated. On the one hand, we studied the reproducibility of what we have observed in solution, in a dry medium, evaluating different surfaces (*this will be explained further in Chapter 3*). In parallel, the synthesis of a second generation of bicolor indicators that improve the properties of compounds **16** will be carried out.

As Figure 62 shows, there is room for further improvement. For instance, on the horizontal axis, having a higher delta lambda value. It would also make it even easier to detect such an unusual event as *ββ0ν*. On the vertical axis, increasing the intensities of the different species, especially the chelated species, will also introduce a significant improvement in their photochemical properties.
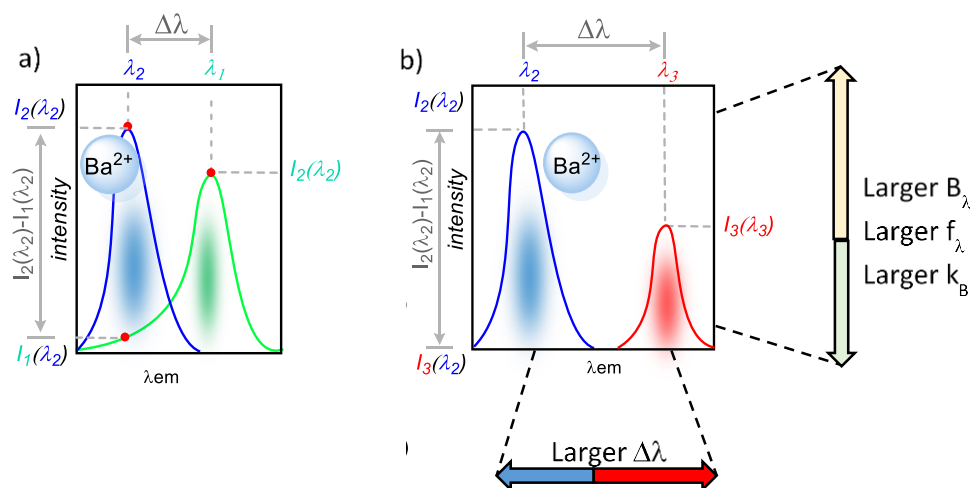
Figure 62. - a) Schematic illustration of the behavior of FBI-G$_1$ (**16**). b) Schematic illustration of the behavior of FBI-G$_2$ and its improvements.

The main idea underlying this part of the work was to permute the nitrogen atom and the carbon atom on which the phenyl is bonded. In this way, the torsional motion observed in the first generation, when FBI chelates barium, would be compatible with this new structure, whereas the photophysical properties of the resulting two-component fluorophore could be improved, although this behavior can not be predicted.
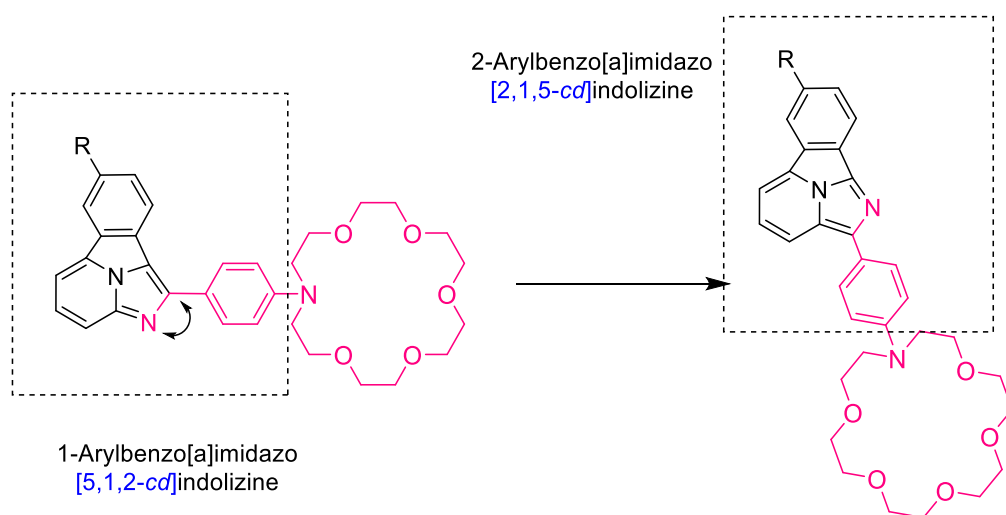
Figure 63.- Proposed structure for the second generation of FBI. The two different fluorophore scaffolds are emphasized.

In this regard, the work of Lévesque et al. was of great interest.[77] Since the reported structures were based on a 2-arylbenzo[a]imidazo[2,1,5-*cd*]indolizine scaffold (Figure 63), closely related to the 2-arylbenzo[a]imidazo[5,1,2-*cd*]indolizine fluorophore described in our previous work.

In order to synthetize the second-generation scaffolds we started by generating oxime **18** from aldehyde **17** was carried out (Scheme 19). Product **18** was obtained in 80% yield. The oxime formed was reacted without further purification, with zinc powder, in acetic acid, generating product **19** quantitatively.
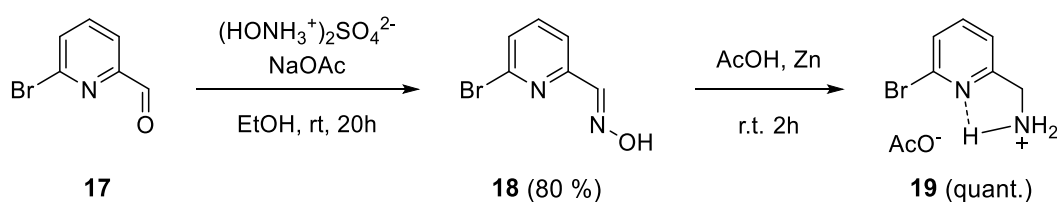
Scheme 19.- Synthesis of the oxime **18** and its subsequent reduction.

Next, amine **19** was used together with the corresponding acyl chlorides in the formation of amides **20a** and **20b**. Both products were obtained in excellent yields (Scheme 20).

---

[77] Lévesque, É.; Bechara, W. S.; Constantineau-Forget, L.; Pelletier, G.; Rachel, N. M.; Pelletier, J. N.; Charette, A. B. *J. Org. Chem.* **2017**, *82*, 5046–5067.
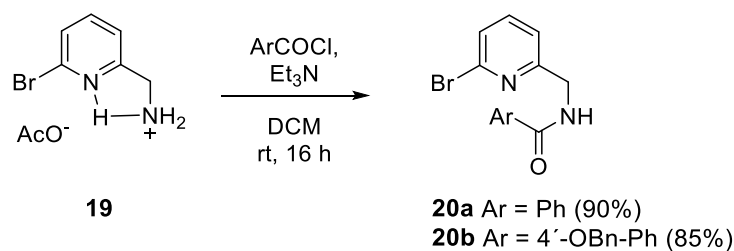
Scheme 20.- Formation of amides **20**.

After the corresponding workup, intramolecular cyclization proceeded between the carbonyl of the amide group and the nitrogen of the pyridine, generating the imidazole ring. After 20 hours of reaction, the new imidazopyridine structure was formed, **21a-b** (Scheme 21).
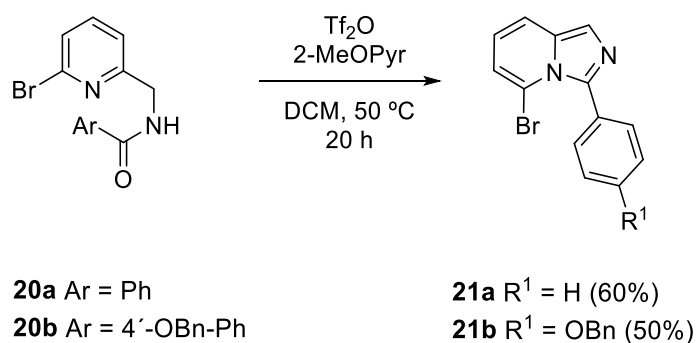
Scheme 21.- Synthesis of products **21**.

The next stage was the formation of tetracycle **22** (Scheme 22). This reaction, although described in the literature as lasting two and a half hours, was left overnight. The reason is that in our first tests, we observed that the conversion into compounds **22a,b** was not complete.
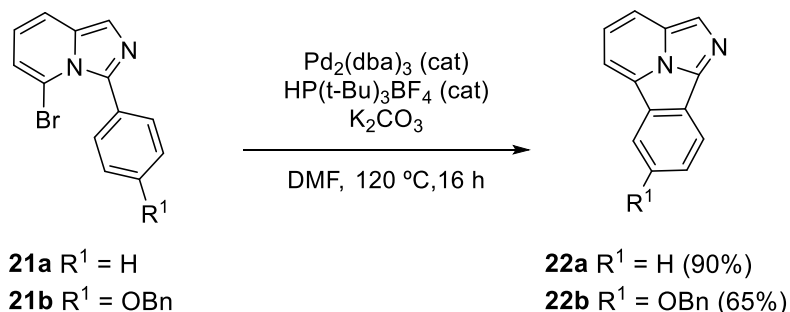
Scheme 22.- Synthesis of molecules **22**.

Once the core benzo[a]imidazo[2,1,5-*cd*]indolizine was obtained, the emission colors were evaluated, in order to anticipate if the change between the nitrogen and the carbon atom affects to the photophysical properties of this second-generation fluorophore.
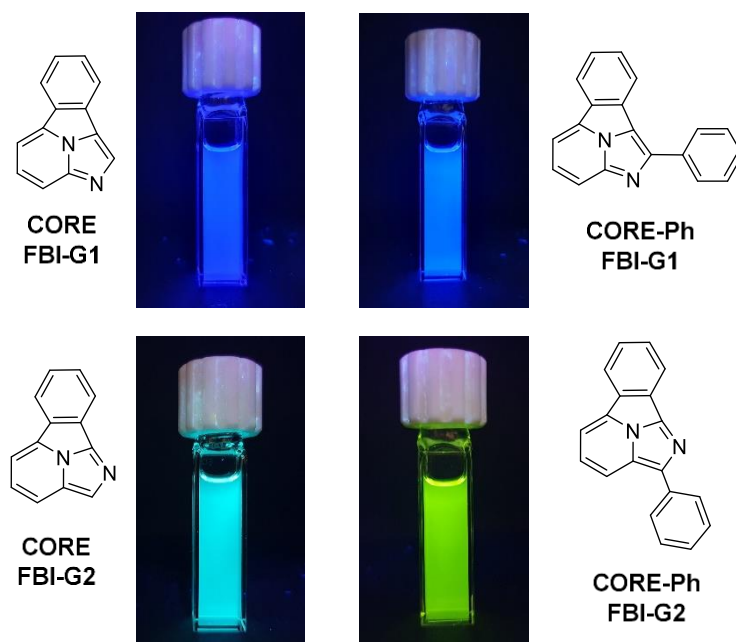
Figure 64.- Comparison of the emission colors between cores of FBI-G1 and FBI-G2. $5 \cdot 10^{-5}$ M in MeCN.

As shown in Figure 64, adding prior a 1-phenyl group in the core of the first generation (upper images), do not cause a relevant change in the emission wavelength. However, in the case of the second generation, the presence of this 2-phenyl group changes the emission color. This suggests that the final sensor of the second generation could improve the features described on the previous page, since it appears to be more sensitive to the presence of additional aryl groups.

After these measurements, following the procedure described in the literature, we proceeded to synthetize the final sensor. For this purpose, two possible routes appear in the work of Levesque et al. Both with palladium catalysis. One of them is the direct arylation using the corresponding halide. In our case, 1-bromo-2-iodobenzene. First, the required palladium catalyst was prepared from palladium acetate, following the procedure described by Mestroni et al.[78] Once the catalyst was synthesized, compound **22** was

---

[78] Milani, B.; Anzilutti, A.; Vicentini, L.; O Santi, A. S.; Zangrando, E.; Geremia, S.; Mestroni, G. *Organometallics* **1997**, *16*, 5064–5075.

reacted with the iodine derivative under the conditions described by Lévesque[77] (Scheme 23).
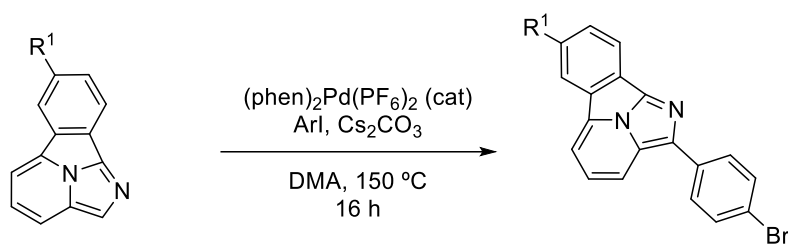
22a R^1 = H (90%)
22b R^1 = OBn (65%)

Scheme 23.- Direct arylation attempt.

Both attempts at direct coupling of the aromatic halide resulted in the recovery of the starting material. After this negative result, the synthetic method was changed. For this, it was first necessary to carry out the bromination of the tetracycle, using the reaction conditions described by Reddy's group.[79] This allowed us to obtain the products **23a,b** with excellent yields in a very short reaction time (Scheme 24).
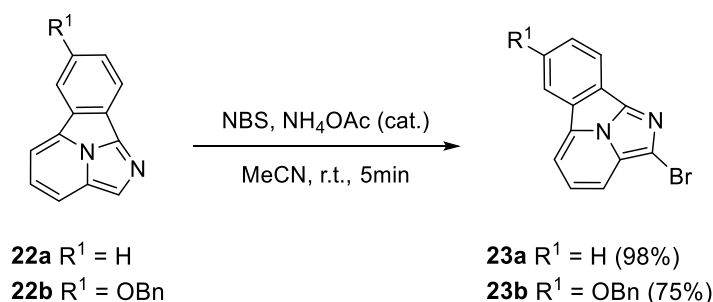
22a R^1 = H
22b R^1 = OBn

23a R^1 = H (98%)
23b R^1 = OBn (75%)

Scheme 24.- Bromation of tetracycles **22**.

The next step was a Suzuki-type C-C coupling between a halide and a boronic acid, using a palladium catalyst and basic medium. Scheme 25 shows the reaction to obtain the coupled product. However, the expected compound was not obtained.

---

[79] Das, B.; Venkateswarlu, K.; Majhi, A.; Siddaiah, V.; Reddy, K. R. *J. Mol. Catal. A* **2007**, *267*, 30–33.

23a R^1 = H
23b R^1 = OBn
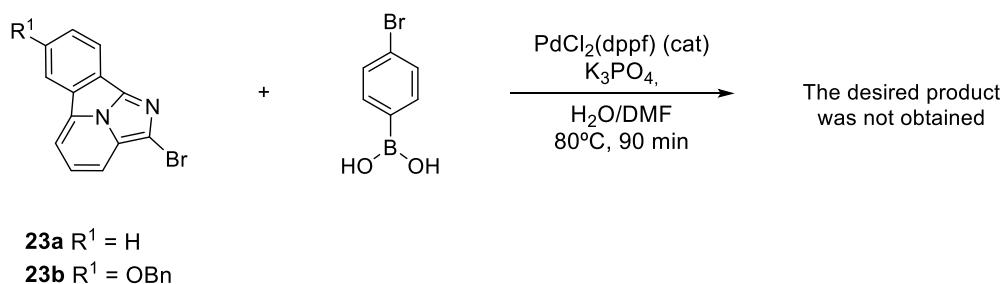
Scheme 25.- First attempt of Suzuki reaction.

One of the possible explanations for the previous result may be the existence of boronic acid homo-coupling. For this reason, the strategy was changed and, instead of building the final sensor step by step, it was proposed to carry out a convergent route and, as a last step, to join both components.

Taking into account this new strategy, the retrosynthesis proposed to obtain the second piece of the puzzle was as shown in Scheme 26.
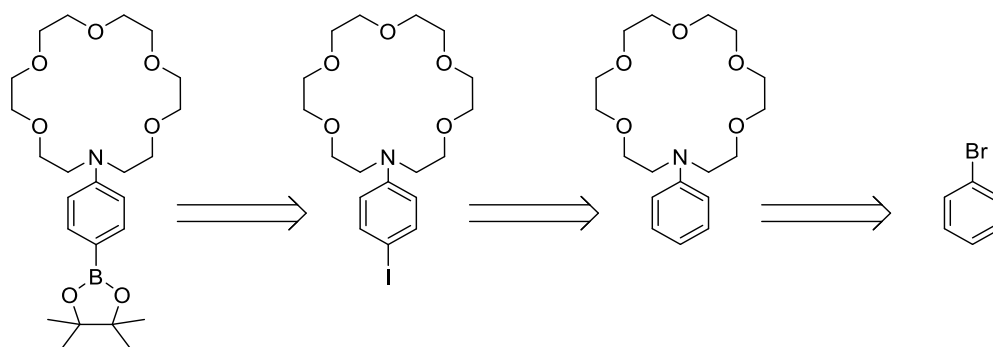
Scheme 26.- Retrosynthetic strategy to avoid problems of Scheme 25.

The first step consisted of the C(sp^2)-N(sp^3) coupling between the crown ether and bromobenzene. For this reaction the conditions already used in the first generation were used (Section 2.3), obtaining compound **25** quantitatively (Scheme 27).
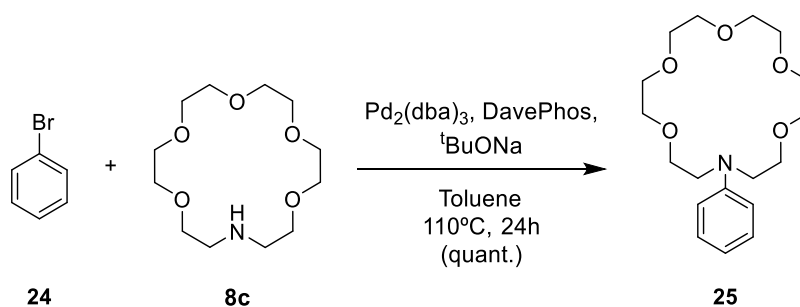
Scheme 27.- Coupling between aza crown ether **8c** and bromobencene **24**.

The next step was the generation of 4-iododerivate **26** from **25** by means of the reaction of this latter precursor with N-iodosuccinimide (NIS). This reaction taken place with a really quantitative yield (Scheme 28).

25 → NIS, NH$_4$OAc (cat.) / MeCN, r.t., 5min → **26**

Scheme 28.-Synthesis of compound **26**.

The last step was the formation of the boronic acid **27** which, a posteriori, will be coupled to compound **23**. For this purpose compound **26** was reacted with the boro-pinacolate dimer as shown in Scheme 29.

26 → B$_2$Pin$_2$, PdCl$_2$(PPh$_3$)$_2$, KOAc / DMSO, 80ºC, 16h (50%)* → **27**

Scheme 29.- Preparation of boronic acid **27**. *Yield estimated by NMR.

By analyzing the NMR spectra of the reaction mixture before column purification, two sets of signals from the *para* system were observed. The intensities were similar, suggesting that only 50% of the product was present. However, after numerous purification attempts, a reasonable amount of compound **27** could not be obtained. In view of that result, the sequence was reversed. Thus, from 2-bromide derivates **23a,b** the corresponding boronates **28a,b** were obtained (Scheme 30).

Scheme 30.- Synthesis of boronic acid **28**. n.d. stands for "not determined" (see text).
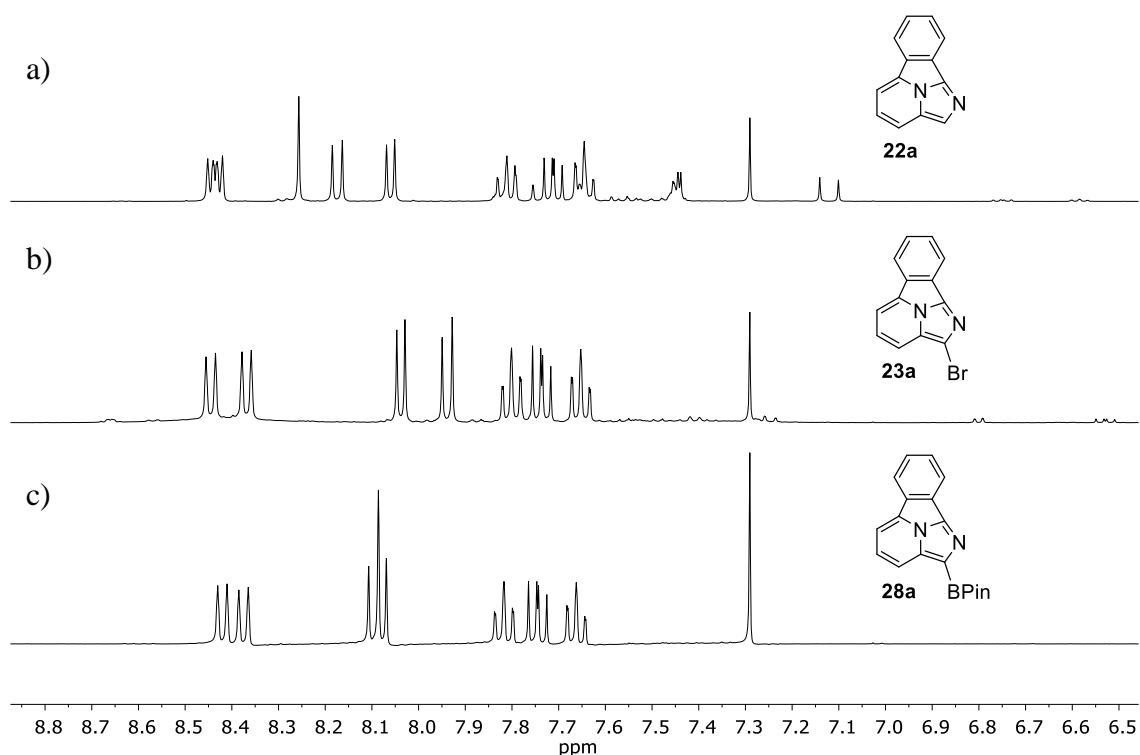
Figure 65.- ^{1}H-NMR of differents steps in FBI-G2 synthesis. CDCl$_3$ as solvent, r.t. a) FBI-G2 Core **22a**. b) Bromination of FBI-G2 Core **23a**. c) Boronic derivate **28a**.

As shown in Figure 65, the aromatic region of the spectrum has a singlet which, after bromination, disappears. The change from bromine to boronic ester involves slight changes in the signals corresponding to reaction product **28a**.
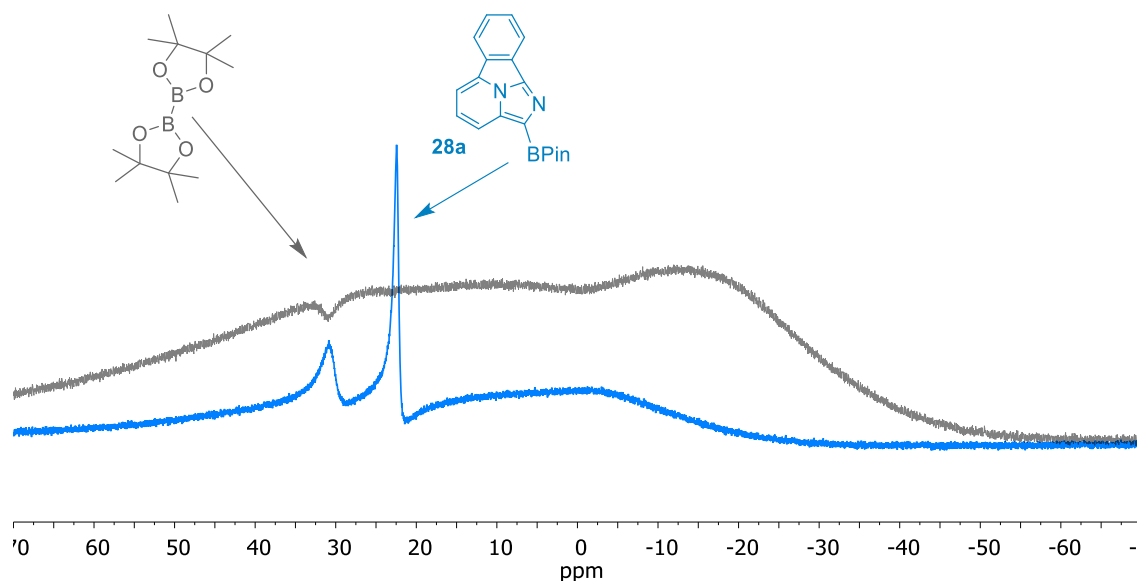
Figure 66.- ^{11}B-NMR spectra of starting material B2Pin2 and compound **28a**. CDCl$_3$ as solvent, r.t.

Furthermore, it is possible to observe by ^{11}B-NMR the change in the shift between the starting material and the product **28a** (Figure 66).

Once the boronic acid was synthesized, Suzuki coupling with compounds **28a,b** and palladium catalysis was carried out. The reaction between compounds **28** and the halogenated derivative **26** was carried out under the conditions shown in Scheme 31. After one and a half hours of reaction, the final products of the second generation of bicolor sensors (FBI-G2) were obtained with very low yields.
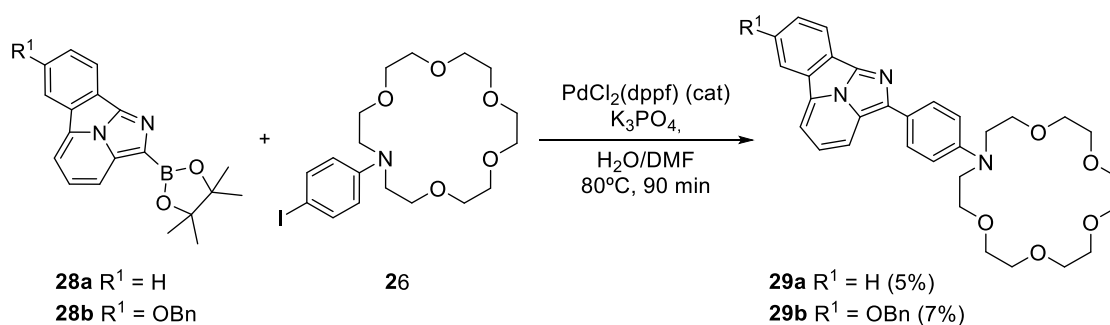
Scheme 31.- Synthesis of final products **29**.

After purification of compounds **28**, crystals suitable for X-ray diffraction were obtained. Unfortunately, the structure obtained was not as expected. The result was the structure of the bromine derivatives 27, instead of boronic acid (Figure 67). This is the reason why the yield has been set as "n.d." in Scheme 30.
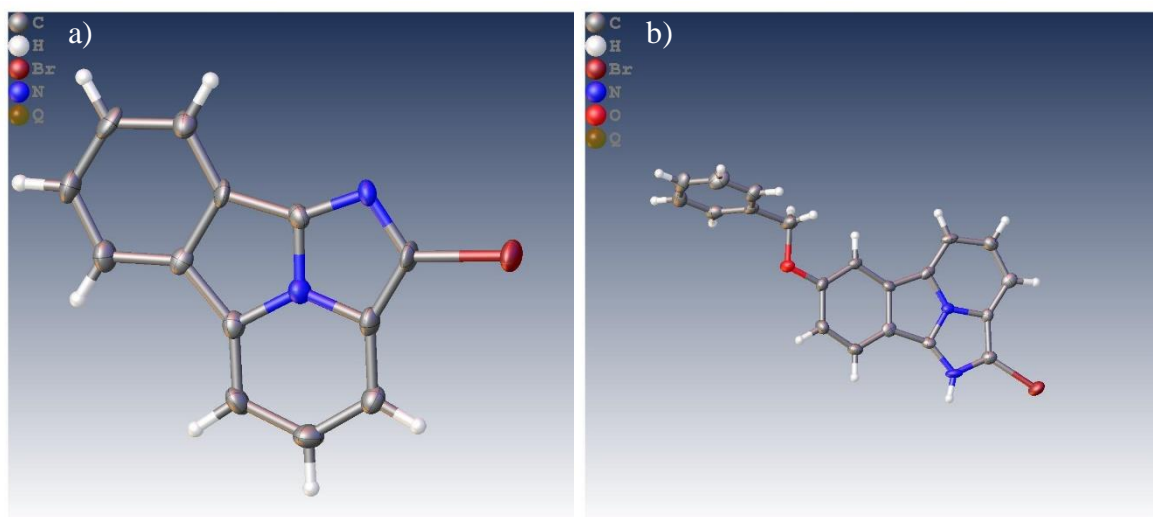
Figure 67.- X-ray diffraction structures of compounds a) **23a** and b) **23b**

The sample contained about 10% of a second compound, but it was not possible to elucidate its structure in X-ray assays. In view of this failure, it is not surprising compounds **29** were obtained in very low yields. For this reason, since boronic acid was the minor product in the starting mixture, the Suzuki coupling should have much higher yields. In summary, the suitable synthesis of boronic esters **28a,b** remains as an objective to be achieved. However, the low amount of compounds **29a,b** was enough to measure their photophysical properties.

As in the case of generation of FBI (FBI-G1), after obtaining the final compounds **29a,b**, $5 \cdot 10^{-5}$ M solutions were prepared in order to observe the behavior in solution. In Figure 68, it can be seen how compound **29a** seems to shift its absorption maxima towards lower wavelengths, maintaining the same trend. On the other hand, in the emission spectrum, it can be seen how this second generation also presents the desired bicolor behavior. In the case of sensor **29a**, its emission maximum is located at 622 nm. Once the barium cation is captured, the hypsochromic shift places the new maximum at 550. In addition, it can be seen how the emission intensity also increases when the metal cation is captured.
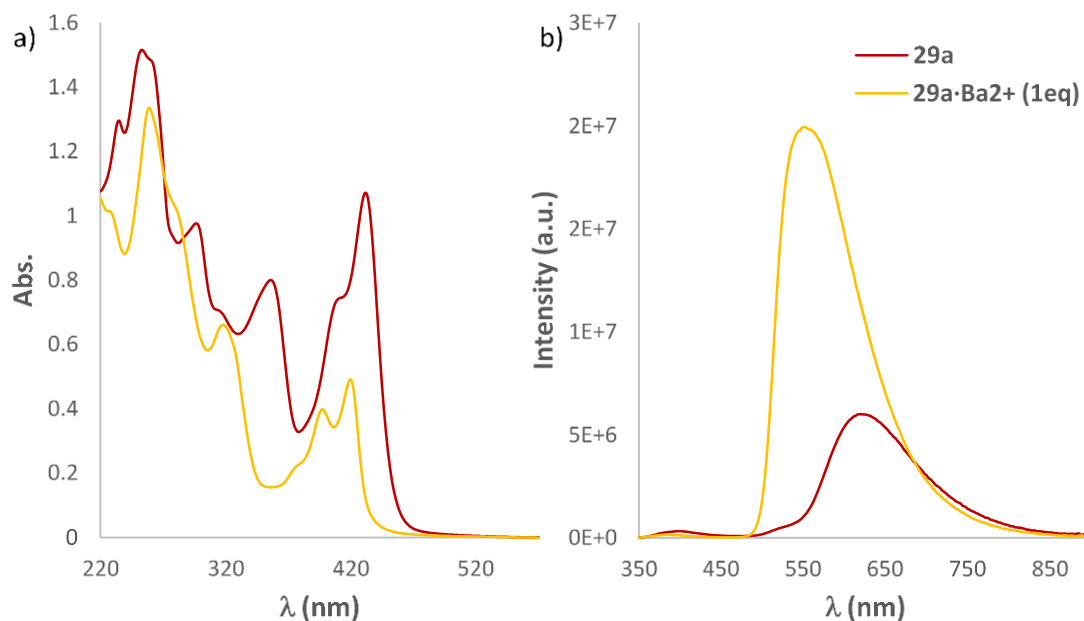
Figure 68.- a) Absorbance spectra for compound **29a** and **29a·Ba^{2+}** (1 eq), $5 \cdot 10^{-5}$ M in MeCN, r.t. b) Fluorescence spectra for compound **29a** and **29a·Ba^{2+}** (1 eq), $5 \cdot 10^{-5}$ M in MeCN, r.t., $\lambda_{exc} = 325$ nm.

The second compound synthesized, **29b**, does not have a very remarkable absorbance spectrum (Figure 69.a). It does not present very defined maxima and, although changes are seen between the free and chelated species, they are not very large changes. However, the emission spectrum (Figure 68.b) does show this important change in wavelength. In addition, the presence of the benzyloxy group shifts these maxima slightly more towards the red. In the absence of barium, the maximum is 640 nm. In the presence of Ba^{2+}, the maximum drops to 564 nm. Moreover, once the barium is captured, the intensity increases more with respect to the free species
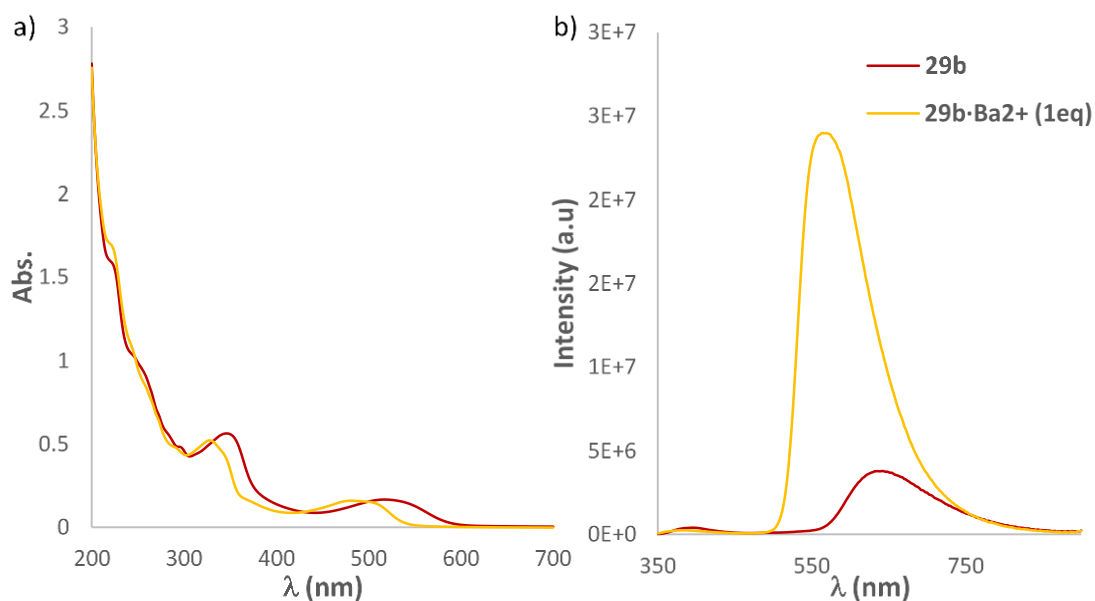
Figure 69.- a) Absorbance spectra for compound **29b** and **29b·Ba²⁺** (1 eq), 5·10⁻⁵ M in MeCN, r.t. b) Fluorescence spectra for compound **29b** and **29b·Ba²⁺** (1 eq), 5·10⁻⁵ M in MeCN, r.t., λ_{exc} = 325 nm.

2.10.- PHOTOPHYSICAL STUDIES OF FBI G2

As in the previous case, photophysical characterization was performed for the two new compounds **29a** and **29b**. At this point the values obtained for the two products of the second generation are shown.

2.10.1.- Molar extinction coefficient, ε

Figure 70 shows the different UV-Vis spectra at concentrations in the range of 5·10⁻⁵ - 5·10⁻⁹ M. Within this range, the Beer-Lambert was applied to determine the molar extinction coefficient by linear regression, as it shown in Figure 71.
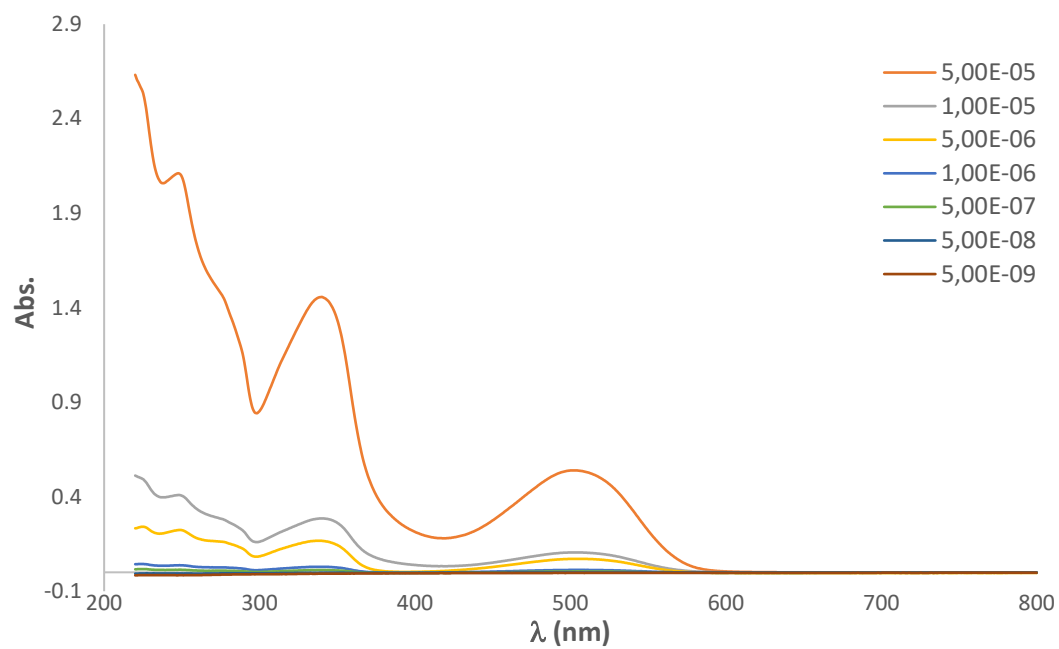
Figure 70.- Absorbance spectra for compound **29a** at different concentrations, MeCN, r.t.
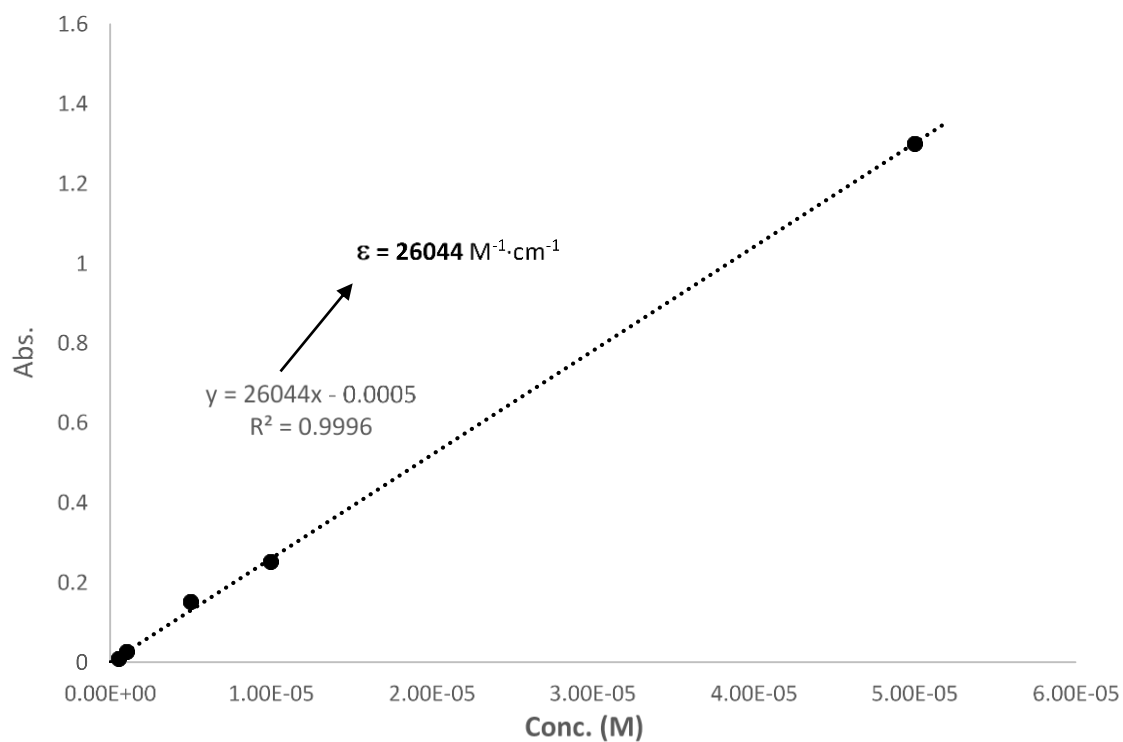
Figure 71.- Linear fit of the values obtained for compound **29a** at λ = 325 nm.

Thus, the values obtained for ε, $(cm^{-1} \cdot M^{-1})$ for the second generation of FBI were those shown in Table 17. In addition, from these measures, it was also possible to set the working limit with these compounds, $5 \cdot 10^{-7}$ M being the lowest possible working concentration. At concentrations lower than the above mentioned, the characteristic absorbance bands of compound **29a** are no longer visible.

Compound	ε without barium $(cm^{-1} \cdot M^{-1})$	ε with barium $(cm^{-1} \cdot M^{-1})$
29a	26044	30117
29b	10272	10523

Table 17.- ε values for FBI-G2 compounds.

2.10.2.- Job's Plot

The Job's Plot, in this case, is the same as for the first generation due to the binding moiety is still the crown 6 ether unit. Therefore, these compounds bind barium perchlorate in a 1:1 stoichometry.

2.10.3.- Quantum Yields, ϕ_λ

The quantum yields, in this case, were calculated using the integrating sphere technique.
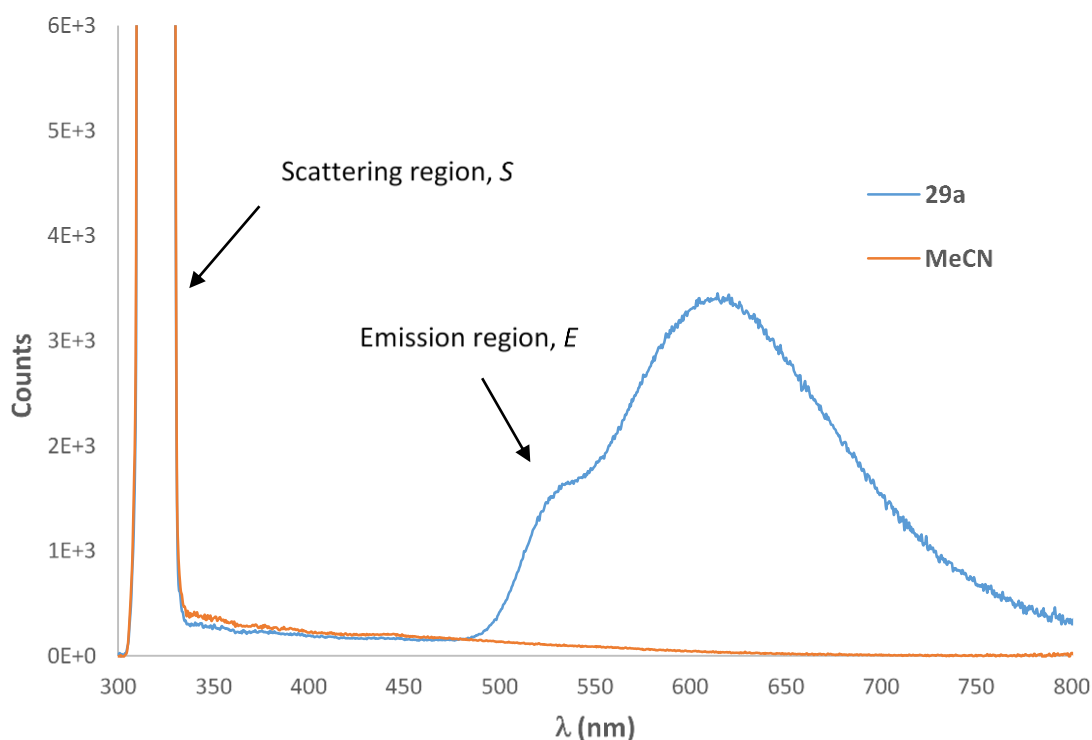
Figure 72.- Quantum yield plot for compound **29a**, 10^{-7} M, MeCN, r.t.

As it can be seen in Figure 72, the blue line represents the emission of compound **29a** in the integrating sphere. The orange line corresponds to the reference (solvent). The ratio between the integrals of the two spectra corresponds to the value of the quantum yield. The calculation of the quantum yield by integrating sphere follows the Equation 11.

$$\phi_\lambda = \frac{E_c - E_r}{S_r - S_c} \qquad (11)$$

Where E is the integral of emission region of compound (E_c) and reference (E_r) and S is the integral of the scattering region of compound (S_c) and reference (S_r).

The values obtained for compounds **29a,b** are shown in Table 18. It is noteworthy that the quantum yields of the Ba^{2+} - coordinated species are larger than those measurements for the free ligands. This difference is particularly high in the case of compound **29b**.

Compound	ε without barium ($cm^{-1} \cdot M^{-1}$)	ε with barium ($cm^{-1} \cdot M^{-1}$)	ϕ_λ without barium	ϕ_λ with barium
29a	26044	30117	0.23	0.55
29b	10272	10523	0.08	0.43

***Table 18.**-* ε and ϕ_λ values for FBI-G2 compounds. ϕ_λ values measured with integrating sphere.

2.10.4.- Molecular Brightness, B_λ

As it could be anticipated from the previous results for the molar extinction coefficients and quantum yields, the molecular brightness of compounds **29a,b** show a larger increase in the coordinated state with respect to the free ligands (Table 19). This is a good starting point for further developments.

Compound	ε without barium ($cm^{-1} \cdot M^{-1}$)	ε with barium ($cm^{-1} \cdot M^{-1}$)	ϕ_λ without barium	ϕ_λ with barium	B_λ ($\cdot 10^3$) ($cm^{-1} \cdot M^{-1}$) without barium	B_λ ($\cdot 10^3$) ($cm^{-1} \cdot M^{-1}$) with barium
29a	26044	30117	0.23	0.55	5.990	16.564
29b	10272	10523	0.08	0.43	0.822	4.525

***Table 19.**-* ε, ϕ_λ, B_λ values for FBI compounds.

2.10.5.- Discrimination factor, f

In the case of the second generation the calculation of f was not carried out at the maximum wavelenght. In this case, the highest value of f is found at a wavelength slightly lower than the maximum, where the contribution of the free species is as small as possible, as shown in Figure 73.
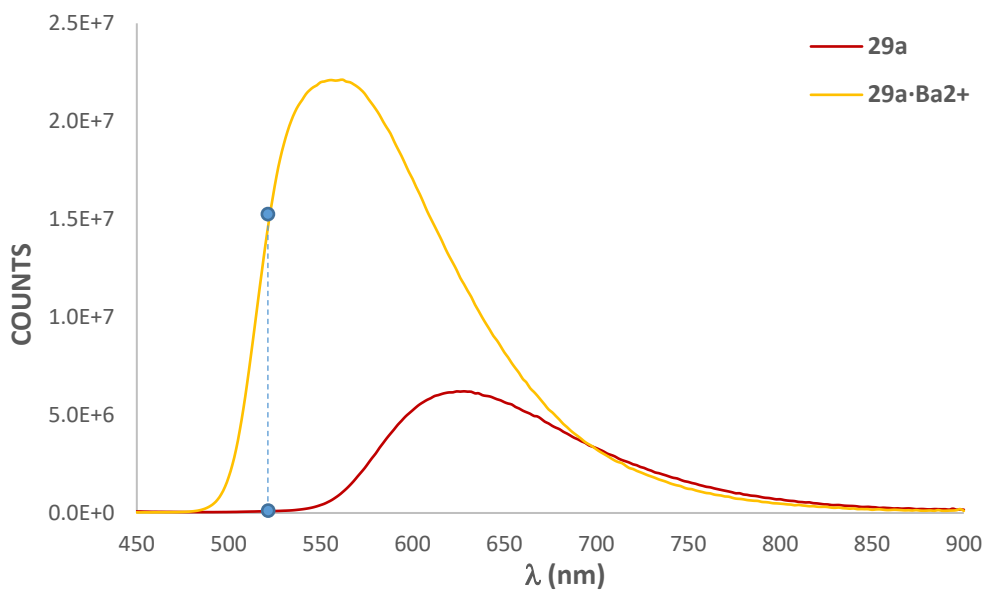
Figure 73.- Values of **29a** and **29a·Ba2+** for the calculation of discrimination factor a 524 nm.

Under these conditions, the f_λ values shown in Table 20 show that the discrimination factor for compound **29a** is especially high.

Compound	λ (nm)	f_λ
29a	524	210.6
29b	528	30.3

Table 20.- f values for compounds **29**.

2.10.6.- Binding constant, K_b

As in the FBI-G1 case, the values of binding constant K_b were measured from the emission spectra of **29a** at different concentrations shown in Figure 74
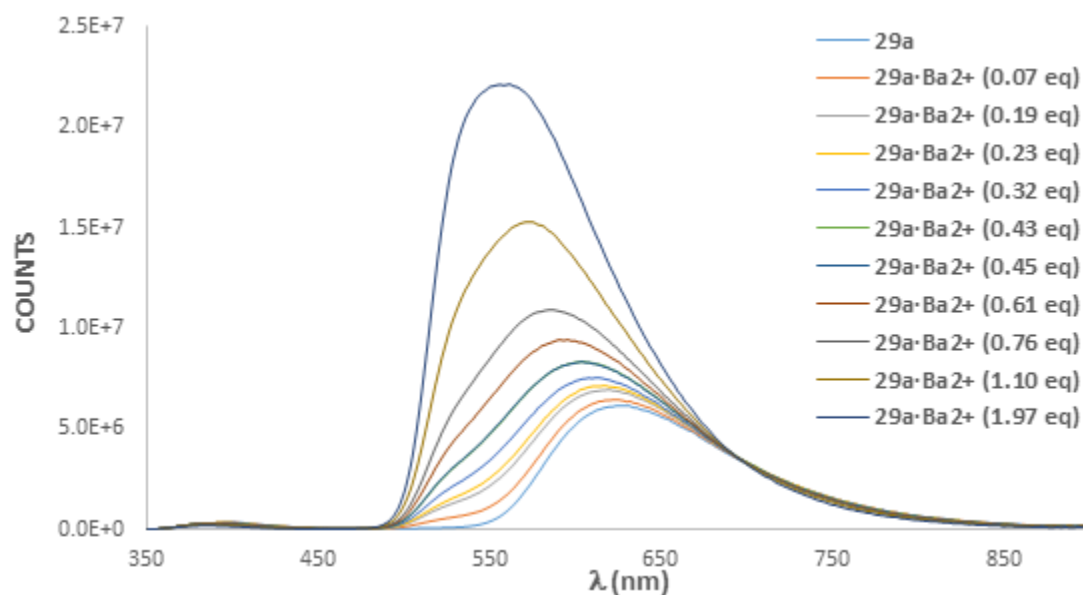
Figure 74.- Emission spectra of compound **29a** with different equivalents of barium perchlorate. $5 \cdot 10^{-5}$M in MeCN, r.t. $\lambda_{exc} = 325$ nm.

Once spectra were recorded, the data processing was done by means of the Benesi-Hildebrand method. Taking the maximum values of the different spectra, we performed a linear fit. In this case, the values of Kb for compound **29a** was $1.17 \cdot 10^7$ M^{-1}, a ca. three orders of magnitude higher than that measured for **16a** ($5.03 \cdot 10^4$ M^{-1}, _vide supra_). This means that, as for as the binding ability is concerned, the **29a** is much more efficient than its first generation congener **16a**.

2.10.7.- Lifetime, τ1

For the lifetime measurement, the spectra with and without barium were recorded, as for compound **16a**. With these data, the lifetimes for the second generation were as follows.
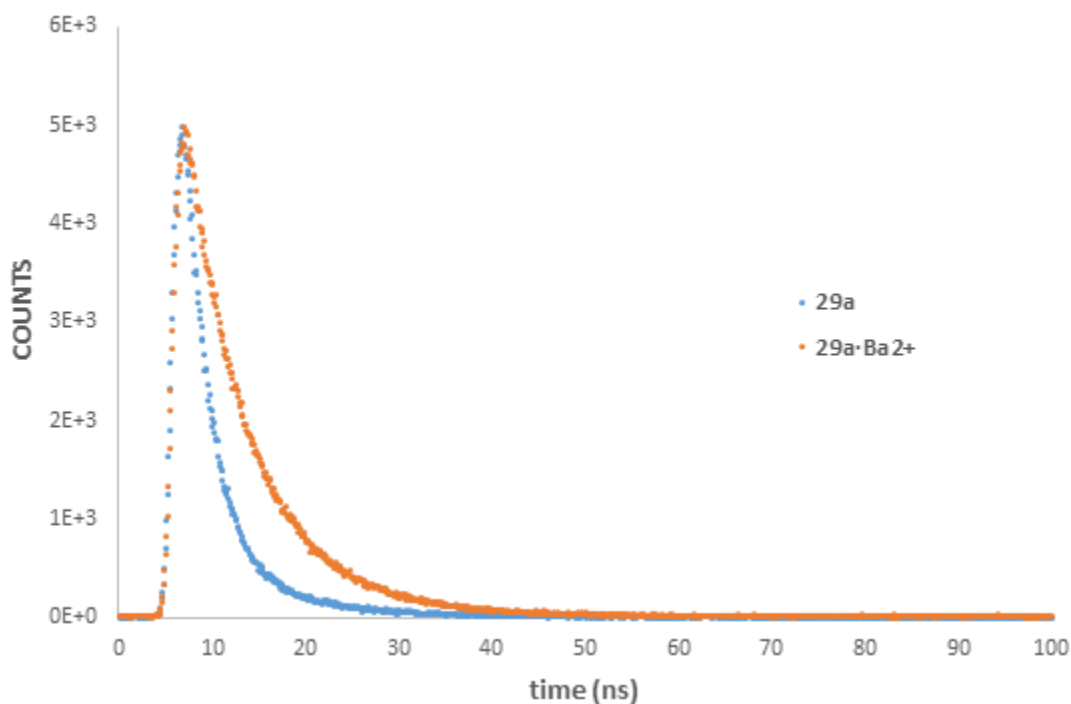
Figure 75.- Raw lifetime spectra of **29a** and **29a-Ba^{2+}**.1·10^{-5} M in MeCN, r.t., light source: 485nm laser. Pulse: 100ns.

After recording these spectra, the lifetime values obtained were those reported in Table 21:

	Periodic Pulse (nm)	τ_1 (ns)	Rel. (%)	χ^2
29a	**50**	2,95 11,14	72,80 27,20	1,273
	100	2,87 9,73	70,63 29,37	1,168
29a·Ba2+	**50**	6,86	100	1,302
	100	7,22	100	1,418

Table 21.- Lifetime values of **29a** and **29a·Ba^{2+}**, with their contribution percentage and χ^2 value of the fit, where χ^2 is a coefficient that represents how accurate the fit is. The adjustment is correct if this value is between 1 and 2.

In contrast with FBI-G1, FBI-G2 congener has two different lifetimes (n = 2 in Eq. 8). The major component, with a contribution of 70%, lies below 3 ns. However, there is a minor contribution (30%) for a lifetime between 9 and 11 ns (depending on the laser pulse used). In contrast, in the presence of the barium salt, again, a single value for τ_1 is observed. Furthermore, both in Figure 75 and Table 21 it can be observed that in the case

of the chelated compound, the lifetime values are much more than twice as long as in the case of the free species.

2.10.8.- Absorption cross section, σ_λ

From the calculated values of ε, in section, and applying equation 9, the values of σ could be obtained in a simple way. These values are shown in Table 22.

Compound	without barium		with barium	
	ε $(cm^{-1}\cdot M^{-1})$	σ_λ $(Å^2)$	ε $(cm^{-1}\cdot M^{-1})$	σ_λ $(Å^2)$
29a	26044	1	30117	1.15
29b	10272	0.39	10523	0.4

Table 22.- σ_λ values for compounds **29a-f**.

2.10.9.- Selectivity with respect other metals

As it discussed above, the requirements of the NEXT project involve the development of a fluorescent sensor selective to Ba^{2+}. Therefore, as with compound **16a**, the emission of compound **29a** against other metals was evaluated. In the first-generation compound **16a** it was observed that the emission wavelength was only affected in the presence of barium or strontium. The emission spectra for **29a** in the absence and in the presence of different metal perchlorates are show in Figure 76.
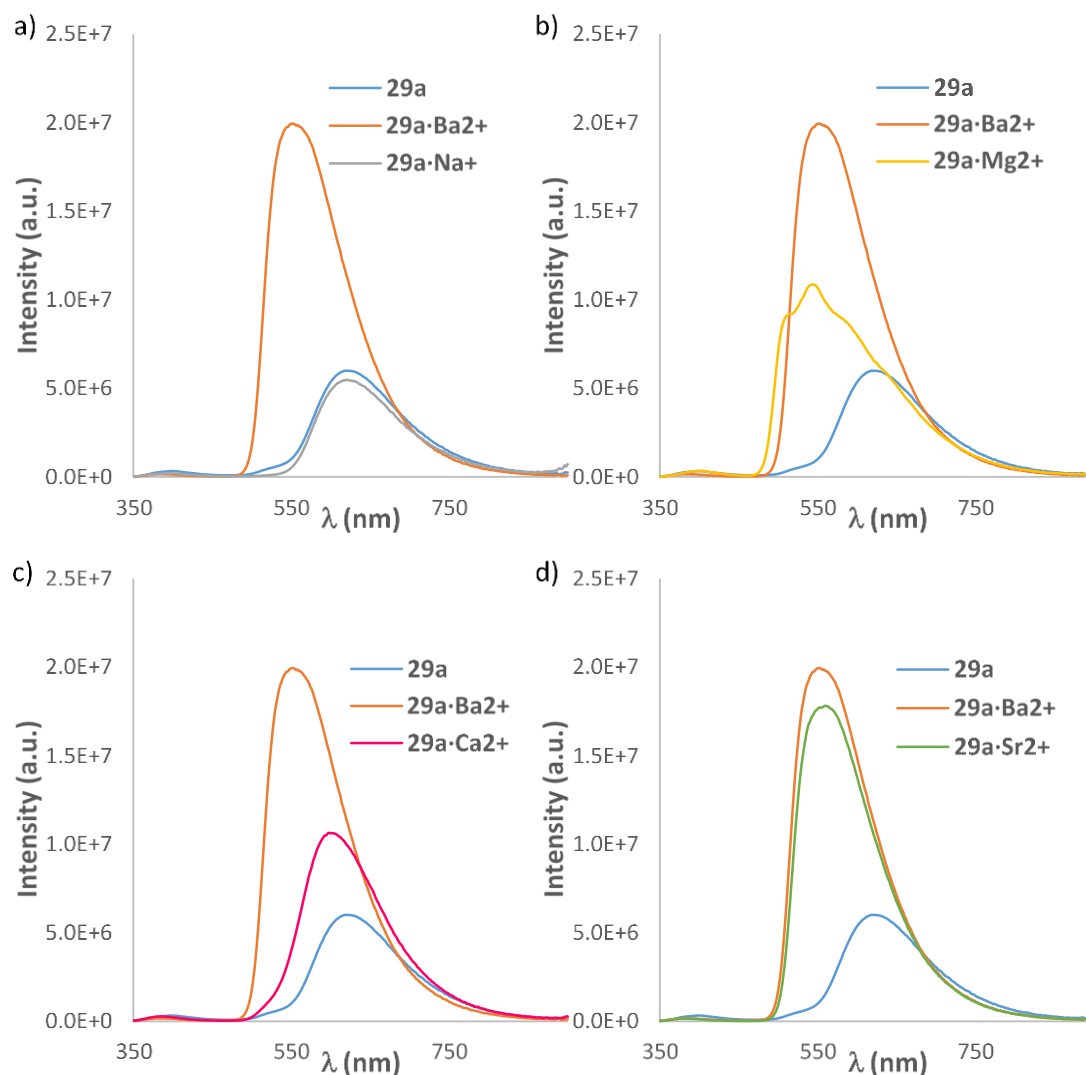
Figure 76.- Emission spectra for **29a** in presence of different metal salts: a) sodium perchlorate, b) magnesium perchlorate, c) calcium perchlorate, d) strontium perchlorate. $5 \cdot 10\text{-}5$ M in MeCN, r.t., $\lambda_{exc} = 325$ nm

Unlike fluorescence indicator **16a**, almost all metals cause a change in emission wavelength of **29a**. Sodium (Figure 76.a) is the only one that does not cause bicolor behavior, since there is no clear shift between the free and chelated species.

Although the rest of the metals caused bicolor behavior (Figure 76.b-d), it should be noted that each one does so at different wavelengths. Therefore, compound **29a** may be promiscuous compared to **16a**. However, by presenting unique shifts for each metal, compound **29a** can be considered a highly versatile and selective sensor.

2.11.- Conclusions

- Throughout this Chapter a synthesis by two different routes for the first generation of fluorescent indicators has been effectively developed. In all the compounds obtained the ability to trap barium has been observed. Three of them, in addition, present a bicolor behavior.

- After all the photophysical analysis, it has been possible to verify how compound **16a** has outperformed its counterparts.

- Compound **16a** is the one that shows the best yield during its synthesis.

- In the case of second generation, the synthesis was carried out by means of a very different synthetic route, with stages of very high yields but with a considerable increase in the number of steps. Nevertheless, two compounds of a new family have been synthesized, although with low final yields, despite the convergent character of the synthetic route.

- The photophysics of these compounds seems to improve what was observed for by the first generation. In this case, the selectivity towards other metals is lower. However, after chelation of each of the metals tested, the wavelength is different, making compound **29a** a very versatile sensor.

Parameter	16a	16a·Ba^{2+}	29a	29a·Ba^{2+}
λ_{exc} (nm)	252		325	
λ_{em} (nm)	498	428	624	556
$\Delta\lambda$ (nm)	70		68	
ε (cm^{-1}·M^{-1})	30052	22043	26044	30117
ϕ	0.67	0.45	0.23	0.55
B (·10^3) (cm^{-1}·M^{-1})	20.13	9.92	5.99	16.56
f	179.7		210.6	
K$_b$ (M^{-1})	5.03·104		1.17·107	
τ_1 (ns) (pulse: 50ns)	3.39 (100%)	4.29 (100%)	2.95 (100%) 11.14 (100%)	6.86 (100%)
τ_1 (ns) (pulse: 100ns)	3.4 (100%)	4.27 (100%)	2.86 (100%) 9.73 (100%)	7.22 (100%)
σ (Å^2)	1.15	0.84	1.00	1.15

Table 23.- Comparision table of compounds **16a**, **16a·Ba^{2+}**, **29a** and **29a·Ba^{2+}**.

2.12.- Future goals

In order to take advantage of the favorable features of the second generation of fluorescent sensors, the following aspects should be addressed:

- Optimize the synthesis of compounds **29**, especially the last stages.

- Explore synthetic alternatives for the second generation.

- Extend the scope with different substituents in FBI-G2.

- Design new generations to improve the parameters of photophysical interest.

Chapter III

Surface Studies, Chemical Modifications and Dry Conditions Chelation

3.1.- OBJECTIVES

This chapter deals with the search for a surface on which to anchor a sensor. The following main objectives can be enumerated:

- To find a suitable surface that meets the requirements of the NEXT-BOLD project.
- To introduce different substituents on the sensor in order to get the best system to anchor on the surface.

To study the photophysical properties once the molecule is linked on the surface and compare it with that observed in solution.

3.2.- PRELIMINARY EXPERIMENTS IN SURFACE

Due to the nature of the NEXT experiment, it is necessary to develop a sensor that maintains its properties in the gas phase. This is, it must keep its bicolor behavior, be able to chelate barium in dry media and not present issues with the surface.

In Chapter 2, the different stages have been explained, starting with the synthesis and ending with the photophysical analysis. As mentioned at the beginning of the section, during the synthetic development of the second generation, some surface tests were performed with the first generation of FBI. The bicolor sensor **16a** has proved to be significantly the best of its family. In synthetic terms, it was the compound that gave the best yield. Moreover, its photophysical properties in solution were better than more of its analogues **16b-f**.

First, a direct adsorption of compound **16a** was chosen. In this way it was possible to evaluate if the photophysical behavior was similar to the behavior in solution. However, in the long term, it is necessary to seek stronger interactions, whether electrostatic or covalent. This will require modifications of the sensor **16a**, by decorating it with appropriate spacers and functional groups.

3.2.1.- Polymer films. Preparation and emission studies

For the first approach, with the adsorption method, different polymers were tested: polyvinyl alcohol (PVA), poly(methyl methacrylate) (PMMA) and poly(ether blockamide) (PEBAX 2533). The structures of the monomers of each of these polymers are shown in Figure 77.

Polyvinyl alcohol
(PVA)

Poly(methyl methacrylate)
(PMMA)

Poly(ether blockamide)
(PEBAX 2533)
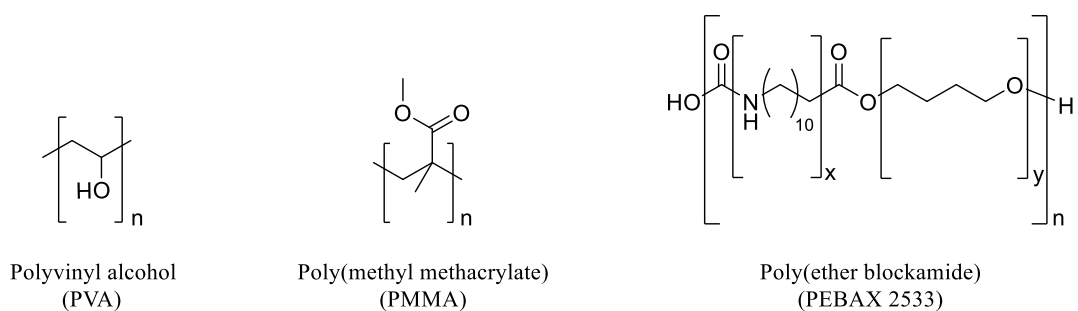
Figure 77.- Structures of employed polymers.

The above mentioned polymers have been widely used by the group of Ikerbasque Research Professor Thomas Schäfer (POLYMAT Institute). For this reason, the preparation of these polymers was carried out in his laboratory.
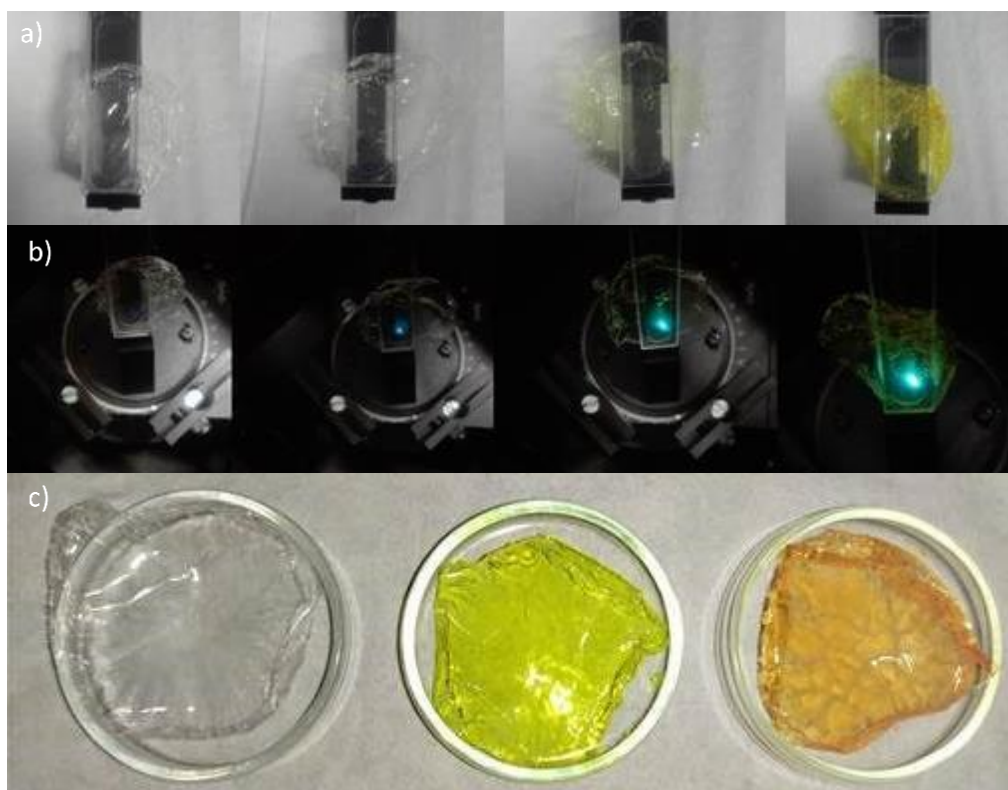
Figure 78.- Polymer films with different concentration of fluorophore.

Starting from a stock solution, three solutions were prepared with 10^{-3}, 10^{-4} and 10^{-5} M concentrations of **16a**. A blank was also prepared. The solution always contains 3 % wt. polymer and 1:3 butanol:isopropanol. It was then deposited on a petri dish (2 cm radius) and left to dry at 60°C for 20 hours. Once these polymers films were prepared their emission spectra were recorded. The results are gathered in **¡Error! No se encuentra el o rigen de la referencia.**. Unfortunately no significant changes in the wavelength of emission spectra of **16a** and **16a·Ba²⁺** could be observed.
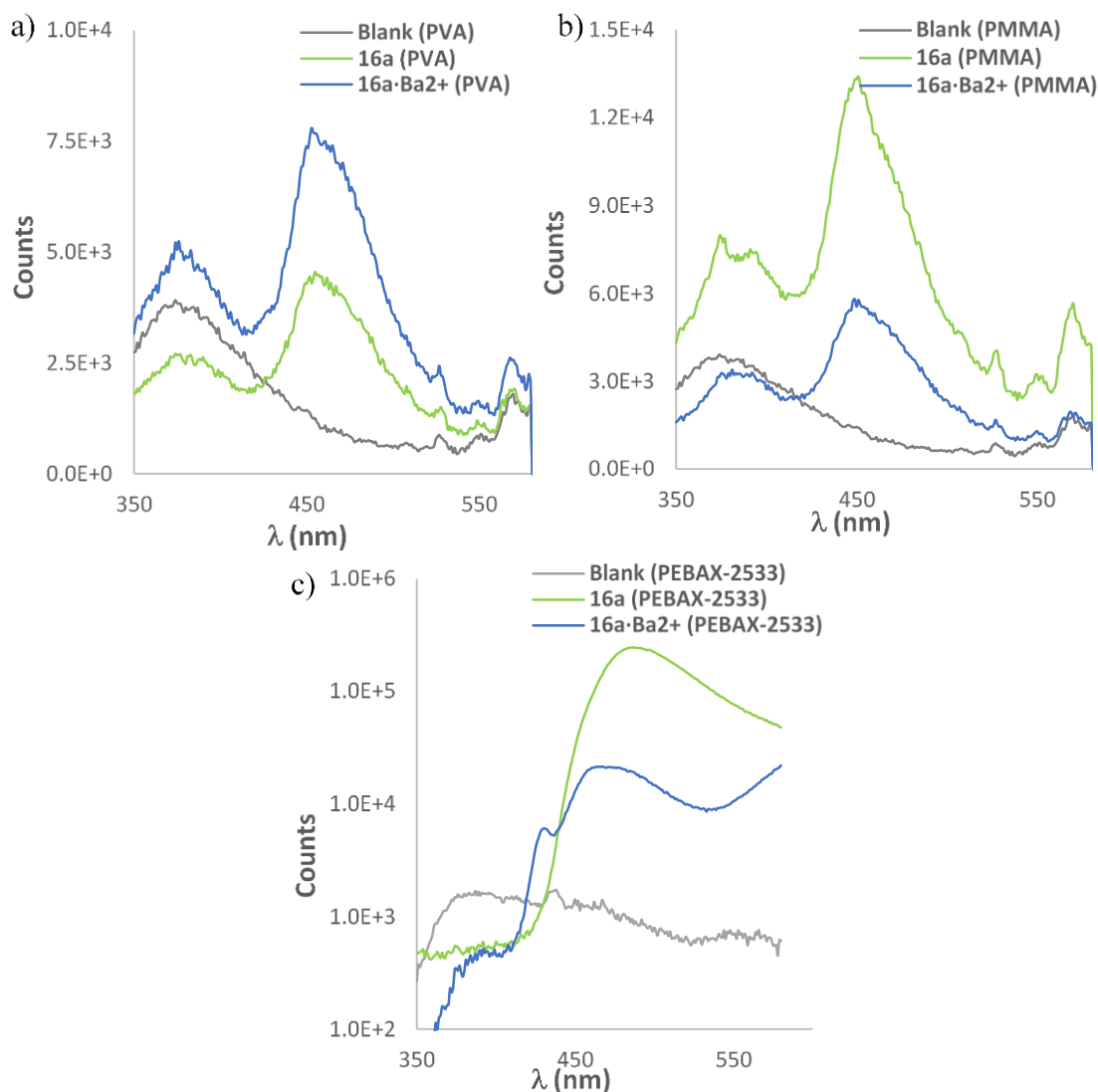
Figure 79.- Emission spectra of compound **16a, 16a·Ba²⁺** supported in films of: a) PVA b) PMMA c) PEBAX-2533. r.t., λ_{exc} = 350 nm.

In the first case, PVA (Figure 79.a), the emission maxima of the **16a** and **16a·Ba²⁺** films remain constant in wavelength. However, the intensity is affected, increasing slightly when barium perchlorate is added to the film. In Figure 79.b, where PMMA was used as

a support polymer, the opposite effect could be seen. In this case, when barium salt was added to the film prepared with compound **16a**, the signal intensity is reduced by about 50%. Finally, when PEBAX-2533 was used (Figure 79.c), the same behavior was observed than in PMMA. The intensity of signal decays slightly in presence of the metallic cation. The maximum, instead, do not exhibit any significant shift.

In view of these results, the polymers were not a suitable support to maintain the properties studied in solution. These unfavorable results are due to the affinity between the heteroatoms present in the polymers and barium. Due to the characteristics and the main goal of the project, the shift in wavelength is essential. Therefore, it was decided to test other supports.

3.2.2.- Metallic surfaces and tectomers

Seeing the ineffectiveness of polymers for this purpose, the use of metallic surfaces such as gold or silver was considered.

Although we knew that we needed a transparent surface, since gold and silver surfaces are well-knwon we decided to start with these surfaces. Afterwards, we could study and understand the behavior of our compounds on a transparent surface.

For this purpose, it was necessary to modify the molecule and place a thiol residue, a functional group that is widely known for its affinity with gold. For the synthesis of this compound it was decided to start from compound **14b**, using the methyl ester as the starting functional group. By reacting this molecule with lithium aluminum hydride, the primary alcohol **30** was obtained after two hours of reaction (Scheme 32).
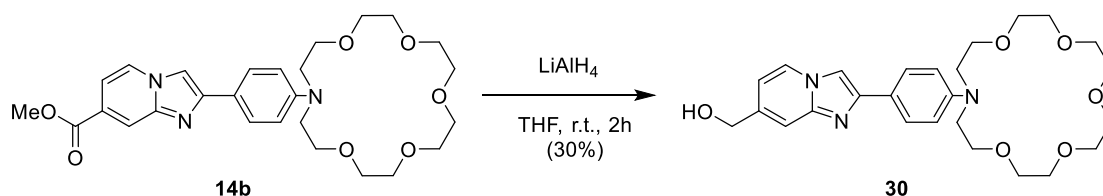
Scheme 32.- Reduction of the carboxylate group in compound **14b**.

Once the alcohol was obtained, it was used as starting material for the formation of ether **31** by a Williamson reaction (Scheme 33).
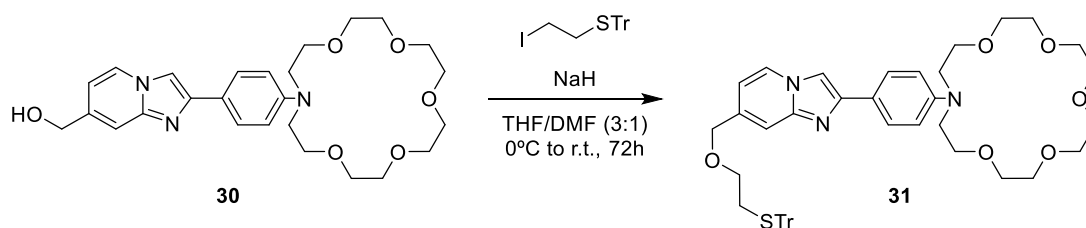
Scheme 33.- Preparation of compound **31** by a Williamson reaction

Unfortunately, desired compound **31** could not be obtained and therefore, this strategy was abandoned. In any case, theorical simulations at the laboratory of Prof. Gómez-Cadenas (Donostia International Physics Center, DIPC) showed that a large distance ca. 10 nm between the fluorophore and the surface is required in order to avoid photon quenching. Therefore, this would require larger spacers associated with complex synthesis.

Due to the impossibility of synthesizing a 10 nm linker, the alternative to this problem was to place a tectomer layer between the metal surface and the FBI molecule. For this purpose, the group of Prof. Cebolla, in the University of Zaragoza, was contacted. These tectomer films were prepared and supplied by Prof. Cebolla's Group.

Tectomers are glycine oligopeptides that interact with each other, generating rigid structures around a carbon chain. The nomenclature of these compounds depends on their oligopeptide tails. Thus, a 2T tectomer will have two oligoglycine tails; the 3T, three tails and, finally, the 4T, four tails (Scheme 34).

2-Tailed oligoglycine (2T)

3-Tailed oligoglycine (3T)

4-Tailed oligoglycine (4T)
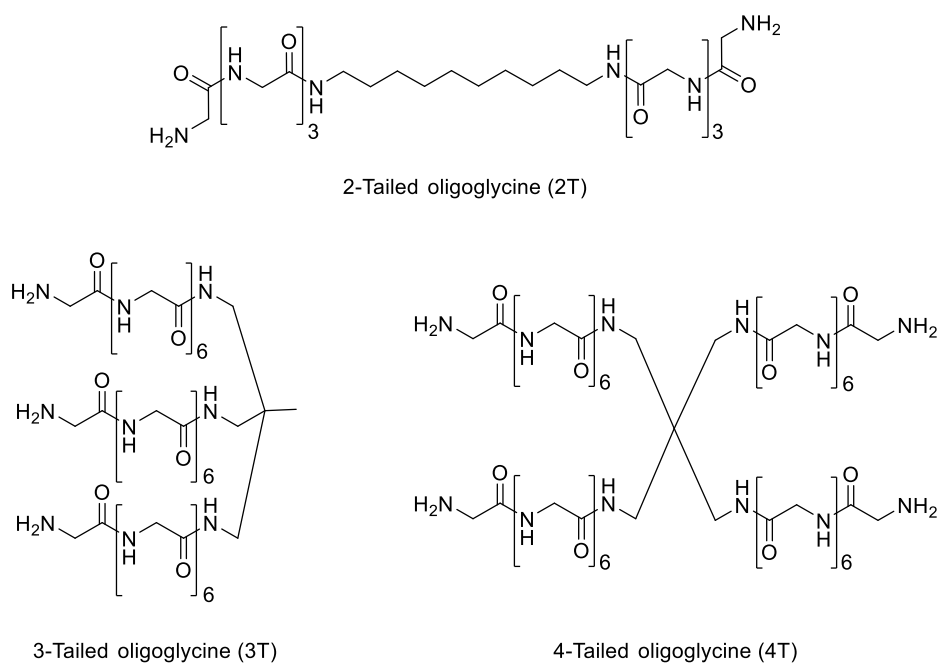
Scheme 34.- Structures of 2-, 3- and 4-tailed tectomers.

For this, 2T (Figure 80) and 4T (Figure 81) tectomer layers were prepared and characterized by AFM and SEM. The surfaces tested with tectomers were gold, silver and graphene oxide. In addition, different tectomer layer thicknesses were evaluated on each one.
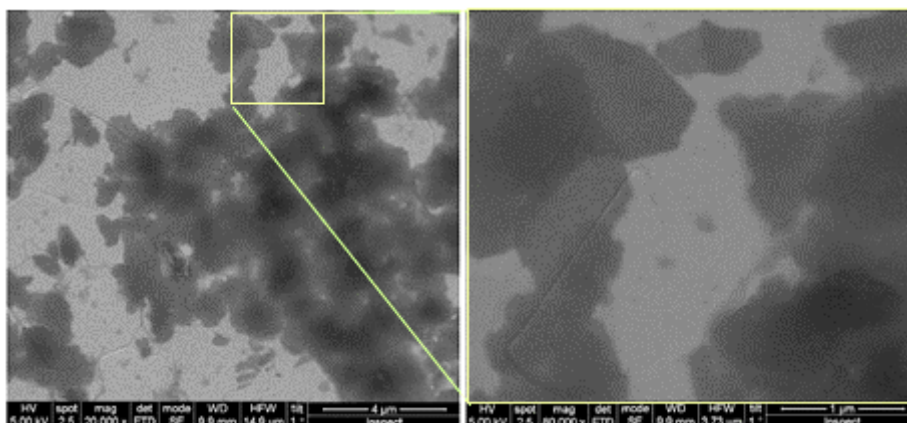
Figure 80.- SEM image of gold foil coating with 2T tectomers.
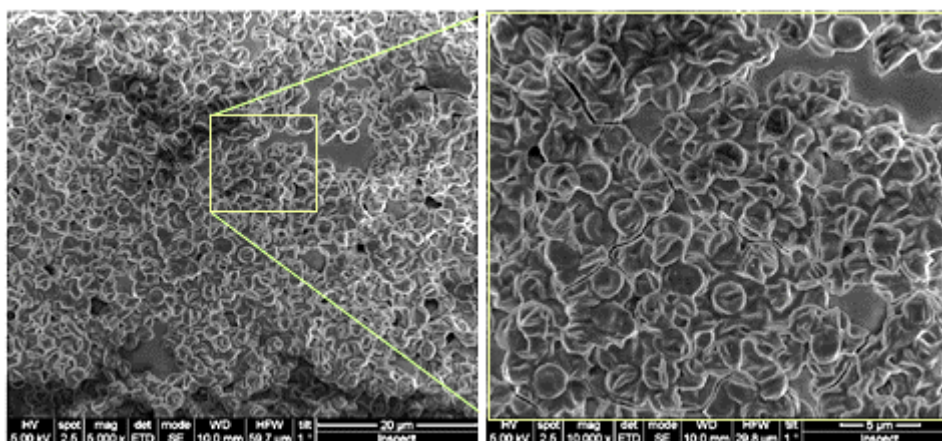
Figure 81.- SEM image of gold foil coating with 4T tectomers

As it can be seen in Figure 80, the coating with 2T tectomers is less homogeneous than with the use of 4T tectomers (Figure 81). In contrast, 4T tectomers generate a very irregular surface that is not adequate to support the fluorophore.

After optimization of the process, Professor Cebolla's group was able to generate 2T tectomer layers with a full coating and a regular surface (Figure 82 and 81).
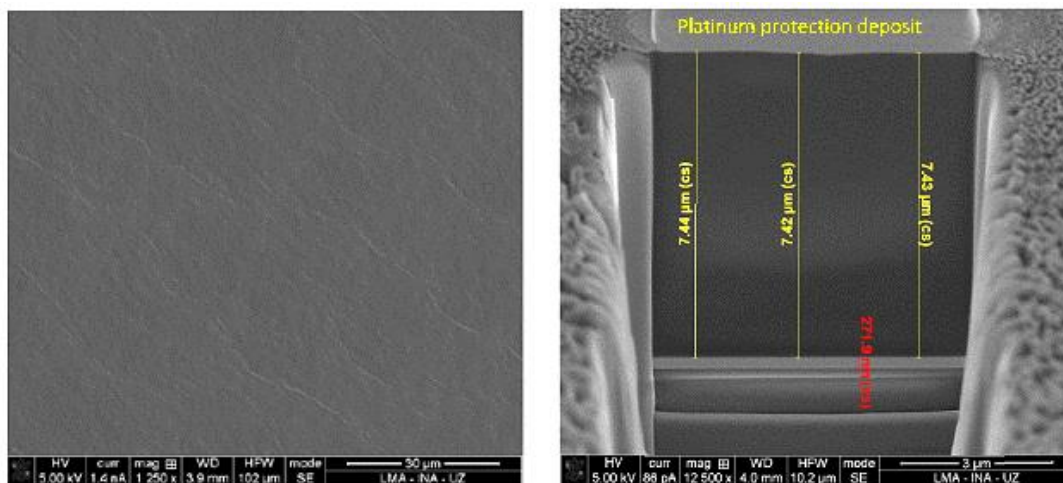
Figure 82.- 7.4 µm 2T tectomer coating on gold foil.
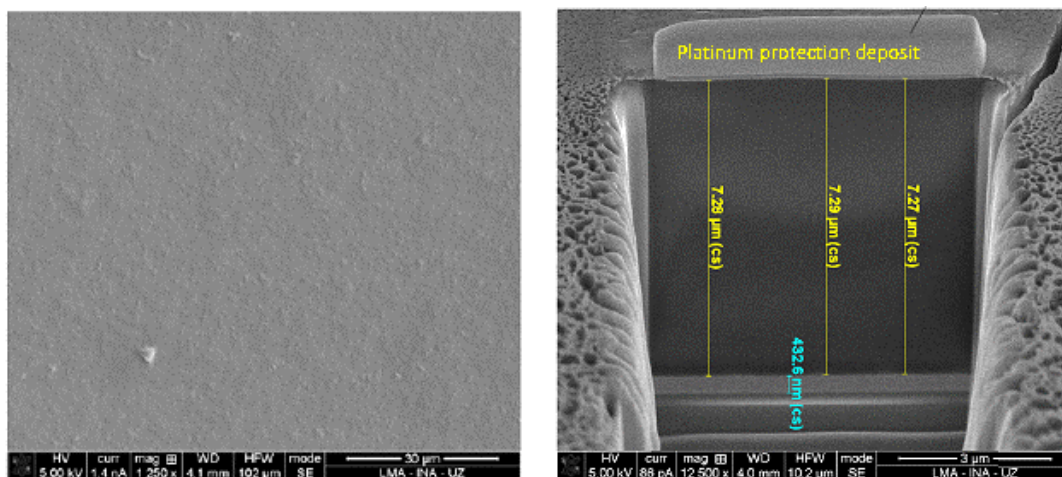
Figure 83.- 7.3 μm 2T tectomer coating on silver foil.

As can be seen in Figure 82 and 81, the tectomer layers were uniform, smooth and thick; approaching the 10 nm. After incorporation of these oligomers on the metal surface, the functional group with which the fluorophore has to react is the amine group (see Scheme 34). For this purpose, the FBI modification proposed was the formation of a carboxylic acid in order to form a peptide bond between the sensor and the terminal amines of the tectomers. For this purpose, an alkaline hydrolysis was performed using sodium hydroxide in an acetone/water mixture (Scheme 35). Unfortunatelly, the obtained crude was insoluble.
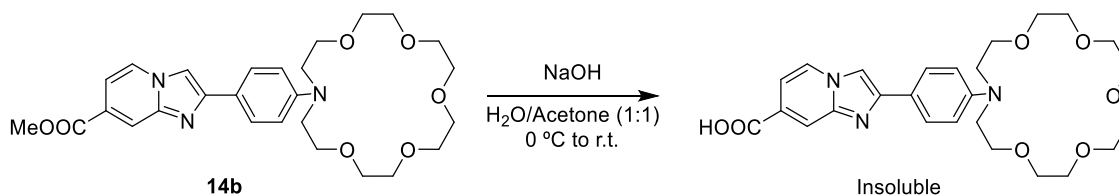
Scheme 35.- Hydrolysis attempt of **14b**.

For this reason, molecule **16a** was used directly. The fluorescence emission measurements of this adsorbed system on the tectomers, generated signals very similar to those observed on the polymers (Figure 84). This may be due to the competition for barium tagging between the fluorescent sensor and the surface amino groups.
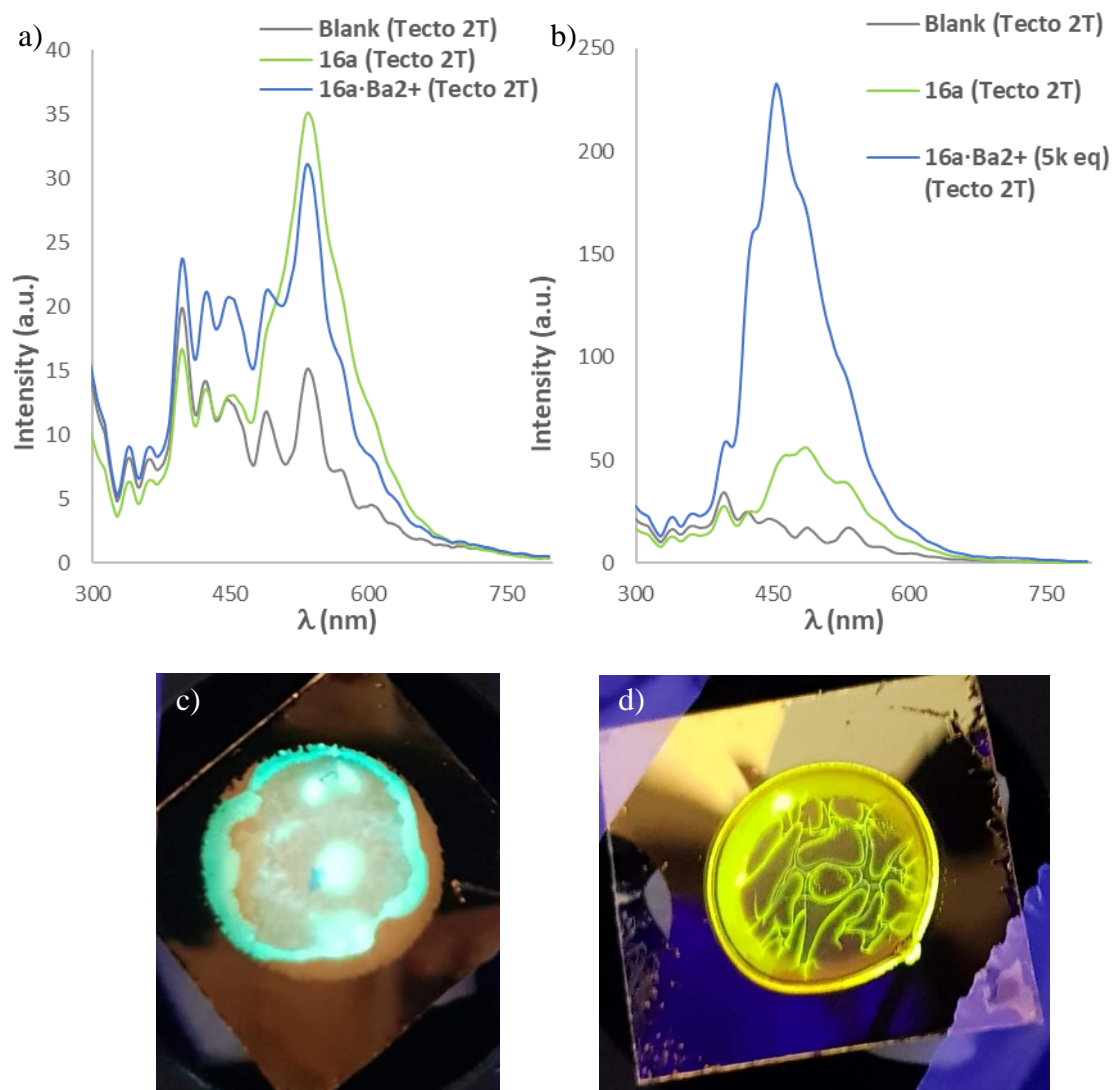
Figure 84.- Emission spectre for compound **16a** adsorbed into a tectomer layer in free state and with a) 1 eq of barium perchlorate b) 5000 eq. of barium perchlorate. r.t., $\lambda_{exc} = 250$ nm c) Photograph of **16a·Ba^{2+}** solution drop on tectomer. d) Photograph when the drop was dried.

As it can be appreciated in Figure 84, the emission spectra do not show a shift in wavelength. In the lower photographs of Figure 84, it can be seen that when a chelated solution (blue) was poured on the tectomer, it returned to the initial wavelength of compound **16a** (green) once it was dried.

Despite these unsatisfactory results, tectomers are promising materials that can be well supported on the surface, favoring the formation of a monolayer of our molecule on this material. However, the surface of the tectomer would have to be modified to avoid competition for barium ions. This could be a starting point for a new line of research in the future.

At this point, the results studied on the surface were all unfavorable. Therefore, an alternative strategy was considered: adsorbing the **16a** molecule on a material and, then, "building" the support layer. This material was silica powder.

3.2.3.- Silica pellets

After the measurements carried out with the different surfaces and the results briefly shown above, the silica powder allowed to adsorb the **16a** molecule on it and to form compacted silica pellets.

This methodology allowed, in the short term, to evaluate the photophysical behavior of this compound in the dry state, without the need to modify the sensor.

The experiments began by adding an FBI solution in acetonitrile of known concentration to a known mass of silica gel. The solvent was then evaporated under reduced pressure, resulting in an FBI-silica powder of known molality. Finally, with the resulting powder, a tablet was prepared by mechanical compression.
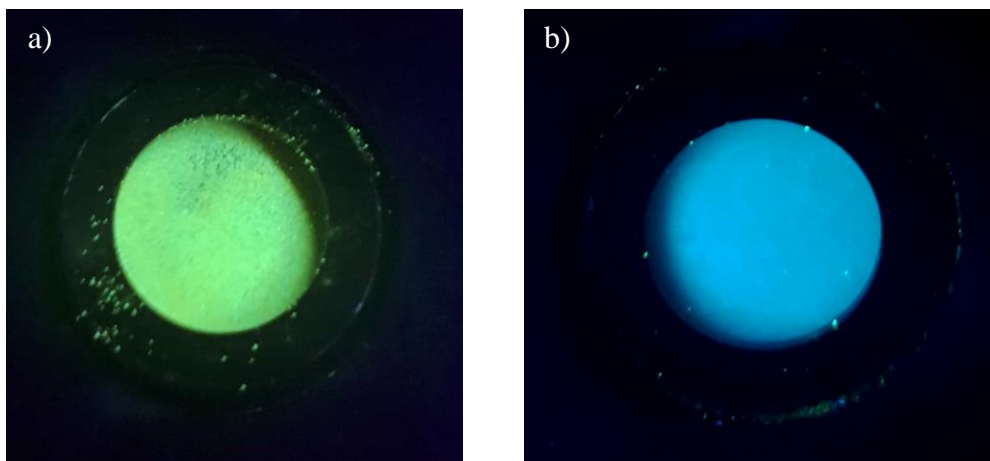
Figure 85.- Silica pellets of a) **16a** and b) **16a·Ba^{2+}** under UV lamp. $\lambda_{exc} = 365$ nm.

In a first approach, in addition to **16a** tablets, **16a·Ba^{2+}** tablets were also prepared. For this purpose, the method described above was employed, using in this case a dilution of the already chelated molecule. The fluorescence emission of both pellets was then measured, as well as a silica-only blank in order to adjust the baseline.
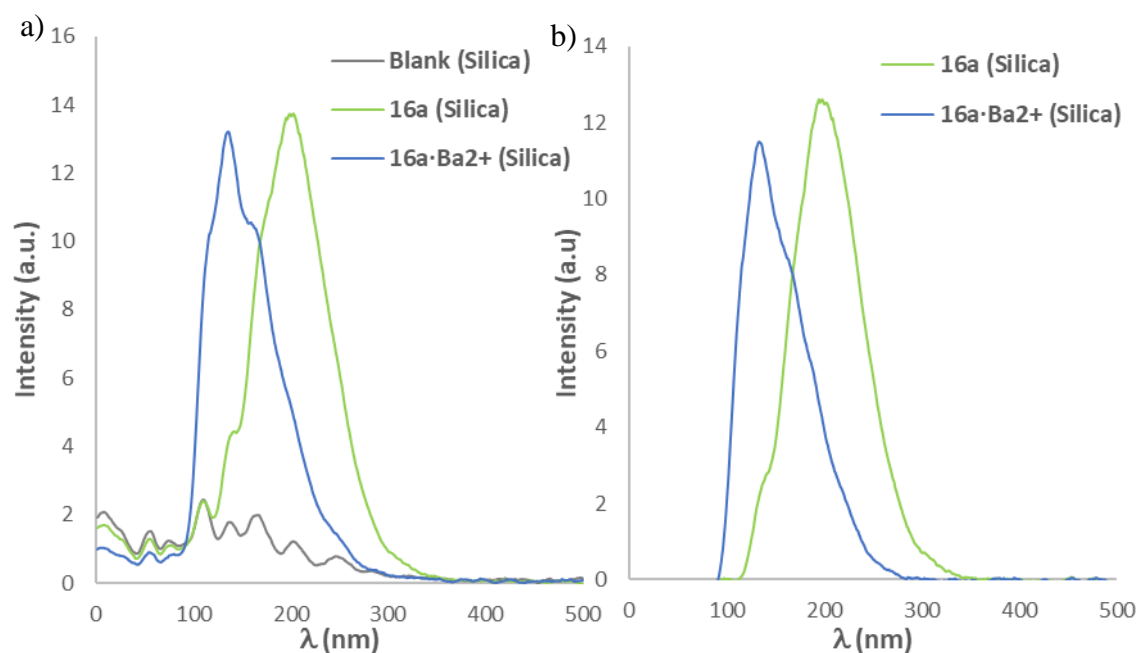
Figure 86.- a) Emission spectra of **16a** and **16a·Ba²⁺** in silica pellets and blank silica pill. b) Emission spectra with blank signal subtraction. r.t., λ_{exc} = 250 nm.

In contrast to what was observed with polymers and tectomers, the behavior of the FBI molecule adsorbed on silica, is generally similar to that studied in solution (Figure 32 and Figure 86). The behavior shown in the dry state is practically the same as in solution. The major difference was the intensity of the signals. This promising result allowed further progress to be made. So far, in both polymers and silica, solutions of the chelated FBI compound **16a** were prepared and then the surface was formed by using these previously prepared solutions.

Due to the nature of the NEXT project and its main objective, the sensor must be able to capture barium atoms in the environment. For this reason, and in collaboration with Prof. Gómez-Cadenas' group (DIPC), especially with Prof. Celia Rogero and Pablo Herrero (Materials Physics Center, MPC - UPV/EHU-CSIC), it was decided to simulate more realistic conditions.

For this purpose, silica pills with adsorbed compound **16a** were prepared and then barium perchlorate was sublimated in a high-vacuum chamber. In this way it was possible to study the behavior of dry fluorophore on a solid support in the presence of barium cations in the gas phase.

In the gas phase, when molecules are deposited, they tend to be arranged in layers rather than in clusters. This allowed a cleaner analysis of the electronic and chemical structure at the surface. Two steps are required for this: Prepare or clean a substrate (not necessary with silica) and then evaporate the compound on it. Once the substrate was prepared, gas evaporation of barium perchlorate was carried out on the substrate. This can be done from liquid material (Atomic Layer Deposition) or, in the case of this work (performed at MPC), in solid state. The technique for the second case is called Molecular Beam Epitaxy, which refers to the fact that the molecules grow epitexially (in layers) and at a very slow, controlled and reproducible rate. This is a few Å per minute.

The technique is summarized in Figure 87.[80] The crucible [10] contains the material to be evaporated and which faces to the sample. Normally, it is heated with a filament [11], (Knudsen effusion cell, [2, 10-13]), although there are also other very common techniques such as using a high-energy electron beam to heat the crucible (electron-beam evaporator). When the material reaches a certain temperature, the molecules sublimate and a gas beam is produced and directed at the substrate.

The deposition rate is usually calibrated with a quartz microbalance (QMB) [1, 6-9]. The microbalance consists of a piece of quartz that oscillates at MHz frequencies. When material is deposited on the quartz, the frequency of oscillation decreases proportionally to the amount of mass per area that is coating the quartz. Thus, measuring the derivative of the frequency is equivalent to measuring the rate of deposition (mass/time). If the density of the molecule and its size are known, it can be translated into Å/min and layers/min.

---

[80] Gutzler, R.; Heckl, W. M.; Lackinger, M. *Rev. Sci. Instrum.* **2010**, *81*, 015108.
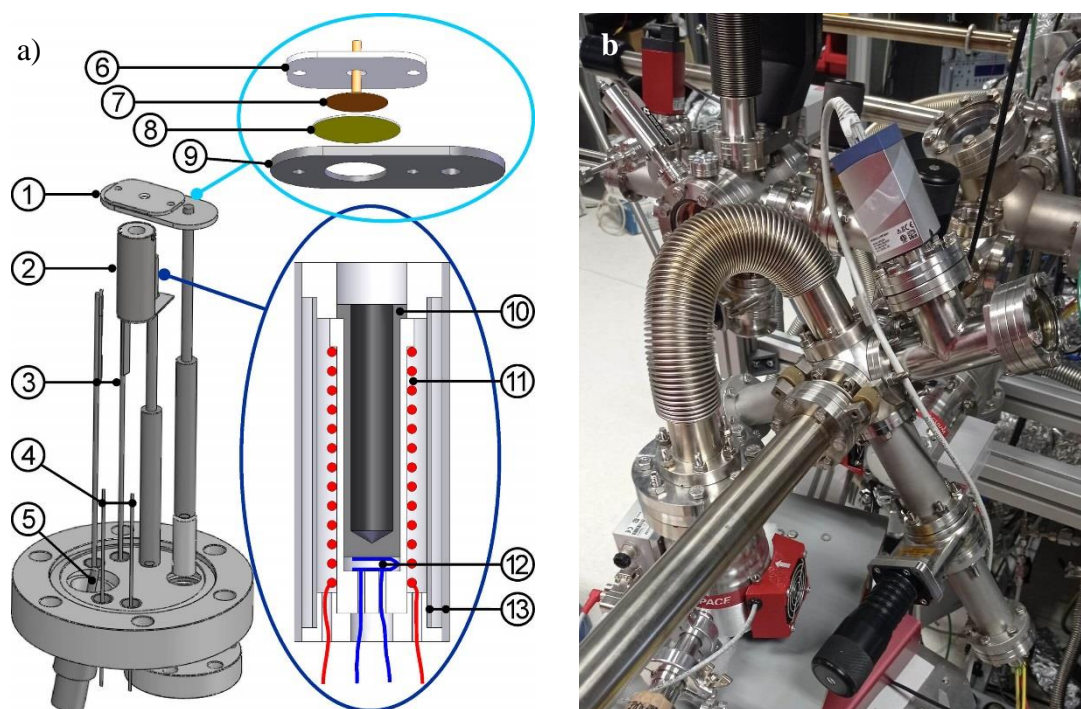
Figure 87.- a) Schematic design of molecular evaporator. *(Taken from reference 84)*. b) Photography of the real system employed in this work.

As it is shown in Figure 88, molecule **16a** maintains its bicolor behavior when working in gas-phase conditions. This result reflects the robustness and versatility of working conditions of the FBI **16a** sensor. This is possibly one of the most important results of this work.
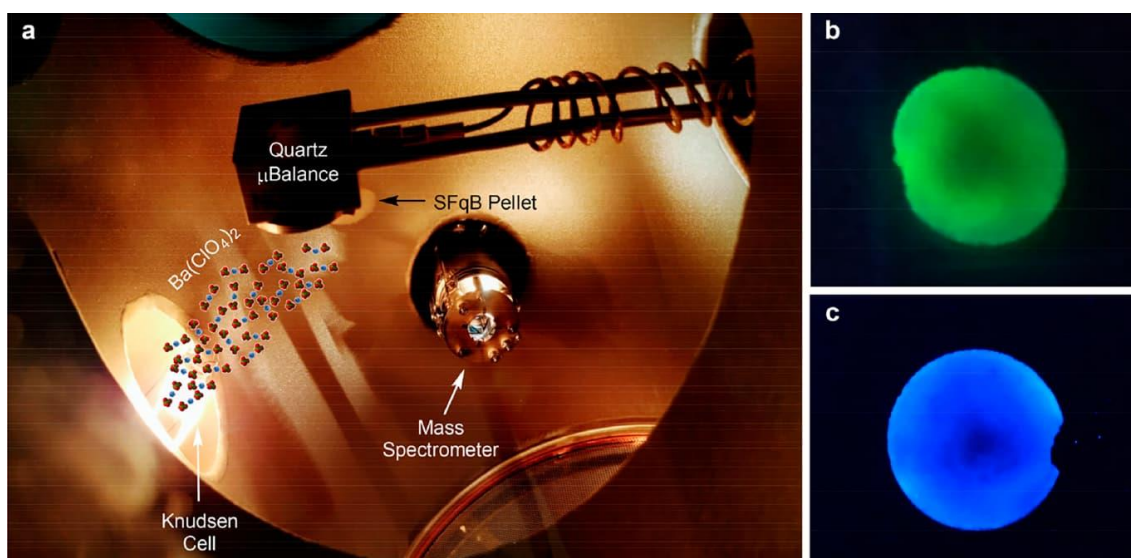
Figure 88.- a) Photograph of the Ultra-High Vacuum (UHV) chamber used for sublimation. b) Silica pellet with **16a**, before sublimation of barium perchlorate. c) Silica pellet with **16a**, after sublimation of barium perchlorate. Both pictures was taken under UV lamp λ_{exc} = 365 nm.

Compound **16a** can be qualified as one of the first functional macromolecular gas-phase sensors. In literature this field is practically unexplored. It should be noted that, in solids, the use of larger amounts of barium salt is necessary. The amount of metallic salt was larger in order to get the maximum number of chelated molecules. This may be due to three reasons:

- The freedom of movement of the molecules. This movement is much more restricted in solids than in liquids.
- Assuming a homogeneous arrangement throughout the powder, not all fluorophore molecules are accessible to the barium cations.
- Silica, and more specifically, its oxygen atoms, may interfere in this respect. However, in a lesser extent than the nitrogens of other supports.

3.2.4.- Indium-Tin Oxide (ITO)

In the previous section it was explained how it was possible to demonstrate that the FBI sensor is able to work in dry and solid conditions, maintaining its most important photophysical characteristics. After these awesome results, the search for a transparent surface on which to support the fluorophores was resumed.

ITO (Indium Tin Oxide) is a solid mixture of indium oxide and tin oxide prepared as a film on another substrate. In this work, the other substrate is quartz. Figure 89[81] shows, schematically, the steps for the synthesis and deposition of ITO.

---

[81] Dong, L.; Zhu, G. S.; Xu, H. R.; Jiang, X. P.; Zhang, X. Y.; Zhao, Y. Y.; Yan, D. L.; Yuan, L.; Yu, A. B. *J. Mater. Sci.: Mater. Electron.* **2019**, *30*, 8047–8054.
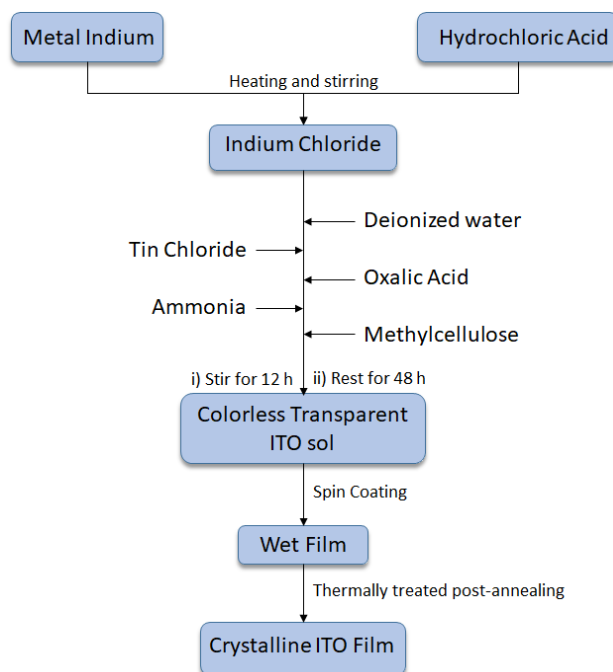
Figure 89.- Schematic preparation of ITO Films.

Quartz does not conduct electricity, whereas ITO is a semiconductor. For this reason, the way to classify ITO is based on its resistivity (Ω/sq), which is inversely proportional to the thickness of the film formed by the ITO.

Prof. Fernando P. Cossío performed theoretical calculations where the interaction of certain functional groups with the surface was evaluated. These DFT calculations (B3LYP-D3/6-31G(d)&LanL2DZ level of theory) were performed with benzoic acid, benzyl alcohol and benzoic hydroxamic acid (Figure 90).
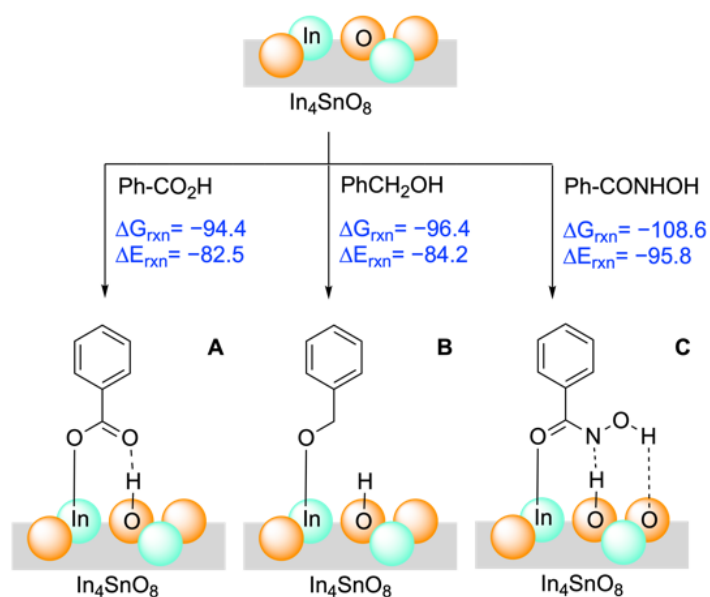
Figure 90.- Model DFT calculations to estimate binding energy between In4SnO8 and benzoic acid (A), benzyl alcohol (B) and benzoic hydroxamic acid (C). Reaction (ΔE_{rxn}) and Gibbs (ΔG_{rxn}, at 298 K) are in kcal/mol.

The interaction energies between ITO and a carboxylic acid, a hydroxamic acid and a primary alcohol were calculated. The results were very favorable, so that all three groups could be used in practical experiments.

As explained in Chapter II and as it has worked well in silica, the strategy is to functionalize compound **16a** in order to generate a linker with one of the three functional groups evaluated in the theoretical studies. In addition, as seen in the emission spectra of compound **16c**, a small shoulder appears in the zone of interest. For this reason, the main idea is to disconnect the linker group from the fluorophore. For this purpose, the first option considered was to place a bromine atom in one of the two positions of the pyridine ring (structures represented below, the first one being preferred).
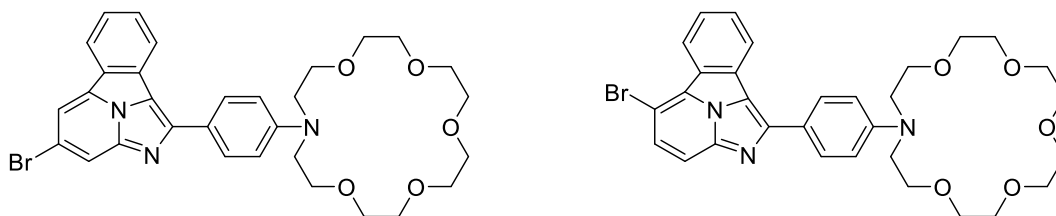
Scheme 36.- Target compounds for initial bromination of compound **16a**.

First, a methodology developed in the group[82] was used to attempt the bromination of compound **16f** since it was prepared. The result was negative, disappearing typical signals of compound **16f** in NMR (Scheme 37).

16f
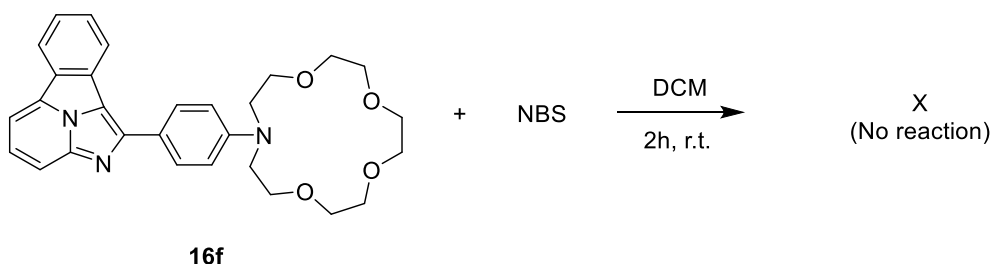
Scheme 37.- Bromination attemp of **16f**.

The same methodology was repeated, as a control test, with a less advanced substrate, giving as the only product the insertion of Br in the expected position of the 2-arylimidazo[1,2-*a*]pyridine.

13a   **31**
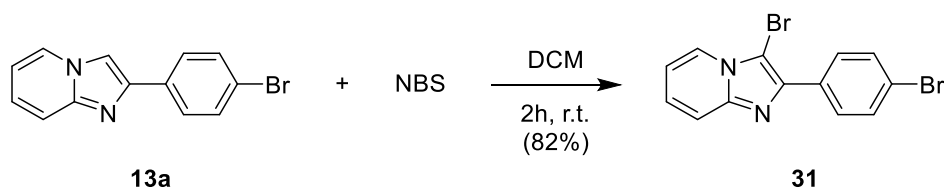
Scheme 38.- Bromination of compound **13a**.

Due to the undesired bad results, another methodology was searched in which the bromination was perform done of anilines and phenols using NBS and ammonium acetate catalysis[83] (Scheme 39).

2a   **32**
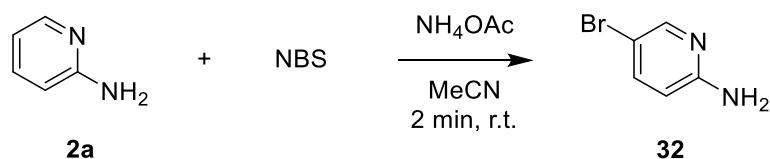
Scheme 39.- Bromination of 2-aminopyridine.

[82] Arias, L..Regioselective Synthesis and Functionalization of 2- and 3-Aryl Benzo[*b*]furans. Application to Medicinal Chemistry. Ph.D. Thesis, University of Basque Country, September 2014.

[83] Das, B.; Venkateswarlu, K.; Majhi, A.; Siddaiah, V.; Reddy, K. R. *J. Mol. Cat. A Chem.* **2007**, *267*, 30–33.

When th reaction was carried out with another of the final products that were already prepared, in this case, compound **16b, t**he brominated position is the one desired (Scheme 40).
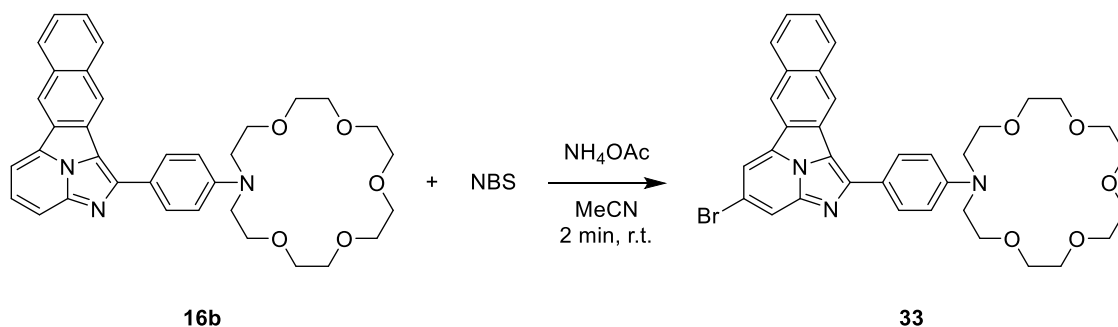
Scheme 40.- Halogenation of fluorophore **16b**.

In view of the good result of the reaction, it was finally tested on the molecule of interest, **16a**. The result was bromination at a totally different position and of no interest for the synthesis of the linker. The disappearance of the *para* system was verified by NMR. The necessary experiments were not performed to determine exactly on which carbon of the system the bromine was bound.
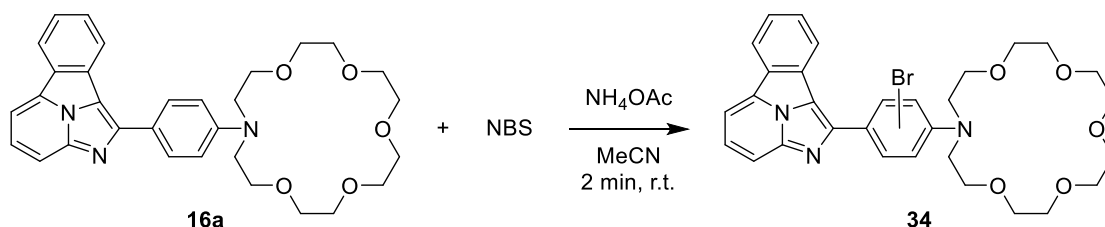
Scheme 41.- Halogenation attempt of FBI **16a**.

In addition, repeat halogenation of 2-aminopyridine with NCS and NIS was also attempted. The results were unsuccesfully.

Not being able to brominate compound **16a** and with the fast and efficient methodology of aniline bromination, it was set as a new goal to functionalize 2-aminopyridine and start assembling the rest of the fragments from that early precursor (Scheme 42).
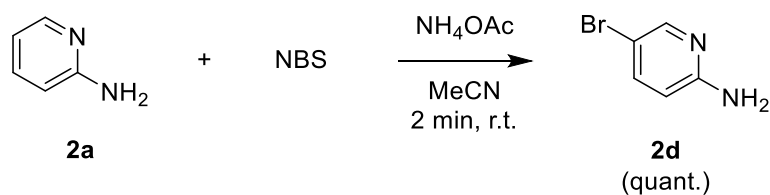
Scheme 42.- Bromination of 2-aminopyridine.

With brominated aminopyridine **2d**, the necessary conditions were used to perform a Heck-type C-C coupling reaction. After 20 hours of reaction, compound **35** was obtained in excellent yield (Scheme 43).
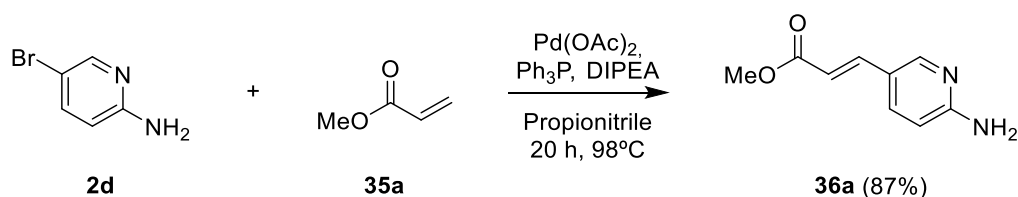
Scheme 43.- Heck coupling reaction between **2d** and **35a**.

The next step was the double addition reaction to generate the starting material for the preparation of the fluorescent sensor. Compound **13d** was obtained satisfactorily but in a moderate yield, lower than those observed for the other compounds **13**.
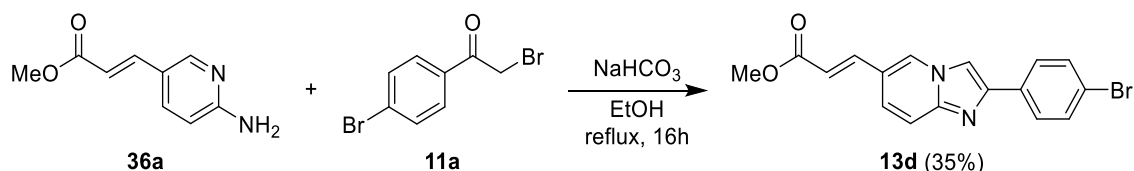
Scheme 44.- Synthesis of **13d**.

In parallel, and starting from the commercial 2-amino-4-bromopyridine, the same reactions were carried out to obtain the double addition reaction product, in the position of greatest interest.
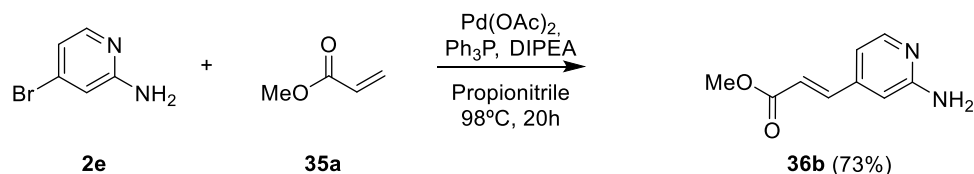
Scheme 45.- Synthesis of product **36b**.

Compound **36b** was obtained in good yield, but slightly lower than in the other position. However, after the double addition reaction, the solid generated was totally insoluble. This made it impossible to record an NMR spectrum.
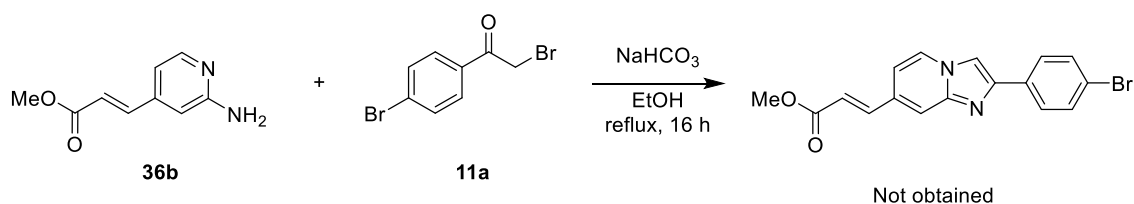
Scheme 46.- Attempt of double adition reaction between **36b** and **11a**.

Once the double addition product with acrylate was obtained, **13d**, the next step was to try to hydrogenate the double bond to switch off the conjugation of the system, one of the main problems of compound **16c** as far as photophysics is concerned. For this hydrogenation, different procedures were carried out, which are shown in Scheme 47 and Table 24.
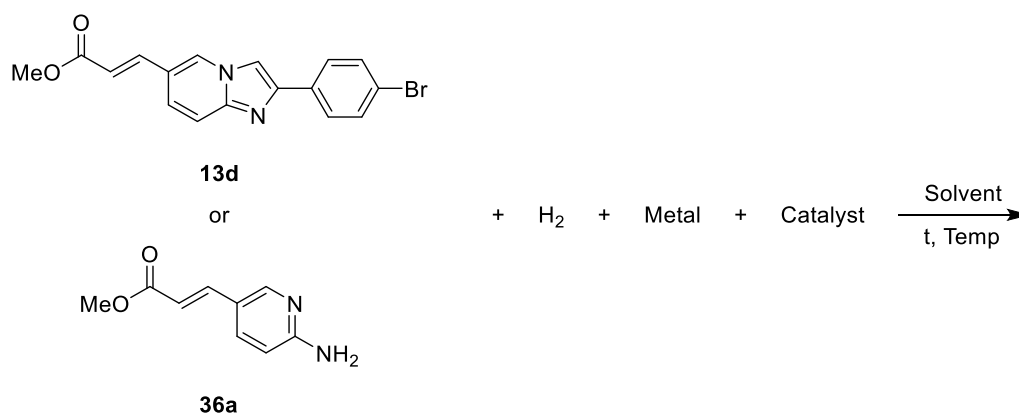
Scheme 47.- General scheme for hydrogenation of molecule **13d**.

Entry	SM	H₂ Source	Metal	Catalyst	Solvent	Time, h	Temp, ºC	Result
1	13d	H₂ Atmosphere	Mg	-	MeOH	16	r.t.	SM
2	13d	H₂ Atmosphere	Mg	HCl	MeOH	16	r.t.	SM
3	13d	Flow hydrogenator system	-	Pd(C)	MeOH/ EtOH/ DMF/ DCM*	Flow from 0.5 ml/min to 2.0 ml/min*	From r.t. to 60 ºC*	SM
4	13d	Flow hydrogenator system	-	Ni-Raney				-
5	36a	Flow hydrogenator system	-	Pd(C)				SM

Table 24.- Hydrogenation conditions.

* In all experiments carried out in the flow hydrogenator system, different conditions were tested: varying starting reagent flow, temperature, H2 pressure and different solvents (MeOH, EtOH, DMF, DCM).

First, hydrogenation conditions with magnesium and a hydrogen balloon were used. At first by bubbling in the solution and then by maintaining the H₂ atmosphere. (Table 24, entry 1).

After recovery of the starting material, the reaction was repeated in acid media, adding a few drops of 1N HCl (Table 24, Entry 2). After 16 hours, the reaction was stopped and, again, the product obtained was the starting material.

It was decided to change the strategy and use a flow system to hydrogenate the double bond. First (Table 24, Entry 3) a Palladium/Carbon cartridge, 1 bar hydrogen pressure and room temperature were used. Again, the starting material was collected. The conditions were changed by increasing the pressure, temperature and reactant flow rate. The solvent used was also varied. In all cases the starting material was partially or totally recovered.

Finally, the catalyst was changed, using a Nickel-Raney cartridge (Table 24, Entry 4). In this case, none of the conditions employed permitted the formation of the reduced product or allowed recovery of the starting material.

In order to test on another molecule product **36a** was used as starting material (Table 24, Entry 5). The palladium/carbon catalyst was returned and, after different attempts, the starting material was recovered.

On the other hand, the reduction of the methyl ester of the acrylate was carried out using a common methodology in literature such as the use of lithium aluminum hydride (Scheme 48). However, the compound obtained not only showed the change from ester to alcohol but also reduced the *trans* olefin (Scheme 48) of the starting compound. This was verified by NMR (Figure 91).
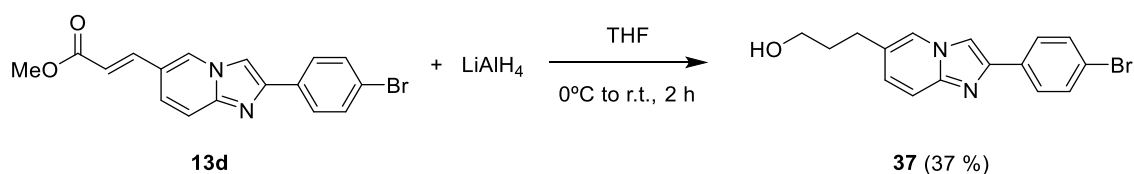
Scheme 48.- Reduction of compound **13d**.
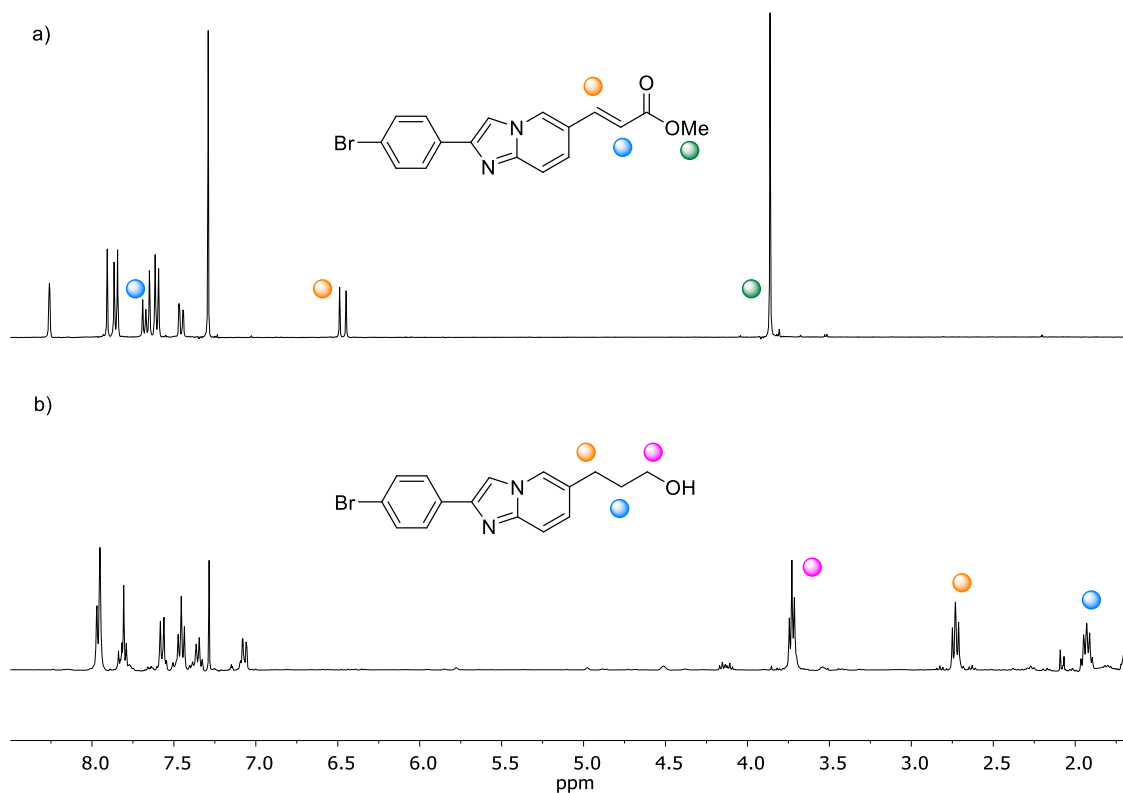
Figure 91.- NMR spectra for compound a) **13d** and b) **37**.

As it can be seen in the spectra, the ester signal, as expected, disappeared after the reaction with the lithium aluminum hydride. In addition, the CH groups of the acrylate were also reduced to methylenes (orange and blue dots in Figure 91).

In view of the results obtained, we proceeded to develop the complete sensors. First, cesium carbonate was used as the base to avoid the possible decarboxylation of the methyl ester during the coupling of the aza-crown ether. The reaction did not progress and the starting material was obtained.
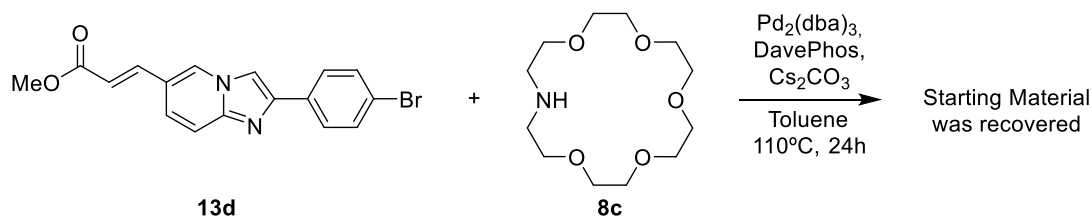
Scheme 49.- Attempt of coupling of crown ether.

In view of this result, the synthesis of the final fluorophore was approached using Route A (*vide supra*), starting with the [8 + 2] cycloaddition under microwave irradiation, estimating by NMR the formation of the expected product, but with a very low conversion. Unfortunately, the compound could not be isolated.
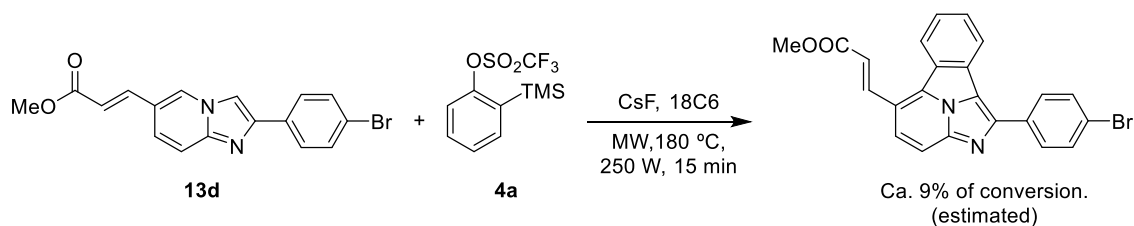
Scheme 50.- Microwave assisted [8 + 2] cycloaddition for compound **13d**.

In case the methyl ester could influence in reactivity, the coupling reaction of the crown ether with a benzyl acrylate was also tested. The appearance of the expected signals was not observed via NMR. Moreover, under the UV lamp (λ_{exc}: 365 nm), it did not fluoresce noticeably as did its counterpart.
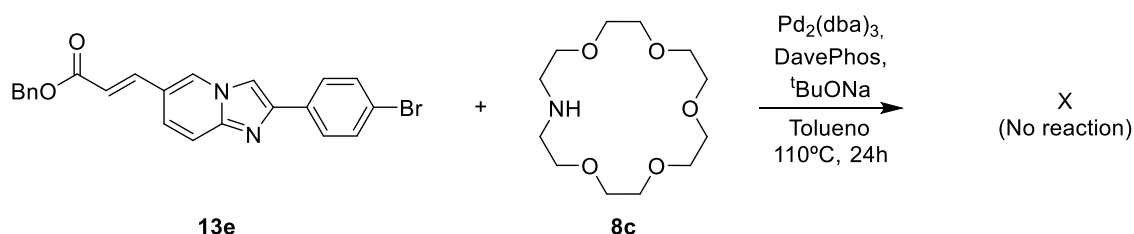
Scheme 51.- Attempt of coupling of aza crown ether to benzyl acrylate derivate.

Analyzing the results, it could be observed that the best option, for the moment, could be the compound with the methyl ester, **16c**. Therefore, this compound was taken as a reference to prepare and modificate this group by others that can be anchored to the surface in a covalent or electrostatic way.

Firstly, carboxylic acid formation was tried. To do that, alkaline hydrolysis of compound **16c** was carried out with sodium hydroxide. Unfortunately, after 16 hours of reaction, a NMR spectrum was recorded and it could be seen that the crown ether signals have disappeared.

As an alternative approach, the hydrolysis on the starting material **13b** was considered as a previous step to carry out the synthetic route explained in the previous chapter. First the coupling of the crown ether and then the [8 + 2] cycloaddition. Therefore, the corresponding double addition product **13b** was hydrolyzed with NaOH to yield, after the work-up, the carboxylic acid (Scheme 52).

Scheme 52.- Hydrolysis of compound **13b**.

Subsequently, **13f** was used as starting material to generate the compound resulting from the crown ether coupling. Unfortunately, the adduct formed is the amide shown in Scheme 53.

Scheme 53.- Unexpected coupling of aza-crown ether **8c** and carboxylic acid **13f**.

The process, therefore, had to follow the opposite sequence: first generate the system anchored to the crown ether and then hydrolyze to the carboxylic acid.

Scheme 54.- Palladium catalyzed coupling between **13b** and **8c**.

After carrying out the hydrolysis of compound **14b** and the corresponding workup, an insoluble white solid was obtained which could not be purified or caracterisize.

In parallel, the starting imidazopyridine **13b** was reduced to the corresponding primary alcohol using lithium aluminum hydride (Scheme 55). Next, alcohol **13g** was used as starting material for the coupling with the crown ether **8c**. Unfortunately, this reaction did not work.
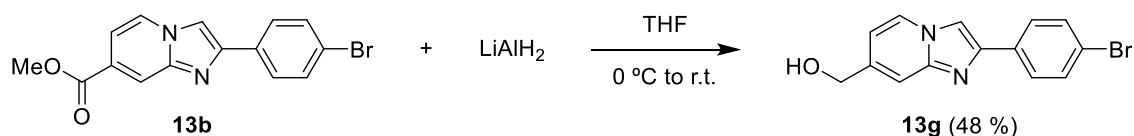
Scheme 55.- Reduction of methyl ester into a primary alcohol.

Additionally, we also worked on the synthesis of the sensor starting from a double addition product with an "extra" bromine atom. This bromine atom could be useful for further functionalization of the fluorophore. The synthetic approach began as indicated in Scheme 56.
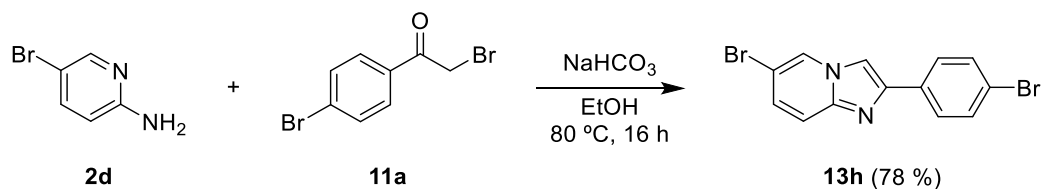
Scheme 56.- Preparation of double brominated molecule **13h**.

Subsequently, when $C(sp^2)$-$N(sp^3)$ coupling between the crown ether **8c** and product **13h** was attempted, the adduct obtained was not the desired one (Scheme 57). The crown ether was attached to the C of position 6 of aminopyridine **13h**, which, in the end, will hinder, due to steric hindrance, the [8+2] cycloaddition.
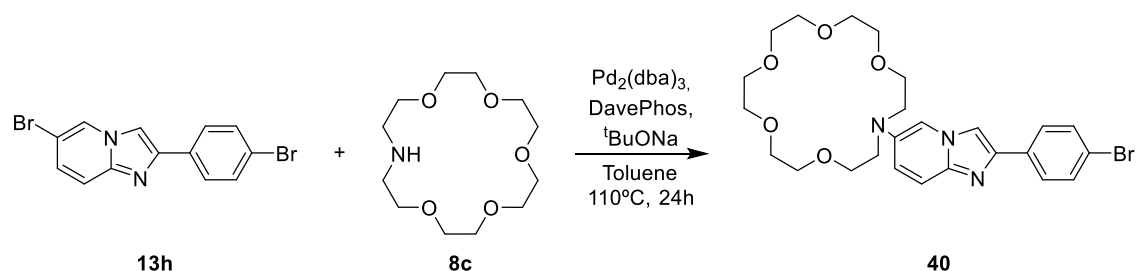
Scheme 57.- Unexpected coupling of aza-crown ether **8c**.

Seeing that the bromine at position C6 of the imidazopyridine seemed to have preference for the bicyclic position, a Suzuki-type coupling was tried, which would generate a terminal double bond at that position. The result, again, was the opposite of the desired one, as it is shown in Scheme 58.
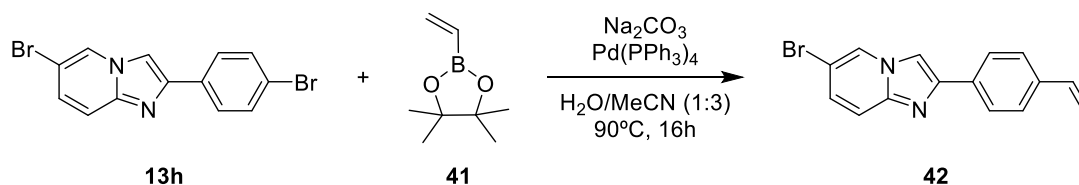
Scheme 58.- Suzuki-type C-C coupling.

In summary, decorating of first generation FBI compounds with appropiate spacers and functional groups resulted to be much more problematic than expected. Further functionalization paths involving second-generation molecules of type **29** are resulting more successfully and are under active investigation in our group.

3.3.- CONCLUSIONS

This chapter has described the first studies of fluorescent barium tagging sensors carried out on different surfaces. Although the work has just begun and much remains to be done, some initial conclusions can be highlighted:

- The tested polymers have too much affinity for barium, which is actively competitive against FBI. In addition, the polymeric environment restricts the conformational freedom required to pass from the free to the Ba^{2+}-bound state.
- Metallic surfaces are not transparent, therefore, they are not suitable. However, they have made it possible to use tectomers to anchor the molecule. These

tectomers have shown some intrinsic affinity for barium. However, they can favor the formation of an FBI monolayer.

- On silica, the observed bicolor behavior is similar than that observed in solution. This has also been possible in dry conditions (pellets prepared from solutions) and in gas phase (barium perchlorate sublimated on an FBI pellet).

- ITO has very interesting properties for the NEXT-BOLD project. However, it has not been possible to find a way to covalently bind an FBI compound, despite favorable theorical predictions. It also presents complications in measurement due to the fluorescence emission of the material itself.

3.4.- FUTURE GOALS

The following goals are actively investigated in the research group:

- Modify the surface of tectomeres to cap centers that may compete with barium.
- Find a synthetic route to generate functional groups suitable for the formation of a covalent interaction between the ITO and the sensor.
- Explore other possible surfaces such as muskovite or quartz.
- Study the second generation of FBI on the surfaces.

ANNEXES

PROCEDURES AND SPECTRA

I.- GENERAL INFORMATION

All experiments requiring a dry atmosphere were performed using conventional vacuum line and Schlenk techniques. The commercial reagents were purchased from Sigma MERK (Sigma-Aldrich), TCI (Tokio Chemical Industry CO), abcr Gmbh and STREM and were used without further purification. Toluene and THF were purified by MBSPS 800 MBraun solvent purification system. EtOH (Ethanol, 96 %vol, VWR) MeOH (Methanol <0.1% water, VWR). Chloroform (stabilized with about 0,6 % of ethanol, MERCK), DMF (*N,N*-dimethylformamide, anhydrous 99,8%, MERCK). Hexane (95% alkanes mixture for synthesis, Panreac). EtOAc (Ethyl acetate ExpertQ® ACS, ISO, Reag., Scharlab). MeCN (Acetonitrile UVASOL® MERCK)

II.- ANALYTICAL METHODS

Thin layer chromatographies (TLC) were performed on aluminum TLC plates (silica gel coated with flourescent indicator F254), and visualized either by exposure to UV light or staining with potassium permanganate.

Flash column chromatographies were carried out with silica gel 60 (0.040- 0.063 mm) eluting with gradient of polarity from hexane to an hexane:ethyl acetate:methanol mixture in a 1:4:0.1 ratio.

Centrifugal thin-layer chromatography. Purification of samples was performed on a Chromatotron (model 7294T) by Harrison Research. Silica rotors were prepared by deposition of a slurry mixture of 75 g of silicagel 60 Å with fluorescence indicator (Sigma Aldrich ref. 28856), 30 g of calcium sulfate hemihydrate (Sigma Aldrich ref. 12090) and 187 mL of cold distilled water (8 °C) on a glass rotor. After air-drying for 48 h, the rotor with the sorbent bound was scrapped to polish its surface and remove unwanted sorbent at the edge and center of the rotor.

Fourier Transform Infra-Red (FTIR) Spectroscopy spectra were recorded on an FT-IR spectrometer equipped with a diamond detection and single-reflection ATR module; wavenumbers are given in cm^{-1}.

Melting points (M.p.) were determined using a Büchi Melting Point B-540 apparatus.

Nuclear Magnetic Resonance Spectroscopy. ^{1}H NMR, ^{11}B NMR, ^{13}C NMR spectra were recorded at 400 or 500 MHz and 101 or 126 MHz for ^{13}C NMR, equipped with a z gradient BBOF probe, in CDCl$_3$ or Methanol-d_4. The data are reported as s = singlet, d = doublet, t = triplet, m = multiplet or unresolved, br s = broad signal, coupling constant(s) in Hz, integration. The ^{1}H spectra were recorded using noesygppr1d sequence from Bruker's library at 500.13 MHz. A time domain of 64 k and a spectral width of 10000 Hz. Interpulse delay: 1 s. Adquistion time: 3 s. Number of scans: 64. Mixing time: 0.01 s. The DOSY experiment was record using the lebbpgp2s sequence from the library of Bruker. The number of scans was 16. The strength of the gradient was changed from 2 % to 95% using 50 G cm^{-1} gradient unit. The value of big delta Δ was 200 ms and little delta δ was 400 ms. To avoid the eddy current a delay 5 ms was used.

Mass spectrometry (MS) and high-resolution mass spectrometry (HRMS). High-resolution mass spectra (HRMS) were recorded on HPLC Agilent 1200 Series system coupled to a hybrid quadrupole-time of flight (LC-QTOF) mass spectrometer Agilent 6530 from Agilent Technologies (Santa Clara, CA, USA). Mobile phase was composed by 0.1 % formic acid: acetonitrile 0.1% formic acid (50:50). Gas Temp. 325ºC; Drying gas: 5 l/min; Nebulizer: 40 psig; Shealt gas Temp. 375 ºC; Shealt gas flow: 11 l/min. Vcap: 3500 V(+).

UV/Vis and Fluorescence Spectroscopy. UV-Vis spectra were acquired on a Shimatzu UV-2600 Spectrophotometer. Emission spectra in solid state and in solution were acquired on an Agilent Cary Eclipse Fluorescence Spectrophotometer and Edinburgh FLS-1000. Excitation and emission monochromator bandwidth was fixed at 5 nm. Film samples were measured on a FS920 single photon counting spectrofluorimeter from Edinburgh Instruments (Edinburgh, Scotland, UK). Excitation and emission monochromator bandwidth was fixed at 3 and 1 nm, respectively.

Preparation of powdery solid samples on silica. A suspension of a weighted quantity of silicagel 35–70 μm (WET&DRY ref SIL200) on a solution of a known concentration of **16a** alone, or mixed with 1 eq. of Ba(ClO$_4$)$_2$ on acetonitrile was evaporated under reduced pressure to obtain a silica-supported **16a-Ba^{2+}** powdery sample.

Preparation of solid samples on silica pellet. Pristine silica disks were prepared by transferring neat silicagel (35–70 μm, WET&DRY ref SIL200) into an agate mortar. The powder was grinded, with an agate pestle, until the sample had the consistency of fine flour. 30–50 mg of the sample were transferred to a hand press pellet-holder, and compressed to 10 Ton. After 10 minutes, the pressure was released, and the pellet (~1.3 cm diameter) weighted. For the preparation of **16a**-containing pellets, the required amount of an acetonitrile solution of **16a** ($5 \cdot 10^{-6}$ M, $5 \cdot 10^{-5}$ M or $1.2 \cdot 10^{-2}$ M) was dropped on the pellet to fully cover it, and oven dried at 100 °C for 15 minutes. For the preparation of samples containing both $Ba(ClO_4)_2$ and **16a**, the same procedure was used, but the pellets were prepared using a $Ba(ClO_4)_2$-containing powdery sample ([Ba] = $5.8 \cdot 10^{-5}$ mmol/mg).

Spin coating. Experiments were performed in a SCC-200 (Novocontrol technologies, Germany) apparatus coupled to a vacuum pump D-79112 (KNF, France).

III.- SYNTHETIC PROCEDURES AND ANALYTICAL DATA

Synthesis of 2-(pyridin-2-yl)imidazo[1,2-a]pyridine, 3
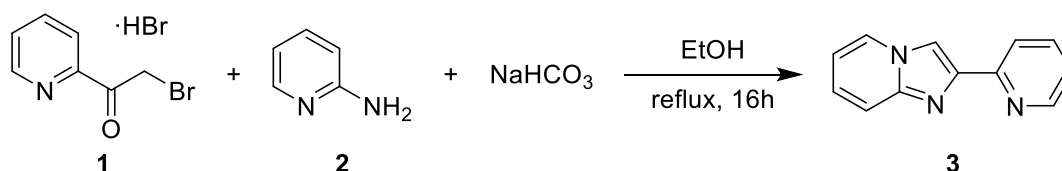
A mixture of 2-aminopyridine **2** (1.25 g, 13.5 mmol, 1.25 eq.), 2-bromo-1-(pyridin-2-yl)ethan-1-one hydrobromide **1** (3 g, 10.8 mmol, 1 eq.) and sodium bicarbonate (1.36 g, 16.2 mmol, 1.5 eq.) in ethanol (35 mL) were mixed in a 100 mL round bottomed flask stirred at 78 °C 16 h. The reaction mixture was concentrated under vacuum, diluted on AcOEt and washed with saturated NaHCO$_3$ solution. The combined organic layers were dried over Na$_2$SO$_4$, filtered and concentrated under reduced pressure, obtaining a yellow solid. The product was identified by comparison with commercial samples or literature data. The product was isolated as a white solid. Yield: 70%. ^{1}H NMR (400 MHz, Methanol-d4) δ 8.61 (ddd, J = 4.9, 1.7, 0.9 Hz, 1H), 8.52 (dt, J = 6.9, 1.2 Hz, 1H), 8.44 – 8.37 (m, 1H), 8.20 – 8.09 (m, 1H), 8.06 – 7.91 (m, 1H), 7.69 – 7.54 (m, 1H), 7.46 – 7.32 (m, 2H), 6.99 (td, J = 6.8, 1.2 Hz, 1H). UV-Vis **3** (MeCN, r.t., 5·10^{-5} M) λ$_{max}$ (nm): 243, 297, 310, 320. **3·Ba^{2+}** (MeCN, r.t., 5·10^{-5} M, 1 eq. Ba^{2+}) λ$_{max}$ (nm): 243, 297, 310, 320. FS **3** (MeCN, r.t., 5·10^{-5} M, λ$_{exc}$ = 250 nm) λ$_{em}$ (nm): 374. **3·Ba^{2+}** (MeCN, r.t., 5·10^{-5} M, 1 eq. Ba^{2+}, λ$_{exc}$ = 250 nm) λ$_{em}$ (nm): 374.

Synthesis of 1-(pyridin-2-yl)benzo[a]imidazo[5,1,2-cd]indolizine, 5
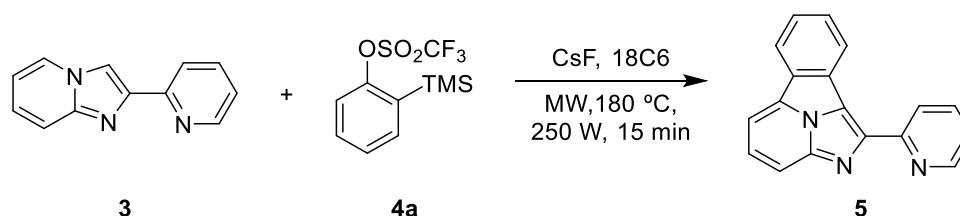
A microwave vial equipped with a magnetic stirrer, was charged with **3** (50 mg, 0.26 mmol, 1.0 eq.), cesium fluoride (38.93 mg, 0.26 mmol, 1 eq.) and 18-crown-6-ether (67.7

mg, 0.26 mmol, 1 eq.) and, then, the vial was capped and kept under Ar current for 5 minutes. To this mixture, the precursor of benzyne **4** (0.062 mL, 0.26 mmol, 1 eq.) was added via syringe and the final mixture was irradiated with MW during 15 min at 180 °C, 100 psi and 250 W. The reaction crude was dissolved in DCM, transferred to a flask and concentrated under reduced pressure. After that, it was purified by flash column chromatography on silica gel (1:2 AcOEt/Hex), obtaining a brown solid. ^{1}H NMR (500 MHz, CDCl$_3$) δ 9.15 – 9.09 (m, 1H), 8.96 (dt, J = 5.1, 1.2 Hz, 1H), 8.58 (d, J = 7.9 Hz, 1H), 8.38 (d, J = 7.9 Hz, 1H), 8.07 (dd, J = 17.7, 7.8 Hz, 2H), 8.00 – 7.90 (m, 2H), 7.89 – 7.81 (m, 1H), 7.70 – 7.62 (m, 1H), 7.37 (ddd, J = 7.4, 4.8, 1.1 Hz, 1H). ^{13}C NMR (126 MHz, CDCl$_3$) δ 153.54, 149.92, 139.41, 136.75, 131.54, 131.16, 130.05, 129.32, 126.77, 125.37, 123.92, 123.10, 122.58, 121.67, 113.67, 109.07. UV-Vis **5** (MeCN, r.t., 5·10^{-5} M) λ$_{max}$ (nm): 254, 311, 323, 396, 417. **5·Ba^{2+}** (MeCN, r.t., 5·10^{-5} M, 1 eq. Ba^{2+}) λ$_{max}$ (nm): 254, 311, 323, 396, 417. FS **5** (MeCN, r.t., 5·10^{-5} M, λ$_{exc}$ = 254 nm) λ$_{em}$ (nm): 428, 451. **5·Ba^{2+}** (MeCN, r.t., 5·10^{-5} M, 1 eq. Ba^{2+}, λ$_{exc}$ = 254 nm) λ$_{em}$ (nm): 428, 451.

Synthesis of 2-(4-chlorophenyl)imidazo[1,2-a]pyridine, 7
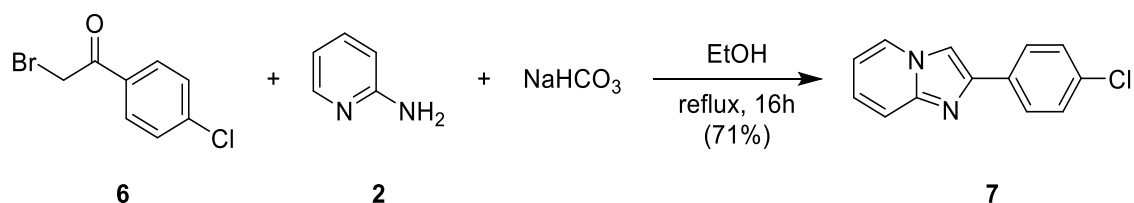
A mixture of 2-aminopyridine **2** (1.53 g, 16.25 mmol, 1.25 eq), 2-bromo-1-(4-chlorophenyl)ethan-1-one **6** (3 g, 13 mmol, 1 equiv.) and sodium bicarbonate (1.63 g, 19.5 mmol, 1.5 eq) in ethanol (40 mL) were mixed in a 100 mL round bottomed flask stirred at 78 °C 16 h. The reaction mixture was concentrated under vacuum, diluted on AcOEt and washed with saturated NaHCO$_3$ solution. The combined organic layers were dried over Na$_2$SO$_4$, filtered and concentrated under reduced pressure, obtaining a pale yellow solid. The product was identified by comparison with commercial samples or literature data. ^{1}H NMR (400 MHz, Acetone-d6) δ 8.50 (d, J = 6.8 Hz, 1H), 8.34 (s, 1H), 8.07 (d, J = 8.6 Hz, 2H), 7.61 – 7.53 (m, 1H), 7.48 (d, J = 8.6 Hz, 2H), 7.27 (ddd, J = 9.1, 6.7, 1.3 Hz, 1H), 6.90 (td, J = 6.8, 1.2 Hz, 1H).

Synthesis of 1-(4-(1,4,7,10,13-pentaoxa-16-azacyclooctadecan-16-yl)phenyl)ethan-1-one, 10
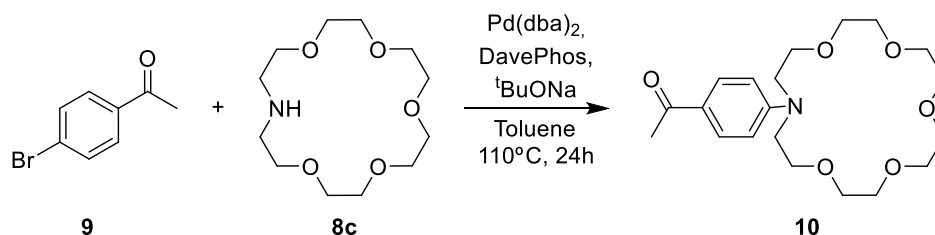
A Schlenk tube equipped with a magnetic stirring bar was charged with Pd(dba)$_2$ (11.6 mg, 0.02 mmol, 1 mol%), DavePhos (47.7 mg, 0.3 mmol, 6 mol%) and ^{t}BuONa (271.7 mg, 2.83 mmol, 1.4 eq.) followed by anhydrous toluene (1 mL) and the air was replaced by a nitrogen atmosphere. To this mixture, 4'-bromoacetophenone **9** (400 mg, 2.02 mmol, 1.0 eq.), the azacrown ether **8c** (606 mg, 2.30 mmol, 1.14 eq.) and anhydrous toluene (2 mL) were added at r.t. The tube was sealed and kept under nitrogen atmosphere in a preheated oil bath at 110 ºC for 24 h. The mixture was cooled to r.t., filtered through a celite pad, and concentrated in vacuo. The crude product was dissolved in chloroform and the impurities were precipitated with hexane. The solvent was removed under reduced pressure to obtain a brown oil. The reaction crude was isolated by flash column chromatography on silica gel (1:3 AcOEt/Hex) for the first subproducts and then, with MeOH, for the desired product. The product was isolates as a brown oil. Yield: 23%. ^{1}H NMR (400 MHz, CDCl3) δ 7.86 (d, J = 9.0 Hz, 2H), 6.69 (d, J = 9.0 Hz, 2H), 3.75 (s, 9H), 3.69 (s, 15H), 2.53 (s, 3H). UV-Vis **10** (MeCN, r.t., 5·10^{-5} M) λ_{max} (nm): 254, 336. **10·Ba^{2+}** (MeCN, r.t., 5·10^{-5} M, 1 eq. Ba^{2+}) λ_{max} (nm): 254, 336. FS **10** (MeCN, r.t., 5·10^{-5} M) λ_{em} (nm): 470. **10·Ba^{2+}** (MeCN, r.t., 5·10^{-5} M, 1 eq. Ba^{2+}) λ_{em} (nm): 374, 428, 453.

Synthesis of compounds 13

11a-b
11a: R$_1$ = p-BrPh
11b: R$_1$ = CH$_2$Br

2a-c
2a: X = CH, R$_2$ = H
2b: X = CH, R$_2$ = CO$_2$Me
2c: X = N, R$_2$ = H

13a-d
13a: X = CH, R$_1$ = p-BrPh, R$_2$ = H
13b: X = CH, R$_1$ = p-BrPh, R$_2$ = CO$_2$Me
13c: X = N, R$_1$ = p-BrPh, R$_2$ = H
13d: X = CH, R$_1$ = CH$_2$Br, R$_2$ = H
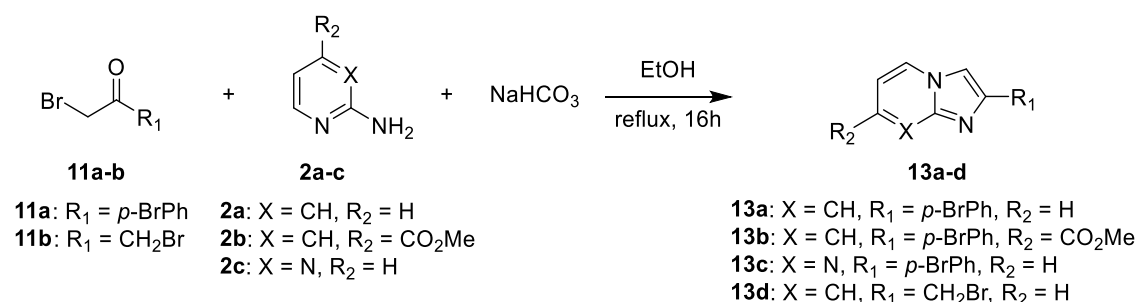
A mixture of 2-aminopyridines **2a,b** or 2-aminopyrimidine **2c** (13.5 mmol, 1.25 eq), bromine derivate **11** (3 g, 10.8 mmol) and sodium bicarbonate (1.36 g, 16.2 mmol, 1.5 eq) in ethanol (35 mL) were mixed in a 100 mL round bottomed flask stirred at 78 ºC 12 h. The reaction mixture was cooled to r.t. and filtered, obtaining a white solid, which was washed with 2 mL of cold chloroform and dried in vacuo. The compounds **13a-d** were identified by comparison with commercial samples or literature data.

2-(4-bromophenyl)imidazo[1,2-a]pyridine, 13a

A mixture of 2-aminopyridine **2a** (1.27 g, 13.5 mmol, 1.25 eq), 2-bromo-1-(4-bromophenyl)ethan-1-one **11a** (3 g, 10.8 mmol, 1 equiv.) and sodium bicarbonate (1.36 g, 16.2 mmol, 1.5 eq) in ethanol (40 mL) were mixed in a 100 mL round bottomed flask stirred at 78 ºC 16 h. The reaction mixture was cooled to r.t. and filtered, obtaining a white solid, which was washed with 2 mL of cold chloroform and dried in vacuo. The product was isolated as a white solid. Yield: 70%. ^{1}H NMR (400 MHz, CDCl$_3$) δ 8.11 (d, J = 6.7 Hz, 1H), 7.86 – 7.79 (m, 4H), 7.62 (d, J = 9.1 Hz, 1H), 7.58 – 7.53 (m, 3H), 7.18 (ddd, J = 9.1, 6.7, 1.3 Hz, 2H), 6.79 (td, J = 6.8, 1.2 Hz, 1H). M.p. 218-220. IR (cm^{-1}): 1632.6, 1496.5, 850.1, 735.9.

Methyl 2-(4-bromophenyl)imidazo[1,2-a]pyridine-7-carboxylate, 13b

A mixture of methyl 2-aminoisonicotinate **2b** (2 g, 13.5 mmol, 1.25 eq), 2-bromo-1-(4-bromophenyl)ethan-1-one **11a** (3 g, 10.8 mmol, 1 equiv.) and sodium bicarbonate (1.36 g, 16.2 mmol, 1.5 eq) in ethanol (40 mL) were mixed in a 100 mL round bottomed flask stirred at 78 ºC 16 h. The reaction mixture was cooled to r.t. and filtered, obtaining a white solid, which was washed with 2 mL of cold chloroform and dried in vacuo. The product was isolated as a white solid. Yield: 68%. ^{1}H NMR (400 MHz, CDCl3) δ (ppm) 8.39 (s, 0H), 8.18 (dd, J = 7.0, 1.0 Hz, 1H), 7.99 (s, 1H), 7.92 – 7.83 (m, 2H), 7.71 – 7.57 (m, 2H), 7.44 (dd, J = 7.1, 1.7 Hz, 1H), 4.00 (s, 3H). M.p. (ºC) 248-250. IR (cm^{-1}): 1714.2, 1469.5, 1230.1, 829.8, 757.7.

2-(4-Bromophenyl)imidazo[1,2-a]pyrimidine, 13c.

2c (1.28g, 13.5 mmol, 1.25 equiv.), **11a** (3 g, 10.8 mmol), NaHCO$_3$ (1.36 g, 16.2 mmol, 1.5 equiv.). The product was isolated as a white solid. Yield: 61%. ^{1}H NMR (400 MHz,

CDCl$_3$) δ (ppm) 8.55 (dd, J = 4.1, 2.0 Hz, 1H), 8.43 (dd, J = 6.7, 2.1 Hz, 1H), 7.91 (d, J = 8.5 Hz, 2H), 7.82 (s, 1H), 7.58 (d, J = 8.5 Hz, 2H), 6.88 (dd, J = 6.7, 4.2 Hz, 1H). M.p. 280-282. IR (cm^{-1}): 1676.2, 1497.5, 826.7, 742.4.

2-(bromomethyl)imidazo[1,2-a]pyridine, 13d.

2a (2.85g, 13.5 mmol, 1.25 equiv.), **11b** (3 g, 10.8 mmol), NaHCO$_3$ (1.36 g, 16.2 mmol, 1.5 equiv.). The product was isolated as a brown oil. Yield 21 %. ^{1}H NMR (400 MHz, CDCl$_3$) δ (ppm) 8.04 (d, J = 6.7 Hz, 1H), 7.53 (d, J = 10.2 Hz, 2H), 7.11 (ddd, J = 8.6, 6.7, 1.3 Hz, 1H), 6.77 – 6.68 (m, 1H), 4.67 (s, 2H).

Synthesis of compounds 14

13a-c
13a: X = CH, R$_2$ = H
13b: X = CH, R$_2$ = CO$_2$Me
13c: X = N, R$_2$ = H

8a-c
8a: n=1
8b: n=2
8c: n=3

14a-c
14a: X = CH, R$_2$ = H, n = 3
14b: X = CH, R$_2$ = CO$_2$Me, n = 3
14c: X = N, R$_2$ = H, n = 3
14d: X = CH, R$_2$ = H, n = 1
14e: X = CH, R$_2$ = H, n = 2
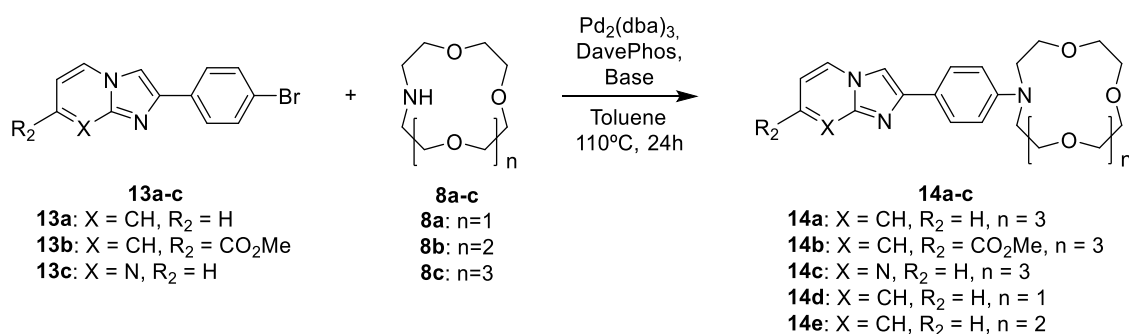
A Schlenk tube equipped with a magnetic stirring bar was charged with Pd$_2$(dba)$_3$ (91.57 mg, 0.1 mmol, 2 mol%), Davephos (118.07 mg, 0.3 mmol, 6 mol%) and ^{t}BuONa (720.75 mg, 7.5 mmol, 1.5 equiv.) followed by anhydrous toluene (3 mL) and the air was replaced by a nitrogen atmosphere. To this mixture, the corresponding imidazo[1,2-a]pyridine **13** (5 mmol, 1.0 equiv.), the azacrown ether **8** (5 mmol, 1 equiv.) and anhydrous toluene (10 mL) were added at r.t. The tube was sealed and kept under nitrogen atmosphere in a preheated oil bath at 110 ºC for 24 h. The mixture was cooled to r.t., filtered through a celite pad, and concentrated in vacuo. The crude product was dissolved in chloroform and the impurities were precipitated with hexane. The solvent was removed under reduced pressure to obtain a brown oil, which was used directly for the next reaction without further purification.

16-(4-(Imidazo[1,2-a]pyridin-2-yl)phenyl)-1,4,7,10,13-pentaoxa-16-azacyclooctadecane, 14a.

Pd$_2$(dba)$_3$ (91.57 mg, 0.1 mmol, 2 mol%), Davephos (118.07 mg, 0.3 mmol, 6 mol%), ^{t}BuONa (720.75 mg, 7.5 mmol, 1.5 equiv.), **13a** (1.36 g, 5 mmol, 1.0 equiv.), **8c** (1.32 g, 5 mmol, 1 equiv.). Brown oil. Yield: 98%. ^{1}H NMR (400 MHz, CDCl$_3$) δ 8.08 (d, J = 6.7 Hz, 1H), 7.80 (d, J = 8.8 Hz, 2H), 7.72 (s, 1H), 7.58 (d, J = 9.1 Hz, 1H), 7.12 (ddd, J = 8.8, 6.8, 1.3 Hz, 1H), 6.84 – 6.64 (m, 4H), 3.67 (dd, J = 7.4, 2.6 Hz, 24H). UV-Vis **14a** (MeCN, r.t., 5·10^{-5} M) λ$_{max}$ (nm): 254, 278, 336. **14a·Ba^{2+}** (MeCN, r.t., 5·10^{-5} M, 1 eq. Ba^{2+}) λ$_{max}$ (nm): 251, 310, 322. FS **14a** (MeCN, r.t., 5·10^{-5} M) λ$_{em}$ (nm): 458. **14a·Ba^{2+}** (MeCN, r.t., 5·10^{-5} M, 1 eq. Ba^{2+}) λ$_{em}$ (nm): 373.

Methyl 2-(4-(1,4,7,10,13-pentaoxa-16-azacyclooctadecan-16-yl)phenyl)imidazo[1,2-a]pyridine-7-carboxylate, 14b.

Pd$_2$(dba)$_3$ (91.57 mg, 0.1 mmol, 2 mol%), Davephos (236.54 mg, 0.6 mmol, 12 mol%), CsCO$_3$ (2.44 g, 7.5 mmol, 1.5 equiv.), **13b** (1.66 g, 5 mmol, 1.0 equiv.), **8c** (1.32 g, 5 mmol, 1 equiv.). ^{1}H NMR (400 MHz, CDCl$_3$) δ 8.13 (d, J = 7.2 Hz, 1H), 8.00 (t, J = 3.6 Hz, 1H), 7.86 (s, 1H), 7.83 (d, J = 8.8 Hz, 2H), 7.38 (dd, J = 7.0, 1.7 Hz, 1H), 6.78 (d, J = 8.9 Hz, 2H), 3.98 (m, 7H), 3.64 (m, J = 4.6 Hz, 20H).

16-(4-(Imidazo[1,2-a]pyrimidin-2-yl)phenyl)-1,4,7,10,13-pentaoxa-16 azacyclooctadecane, 14c.

Pd$_2$(dba)$_3$ (91.57 mg, 0.1 mmol, 2 mol%), Davephos (118.07 mg, 0.3 mmol, 6 mol%), ^{t}BuONa (720.75 mg, 7.5 mmol, 1.5 equiv.), **13c** (1.37 g, 5 mmol, 1.0 equiv.), **8c** (1.32 g, 5 mmol, 1 equiv.). ^{1}H NMR (400 MHz, CDCl$_3$) δ 7.53 – 7.48 (m, 1H), 7.33 (d, J = 7.4 Hz, 1H), 7.27 – 7.24 (m, 2H), 7.01 – 6.96 (m, 2H), 6.93 (d, J = 8.1 Hz, 2H), 3.64 (s, 24H).

10-(4-(Imidazo[1,2-a]pyridin-2-yl)phenyl)-1,4,7-trioxa-10-azacyclododecane, 14d.

Pd$_2$(dba)$_3$ (91.57 mg, 0.1 mmol, 2 mol%), Davephos (118.07 mg, 0.3 mmol, 6 mol%), ^{t}BuONa (720.75 mg, 7.5 mmol, 1.5 equiv.), **13a** (1.36 g, 5 mmol, 1.0 equiv.), **8a** (876.15

mg, 5 mmol, 1 equiv.). ^{1}H NMR (400 MHz, CDCl$_3$) δ 8.11 (dd, J = 6.8, 1.3 Hz, 1H), 7.81 (d, J = 8.8 Hz, 2H), 7.75 (s, 1H), 7.61 (d, J = 9.2 Hz, 1H), 7.14 (ddd, J = 8.9, 6.8, 1.3 Hz, 1H), 6.82 (d, J = 9.0 Hz, 2H), 6.75 (td, J = 6.7, 1.2 Hz, 1H), 3.91 (t, J = 5.0 Hz, 5H), 3.68 (d, J = 4.5 Hz, 11H).

13-(4-(Imidazo[1,2-a]pyridin-2-yl)phenyl)-1,4,7,10-tetraoxa-13-azacyclopentadecane, 14e.

Pd$_2$(dba)$_3$ (91.57 mg, 0.1 mmol, 2 mol%), Davephos (118.07 mg, 0.3 mmol, 6 mol%), ^{t}BuONa (720.75 mg, 7.5 mmol, 1.5 equiv.), **13a** (1.36 g, 5 mmol, 1.0 equiv.), **8b** (1.10 g, 5 mmol, 1 equiv.). ^{1}H NMR (400 MHz, CDCl$_3$) δ 8.11 – 8.05 (m, 1H), 7.81 (d, J = 8.9 Hz, 2H), 7.73 (s, 1H), 7.63 – 7.57 (m, 1H), 7.12 (ddd, J = 9.1, 6.7, 1.3 Hz, 1H), 6.78 – 6.71 (m, 3H), 3.67 (d, J = 12.0 Hz, 20H)

Synthesis of compounds 15

13a-c
13a: X = CH, R$_2$ = H
13b: X = CH, R$_2$ = CO$_2$Me
13c: X = N, R$_2$ = H

4a-b
4a: m = 0
4b: m = 1

CsF, 18C6
MW,180 ºC,
250 W, 15 min

15a-d
15a: X = CH, R$_2$ = H, m = 0
15b: X = CH, R$_2$ = H, m = 1
15c: X = CH, R$_2$ = CO$_2$Me, m = 0
15d: X = N, R$_2$ = H, m = 0
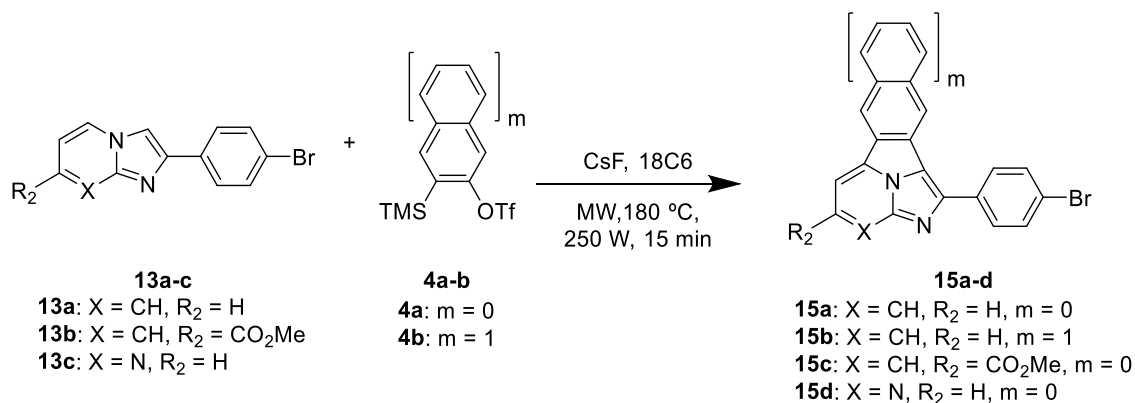
A microwave vial equipped with a magnetic stirrer, was charged with **13** (0.55 mmol, 1.0 eq.), cesium fluoride (83.4 mg, 0.55 mmol, 1 eq.) and 18-crown-6-ether (145.16 mg, 0.55 mmol, 1 eq.) and, then, the vial was capped and kept under Ar current for 5 minutes. To this mixture, the precursor of benzyne **4** (0.55 mmol, 1 eq.) was added via syringe and the final mixture was irradiated with MW during 15 min at 180 ºC, 100 psi and 250 W. The reaction crude was dissolved in DCM, transferred to a flask and concentrated under reduced pressure. After that, it was purified by flash column chromatography on silica gel (1:2 AcOEt/Hex).

1-(4-bromophenyl)benzo[a]imidazo[5,1,2-cd]indolizine, 15a

13a (150 mg, 0.55 mmol, 1.0 eq.), cesium fluoride (83.4 mg, 0.55 mmol, 1 eq.), 18-crown-6-ether (145.16 mg, 0.55 mmol, 1 eq.), benzyne precursor **4a** (0.13 mL, 0.55 mmol, 1 eq.). Yellow solid. Yield: 23%. ^{1}H NMR (400 MHz, CDCl3) δ 8.49 – 8.41 (m, 2H), 8.35 – 8.26 (m, 2H), 8.11 (dd, J = 7.8, 2.1 Hz, 2H), 8.05 – 7.95 (m, 1H), 7.84 (ddd, J = 8.3, 7.2, 1.1 Hz, 1H), 7.80 (d, J = 8.5 Hz, 2H), 7.69 (dd, J = 8.1, 6.9 Hz, 1H).

1-(4-bromophenyl)imidazo[5,1,2-cd]naphtho[2,3-a]indolizine, 15b

13a (150 mg, 0.55 mmol, 1.0 eq.), cesium fluoride (83.4 mg, 0.55 mmol, 1 eq.), 18-crown-6-ether (145.16 mg, 0.55 mmol, 1 eq.), benzyne precursor **4b** (191.63 mg, 0.55 mmol, 1 eq.). Yellow solid. Yield: 17%. ^{1}H NMR (400 MHz, CDCl$_3$) δ 8.90 (s, 1H), 8.78 (s, 1H), 8.33 (d, J = 8.5 Hz, 2H), 8.19 (dd, J = 7.9, 6.1 Hz, 2H), 8.02 (dd, J = 7.8, 2.7 Hz, 2H), 7.97 – 7.91 (m, 1H), 7.84 (d, J = 8.5 Hz, 2H), 7.71 (dd, J = 8.2, 1.5 Hz, 1H), 7.69 – 7.64 (m, 1H).

Methyl 1-(4-bromophenyl)benzo[a]imidazo[5,1,2-cd]indolizine-4-carboxylate, 15c

13b (182.14 mg, 0.55 mmol, 1.0 eq.), cesium fluoride (83.4 mg, 0.55 mmol, 1 eq.), 18-crown-6-ether (145.16 mg, 0.55 mmol, 1 eq.), benzyne precursor **4a** (0.13 mL, 0.55 mmol, 1 eq.). Yellow solid. Yield: 18%. ^{1}H NMR (400 MHz, CDCl$_3$) δ 8.82 (s, 1H), 8.79 (s, 1H), 8.49 (d, J = 8.1 Hz, 1H), 8.45 (d, J = 8.0 Hz, 1H), 8.30 (d, J = 8.2 Hz, 2H), 7.88 (t, J = 7.7 Hz, 1H), 7.81 (d, J = 8.3 Hz, 2H), 7.73 (t, J = 7.7 Hz, 1H), 4.14 (s, 3H).

Synthesis of compounds 16

Route A
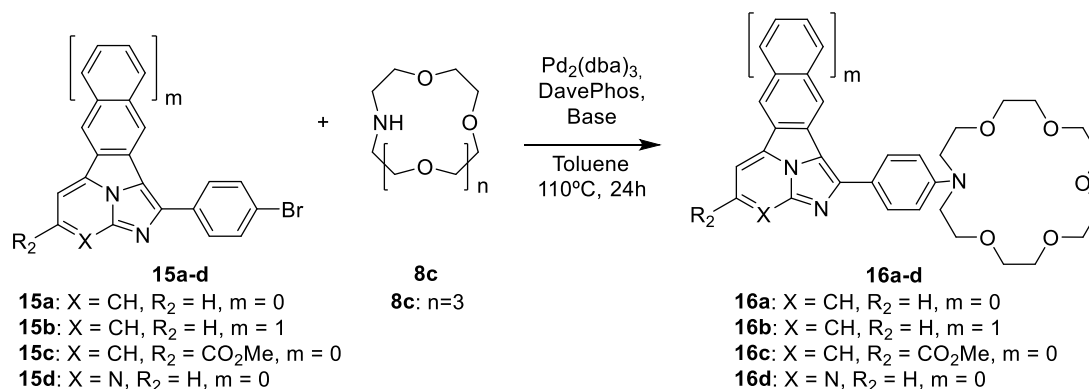
15a-d
15a: X = CH, R$_2$ = H, m = 0
15b: X = CH, R$_2$ = H, m = 1
15c: X = CH, R$_2$ = CO$_2$Me, m = 0
15d: X = N, R$_2$ = H, m = 0

8c
8c: n=3

16a-d
16a: X = CH, R$_2$ = H, m = 0
16b: X = CH, R$_2$ = H, m = 1
16c: X = CH, R$_2$ = CO$_2$Me, m = 0
16d: X = N, R$_2$ = H, m = 0

A Schlenk tube equipped with a magnetic stirring bar was charged with Pd(dba)$_2$ (0.3 mg, $5 \cdot 10^{-4}$ mmol, 0.01 equiv), DavePhos (14.2 mg, 0.003 mmol, 0.06 equiv.) and ^{t}BuONa (6.4 mg, 0.07 mmol, 1.4 eq.) followed by anhydrous toluene (1 mL) and the air was replaced by a nitrogen atmosphere. To this mixture, bromine derivate, **15** (0.05 mmol, 1.0 eq.), the azacrown ether **8c** (14.2 mg, 0.054 mmol, 1.14 eq.) and anhydrous toluene (2 mL) were added at r.t. The tube was sealed and kept under nitrogen atmosphere in a preheated oil bath at 110 °C for 24 h. The mixture was cooled to r.t., filtered through a celite pad, and concentrated in vacuo. The crude product was dissolved in chloroform and the impurities were precipitated with hexane. The solvent was removed under reduced pressure to obtain a brown oil. The reaction crude was isolated by flash column chromatography on silica gel (1:3 AcOEt/Hex) for the first subproducts and then, with MeOH, for the desired product.

Route B

14a-e
14a: X = CH, R_2 = H, n = 3
14b: X = CH, R_2 = CO_2Me, n = 3
14c: X = N, R_2 = H, n = 3
14d: X = CH, R_2 = H, n = 1
14e: X = CH, R_2 = H, n = 2

18a-b
18a: m = 0
18b: m = 1

Pd(OAc)$_2$, XPhos, K_2CO_3

DMF, 160ºC, 16 h

16a-f
16a: X = CH, R_2 = H, m = 0, n = 3
16b: X = CH, R_2 = H, m = 1, n = 3
16c: X = CH, R_2 = CO_2Me, m = 0, n = 3
16d: X = N, R_2 = H, m = 0, n = 3
16e: X = CH, R_2 = H, m = 0, n = 1
16f: X = N, R_2 = H, m = 0, n = 2
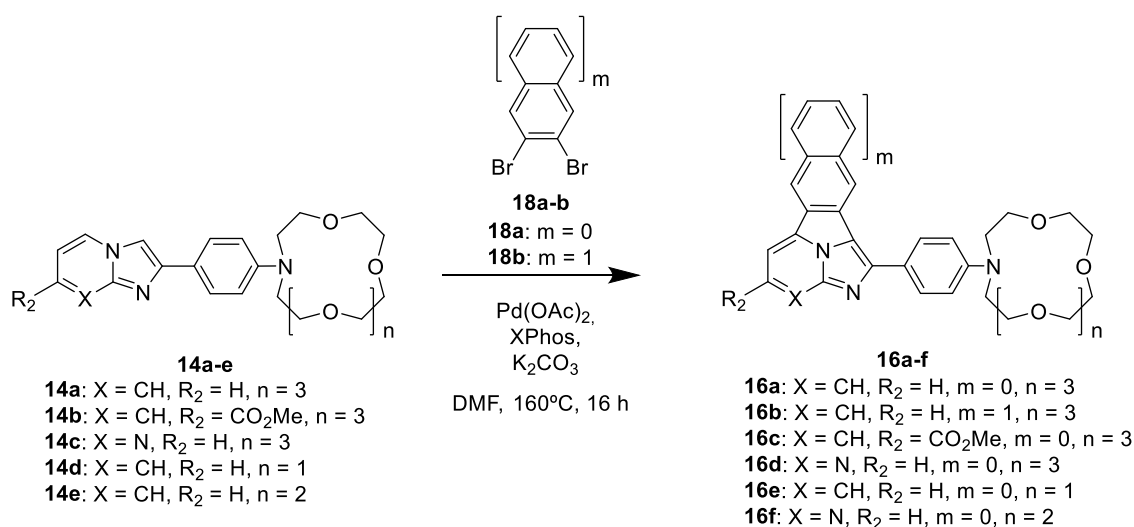
A mixture of Pd(OAc)$_2$ (9.86 mg, 0.044mmol, 4 mol%), XPhos (36.63 mg, 0.077 mmol, 7 mol%) and K_2CO_3 (455.1 mg, 3.29 mmol, 3.0 equiv.) in DMF (2 mL) was introduced in a Schlenk tube under nitrogen atmosphere. To the resulting mixture, compound **14** (1.1 mmol, 1.0 equiv.), the corresponding dibromoarene **18** (1.32 mmol, 1.2 equiv.) and DMF (8mL) were added at r.t. The tube was sealed and kept in a preheated oil bath and stirred at 160 ºC for 38 h. After this time, the reaction mixture was cooled to r.t., filtered through a celite pad and concentrated in vacuo. The crude product was dissolved in chloroform and the impurities were precipitated with hexane. The mixture was concentrated in vacuo and purified by a centrifugal thin-layer chormatography on silica and a gradient of polarity from hexane to an hexane:ethyl acetate:methanol mixture in a 1:4:0.1 ratio.

16-(4-(Benzo[a]imidazo[5,1,2-cd]indolizin-1-yl)phenyl)-1,4,7,10,13-pentaoxa-16-azacyclooctadecane, 16a

Pd(OAc)$_2$ (9.86 mg, 0.044mmol, 4 mol%), XPhos (36.63 mg, 0.077 mmol, 7 mol%), K_2CO_3 (455.1 mg, 3.29 mmol, 3.0 equiv.), **14a** (500mg, 1.1 mmol, 1.0 equiv.), **18a** (0.158 mL, 1.32 mmol, 1.2 equiv.). The product was isolated as a brown solid. Yield: 47%. ^{1}H-NMR (500 MHz, CD$_3$OD) δ 8.55 (d, J = 8.1 Hz, 1H), 8.49 (d, J = 8.2 Hz, 1H), 8.24 (d, J = 7.4 Hz, 1H), 8.21 (d, J = 8.8 Hz, 2H), 8.07 (dd, J = 8.4, 7.3 Hz, 1H), 7.99 (d, J = 8.4 Hz, 1H), 7.88 – 7.82 (m, 1H), 7.71 – 7.65 (m, 1H), 7.09 (d, J = 8.9 Hz, 2H), 3.84 (dd, J = 14.5, 4.8 Hz, 8H), 3.76 – 3.67 (m, 16H). ^{13}C-NMR (126 MHz, CD$_3$OD) δ 180.67, 151.21, 148.01, 140.75, 132.39, 131.56, 130.69, 130.50, 130.15, 128.39, 126.06, 124.53, 123.30,

121.69, 120.64, 114.59, 112.33, 109.98, 71.59, 71.37, 71.11, 71.00, 70.95. IR(solid) ν_{max} 3403, 2910, 2867, 1647, 1602, 1115, 1092, 750 cm^{-1}. HRMS (ESI) (m/z): [M]$^+$ calcd. for $C_{31}H_{35}N_3O_3$, 529,2577; found, 529,2559.

16-(4-(Imidazo[5,1,2-cd]naphtho[2,3-a]indolizin-1-yl)phenyl)-1,4,7,10,13-pentaoxa-16- azacyclooctadecane, 16b

Pd(OAc)$_2$ (9.86 mg, 0.044mmol, 4 mol%), XPhos (36.63 mg, 0.077 mmol, 7 mol%), K$_2$CO$_3$ (455.1 mg, 3.29 mmol, 3.0 equiv.), **14a** (500 mg, 1.1 mmol, 1.0 equiv.), **18b** (377.48 mg, 1.32 mmol, 1.2 equiv.). The product was isolated as a dark brown oil. Yield: 38%. ^{1}H-NMR (500 MHz, CDCl$_3$) δ 8.90 (s, 1H), 8.85 (s, 1H), 8.35 (d, J = 8.8 Hz, 2H), 8.21 (d, J = 8.2 Hz, 1H), 8.17 (d, J = 8.2 Hz, 1H), 7.98 (dd, J =7.8, 1.6 Hz, 2H), 7.88 (dd, J = 8.5, 7.2 Hz, 1H), 7.68 (ddd, J = 8.2, 6.7, 1.4 Hz, 1H), 7.62 (ddd, J = 8.0, 6.7, 1.3 Hz, 1H), 7.05 – 6.99 (m, 2H), 3.84 (dd, J = 9.4, 4.5 Hz, 6H), 3.74 (d, J = 5.9 Hz, 18H). ^{13}C-NMR (126 MHz, CDCl$_3$) δ 163.71, 148.64, 139.97, 133.77, 131.52, 130.94, 130.50, 129.61, 129.00, 128.68, 127.38, 126.95, 126.45, 125.51, 122.83, 122.21, 118.70, 112.95, 112.06, 107.11, 70.95, 68.89, 51.55. IR(solid) ν_{max} 3400, 2862, 1663, 1636, 1605, 1108, 1091, 725 cm^{-1}. HRMS (ESI) (m/z) [M]$^+$ calcd. for $C_{35}H_{37}N_3O_5$, 579.2733; found, 579.2733.

Methyl 1-(4-(1,4,7,10,13-pentaoxa-16-azacyclooctadecan-16yl)phenyl)benzo[a] imidazo[5,1,2-cd]indolizine-4- carboxylate, 16c

Pd(OAc)$_2$ (9.86 mg, 0.044mmol, 4 mol%), XPhos (36.63 mg, 0.077 mmol, 7 mol%), K$_2$CO$_3$ (455.1 mg, 3.29 mmol, 3.0 equiv.), **14b** (564.95 mg, 1.1 mmol, 1.0 equiv.), **18a** (0.158 mL, 1.32 mmol, 1.2 equiv.). The product was isolated as a brown oil. Yield: 32%. ^{1}H NMR (500 MHz, CDCl$_3$) δ 8.74 (s, 1H), 8.73 (s, 1H), 8.49 (dd, J = 15.8, 8.0 Hz, 2H), 8.32 (d, J = 8.9 Hz, 2H), 7.88 – 7.80 (m, 1H), 7.68 (t, J = 7.6 Hz, 1H), 6.97 (d, J = 8.9 Hz, 2H), 4.11 (s, 3H), 3.82 (dd, J = 12.6, 4.9 Hz, 7H), 3.72 (d, J = 5.4 Hz, 17H). ^{13}C-NMR (126 MHz, CDCl$_3$) δ ^{13}C NMR (126 MHz, CDCl$_3$) δ 166.99, 150.37, 149.05, 138.88, 131.50, 129.87, 129.26, 129.24, 128.69, 127.32, 124.88, 123.25, 121.40, 121.11, 121.04, 113.43, 111.89, 108.84, 70.88, 70.84, 70.82, 70.79, 68.67, 52.77, 51.44. IR(solid) ν_{max} 3404, 2911, 2869, 1714, 1647, 1602, 1113, 1092, 749 cm^{-1}. HRMS (ESI) (m/z) [M]$^+$

calcd. for $C_{33}H_{37}N_3O_7$, 587,6702; found, 587,6712.

16-(4-(2,2a1,3-triazacyclopenta[jk]fluoren-1-yl)phenyl)-1,4,7,10,13-pentaoxa-16-azacyclooctadecane, 16d

Pd(OAc)$_2$ (9.86 mg, 0.044mmol, 4 mol%), XPhos (36.63 mg, 0.077 mmol, 7 mol%), K_2CO_3 (455.1 mg, 3.29 mmol, 3.0 equiv.), **14c** (502.19 mg, 1.1 mmol, 1.0 equiv.), **18a** (0.158 mL, 1.32 mmol, 1.2 equiv.). The product was isolated as yellow oil. Yield: 22%. ^{1}H NMR (400 MHz, CDCl$_3$) δ 9.18 (d, J = 5.0 Hz, 1H), 8.46 (dd, J = 6.5, 1.6 Hz, 3H), 7.99 (d, J = 5.0 Hz, 1H), 7.92 (t, J = 7.9 Hz, 1H), 7.69 (t, 1H), 7.65 (t, J = 7.7 Hz, 2H), 7.58 – 7.51 (m, 1H), 3.73 (d, J = 6.5 Hz, 9H), 3.64 (s, 15H). ^{13}C-NMR (101 MHz, CDCl$_3$) δ 150.59, 148.99, 135.29, 133.99, 131.90, 130.90, 130.84, 130.11, 129.32, 128.87, 125.67, 125.11, 121.57, 119.08, 104.76, 70.68, 70.58, 70.40, 70.12, 49.11. IR(solid) ν$_{max}$ 3396, 2922, 2864, 1694, 1603, 1573, 1469, 1348, 113, 753 cm^{-1}. HRMS (ESI) (m/z): [M]$^+$ calcd. for $C_{30}H_{34}N_4O_5$, 530,2577; found, 530,2560.

10-(4-(Benzo[a]imidazo[5,1,2-cd]indolizin-1-yl)phenyl)-1,4,7-trioxa-10-azacyclododecane, 16e

Pd(OAc)$_2$ (9.86 mg, 0.044mmol, 4 mol%), XPhos (36.63 mg, 0.077 mmol, 7 mol%), K_2CO_3 (455.1 mg, 3.29 mmol, 3.0 equiv.), **14d** (452.65 mg, 1.1 mmol, 1.0 equiv.), **18a** (0.158 mL, 1.32 mmol, 1.2 equiv.). The product was isolated as a brown solid. Yield: 40%. ^{1}H-NMR (500 MHz, CDCl$_3$) δ 8.47 (d, J = 8.1 Hz, 1H), 8.40 (d, J = 8.0 Hz, 1H), 8.32 – 8.27 (m, 2H), 7.99 (dd, J = 7.8, 5.5 Hz, 2H), 7.89 (dd, J = 8.5, 7.3 Hz, 1H), 7.81 – 7.72 (m, 1H), 7.59 (t, J = 7.6 Hz, 1H), 6.99 (d, J = 8.9 Hz, 2H), 3.95 (s, 2H), 3.70 (t, J = 5.0 Hz, 6H), 3.67 (s, 8H). ^{13}C-NMR (126 MHz, CDCl$_3$) δ 149.35, 147.87, 139.83, 130.80, 129.77, 129.49, 128.93, 128.75, 126.99, 125.83, 124.07, 123.02, 122.25, 120.73, 112.61, 111.96, 108.01, 71.57, 69.90, 69.61, 52.62. IR(solid) ν$_{max}$ 3403, 2919, 2853, 1670, 1602, 1112, 1092, 748 cm^{-1}. HRMS (ESI) (m/z): [M]$^+$ calcd. for $C_{27}H_{27}N_3O_3$, 441,2052; found, 441,2068. m.p.: 137-139 ºC.

13-(4-(Benzo[a]imidazo[5,1,2-cd]indolizin-1-yl)phenyl)-1,4,7,10-tetraoxa-13-azacyclopentadecane, 16f

Pd(OAc)$_2$ (9.86 mg, 0.044mmol, 4 mol%), XPhos (36.63 mg, 0.077 mmol, 7 mol%), K$_2$CO$_3$ (455.1 mg, 3.29 mmol, 3.0 equiv.), **14e** (404.20 mg, 1.1 mmol, 1.0 equiv.), **18a** (0.158 mL, 1.32 mmol, 1.2 equiv.). The product was isolated as a brown oil. Yield: 40%. ^{1}H NMR (500 MHz, CDCl$_3$) δ 8.50 (d, J = 8.1 Hz, 1H), 8.43 (d, J = 8.0 Hz, 1H), 8.33 (d, J = 8.7 Hz, 2H), 8.03 (dd, J =7.8, 4.7 Hz, 2H), 7.96 – 7.90 (m, 1H), 7.80 (t, J = 7.6 Hz, 1H), 7.62 (t, J = 7.6 Hz, 1H), 6.94 (d, J = 8.7 Hz, 2H), 3.89 (t, J = 6.2 Hz, 5H), 3.81 – 3.71 (m, 15H). ^{13}C NMR (101 MHz, CDCl$_3$) δ 148.53, 147.27, 139.48, 130.86, 129.81, 128.93, 128.25, 127.88, 126.32, 125.01, 124.34, 123.11, 121.46, 120.78, 111.82, 111.30, 108.32, 71.37, 70.30, 70.15, 68.59, 52.79. IR(solid) ν$_{max}$ 3405, 2920, 2867, 1648, 1603, 1114, 1093, 750 cm^{-1}. HRMS (ESI) (m/z): [M]+ calcd. for C$_{29}$H$_{31}$N$_3$O$_4$, 485,2315; found, 485,2322.

Synthesis of (E)-6-bromopicolinaldehyde oxime, 18[77]

17 → **18**
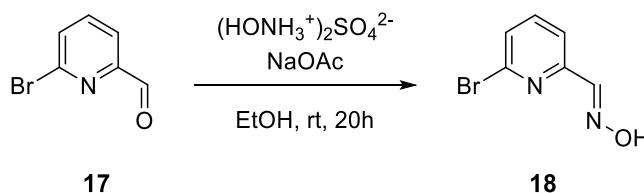
A mixture of 6-bromopyridine-2-carbaldehyde (3.0 g, 16 mmol, 1.0 equiv), hydroxylammonium sulfate ((NH$_3$OH)$_2$SO$_4$) (1.9 g, 11 mmol, 0.7 equiv), and sodium acetate (2.0 g, 25 mmol, 1.5 equiv) were added to a 250 mL roundbottom flask. Then EtOH (40 mL, 0.4 M) was added, and heterogeneous mixture was vigorously stirred at room temperature for 16 h. Magnesium sulfate was added, and mixture was filtered and concentrated under vacuum, obtaining a white solid. Yield 80%. ^{1}H NMR (400 MHz, DMSO-d_6) δ 8.04 (s, 1H), 7.83 – 7.74 (m, 2H), 7.63 (dd, J = 6.7, 2.0 Hz, 1H).

6-Bromopyridin-2-yl)methanammonium Acetate, 19[77]

18 → **19**
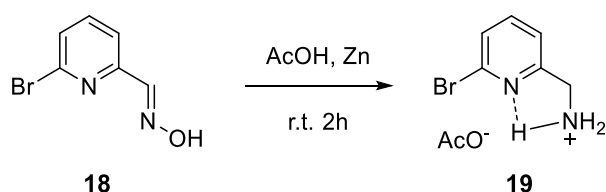
6-bromopyridine-2-carbaldehyde oxime (3.0 g, 15 mmol, 1.0 equiv) and AcOH (120.0 mL, 0.13 M) were added in a roundbottom flask and let stirred. Once starting material is completely solubilized, zinc dust (2.94 g, 45 mmol, 3.0 equiv) was poured in the flask in one portion. Mixture was stirred at room temperature for 20 min and filtered over celite. The filtrate was concentrated under vacuum to obtain a white solid. Yield: Quantitative.; ^{1}H NMR (400 MHz, CDCl$_3$) δ 7.59 (t, J = 7.7 Hz, 1H), 7.44 (d, J = 7.9 Hz, 1H), 7.34 – 7.26 (m, 1H), 4.22 (s, 2H), 1.96 (s, 6H).

Synthesis of compounds 20[77]

19

20a Ar = Ph
20b Ar = 4′-OBn-Ph
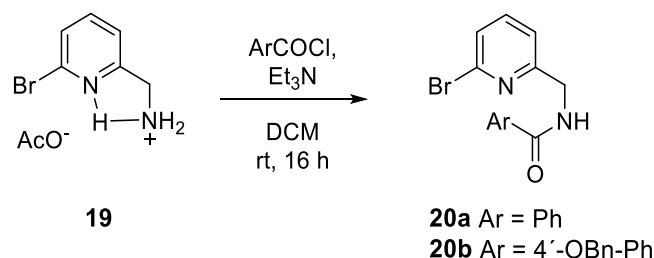
Compound **19** (500 mg, 2.02 mmol, 1.0 equiv) was adedd to a roundbottom flask equipped with a magnetic stirrer and rubber septum and diluted with DCM (0.2 M). Then, the mixture was cooled to 0 °C using an ice−water cooling bath. Triethylamine (10.1 mmol, 5.0 equiv) was added via syringe, followed by the acyl chloride (2.63 mmol, 1.3 equiv). The reaction mixture was warmed to r.t. and stirred for 16 h. The reaction was quenched with Na$_2$CO$_3$ (sat.), phases were separated, and the aqueous layer was extracted three times with DCM. The combined organic layers were dried using MgSO$_4$ (anh.), filtered, and evaporated to dryness.

N-((6-bromopyridin-2-yl)methyl)benzamide, 20a

The resulting mixture was dissolved in a minimal amount of hot EtOAc, and excess hexanes were added. The resulting precipitate was recovered by filtration and washed with cold hexane. White solid. Yield: 95%. ^{1}H NMR (400 MHz, CDCl$_3$) δ 7.93 – 7.82 (m, 2H), 7.61 – 7.50 (m, 2H), 7.50 – 7.40 (m, 3H), 7.35 (d, J = 7.5 Hz, 1H), 4.74 (d, J = 5.4 Hz, 2H).

4-(benzyloxy)-N-((6-bromopyridin-2-yl)methyl)benzamide, 20b

The crude mixture was purified by column chromatography over silica gel using a gradient of polarity from hexanes to hexanes-ethyl acetate in a ratio (1:4). White solid. Yield 90%. ^{1}H NMR (500 MHz, CDCl$_3$) δ 7.86 – 7.80 (m, 2H), 7.55 (t, J = 7.7 Hz, 1H), 7.47 – 7.39 (m, 5H), 7.38 – 7.33 (m, 2H), 7.18 (t, J = 5.5 Hz, 1H), 7.04 (d, J = 8.8 Hz, 2H), 5.14 (s, 2H), 4.73 (d, J = 5.3 Hz, 2H).

Synthesis of compounds 21[77]

20a Ar = Ph
20b Ar = 4´-OBn-Ph

21a R^1 = H
21b R^1 = OBn
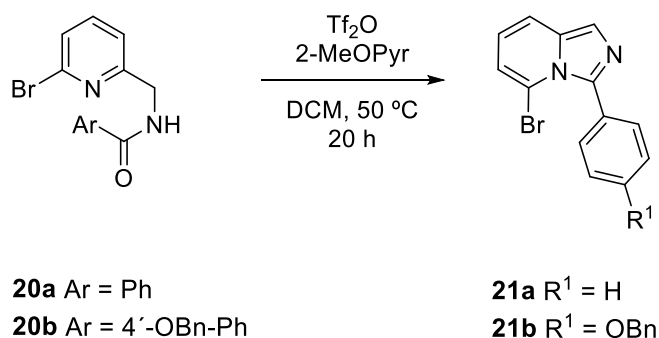
To an argon-flushed glass microwave (sealable) vial were added the corresponding amide **20** (2.50 mmol, 1.0 equiv) and anhydrous DCM (0.50 M). 2-methoxypyridine (2.75 mmol, 1.1 equiv) was added via syringe, and triflic anhydride (3.0 mmol, 1.2 equiv) was added over 2 min via syringe. The reaction mixture was slowly heated to 50 °C using an oil bath and stirred for 16 h. The crude was cooled to r.t. and quenched with Na$_2$CO$_3$ (aq. sat.) and then stirred for 5 min. Phases were separated, and the aqueous layer was extracted three times with DCM. The combined organic layers were dried over anhydrous MgSO$_4$, filtered, and concentrated under vacuum.

5-bromo-3-phenylimidazo[1,5-a]pyridine, 21a

The crude mixture was purified by column chromatography over silica gel using a gradient of polarity from hexanes to mixture hexanes/ethyl acetate 1:4. White solid. Yield: 60%. ^{1}H NMR (400 MHz, CDCl$_3$) δ 7.65 (s, 1H), 7.59 – 7.48 (m, 3H), 7.48 – 7.38 (m, 3H), 6.83 (dd, J = 6.8, 1.0 Hz, 1H), 6.58 (dd, J = 9.0, 6.8 Hz, 1H).

3-(4-(benzyloxy)phenyl)-5-bromoimidazo[1,5-a]pyridine, 21b

The crude mixture was purified by column chromatography over silica gel using a gradient of polarity from hexanes to mixture hexanes/ethyl acetate 1:4. White solid. Yield: 50% ^{1}H NMR (400 MHz, CDCl$_3$) δ 7.64 (s, 1H), 7.56 – 7.32 (m, 8H), 7.12 – 7.01 (m, 2H), 6.83 (dd, J = 6.8, 1.1 Hz, 1H), 6.58 (dd, J = 9.0, 6.8 Hz, 1H), 5.16 (s, 2H).

Synthesis of compounds 22

21a R^1 = H
21b R^1 = OBn

22a R^1 = H
22b R^1 = OBn
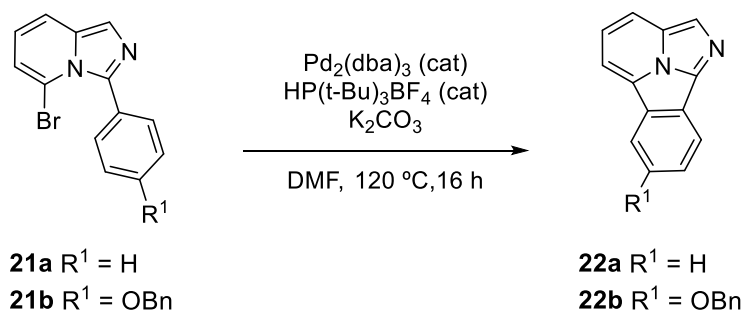
The corresponding 5- bromoimidazo[1,5-a]pyridine (3 mmol, 1.0 equiv) was added to a flame-dried microwave (sealable) vial. Then, Pd$_2$(dba)$_3$ (69 mg, 0.075 mmol, 0.025 equiv), HP(^{t}Bu)$_3$BF$_4$ (88 mg, 0.3 mmol, 0.10 equiv), and K$_2$CO$_3$ (841 mg, 6 mmol, 2.0 equiv) were added to the vial. The vial was seal with a rubber septum and purged with argon. The mixture was dissolved in anhydrous DMF (0.20M) and the reaction was quickly heated to 120 °C using an oil bath and stirred for 2.5 h. The reaction was cooled to r.t., the crude mixture was diluted in EtOAc, and quenched with brine. The layers were separated and the aqueous layer was extracted three times with EtOAc. The combined organic layers were washed twice with brine, dried over anhydrous MgSO$_4$, filtered over a pad of silica gel, and evaporated to dryness.

Benzo[a]imidazo[2,1,5-cd]indolizine, 22a

The crude imidazo[2,1,5-c,d]indolizine was purified by column chromatography over silica gel using a gradient of 1−10% MeOH in DCM. Yellow solid. Yield: 90%. ^{1}H NMR (500 MHz, CDCl$_3$) δ 8.38 (dd, J = 13.6, 8.0 Hz, 1H), 8.21 (s, 1H), 8.12 (d, J = 8.5 Hz, 1H), 7.99 (d, J = 6.8 Hz, 1H), 7.76 (ddd, J = 8.1, 7.3, 1.1 Hz, 1H), 7.65 (dd, J = 8.5, 6.9 Hz, 1H), 7.60 (ddd, J = 8.1, 7.2, 1.0 Hz, 1H).

7-(benzyloxy)benzo[a]imidazo[2,1,5-cd]indolizine, 22b

The crude imidazo[2,1-c,d]indolizine was purified by column chromatography over silica gel using a gradient of 1−10% MeOH in DCM. Yellow solid. Yield: 65%. ^{1}H NMR (400 MHz, CDCl$_3$) δ 8.32 (d, J = 8.7 Hz, 1H), 8.18 (s, 1H), 8.12 (dd, J = 8.5, 2.0 Hz, 1H), 8.00 − 7.90 (m, 2H), 7.66 − 7.58 (m, 1H), 7.56 (d, J = 7.0 Hz, 2H), 7.51 − 7.38 (m, 4H), 5.29 (s, 2H).

Synthesis of compounds 23

22a R^1 = H
22b R^1 = OBn

23a R^1 = H (98%)
23b R^1 = OBn (75%)
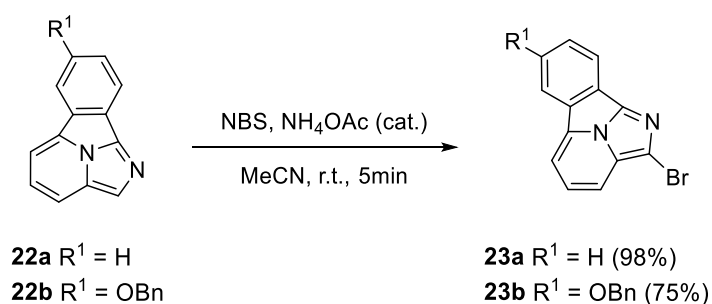
The corresponding indolizine derivate **22** (5 mmol, 1.0 equiv.) was added to a roundbottom flask with ammonium acetate (38.5 mg, 0.5 mmol, 0.1 equiv.) and dissolved in acetonitrile. Then, N-bromosuccinimide (935 mg, 5.25 mmol, 1.05 equiv.) was poured in one portion. The mixture was stirred at r.t. during 5 minutes. The solvent was removed under vacuum. Then, the crude was dissolved in ethyl acetate and washed three times with Na$_2$S$_2$O$_3$.

2-bromobenzo[a]imidazo[2,1,5-cd]indolizine, 23a

Orange solid. Yield: 98%. ^{1}H NMR (400 MHz, CDCl$_3$) δ 8.38 (t, J = 7.7 Hz, 2H), 8.06 (dd, J = 7.7, 5.2 Hz, 2H), 7.80 (td, J = 7.6, 1.1 Hz, 1H), 7.73 (dd, J = 8.5, 7.0 Hz, 1H), 7.65 (td, J = 7.6, 1.2 Hz, 1H).

7-(benzyloxy)-2-bromobenzo[a]imidazo[2,1,5-cd]indolizine, 23b

Orange solid. Yield: 75%. ^{1}H NMR (400 MHz, CDCl$_3$) δ 8.24 (d, J = 8.7 Hz, 1H), 8.02 (d, J = 8.5 Hz, 1H), 7.96 (d, J = 6.9 Hz, 1H), 7.90 (d, J = 2.3 Hz, 1H), 7.64 (dd, J = 8.6, 7.0 Hz, 1H), 7.58 – 7.52 (m, 2H), 7.50 – 7.43 (m, 3H), 7.43 – 7.36 (m, 1H), 5.28 (s, 2H).

Synthesis of 16-phenyl-1,4,7,10,13-pentaoxa-16-azacyclooctadecane, 25
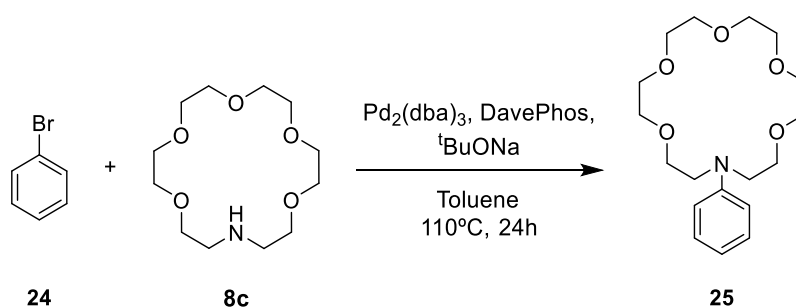
A Schlenk tube equipped with a magnetic stirring bar was charged with Pd(dba)$_2$ (0.3 mg, 5·10^{-4} mmol, 0.01 equiv), DavePhos (14.2 mg, 0.003 mmol, 0.06 equiv.) and ^{t}BuONa (6.4 mg, 0.07 mmol, 1.4 eq.) followed by anhydrous toluene (1 mL) and the air was replaced by a nitrogen atmosphere. To this mixture, bromobencene (0.05 mmol, 1.0 eq.), the azacrown ether **8c** (14.2 mg, 0.054 mmol, 1.14 eq.) and anhydrous toluene (2 mL) were added at r.t. The tube was sealed and kept under nitrogen atmosphere in a preheated oil bath at 110 ℃ for 24 h. The mixture was cooled to r.t., filtered through a celite pad, and concentrated in vacuo. The crude product was dissolved in chloroform and the impurities were precipitated with hexane. The solvent was removed under reduced pressure to obtain a brown oil. Yield: Quantitative. ^{1}H NMR (400 MHz, CDCl$_3$) δ 7.27 – 7.19 (m, 2H), 6.76 – 6.66 (m, 3H), 3.83 – 3.55 (m, 24H).

Synthesis of 16-(4-iodophenyl)-1,4,7,10,13-pentaoxa-16-azacyclooctadecane, 26

25 → **26**

NIS, NH$_4$OAc (cat.)

MeCN, r.t., 5min
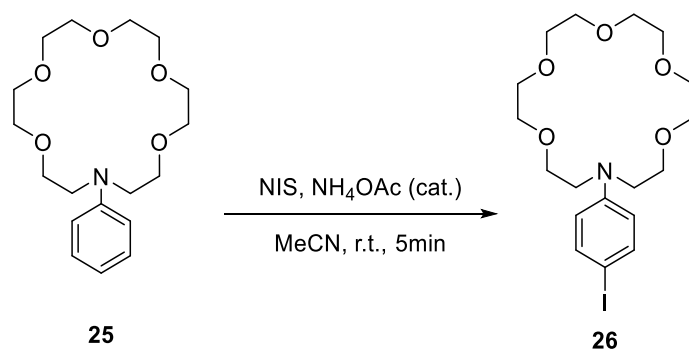
Compound **25** (1.7 g, 5 mmol, 1.0 equiv.) was added to a roundbottom flask with ammonium acetate (38.5 mg, 0.5 mmol, 0.1 equiv.) and dissolved in acetonitrile. Then, N-Iodosuccinimide (1.18 g, 5.25 mmol, 1.05 equiv.) was poured in one portion. The mixture was stirred at r.t. during 5 minutes. The solvent was removed under vacuum. Then, the crude was dissolved in ethyl acetate and washed three times with Na$_2$S$_2$O$_3$. Brown oil. Yield: Quantitative. ^{1}H NMR (400 MHz, CDCl$_3$) δ 7.43 (d, J = 8.3 Hz, 2H), 6.51 (d, J = 8.5 Hz, 2H), 3.66 (d, J = 3.7 Hz, 24H).

Synthesis of 16-(4-(4,4,5,5-tetramethyl-1,3,2-dioxaborolan-2-yl)phenyl)-1,4,7,10,13-pentaoxa-16-azacyclooctadecane, 27

26 → **27**

B$_2$Pin$_2$, PdCl$_2$(PPh$_3$)$_2$, KOAc

DMSO, 80°C, 16h
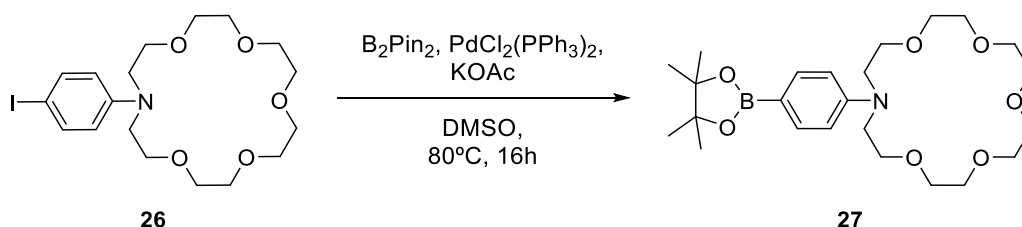
Anhydrous KOAc (175 mg, 1.78 mmol, 3.0 equiv.), PdCl$_2$(PPh$_3$)$_2$ (12 mg, 0.018 mmol, 0.03 equiv.), bis(pinacolato) diboron (166 mg, 0.653 mmol, 1.1 equiv.), **26** (276 mg, 0.593 mmol, 1 equiv.) and DMSO (4.0 mL) sequentially, were added into a Schlenk tube. After three times of vaccum-argon filling cycles, the tube was backfilled with Ar, sealed and immersed in an oil bath at 80 °C for 12 h. The mixture was cooled to r.t., diluted with H$_2$O and extracted three times with Et$_2$O. The organic layers were dried over magnesium sulfate, filtered and the solvent removed under vacuum. The mixture was purified by column chromatography with hexanes/ethyl acetate (2:1) as eluent. White solid. Yield:

50%. (Estimated by NMR). ^{1}H NMR (400 MHz, CDCl$_3$) δ 7.65 (d, J = 8.7 Hz, 2H), 6.65 (d, J = 8.8 Hz, 2H), 3.67 (d, J = 3.5 Hz, 27H), 1.31 (s, 15H).

Synthesis of compounds 28
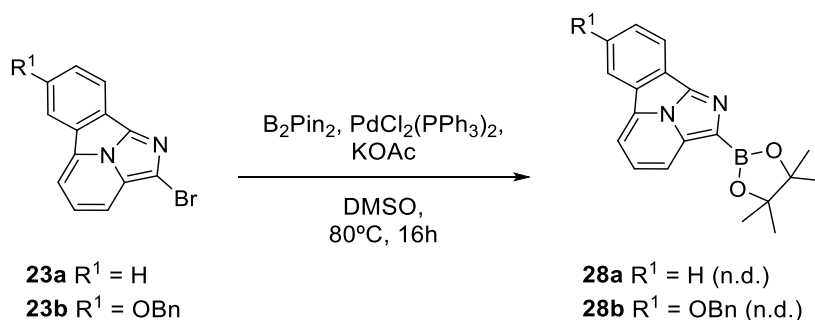
23a R^1 = H
23b R^1 = OBn

28a R^1 = H (n.d.)
28b R^1 = OBn (n.d.)

Anhydrous KOAc (162.8 mg, 1.67 mmol, 3.0 equiv.), PdCl$_2$(PPh$_3$)$_2$ (11.6 mg, 0.017 mmol, 0.03 equiv.), bis(pinacolato) diboron (463 mg, 1.82 mmol, 3.3 equiv.), corresponding compound **23** (0.55 mmol, 1.0 equiv.) and DMSO (4.0 mL) sequentially, were added into a Schlenk tube. After three times of vaccum-argon filling cycles, the tube was backfilled with Ar, sealed and immersed in an oil bath at 80 °C for 12 h. The mixture was cooled to r.t., diluted with H$_2$O and extracted three times with Et$_2$O. The organic layers were dried over magnesium sulfate, filtered and the solvent removed under vacuum. The mixture was purified by column chromatography with hexanes/ethyl acetate (2:1) as eluent.

2-(4,4,5,5-tetramethyl-1,3,2-dioxaborolan-2-yl)benzo[a]imidazo[2,1,5-cd]indolizine, 28a

Anhydrous KOAc (162.8 mg, 1.67 mmol, 3.0 equiv.), PdCl$_2$(PPh$_3$)$_2$ (11.6 mg, 0.017 mmol, 0.03 equiv.), bis(pinacolato) diboron (463 mg, 1.82 mmol, 3.3 equiv.), **23a** (150 mg, 0.55 mmol, 1.0 equiv.) Yield: n.d. Orange Solid. ^{1}H NMR (400 MHz, CDCl$_3$) δ 8.42 (dd, J = 7.9, 1.0 Hz, 1H), 8.37 (dt, J = 8.0, 1.0 Hz, 1H), 8.09 (t, J = 7.6 Hz, 2H), 7.82 (ddd, J = 8.1, 7.3, 1.1 Hz, 1H), 7.75 (dd, J = 8.6, 7.0 Hz, 1H), 7.66 (ddd, J = 8.2, 7.3, 1.1 Hz, 1H), 1.29 (s, 24H).

7-(benzyloxy)-2-(4,4,5,5-tetramethyl-1,3,2-dioxaborolan-2-yl)benzo[a]imidazo [2,1,5-cd]indolizine, 28b

Anhydrous KOAc (162.8 mg, 1.67 mmol, 3.0 equiv.), $PdCl_2(PPh_3)_2$ (11.6 mg, 0.017 mmol, 0.03 equiv.), bis(pinacolato) diboron (463 mg, 1.82 mmol, 3.3 equiv.), **23b** (207.5 mg, 0.55 mmol, 1.0 equiv.) Yield: n.d. Orange Solid. ^{1}H NMR (400 MHz, CDCl3) δ 8.26 (d, J = 8.7 Hz, 1H), 8.05 (d, J = 8.6 Hz, 1H), 7.99 (d, J = 7.0 Hz, 1H), 7.93 (d, J = 2.3 Hz, 1H), 7.67 (dd, J = 8.6, 7.0 Hz, 1H), 7.57 – 7.53 (m, 2H), 7.52 – 7.43 (m, 3H), 7.43 – 7.37 (m, 1H), 5.29 (s, 2H), 1.29 (s, 24H).

Synthesis of compounds 29

28a R^1 = H   **26**   **29a** R^1 = H (5%)
28b R^1 = OBn   **29b** R^1 = OBn (7%)
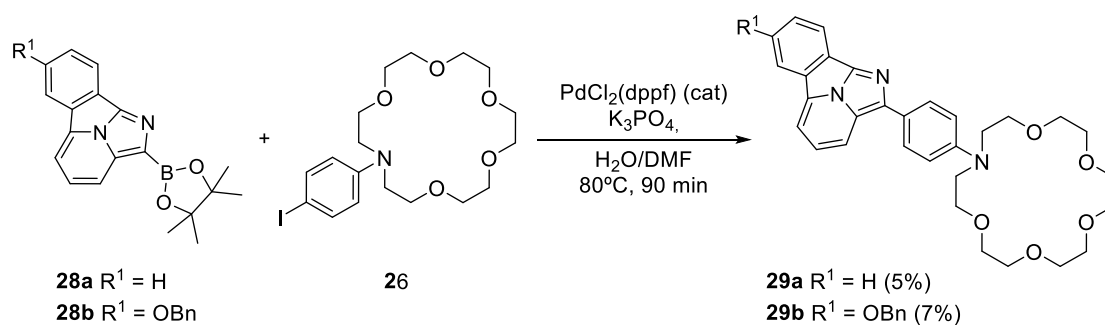
The corresponding boronic acid, **28** (1 mmol, 1.0 equiv.), compound **26** (465.3 mg, 1 mmol, 2.0 equiv.), K_3PO_4 (849.2 g, 4 mmol, 4.0 equiv), and $PdCl_2$(dppf) (73.2 mg, 0.1 mmol, 0.05 equiv) were added to a sealable tube. 17% H_2O in DMF (0.08M) was added, the vial was capped and flushed with argon, and the mixture was heated to 80 °C and stirred for 16 h. EtOAc, brine $NaHCO_3$ (sat.) were added, and mixture was separated. The aqueous phase was extracted three times with EtOAc. The combined organic layers were washed twice with brine, dried over $MgSO_4$, and evaporated to dryness.

16-(4-(benzo[a]imidazo[2,1,5-cd]indolizin-2-yl)phenyl)-1,4,7,10,13-pentaoxa-16-azacyclooctadecane, 29a

28a (318.18 mg, 1 mmol, 1.0 equiv.), **26** (465.3 mg, 1 mmol, 2.0 equiv.), K_3PO_4 (849.2 g, 4 mmol, 4.0 equiv), and $PdCl_2$(dppf) (73.2 mg, 0.1 mmol, 0.05 equiv). Dark red oil. Yield: 5%. ^{1}H NMR (500 MHz, CDCl3) δ 8.50 – 8.45 (m, 1H), 8.42 (dd, J = 10.3, 8.2 Hz,

2H), 8.14 (d, J = 8.8 Hz, 2H), 8.07 (d, J = 7.0 Hz, 1H), 7.84 – 7.76 (m, 1H), 7.69 (dd, J = 8.5, 7.0 Hz, 1H), 7.64 – 7.58 (m, 1H), 6.90 (d, J = 8.9 Hz, 2H), 3.81 (t, J = 6.0 Hz, 5H), 3.72 (s, 20H). ^{13}C NMR (126 MHz, CDCl$_3$) δ 147.54, 141.60, 136.61, 130.48, 129.22, 129.14, 128.01, 127.77, 126.57, 126.42, 124.52, 123.20, 122.51, 121.24, 120.03, 118.14, 112.51, 111.08, 70.98, 69.17, 51.62. IR(solid) ν$_{max}$ 3451, 3054, 2861, 1608, 1520, 1099 1068 cm^{-1}. HRMS (ESI) (m/z): [M]$^+$ calcd. for C$_{31}$H$_{35}$N$_3$O$_3$, 529,2577; found, 529,2538.

16-(4-(7-(benzyloxy)benzo[a]imidazo[2,1,5-cd]indolizin-2-yl)phenyl)-1,4,7,10,13-pentaoxa-16-azacyclooctadecane, 29b

28b (424.31 mg, 1 mmol, 1.0 equiv.), **26** (465.3 mg, 1 mmol, 2.0 equiv.), K$_3$PO$_4$ (849.2 g, 4 mmol, 4.0 equiv), and PdCl$_2$(dppf) (73.2 mg, 0.1 mmol, 0.05 equiv). Dark red oil. Yield: 7%. ^{1}H NMR (500 MHz, CDCl$_3$) δ 8.38 (dd, J = 8.6, 3.2 Hz, 2H), 8.12 (d, J = 8.9 Hz, 2H), 8.00 (d, J = 7.0 Hz, 1H), 7.95 (d, J = 2.4 Hz, 1H), 7.62 (dd, J = 8.4, 7.0 Hz, 1H), 7.59 – 7.53 (m, 2H), 7.52 – 7.43 (m, 3H), 7.43 – 7.35 (m, 1H), 6.90 (d, J = 8.9 Hz, 2H), 5.30 (s, 2H), 3.81 (t, J = 5.8 Hz, 4H), 3.77 – 3.64 (m, 20H). ^{13}C NMR (126 MHz, CDCl$_3$) δ 156.60, 147.14, 140.68, 139.88, 136.78, 136.40, 131.65, 128.69, 128.14, 127.65, 127.58, 126.28, 122.19, 122.11, 120.78, 120.35, 118.61, 118.14, 112.14, 110.82, 107.38, 70.75, 68.85, 51.38. IR(solid) ν$_{max}$ 3484, 2907, 2870, 1609, 1531, 1438, 1235, 1097, 1063 cm^{-1}. HRMS (ESI) (m/z): [M]$^+$ calcd. for C$_{31}$H$_{35}$N$_3$O$_3$, 635,3008; found, 635,2991.

Synthesis of (2-(4-(1,4,7,10,13-pentaoxa-16-azacyclooctadecan-16-yl)phenyl)imidazo[1,2-a]pyridin-7-yl)methanol, 30

In an oven dry round-bottom flask compound **14b** (2.5 g, 7.55 mmol, 1 equiv.) was added and then, the flask was sealed with a rubber septum and filled with argon. Anhydrous THF was poured and the flask was cooled to 0 ºC. Lithium-Aluminum Hydride 2.5M in THF (6.9 mL, 17.36 mmol, 2.3 equiv.) was added via syringe. The mixture was left to

react at r.t. for 2 h. The crude was quenched with distilled water and then, $NaHCO_3$, brine and AcOEt were added and the mixture was separated. The aqueous phase was extracted three times with EtOAc. The combined organic layers were washed twice with brine, dried over $MgSO_4$, and evaporated to dryness. Yield: 30%. ^{1}H NMR (400 MHz, $CDCl_3$) δ 8.03 (d, J = 6.9 Hz, 1H), 7.94 (d, J = 7.6 Hz, 2H), 7.78 (d, J = 5.4 Hz, 1H), 7.58 (s, 1H), 7.43 (t, J = 7.6 Hz, 2H), 6.79 (dd, J = 7.0, 1.6 Hz, 1H), 4.68 (s, 2H), 3.71 – 3.64 (m, 24H).

Synthesis of 3-bromo-2-(4-bromophenyl)imidazo[1,2-a]pyridine, 31
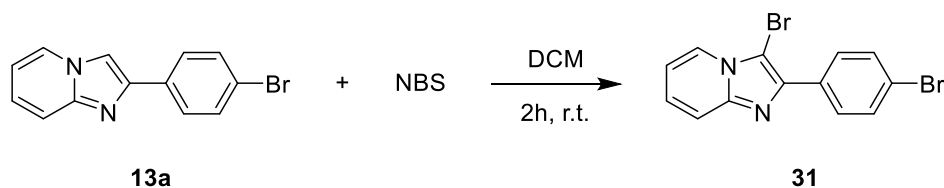
A solution of compound **13a** (100 mg, 0.366 mmol, 1 eq.) in 6 mL of DCM and a solution of NBS (65 mg, 0.366 mmol, 1 eq) in 3 mL of DCM were separately prepared by stirring the mixtures in round bottom flasks until total solution of the solids. The solution of reactant **13a** was then added dropwise over the solution of NBS and the flask was capped with a rubber septum. The mixture was stirred for 2 hours. The crude was evaporated and purified by column chromatography on silica gel, using Hexane/Ethyl acetate as eluent to afford the compound **31**. ^{1}H NMR (400 MHz, $CDCl_3$) δ 8.20 (d, J = 6.9 Hz, 1H), 8.04 (d, J = 8.6 Hz, 2H), 7.67 (d, J = 9.1 Hz, 1H), 7.63 (d, J = 8.5 Hz, 2H), 7.34 – 7.30 (m, 1H), 6.99 (dd, J = 6.9, 1.2 Hz, 1H).

Synthesis of 5-bromopyridin-2-amine, 32
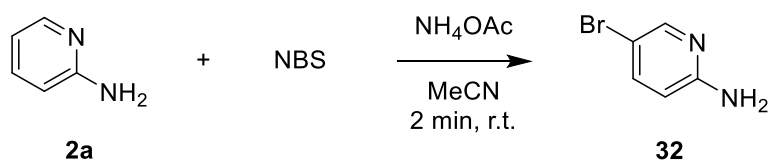
2-aminopyridine **2a** (470.25 mg, 5 mmol, 1.0 equiv.) was added to a roundbottom flask with ammonium acetate (38.5 mg, 0.5 mmol, 0.1 equiv.) and dissolved in acetonitrile. Then, N-bromosuccinimide (935 mg, 5.25 mmol, 1.05 equiv.) was poured in one portion. The mixture was stirred at r.t. during 5 minutes. The solvent was removed under vacuum.

Then, the crude was dissolved in ethyl acetate and washed three times with $Na_2S_2O_3$. ^1H NMR (400 MHz, $CDCl_3$) δ 8.22 – 7.97 (d, J = 2.5 Hz 1H), 7.52 (dd, J = 8.8, 2.5 Hz, 1H), 6.44 (d, J = 8.8 Hz, 1H).

Synthesis of 16-(4-(4-bromoimidazo[5,1,2-cd]naphtho[2,3-a]indolizin-1-yl)phenyl)-1,4,7,10,13-pentaoxa-16-azacyclooctadecane, 33
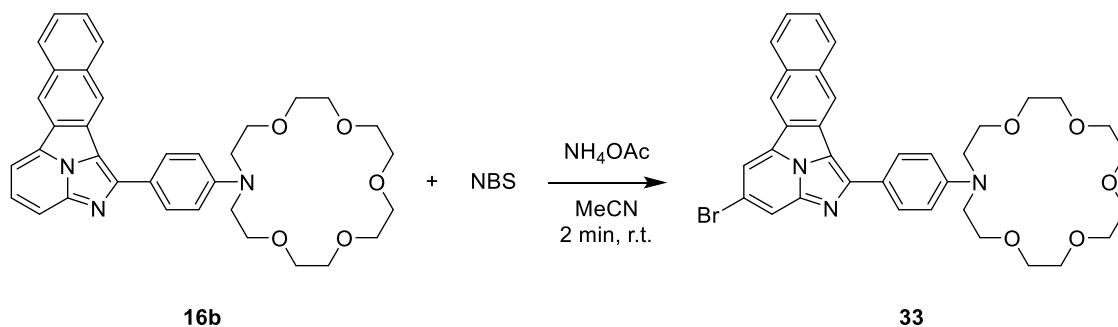
Compound **16b** (2.9 g, 5 mmol, 1.0 equiv.) was added to a roundbottom flask with ammonium acetate (38.5 mg, 0.5 mmol, 0.1 equiv.) and dissolved in acetonitrile. Then, N-bromosuccinimide (935 mg, 5.25 mmol, 1.05 equiv.) was poured in one portion. The mixture was stirred at r.t. during 5 minutes. The solvent was removed under vacuum. ^1H NMR (500 MHz, CD_3OD) δ 8.59 – 8.52 (m, 1H), 8.49 (d, J = 8.2 Hz, 1H), 8.30 – 8.19 (m, 3H), 8.15 – 8.03 (m, 2H), 7.99 (d, J = 8.4 Hz, 1H), 7.93 – 7.80 (m, 1H), 7.72 – 7.63 (m, 1H), 7.09 (d, J = 8.9 Hz, 2H), 3.91 – 3.77 (m, 8H), 3.77 – 3.60 (m, 16H).

Synthesis of 16-(4-(benzo[a]imidazo[5,1,2-cd]indolizin-1-yl)-bromophenyl)-1,4,7,10,13-pentaoxa-16-azacyclooctadecane, 34
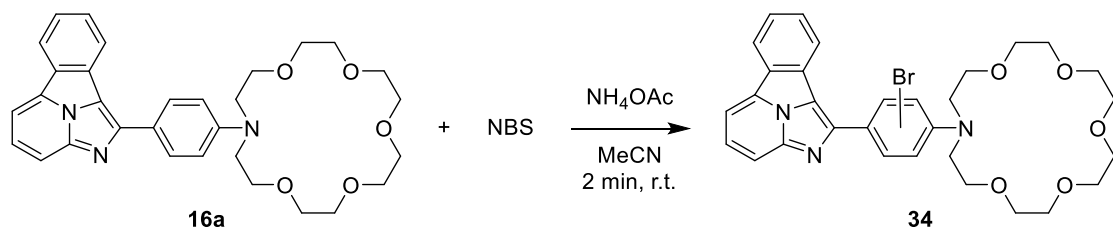
Compound **16b** (2.65 g, 5 mmol, 1.0 equiv.) was added to a roundbottom flask with ammonium acetate (38.5 mg, 0.5 mmol, 0.1 equiv.) and dissolved in acetonitrile. Then, N-bromosuccinimide (935 mg, 5.25 mmol, 1.05 equiv.) was poured in one portion. The mixture was stirred at r.t. during 5 minutes. The solvent was removed under vacuum.

Synthesis of Methyl (E)-3-(6-aminopyridin-3-yl)acrylate, 36a
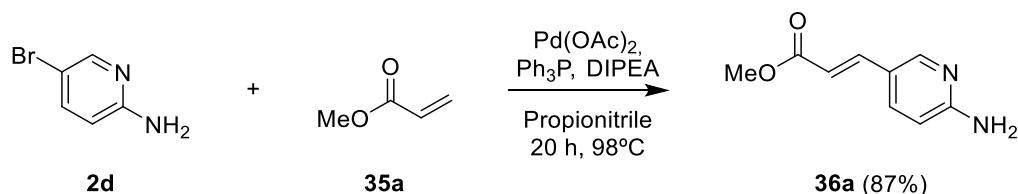
A mixture of 2-amino-5-bromopyridine **2d** (2.25 g, 13.0 mmol, 1 equiv.), methyl acrylate (1.68 g, 19.7 mmol, 1.5 equiv.), Pd(OAc)$_2$ (0.31 g, 1.3 mmol, 0.1 equiv.), tri-o-tolylphosphine (0.73 g, 2.6 mmol, 0.2 equiv.), and diisopropylethylamine (3.5 mL, 20.0 mmol, 1.5 equiv.) in 50 mL of propionitrile was heated at reflux overnight. The dark mixture was filtered through a Celite pad, and the filtrate was concentrated. After purification by column chromatography on silica gel (MeOH/CH$_2$Cl$_2$ 1:40) product 36a was isolated. Yield 87%. ^{1}H NMR (400 MHz, CDCl$_3$) δ 8.14 (d, J = 2.3 Hz, 1H), 7.67 (dd, J = 8.7, 2.4 Hz, 1H), 7.58 (d, J = 16.0 Hz, 1H), 6.61 (d, J = 8.9 Hz, 1H), 6.26 (d, J = 16.0 Hz, 1H), 3.79 (s, 3H).

Synthesis of Methyl (E)-3-(2-(4-bromophenyl)imidazo[1,2-a]pyridin-6-yl)acrylate, 13d
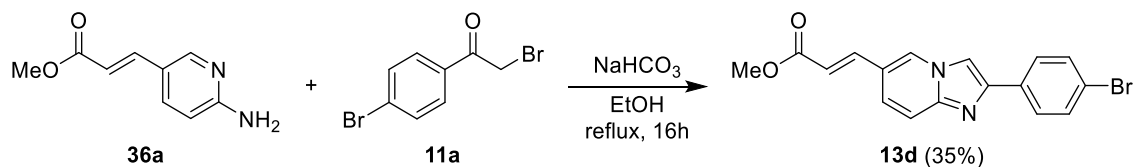
A mixture of **36a** (1.0 g, 5.6 mmol, 1.25 eq), bromine derivate **11** (1.25 g, 4.5 mmol) and sodium bicarbonate (0.57 g, 6.7 mmol, 1.5 eq) in ethanol (35 mL) were mixed in a 100 mL round bottomed flask stirred at 78 ºC 12 h. The reaction mixture was cooled to r.t. and filtered, obtaining a white solid, which was washed with 2 mL of cold chloroform and dried in vacuo. ^{1}H NMR (400 MHz, CDCl$_3$) δ 8.28 – 8.24 (m, 1H), 7.91 (s, 1H), 7.85 (d, J = 8.5 Hz, 2H), 7.68 (d, J = 6.9 Hz, 1H), 7.65 (s, 1H), 7.63 – 7.58 (m, 2H), 7.46 (dd, J = 9.4, 1.8 Hz, 1H), 6.47 (d, J = 15.9 Hz, 1H), 3.86 (s, 3H). ^{13}C NMR (101 MHz, CDCl$_3$) δ 170.95, 166.96, 140.41, 132.19, 131.94, 127.57, 127.17, 122.36, 120.95, 119.47, 118.97, 118.34, 117.89, 108.86, 51.90.

Synthesis of Methyl (E)-3-(2-aminopyridin-4-yl)acrylate, 36b
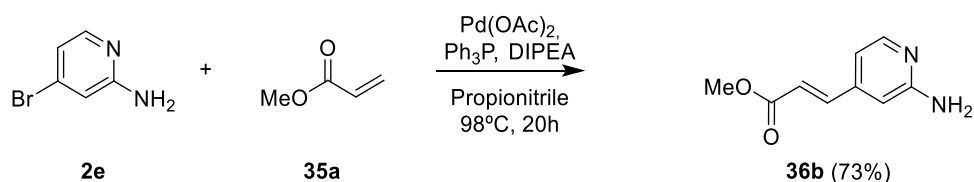
A mixture of 2-amino-4-bromopyridine **2e** (2.25 g, 13.0 mmol, 1 equiv.), methyl acrylate (1.68 g, 19.7 mmol, 1.5 equiv.), Pd(OAc)₂ (0.31 g, 1.3 mmol, 0.1 equiv.), tri-o-tolylphosphine (0.73 g, 2.6 mmol, 0.2 equiv.), and diisopropylethylamine (3.5 mL, 20.0 mmol, 1.5 equiv.) in 50 mL of propionitrile was heated at reflux overnight. The dark mixture was filtered through a Celite pad, and the filtrate was concentrated. After purification by column chromatography on silica gel (MeOH/CH₂Cl₂ 1:40) product **36b** was isolated. Yield 73%. ¹H NMR (400 MHz, DMSO-d_6) δ 8.44 (d, J = 5.3 Hz, 1H), 8.21 (d, J = 7.1 Hz, 1H), 7.67 (d, J = 16.1 Hz, 1H), 7.53 (d, J = 5.3 Hz, 1H), 6.87 (d, J = 16.1 Hz, 1H), 3.78 (s, 3H).

Synthesis of 3-(2-(4-bromophenyl)imidazo[1,2-a]pyridin-6-yl)propan-1-ol, 37
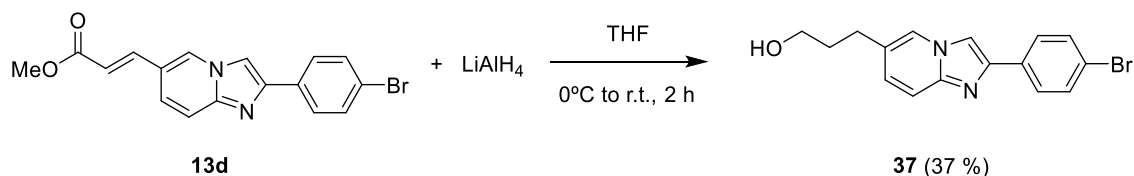
The compound **13d** (300 mg, 0.84 mmol, 1 eq.) were dissolved in dry THF (10 mL) in a dry flask under argon atmosphere. Then a solution of LiAlH₄ (2.5 M) in THF (1.93 mmol, 2.3 eq.) was added dropwise at 0°C. The mixture was stirred at room temperature for 2 h and was quenched adding an excess of MeOH in an ice bath. The solution was concentrated, dissolved in DCM and washed with NaHCO3 (sat). White off solid. Yield: 37%. ¹H NMR (400 MHz, Chloroform-d) δ 7.87 (d, J = 7.2 Hz, 3H), 7.79 – 7.66 (m, 1H), 7.48 (d, J = 8.9 Hz, 1H), 7.36 (t, J = 7.7 Hz, 2H), 7.29 – 7.23 (m, 1H), 6.98 (dd, J = 9.3, 1.7 Hz, 1H), 3.64 (t, J = 6.2 Hz, 3H), 2.64 (t, J = 7.6 Hz, 2H), 1.91 – 1.78 (m, 2H).

Synthesis of 2-(4-bromophenyl)imidazo[1,2-a]pyridine-7-carboxylic acid, 13f

A solution of **13b** (500 mg, 1.5 mmol) in a mixture of H_2O/acetone (1:1) was cooled to 0°C and then 1.0 N NaOH (7.5 mL, 7.5 mmol) was added dropwise. The mixture was warmed to r.t. and stir for 5 hours. The solution was concentrated in vacuo, and the residue was dissolved in H2O. The pH was adjusted to 3 with 0.1 N HCl, and the solid precipitate was collected by filtration and dried to give 13f. White solid. Yield: 67%. ^1H NMR (400 MHz, DMSO-d_6) δ 8.81 (s, 1H), 8.77 (d, J = 7.0 Hz, 1H), 8.23 (s, 1H), 8.00 (d, J = 8.5 Hz, 2H), 7.75 (d, J = 8.5 Hz, 2H), 7.54 (dd, J = 7.0, 1.6 Hz, 1H).

Synthesis of (2-(4-bromophenyl)imidazo[1,2-a]pyridin-7-yl)(1,4,7,10,13-pentaoxa-16-azacyclooctadecan-16-yl)methanone, 39

A Schlenk tube equipped with a magnetic stirring bar was charged with $Pd_2(dba)_3$ (17.4 mg, 0.019 mmol, 2 mol%), Davephos (22.4 mg, 0.057 mmol, 6 mol%) and ^tBuONa (136.7 mg, 1.41 mmol, 1.5 equiv.) followed by anhydrous toluene (3 mL) and the air was replaced by a nitrogen atmosphere. To this mixture, the imidazo[1,2-a]pyridine **13f** (300 mg, 0.95 mmol, 1.0 equiv.), the azacrown ether **8** (0.95 mmol, 1 equiv.) and anhydrous toluene (10 mL) were added at r.t. The tube was sealed and kept under nitrogen atmosphere in a preheated oil bath at 110 °C for 24 h. The mixture was cooled to r.t., filtered through a celite pad, and concentrated in vacuo. The crude product was dissolved in chloroform and the impurities were precipitated with hexane. The solvent was removed under reduced pressure to obtain a brown oil. Yield: n.d.

Synthesis of (2-(4-bromophenyl)imidazo[1,2-a]pyridin-7-yl)methanol, 13g

The compound **13b** (300 mg, 0.9 mmol, 1 eq.) were dissolved in dry THF (10 mL) in a dried flask under argon atmosphere. Then, a solution of $LiAlH_4$ (2.5 M) in THF (2.1 mmol, 2.3 eq.) was added dropwise at 0°C. The mixture was stirred at room temperature for 2 h and was quenched adding an excess of MeOH in an ice bath. The solution was concentrated, dissolved in DCM and washed with $NaHCO_3$ (sat). White off solid. Yield: 48%. ^{1}H NMR (400 MHz, CD_3OD) δ 8.33 – 8.24 (m, 1H), 8.10 (s, 1H), 7.75 (d, J = 8.6 Hz, 1H), 7.55 – 7.48 (m, 1H), 7.46 (s, 1H), 6.84 (dd, J = 6.8, 1.8 Hz, 1H), 4.61 (d, J = 1.4 Hz, 2H).

Synthesis of 6-bromo-2-(4-bromophenyl)imidazo[1,2-a]pyridine, 13h
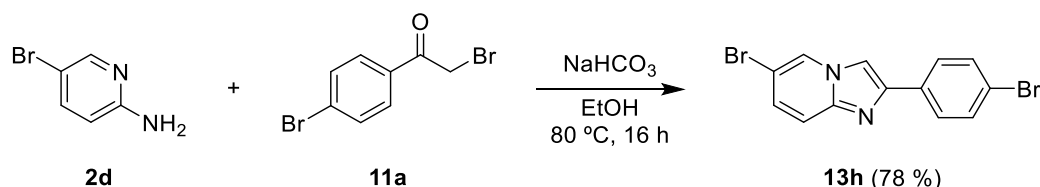
A mixture of 2-amino-5-bromopyridine **2d** (2.3 g, 13.5 mmol, 1.25 eq), bromine derivate **11** (3 g, 10.8 mmol) and sodium bicarbonate (1.36 g, 16.2 mmol, 1.5 eq) in ethanol (35 mL) were mixed in a 100 mL round bottomed flask stirred at 78 ºC 12 h. The reaction mixture was cooled to r.t. and filtered, obtaining a white solid, which was washed with 2 mL of cold chloroform and dried in vacuo. ^{1}H NMR (400 MHz, $CDCl_3$) δ 8.30 (dd, J = 1.9, 0.9 Hz, 1H), 7.83 (d, J = 8.8 Hz, 3H), 7.63 – 7.58 (m, 2H), 7.55 (d, J = 9.5 Hz, 1H), 7.31 – 7.25 (m, 2H). ^{13}C NMR (101 MHz, $CDCl_3$) δ 145.47, 144.10, 132.12, 131.92, 128.46, 127.57, 125.56, 122.28, 118.11, 108.32, 107.23.

Synthesis of 16-(2-(4-bromophenyl)imidazo[1,2-a]pyridin-6-yl)-1,4,7,10,13-pentaoxa-16-azacyclooctadecane, 40
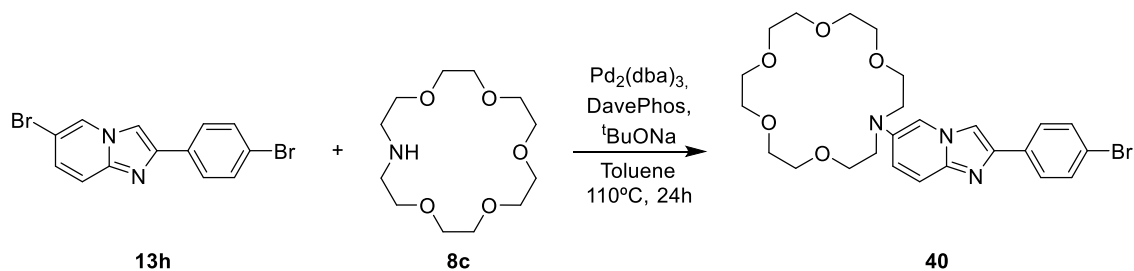
A Schlenk tube equipped with a magnetic stirring bar was charged with $Pd_2(dba)_3$ (17.4 mg, 0.019 mmol, 2 mol%), Davephos (22.4 mg, 0.057 mmol, 6 mol%) and ^tBuONa (136.7 mg, 1.41 mmol, 1.5 equiv.) followed by anhydrous toluene (3 mL) and the air was replaced by a nitrogen atmosphere. To this mixture, the imidazo[1,2-a]pyridine **13h** (334 mg, 0.95 mmol, 1.0 equiv.), the azacrown ether **8** (0.95 mmol, 1 equiv.) and anhydrous toluene (10 mL) were added at r.t. The tube was sealed and kept under nitrogen atmosphere in a preheated oil bath at 110 °C for 24 h. The mixture was cooled to r.t., filtered through a celite pad, and concentrated in vacuo. The crude product was dissolved in chloroform and the impurities were precipitated with hexane. The solvent was removed under reduced pressure to obtain a brown oil. Yield: n.d.

Synthesis of 6-bromo-2-(4-vinylphenyl)imidazo[1,2-a]pyridine, 42
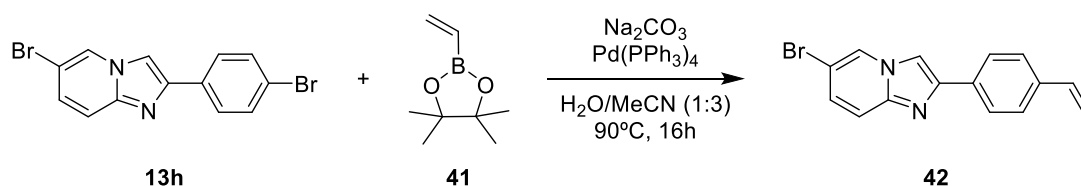
A mixture of **13h** (300 mg, 0.85 mmol, 1 equiv.), boronic ester 41 (247 mg, 1.1 mmol, 1.3 equiv.), Na_2CO_3 (135 mg, 1.28 mmol, 1.5 equiv.), and $Pd(PPh_3)_4$ (98 mg, 0.085 mmol, 0.1 equiv.) in solution of 3 mL of H_2O and 3 mL of DMF was heated at 90 °C for 6 h. The reaction mixture was allowed to cool, diluted with EtOAc, washed with brine (2 times), and then the organic phase was dried over anhydrous sodium sulfate, filtered and concentrated. Yield: n.d.

IV. NMR, UV-VIS AND EMISSION SPECTRA

2-(pyridin-2-yl)imidazo[1,2-a]pyridine, 3.
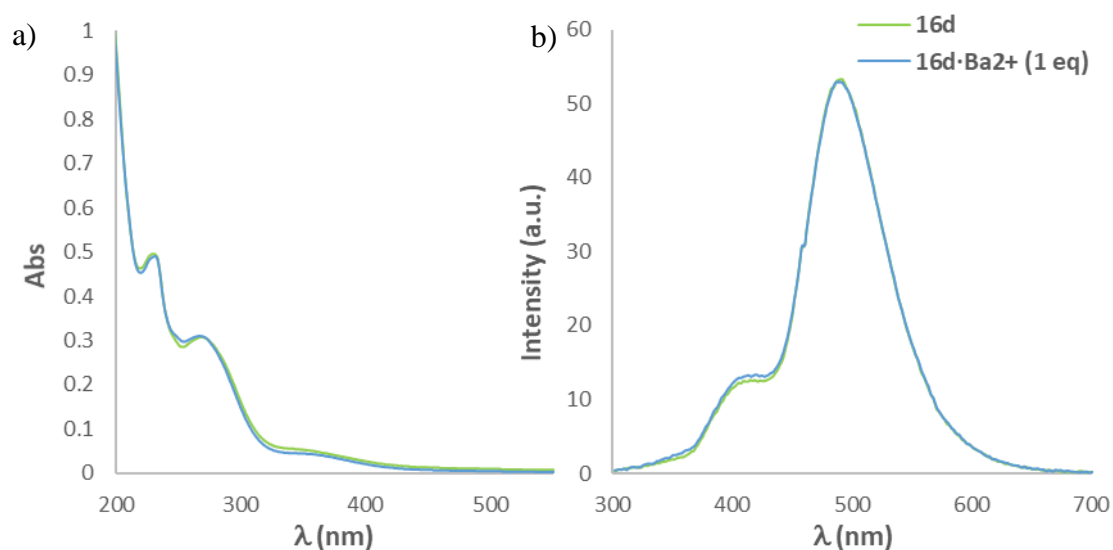
¹H-NMR (CDCl₃)
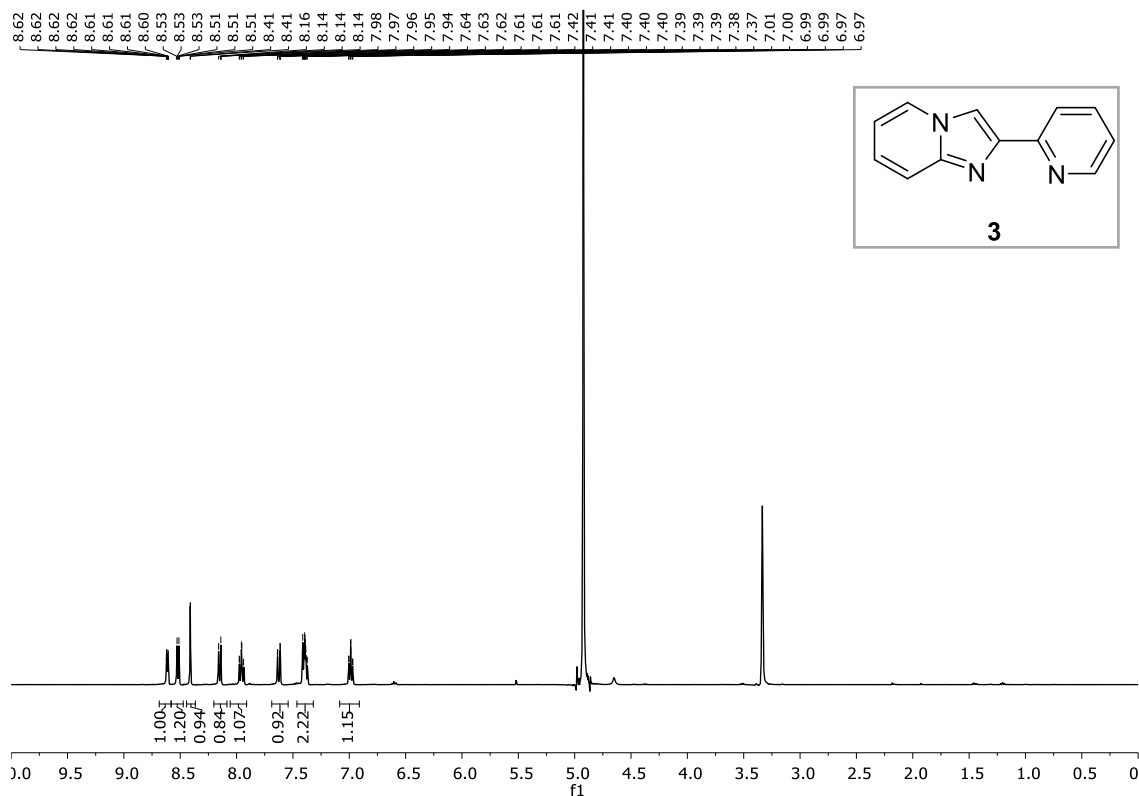
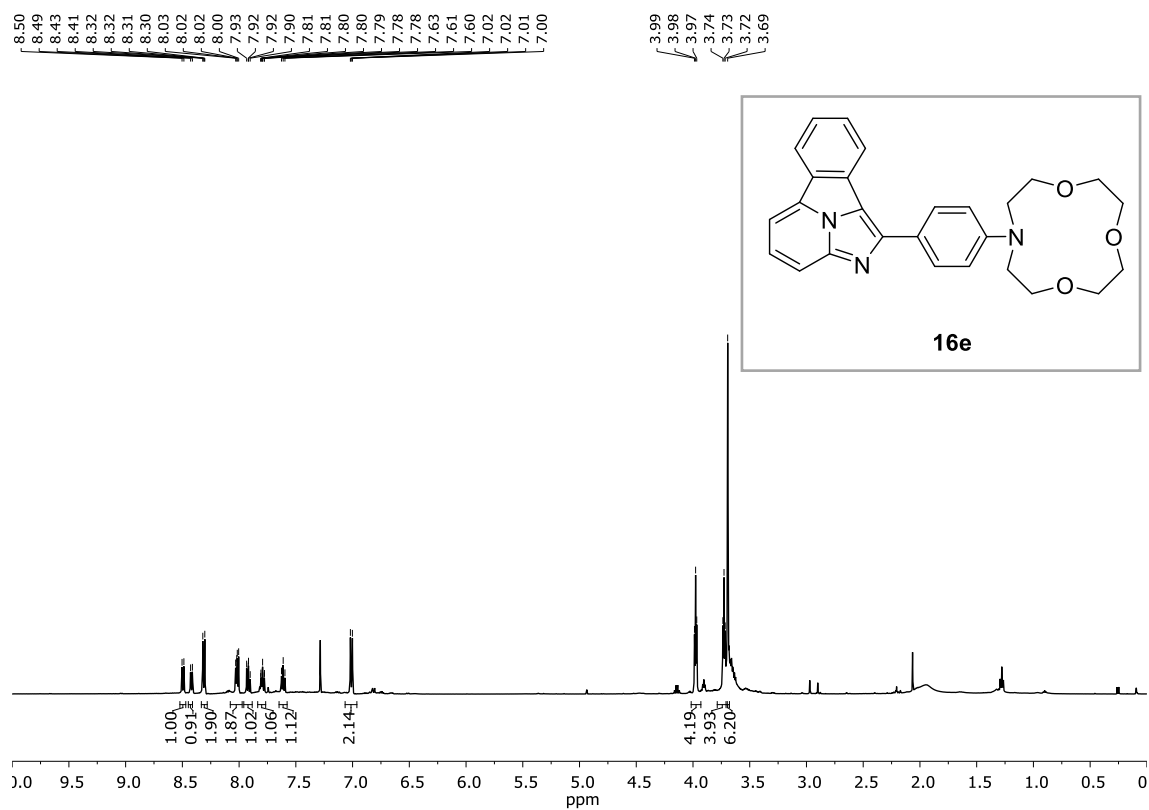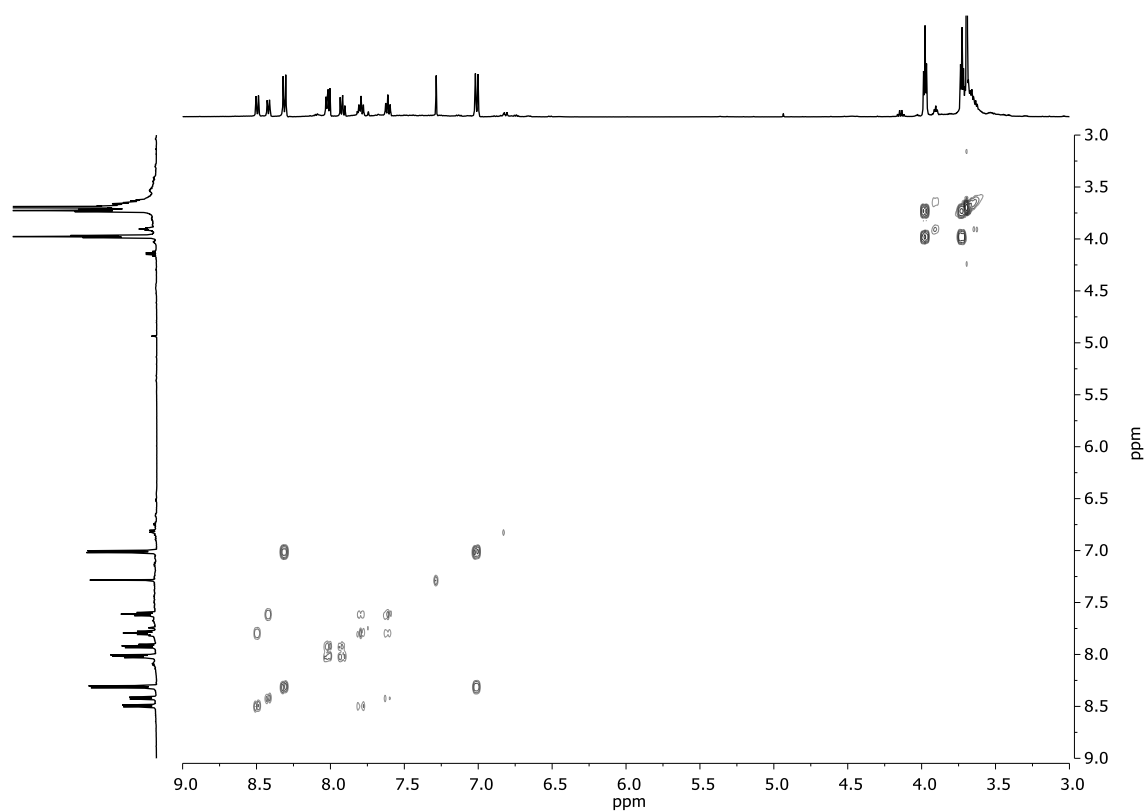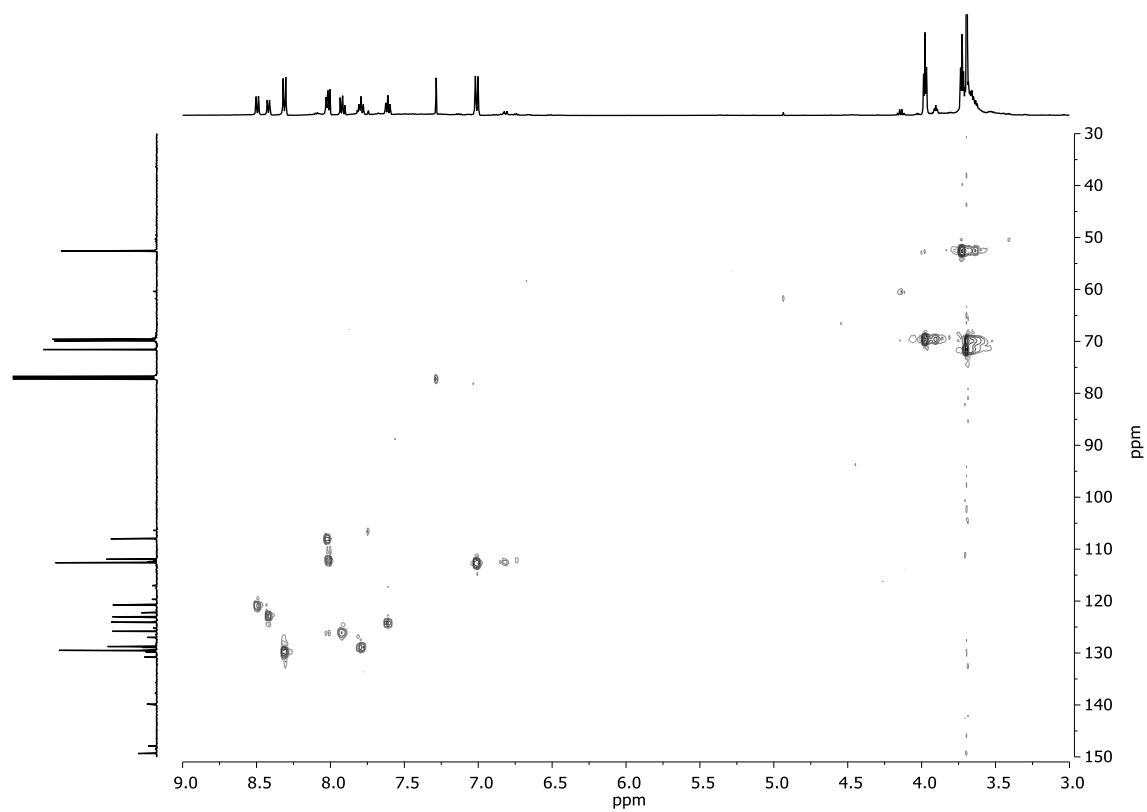## UV-VIS (a) and FS (b) (MeCN)
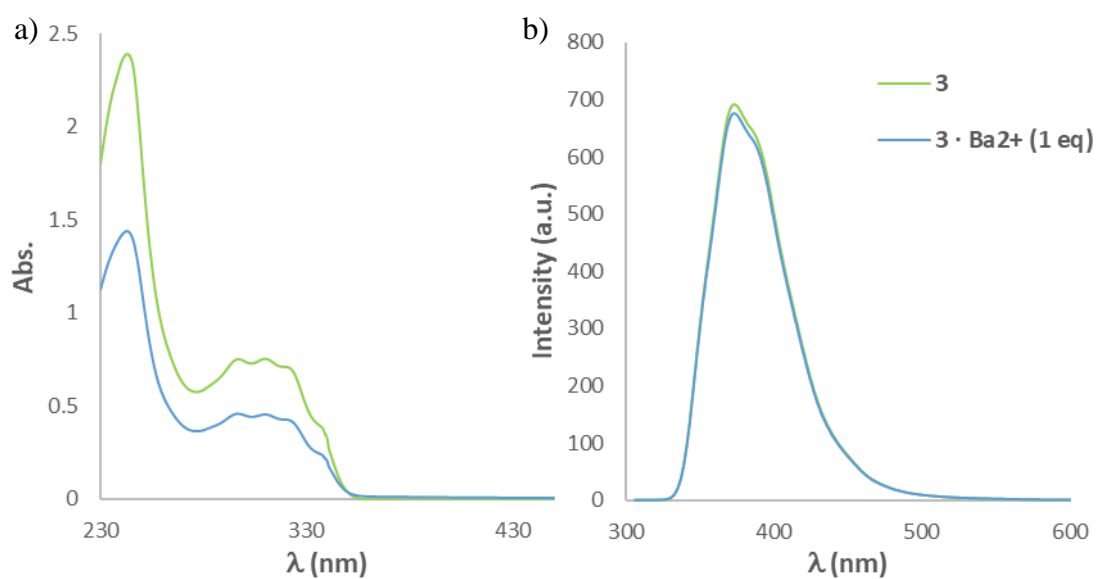
Figure 92. - a) Absorbance spectra for compound **3** and **3·Ba²⁺** (1eq), $5 \cdot 10^{-5}$ M in MeCN, r.t. b) Fluorescence spectra for compound **3** and **3·Ba²⁺** (1eq), $5 \cdot 10^{-5}$ M in MeCN, r.t., λ_{exc} = 250 nm.
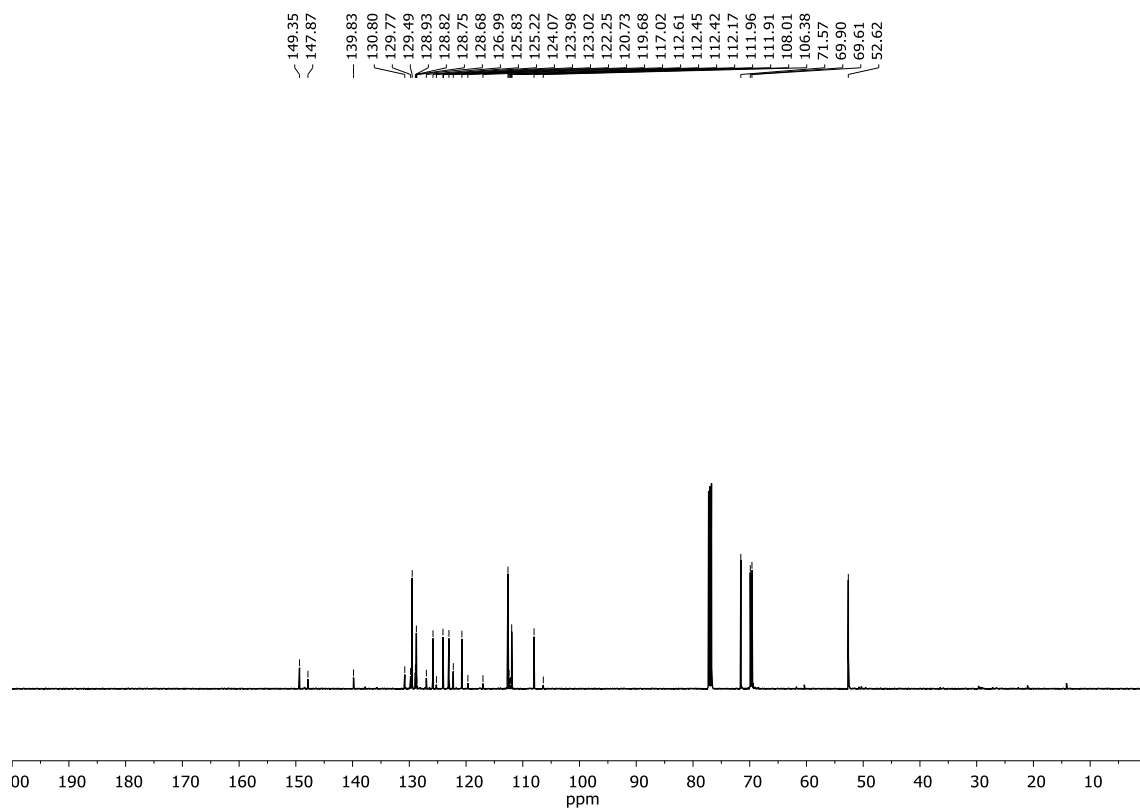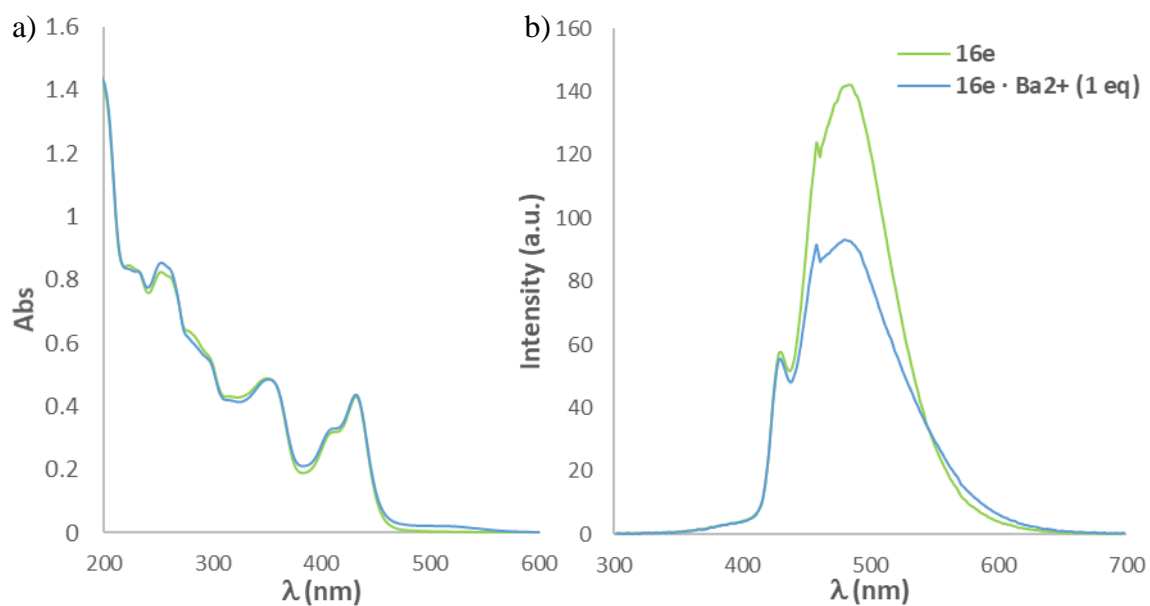
Synthesis of 1-(pyridin-2-yl)benzo[a]imidazo[5,1,2-cd]indolizine, 5

^{1}H-NMR (CDCl$_3$)
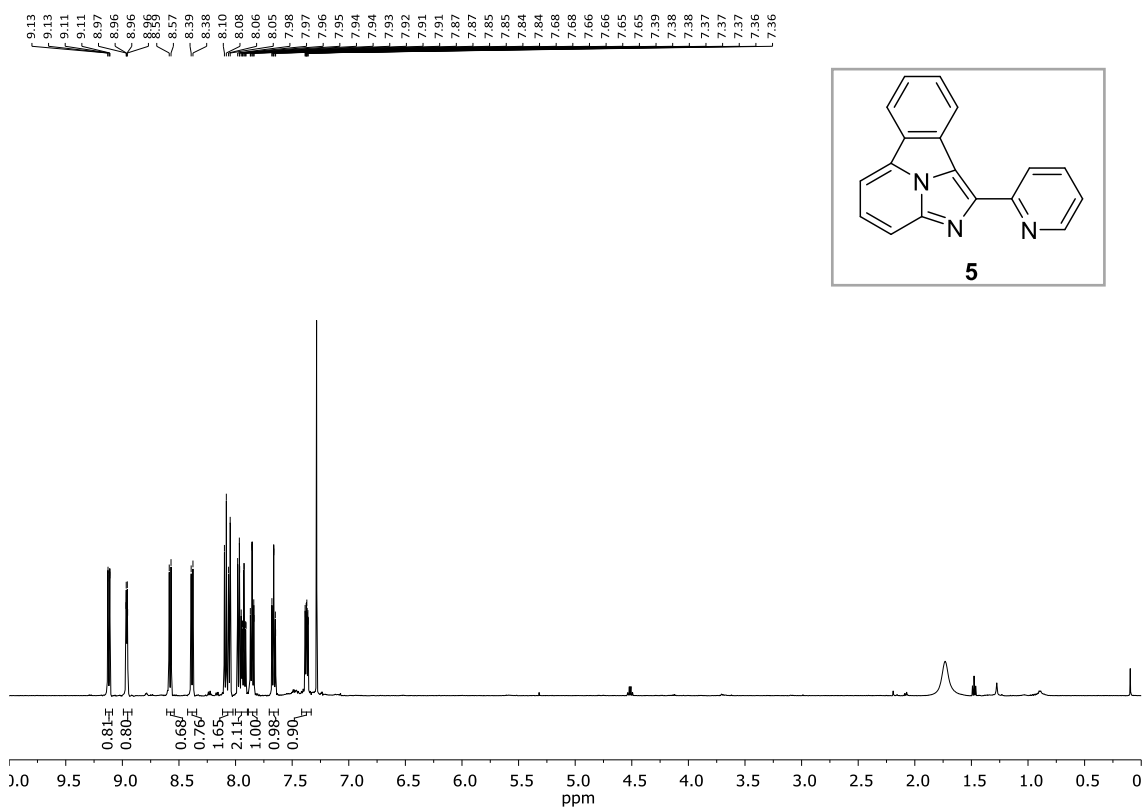
g-COSY (CDCl$_3$)
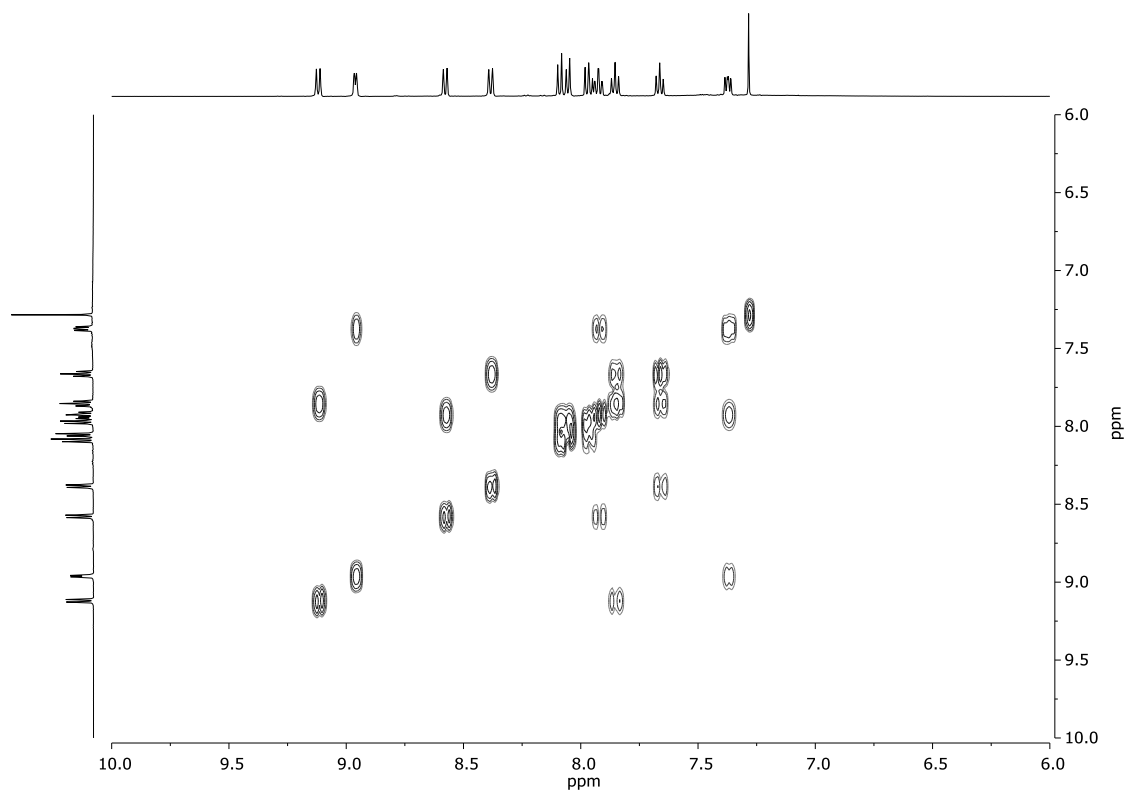
g-HSQC (CDCl₃)
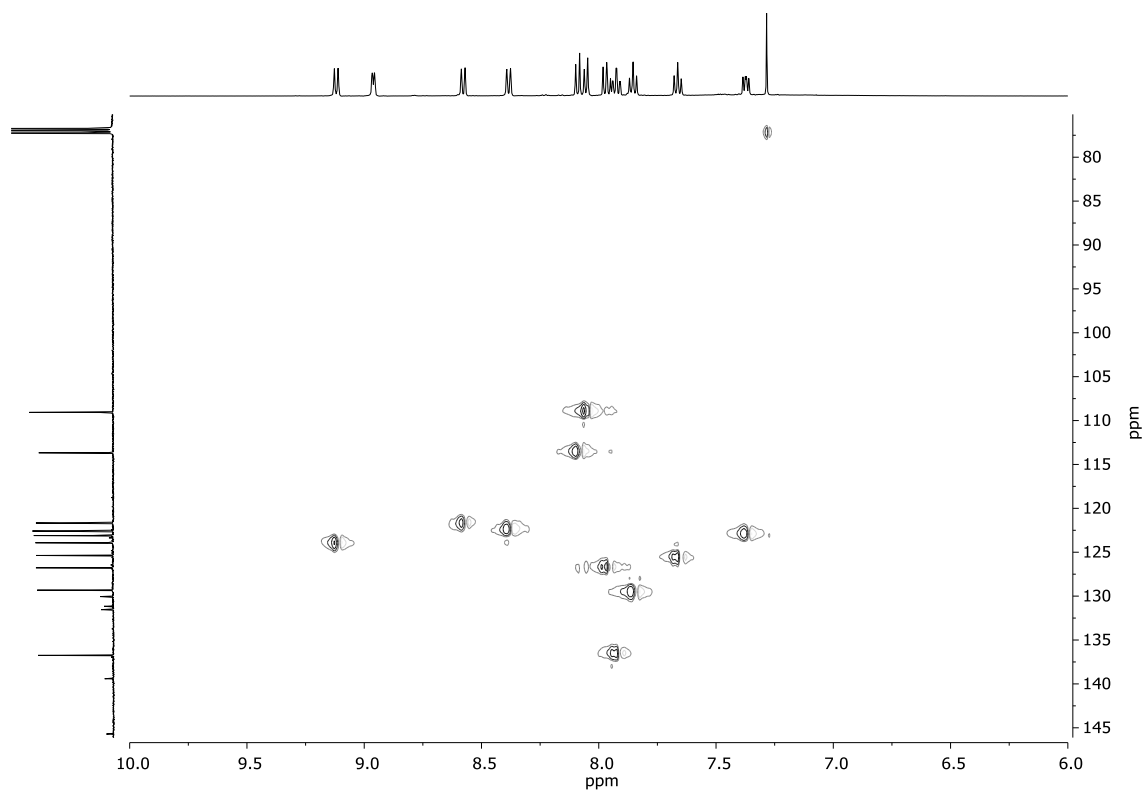
¹³C-NMR (CDCl₃)
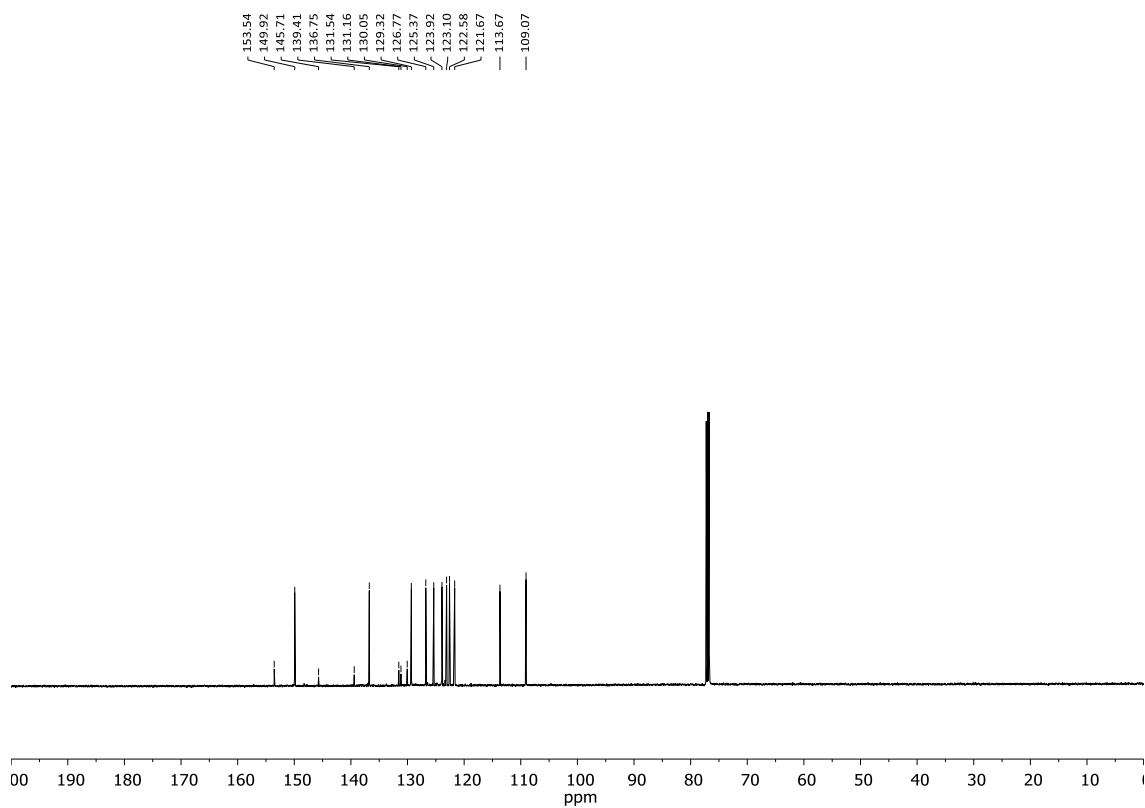
UV-VIS (a) and FS (b) (MeCN)
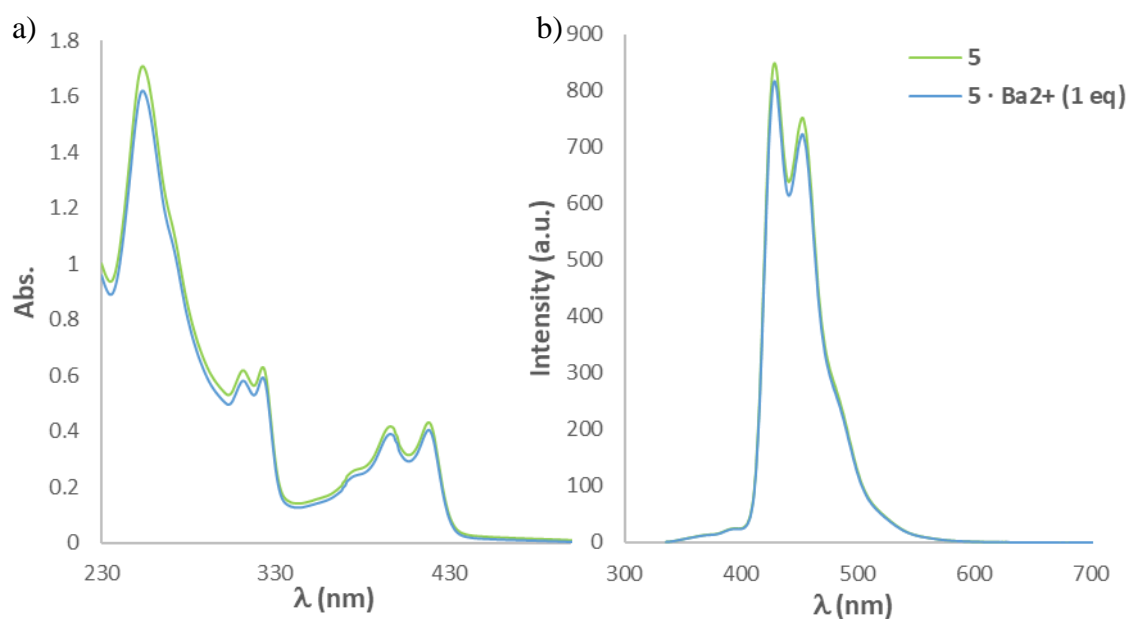
Figure 93.- a) Absorbance spectra for compound **5** and **5·Ba²⁺** (1eq), 5·10⁻⁵ M in MeCN, r.t. b) Fluorescence spectra for compound **5** and **5·Ba²⁺** (1eq), 5·10⁻⁵ M in MeCN, r.t., λ_{exc} = 254 nm.

2-(4-chlorophenyl)imidazo[1,2-a]pyridine, 7

¹H-NMR (Acetone-d₆)
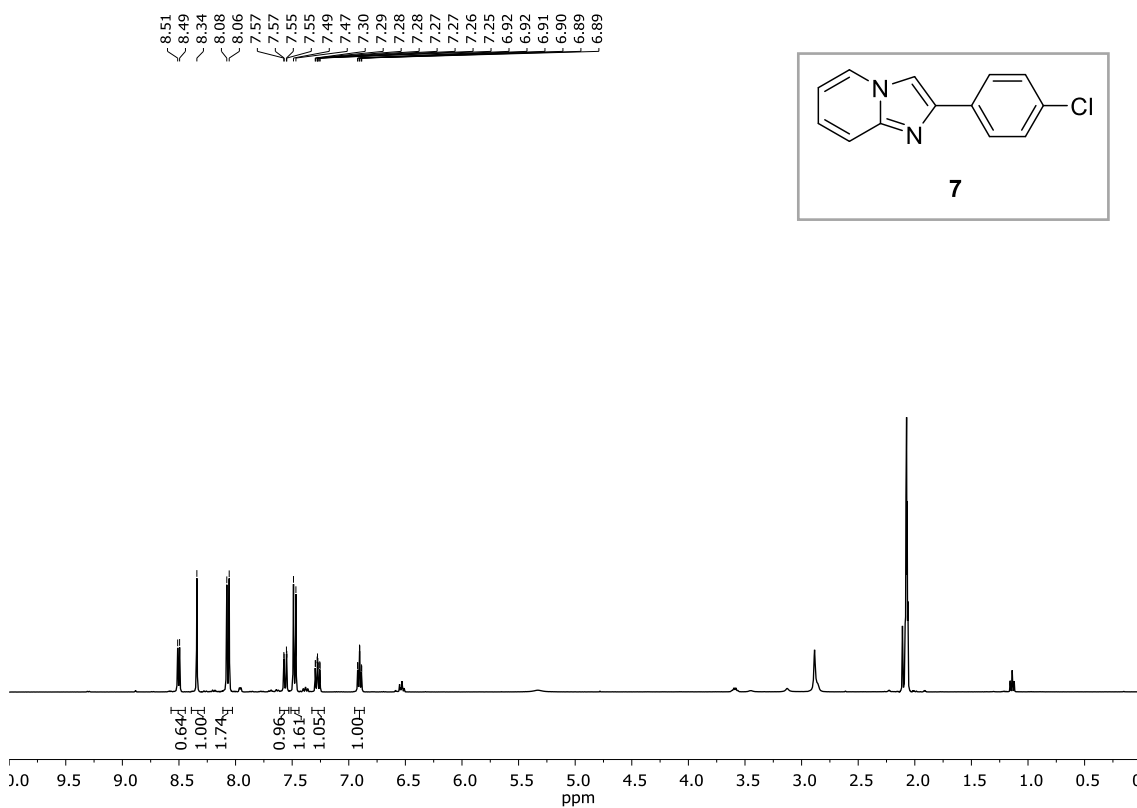
1-(4-(1,4,7,10,13-pentaoxa-16-azacyclooctadecan-16-yl)phenyl)ethan-1-one, 10

¹H-NMR (CDCl₃)
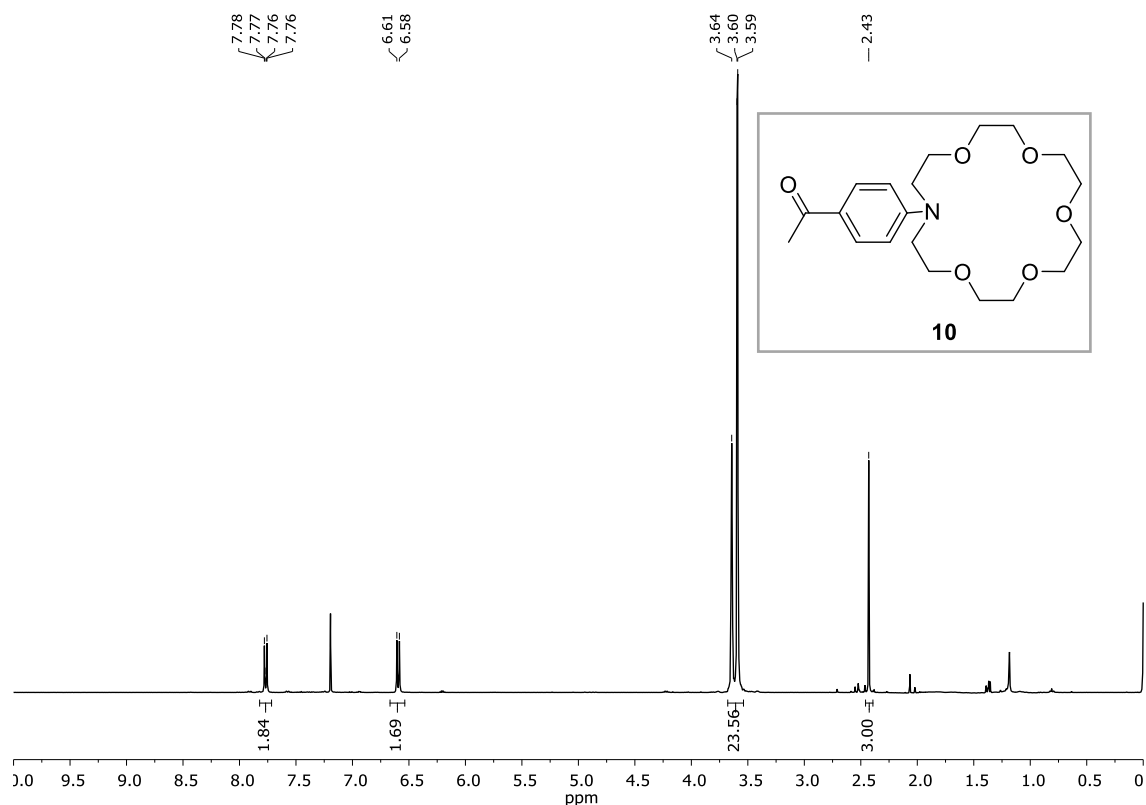
2-(4-bromophenyl)imidazo[1,2-a]pyridine, 13a

¹H-NMR (CDCl₃)
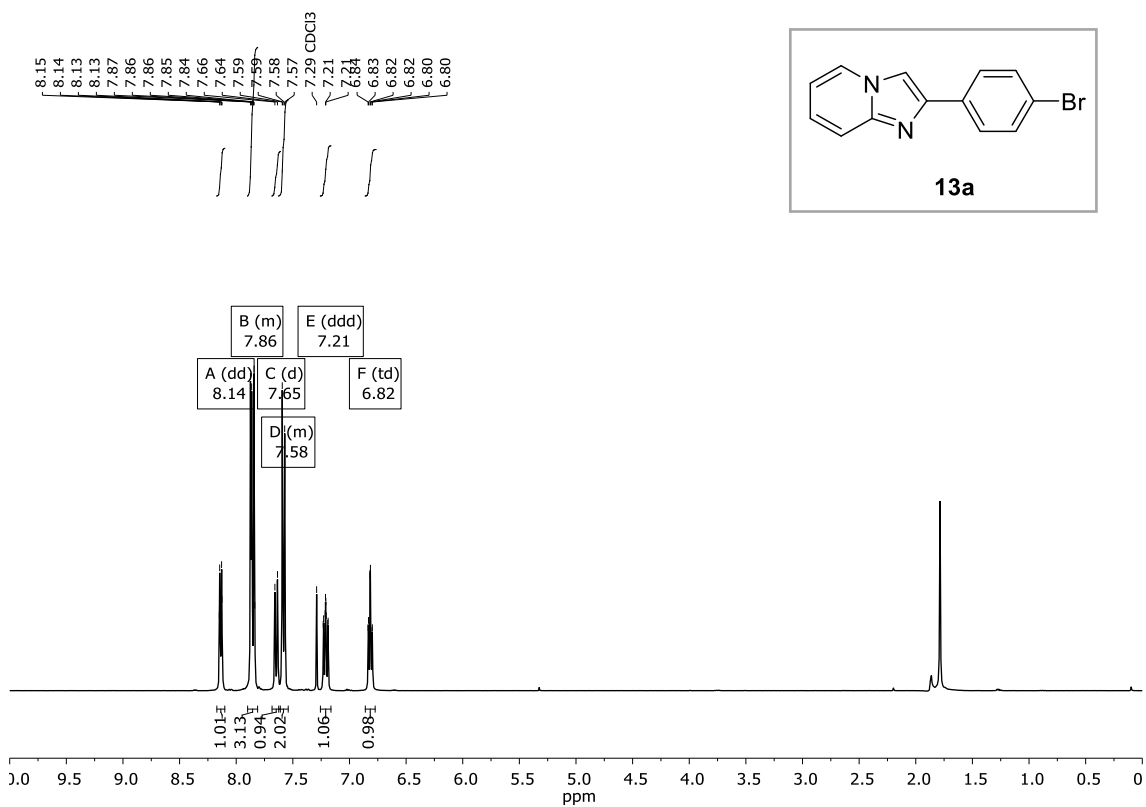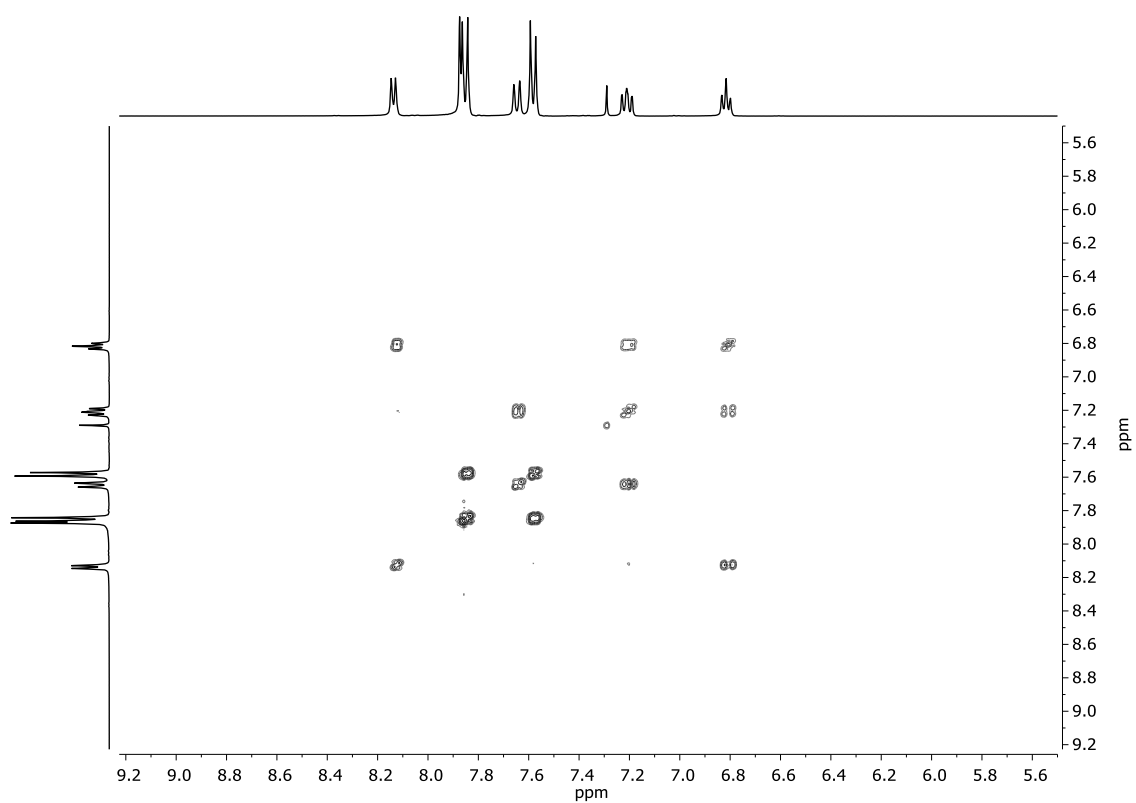
g-COSY (CDCl₃)

g-HSQC (CDCl₃)

^{13}C-NMR (CDCl$_3$)

145.69
144.64

132.71
131.79
127.50
125.57
124.90
121.82
117.53
112.58
108.17

DEPT-135 (CDCl$_3$)

131.79
127.50
125.58
124.91

117.53
112.58
108.18
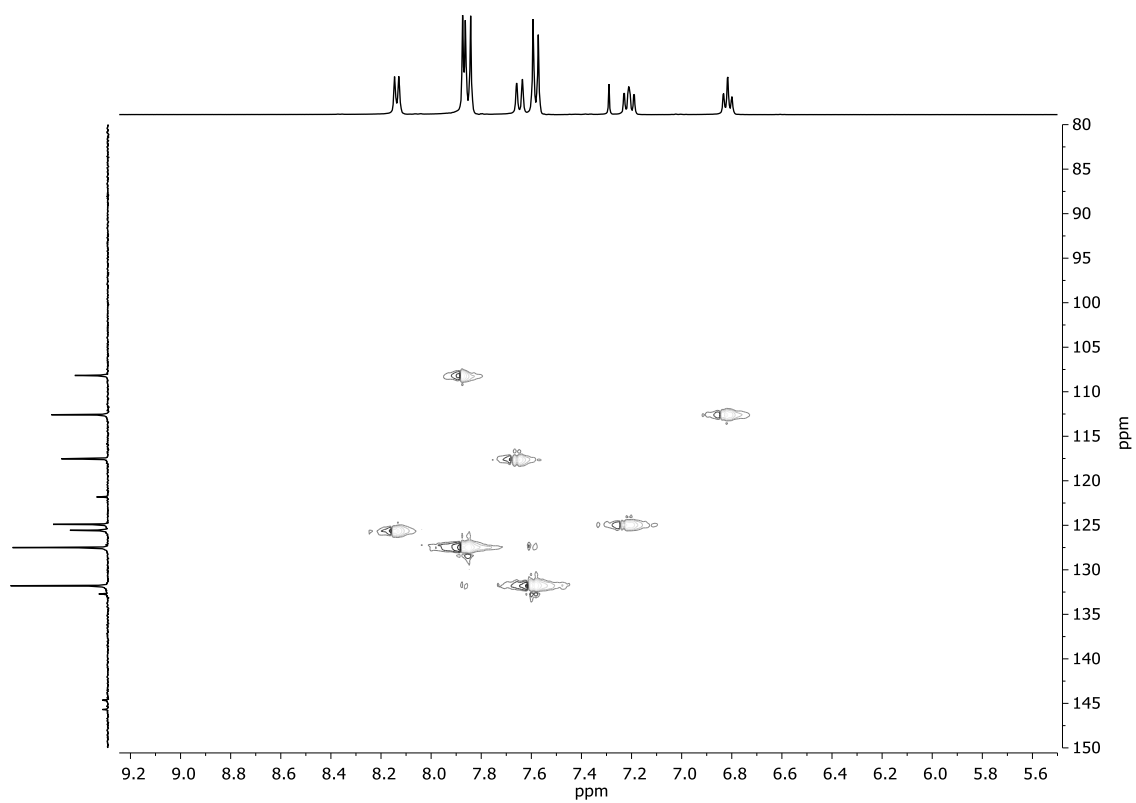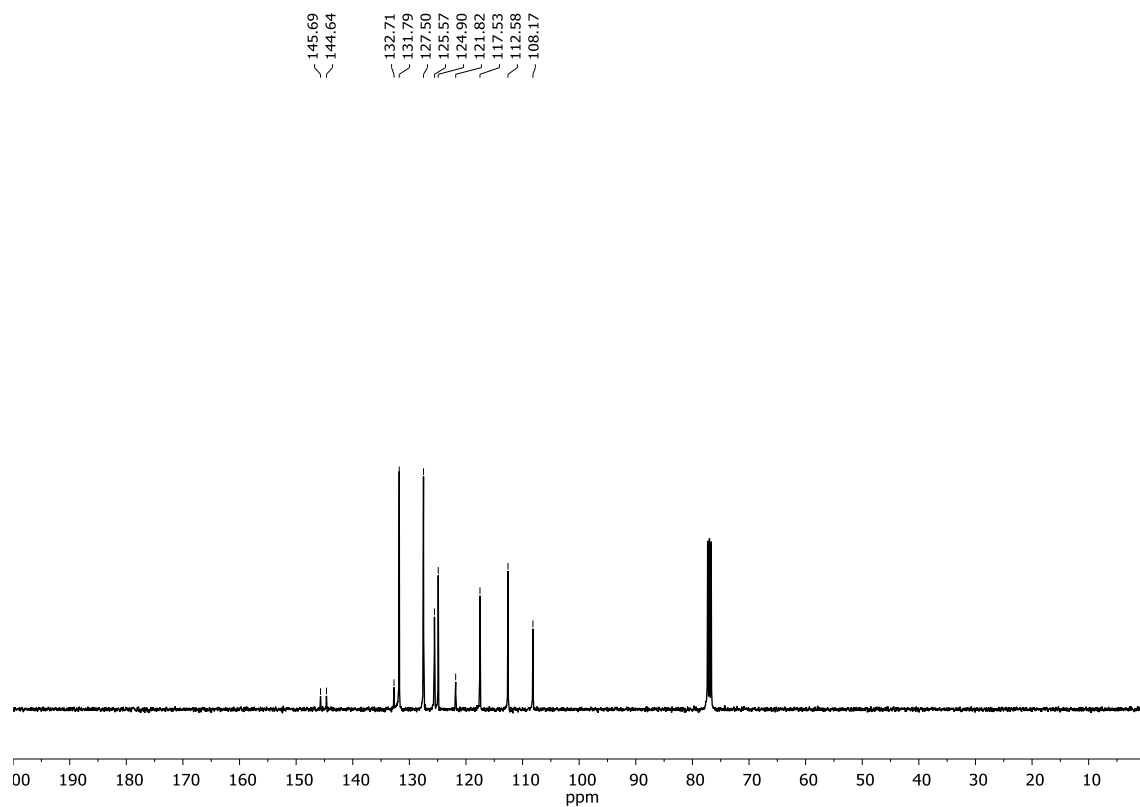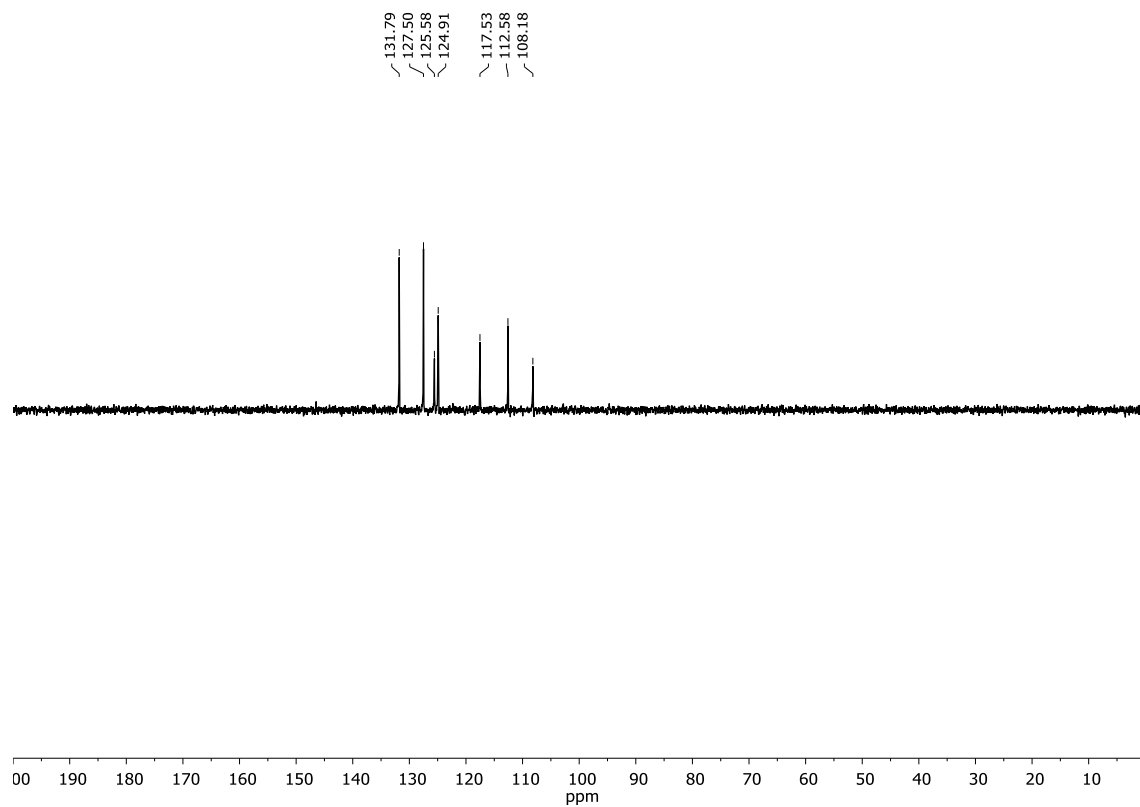
Methyl 2-(4-bromophenyl)imidazo[1,2-a]pyridine-7-carboxylate, 13b

^{1}H-NMR (CDCl$_3$)
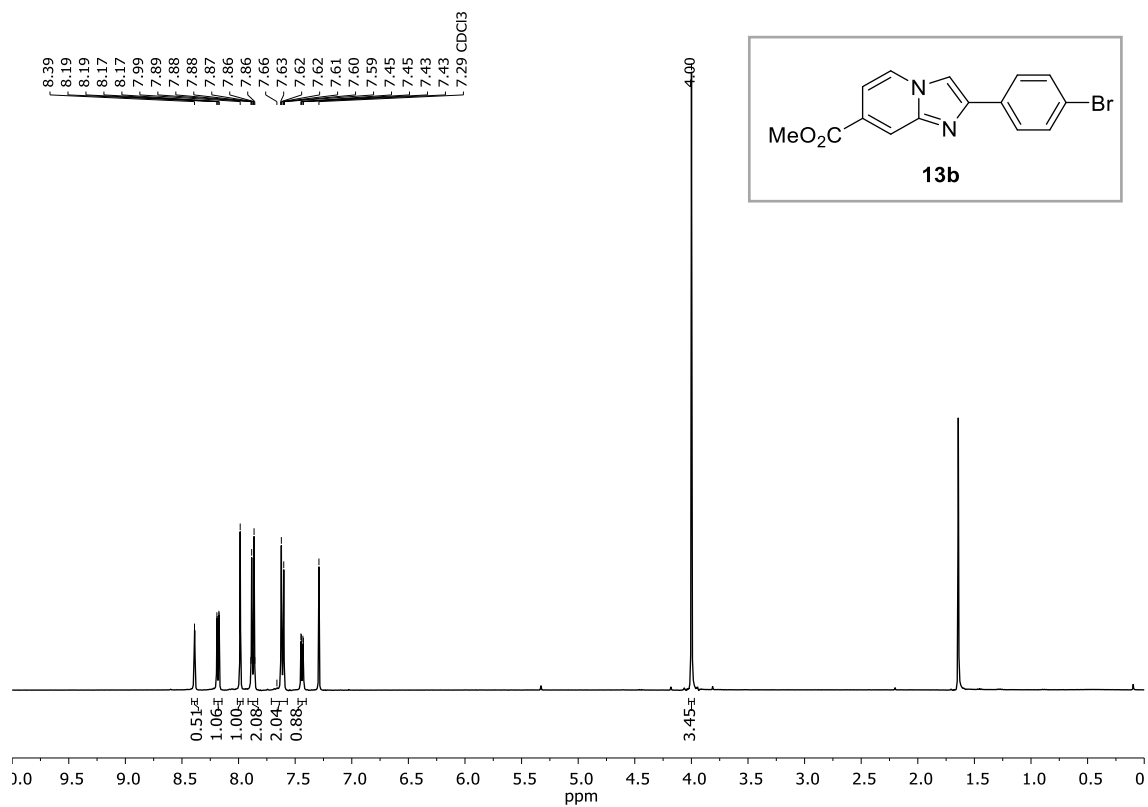
g-COSY (CDCl$_3$)
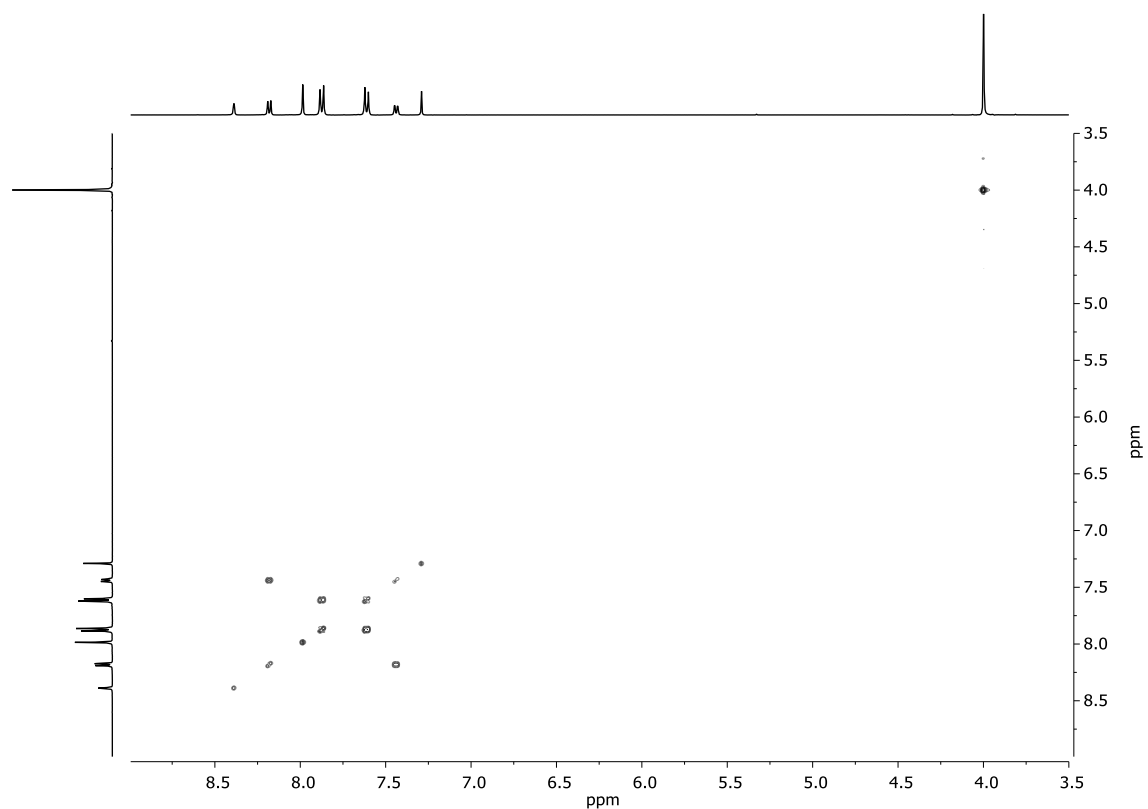
g-HSQC (CDCl₃)

¹³C-NMR (CDCl₃)

135-DEPT (CDCl₃)

132.16
127.86
125.26
120.35
112.18
109.85
52.82

00 190 180 170 160 150 140 130 120 110 100 90 80 70 60 50 40 30 20 10
ppm
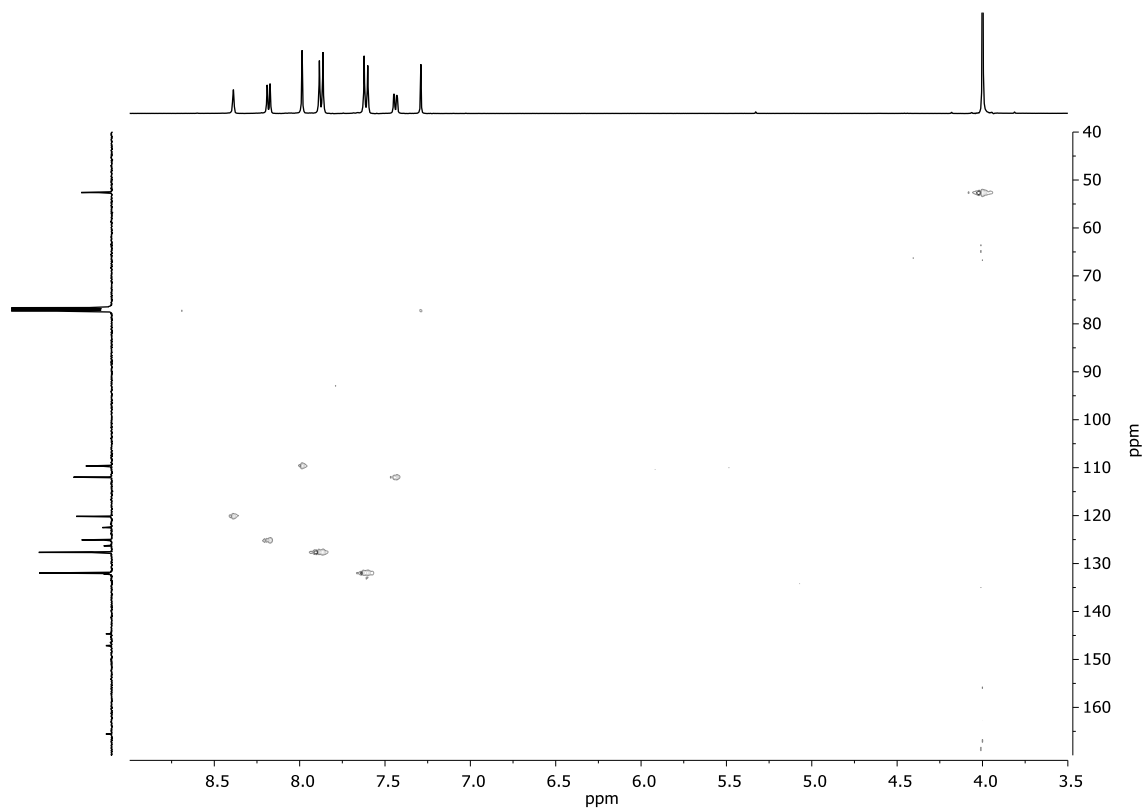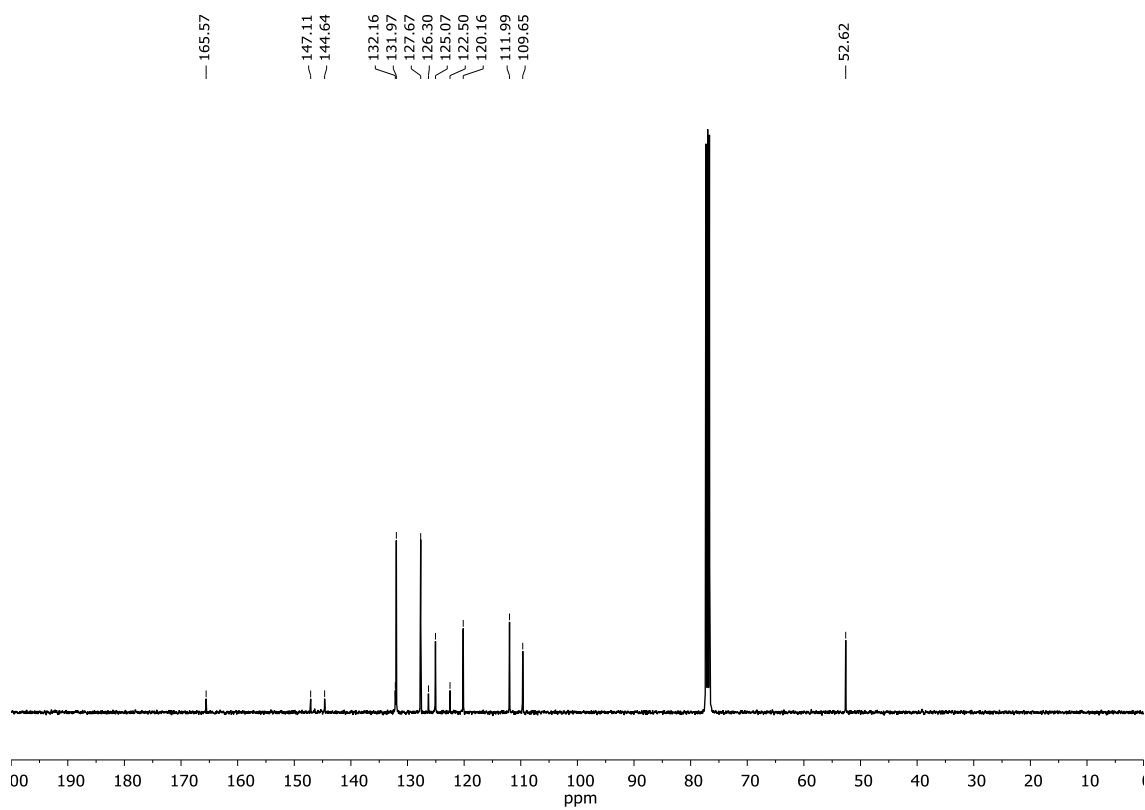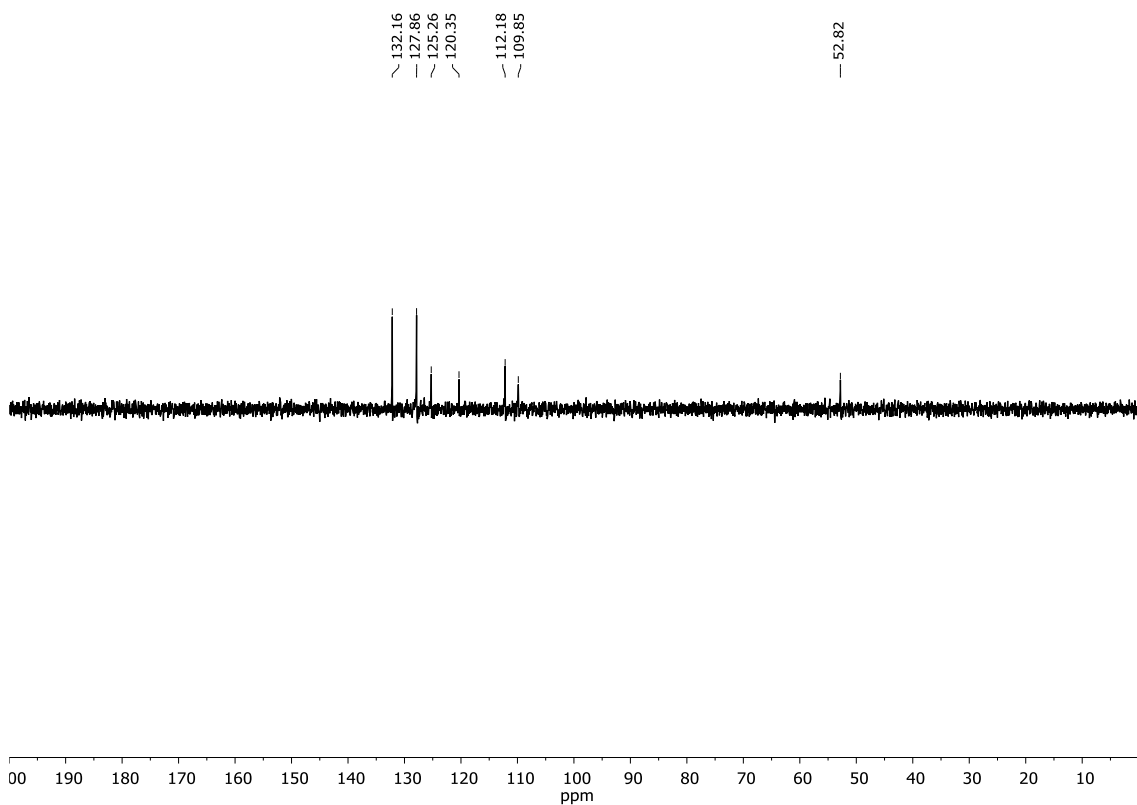
2-(4-bromophenyl)imidazo[1,2-a]pyrimidine, 13c

¹H-NMR (CDCl₃)

8.58
8.57
8.57
8.56
8.46
8.45
8.44
8.44
7.94
7.93
7.92
7.92
7.84
7.61
7.61
7.59
7.59
6.91
6.90
6.89
6.88

13c

0.90
1.05
2.04
1.00
1.99
0.96

).0 9.5 9.0 8.5 8.0 7.5 7.0 6.5 6.0 5.5 5.0 4.5 4.0 3.5 3.0 2.5 2.0 1.5 1.0 0.5 0
ppm

g-COSY (CDCl₃)

g-HSQC (CDCl₃)

^{13}C-NMR (CDCl$_3$)

150.10
148.73
146.36
132.91
132.08
131.92
127.79
122.67
108.93
106.17
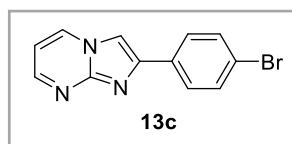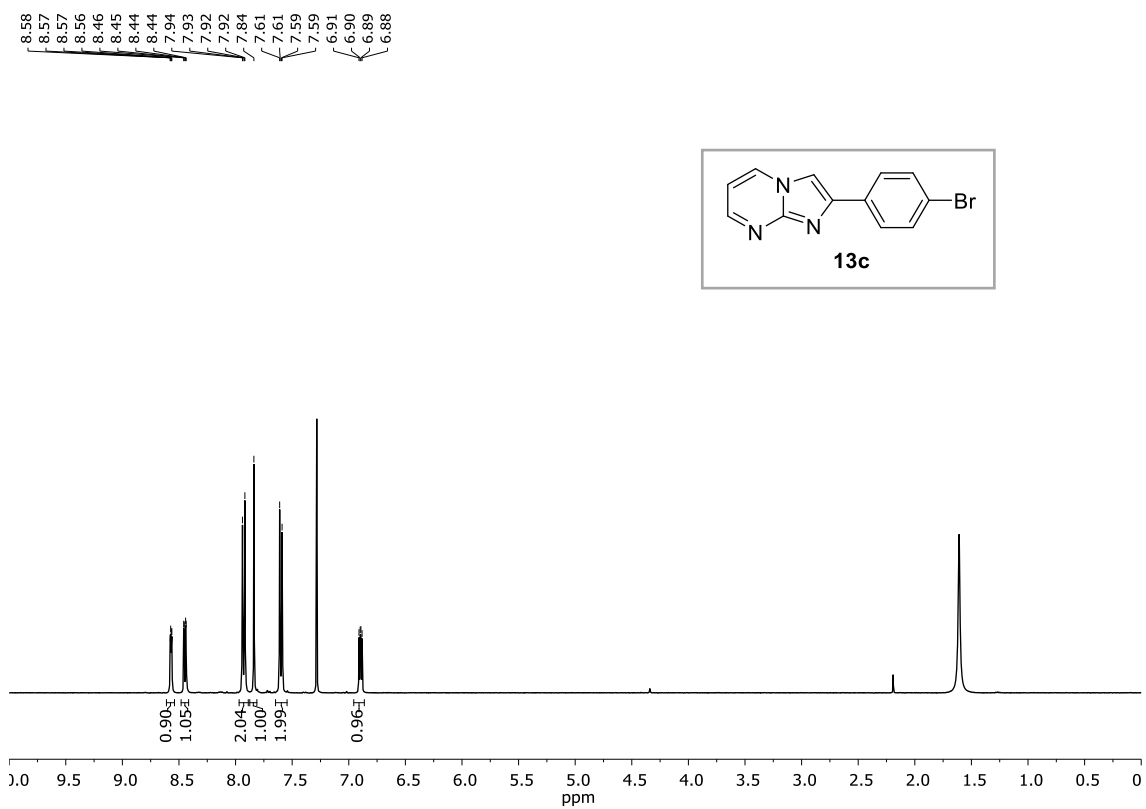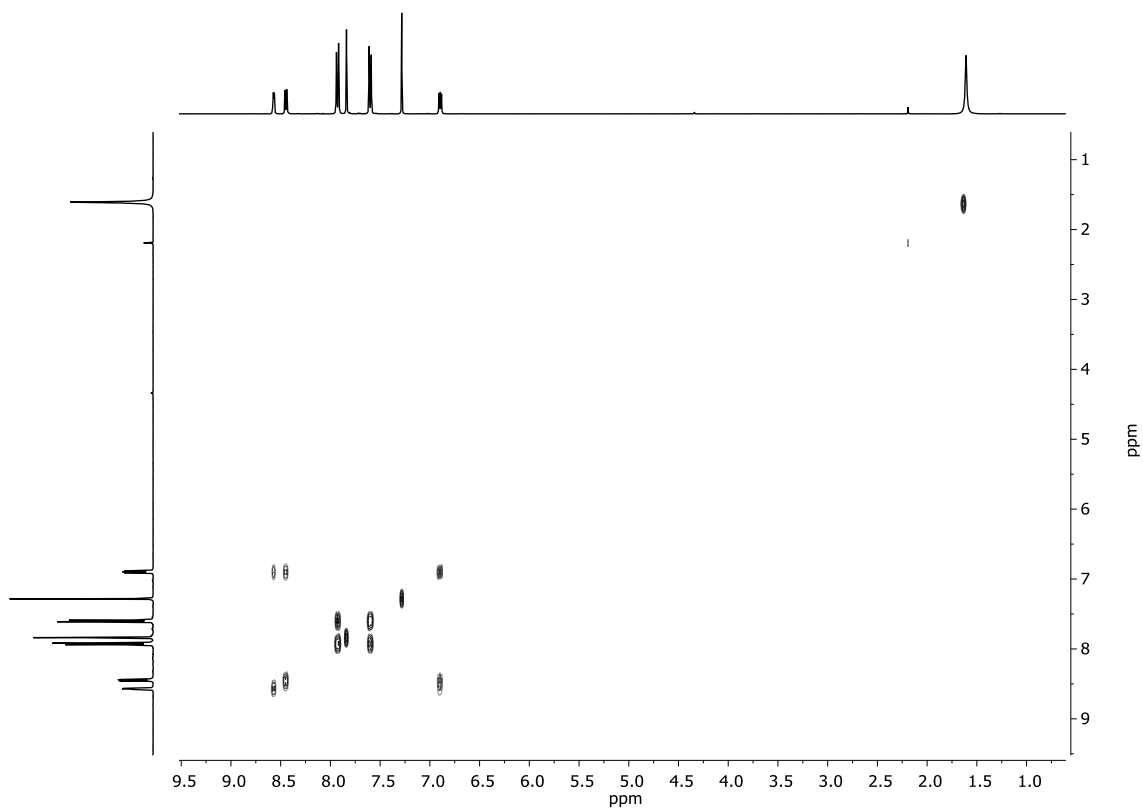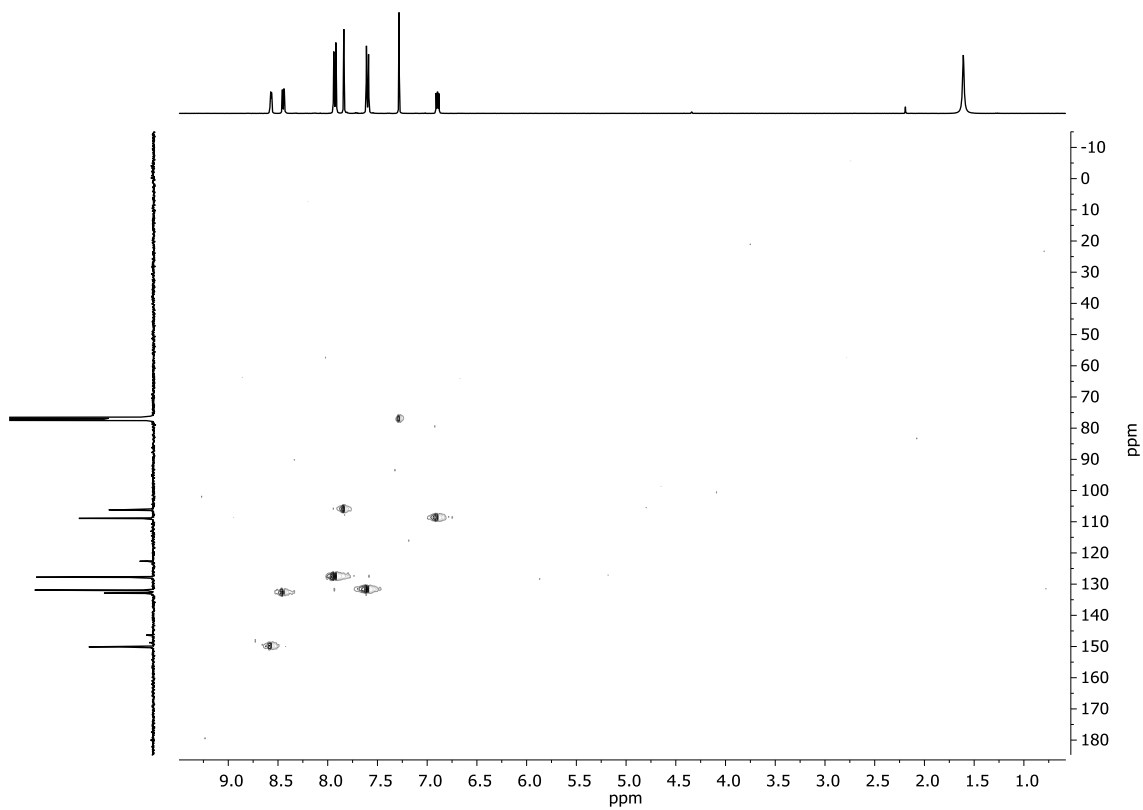
135-DEPT (CDCl$_3$)
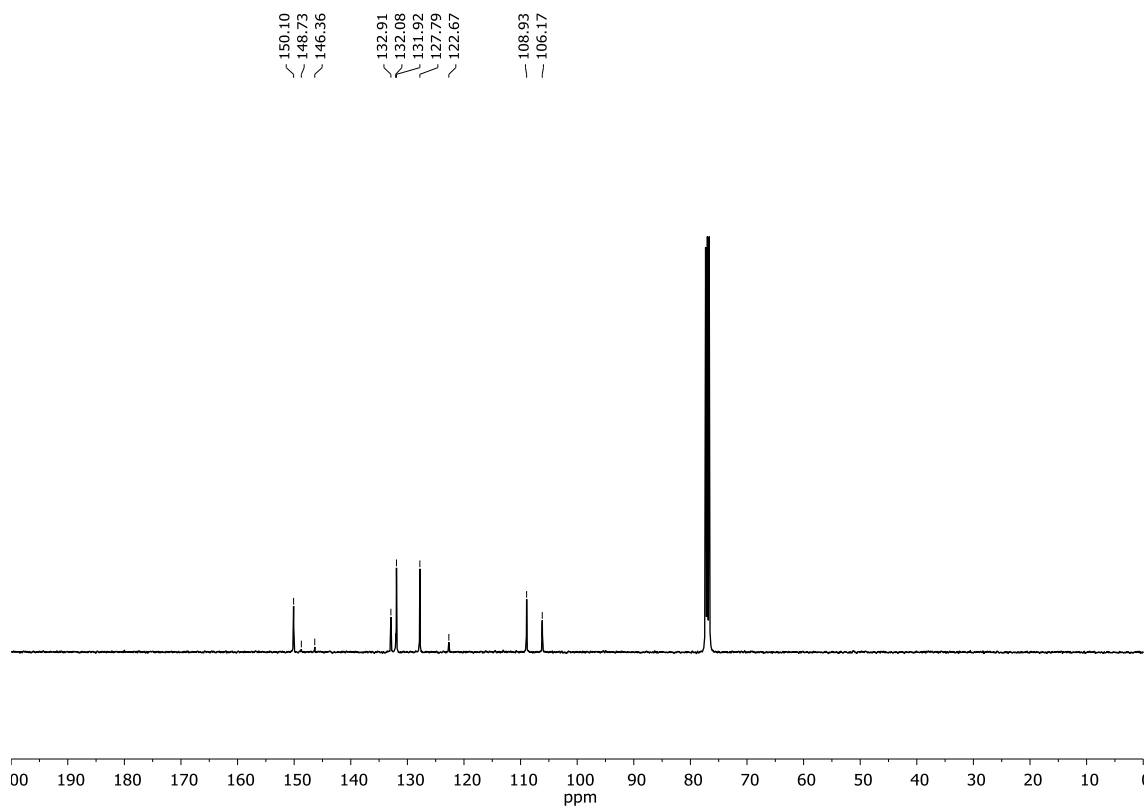
150.27
133.08
132.08
127.94
109.10
106.33
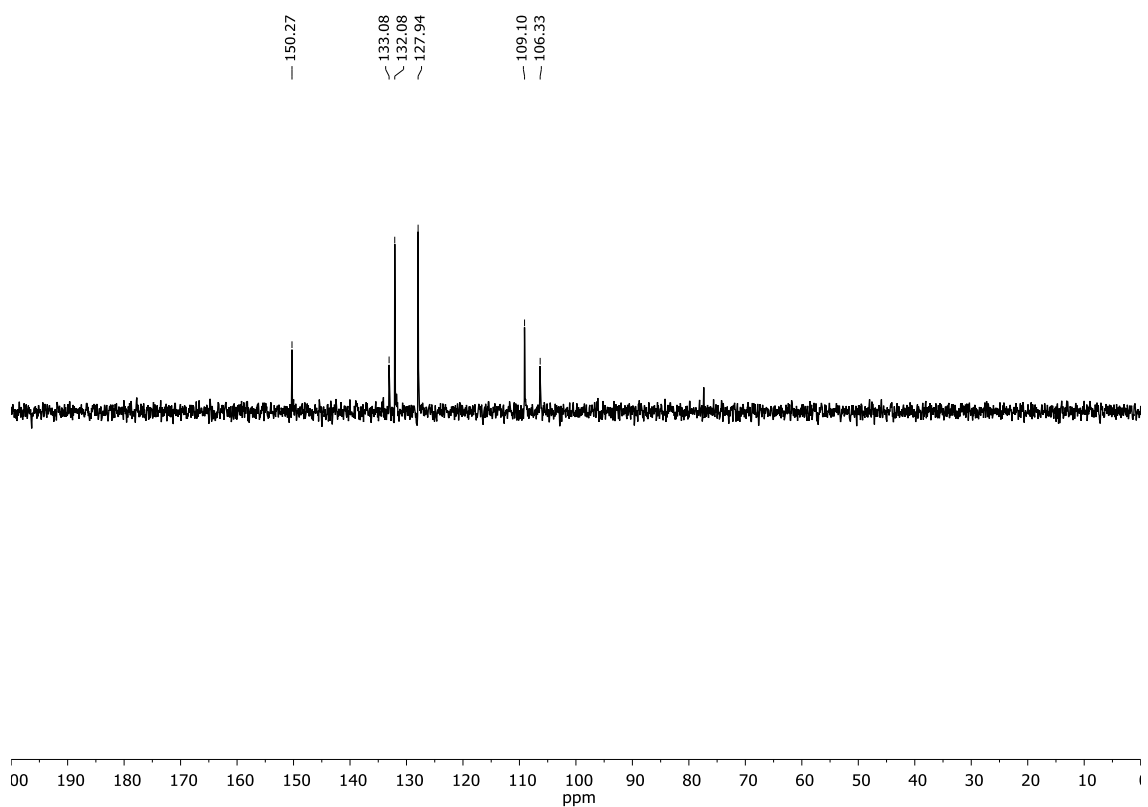
2-(bromomethyl)imidazo[1,2-a]pyridine, 13d
^{1}H-NMR (CDCl$_3$)
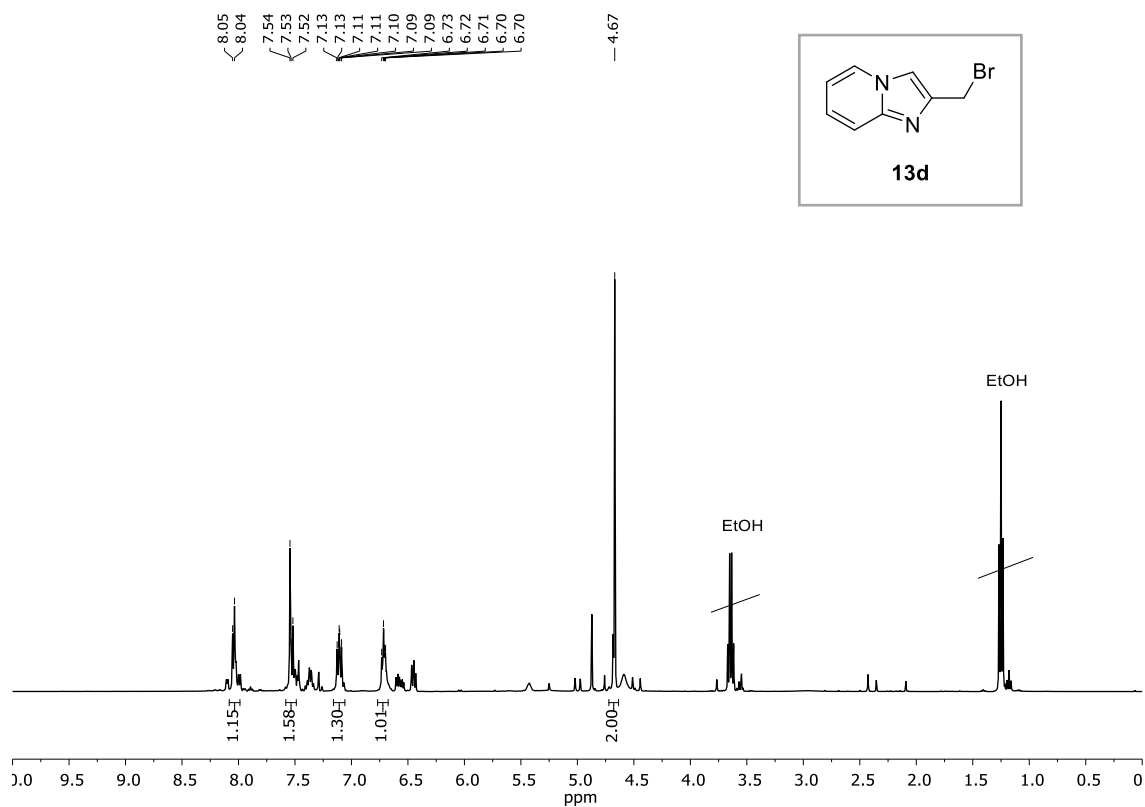
16-(4-(imidazo[1,2-a]pyridin-2-yl)phenyl)-1,4,7,10,13-pentaoxa-16-azacyclooctadecane, 14a
^{1}H-NMR (CDCl$_3$)
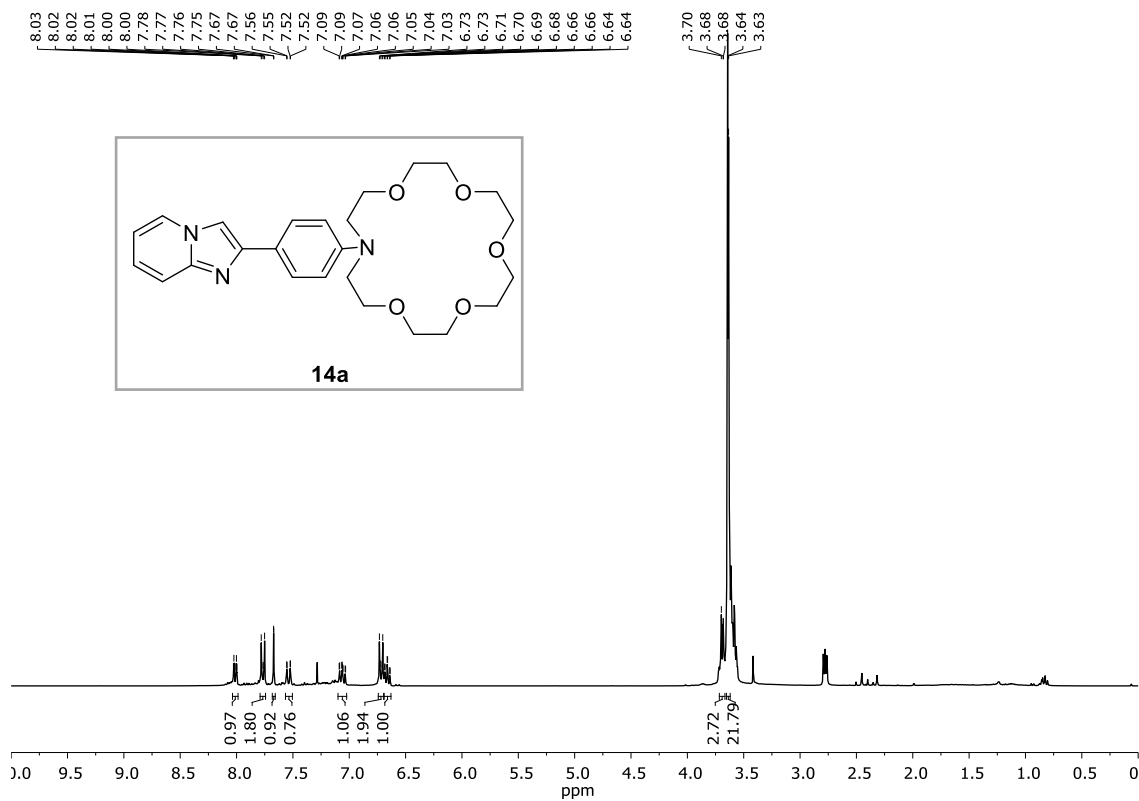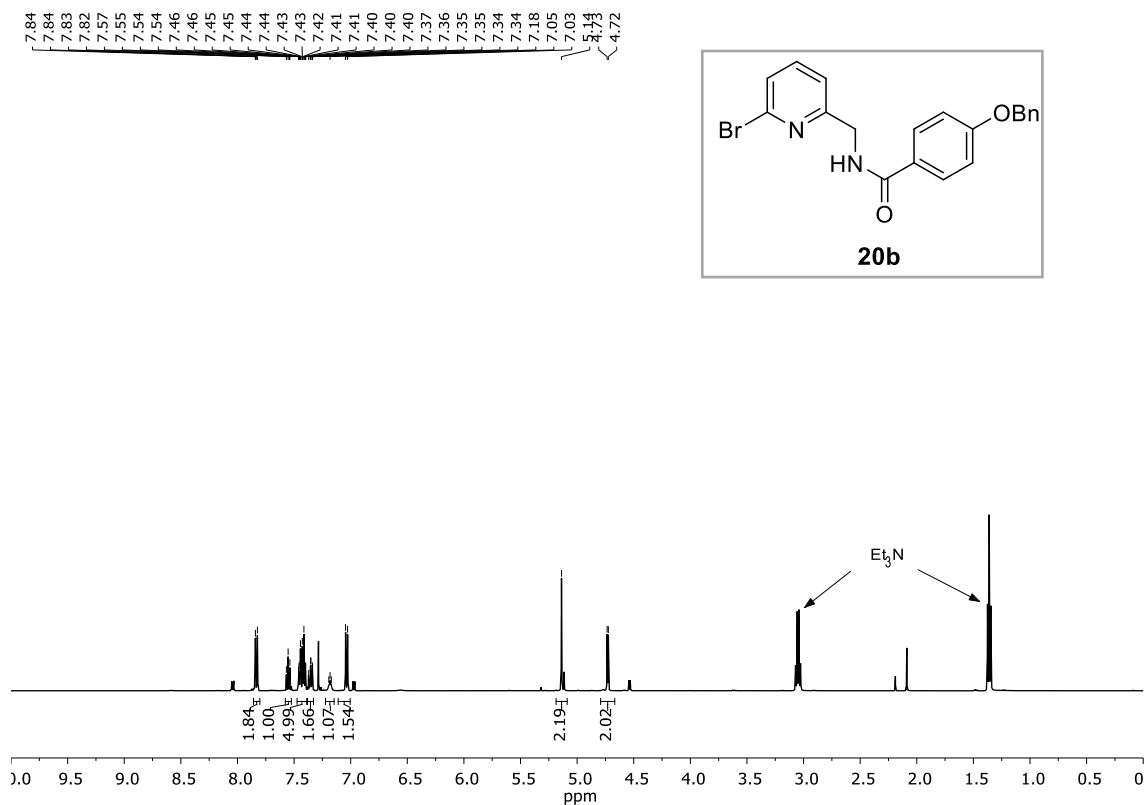
UV-VIS (a) and FS (b) (MeCN)
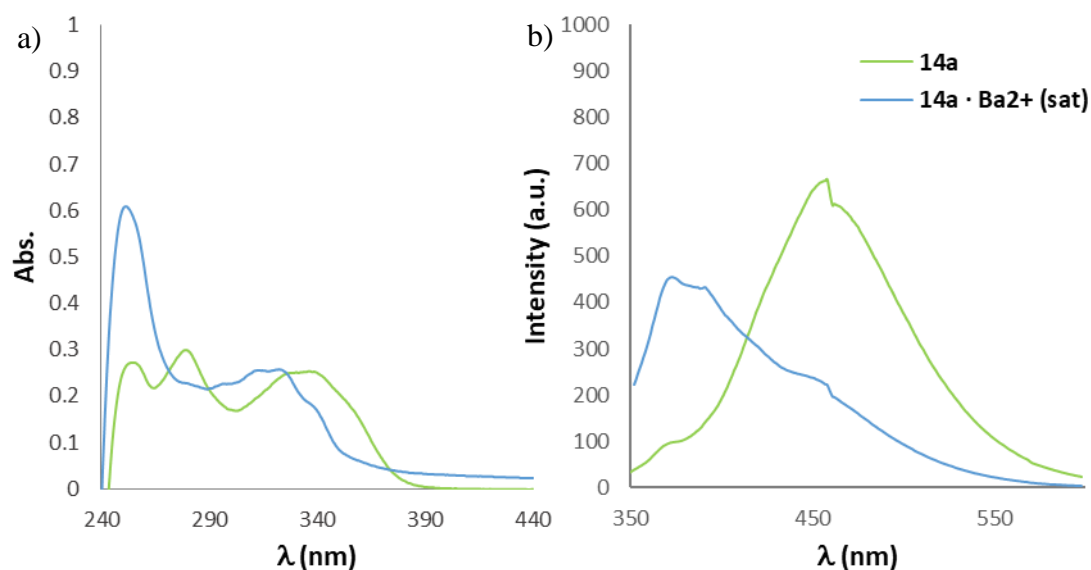
Figure 94.- a) Absorbance spectra for compound **14a** and **14·Ba^{2+}** (1eq), $5\cdot10^{-5}$ M in MeCN, r.t. b) Fluorescence spectra for compound **14a** and **14·Ba^{2+}** (1eq), $5\cdot10^{-5}$ M in MeCN, r.t., λ_{exc} = 278 nm.

Methyl 2-(4-(1,4,7,10,13-pentaoxa-16-azacyclooctadecan-16-yl)phenyl)imidazo[1,2-a]pyridine-7-carboxylate, 14b.
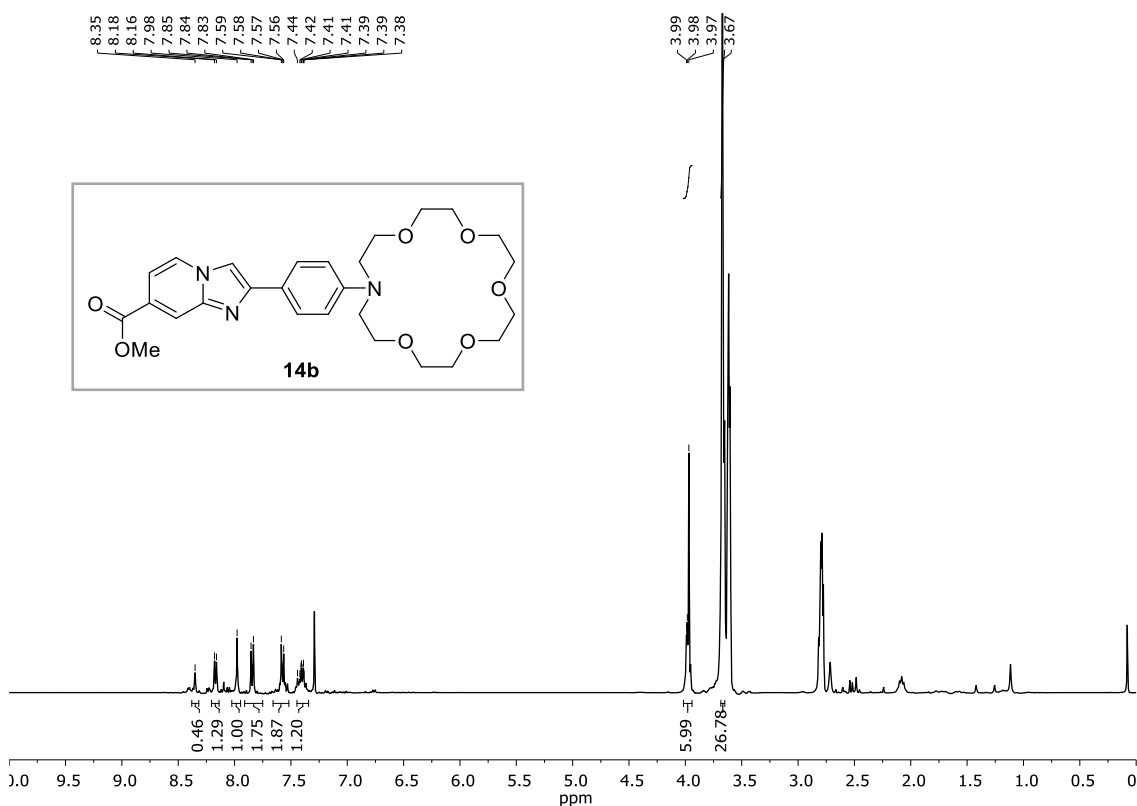
10-(4-(imidazo[1,2-a]pyridin-2-yl)phenyl)-1,4,7-trioxa-10-azacyclododecane, 14d
^{1}H-NMR (CDCl$_3$)
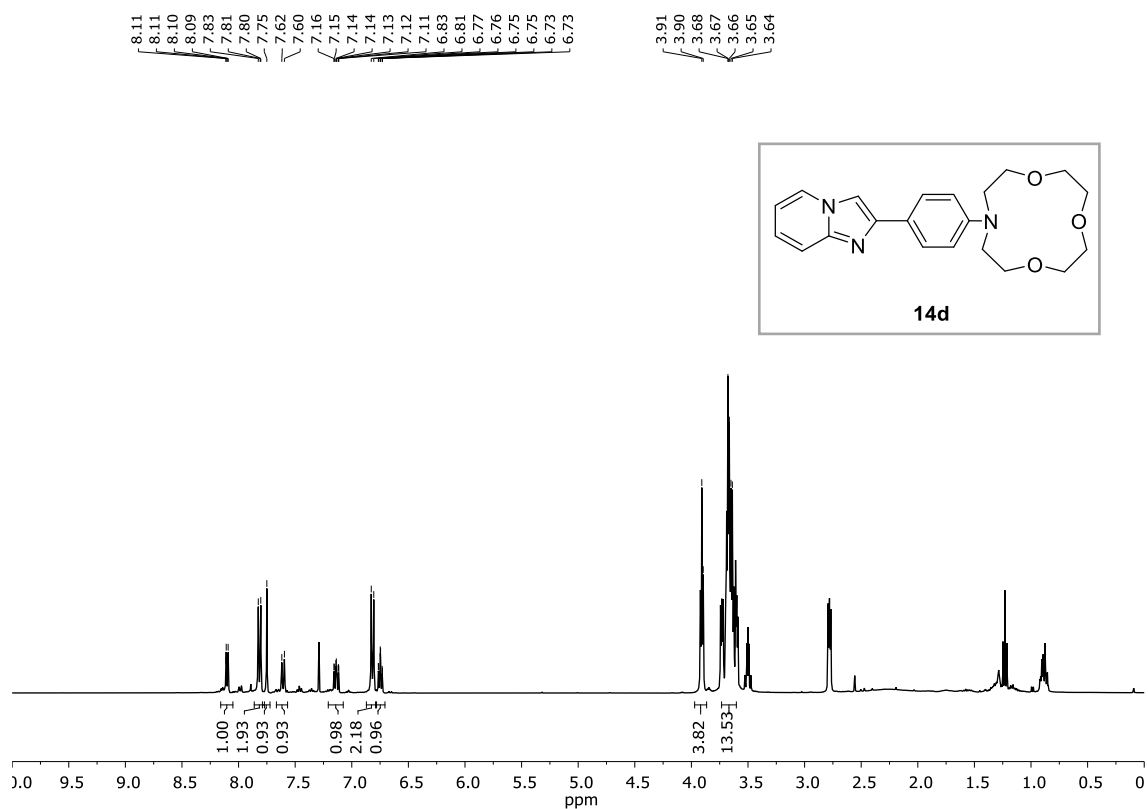
13-(4-(imidazo[1,2-a]pyridin-2-yl)phenyl)-1,4,7,10-tetraoxa-13-azacyclopentadecane, 14e
^{1}H-NMR (CDCl$_3$)

181
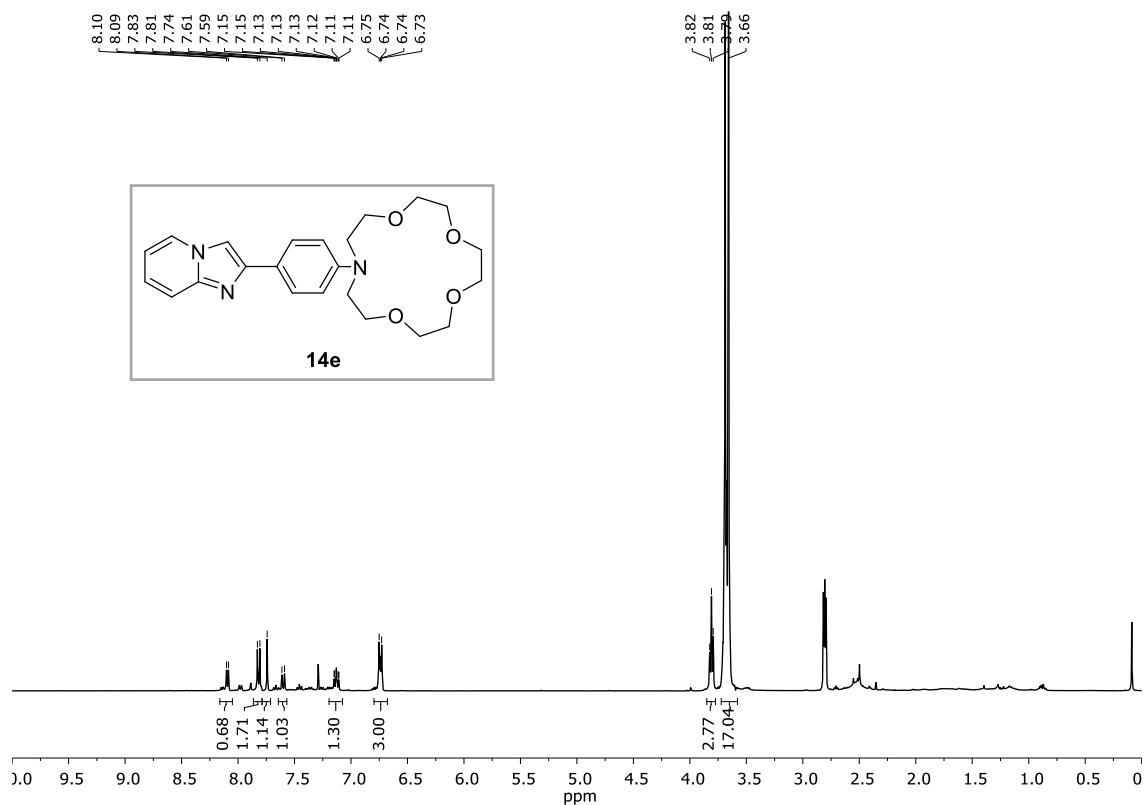
1-(4-bromophenyl)benzo[a]imidazo[5,1,2-cd]indolizine, 15a
^{1}H-NMR (CDCl$_3$)
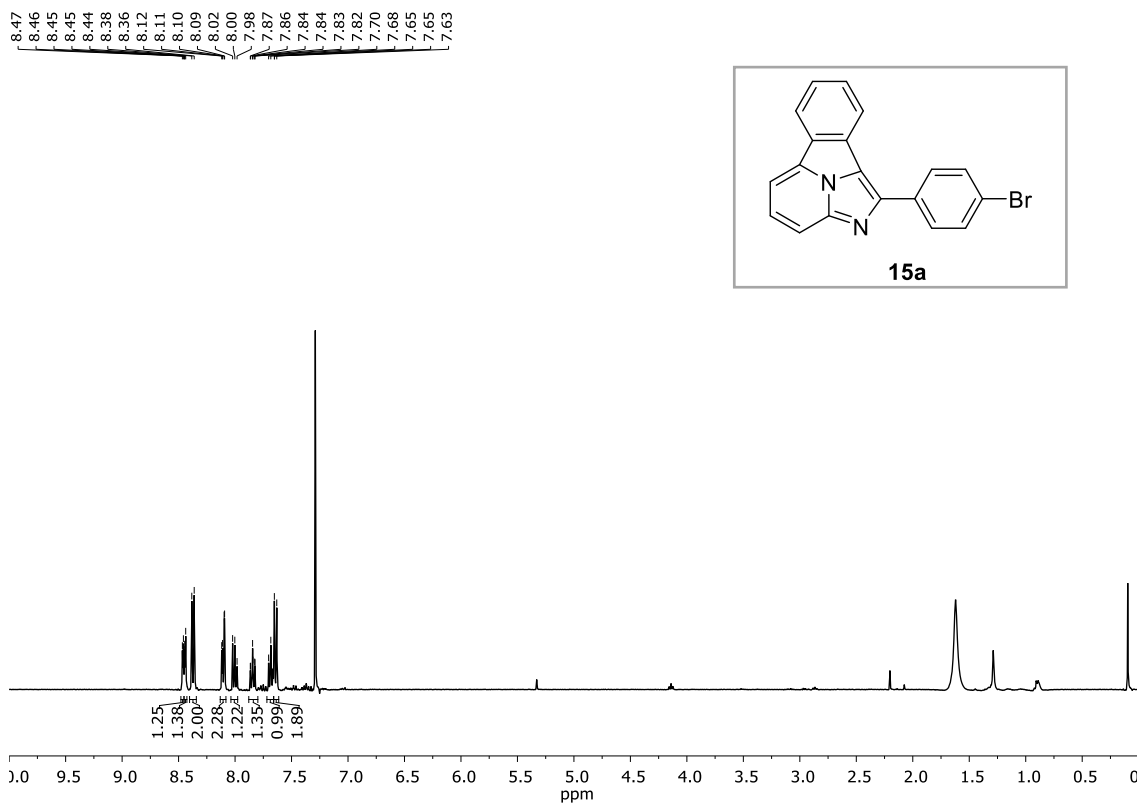
1-(4-bromophenyl)imidazo[5,1,2-cd]naphtho[2,3-a]indolizine, 15b

^{1}H-NMR (CDCl$_3$)
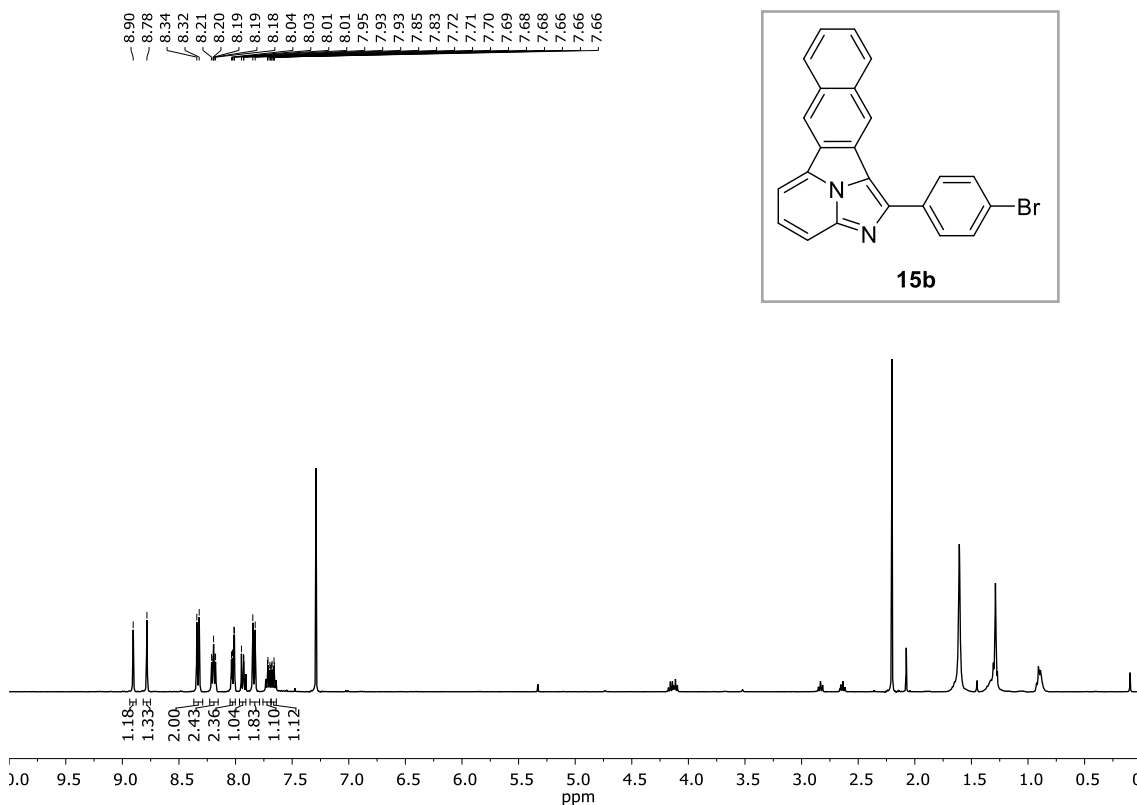
Methyl 1-(4-bromophenyl)benzo[a]imidazo[5,1,2-cd]indolizine-4-carboxylate, 15c

¹H-NMR (CDCl₃)
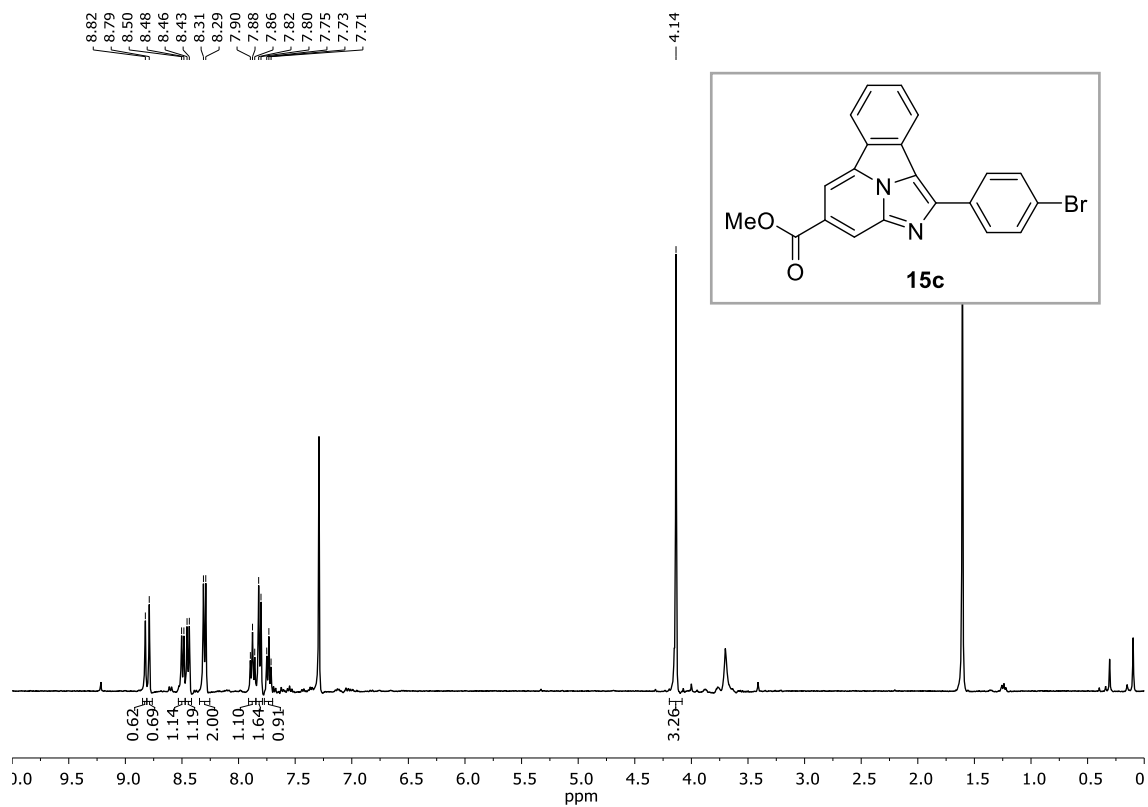
16-(4-(benzo[a]imidazo[5,1,2-cd]indolizin-1-yl)phenyl)-1,4,7,10,13-pentaoxa-16-azacyclooctadecane, 16a

^{1}H-NMR (CD$_3$OD)
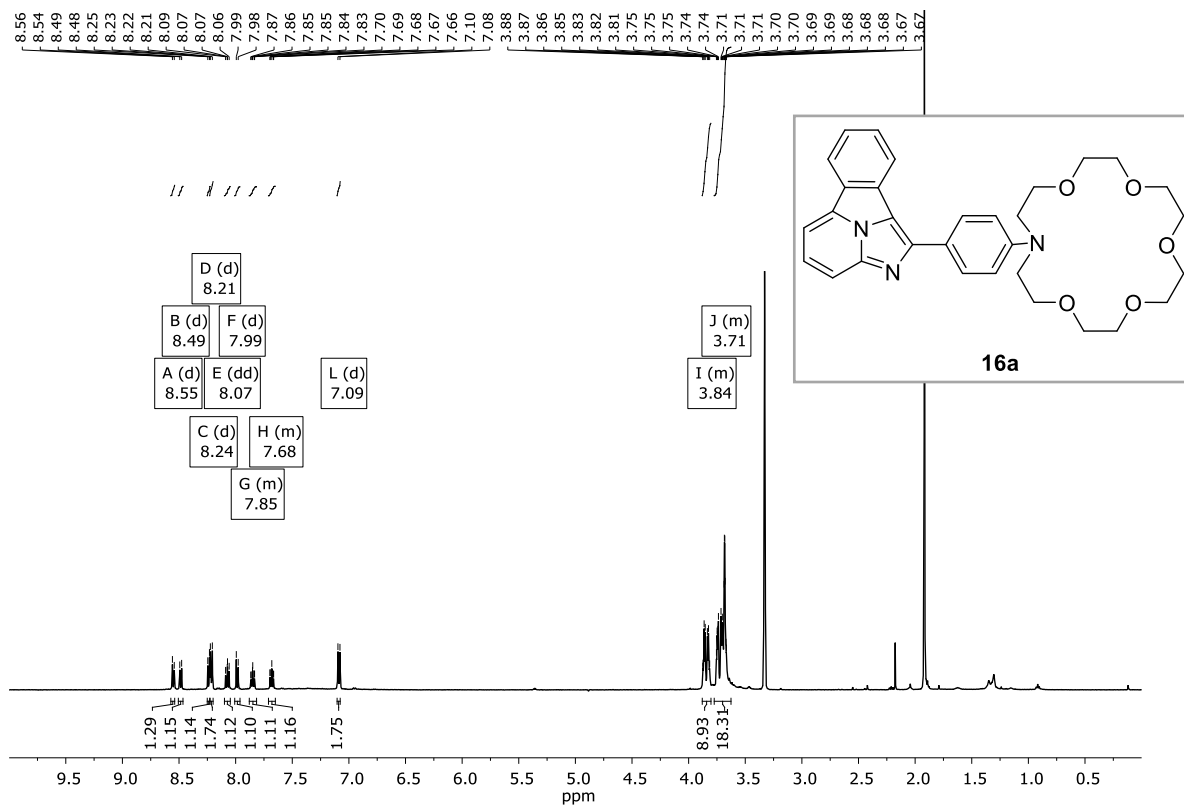
g-COSY (CD$_3$OD)
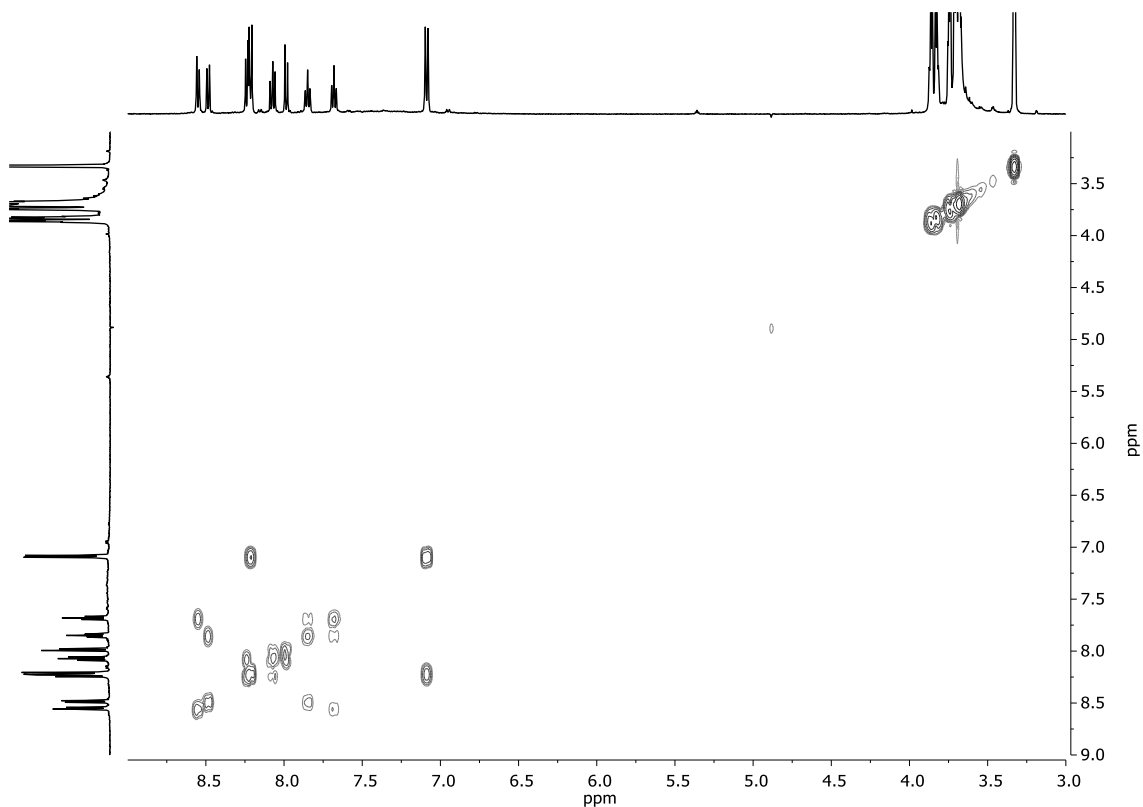
g-HSQC (CD₃OD)
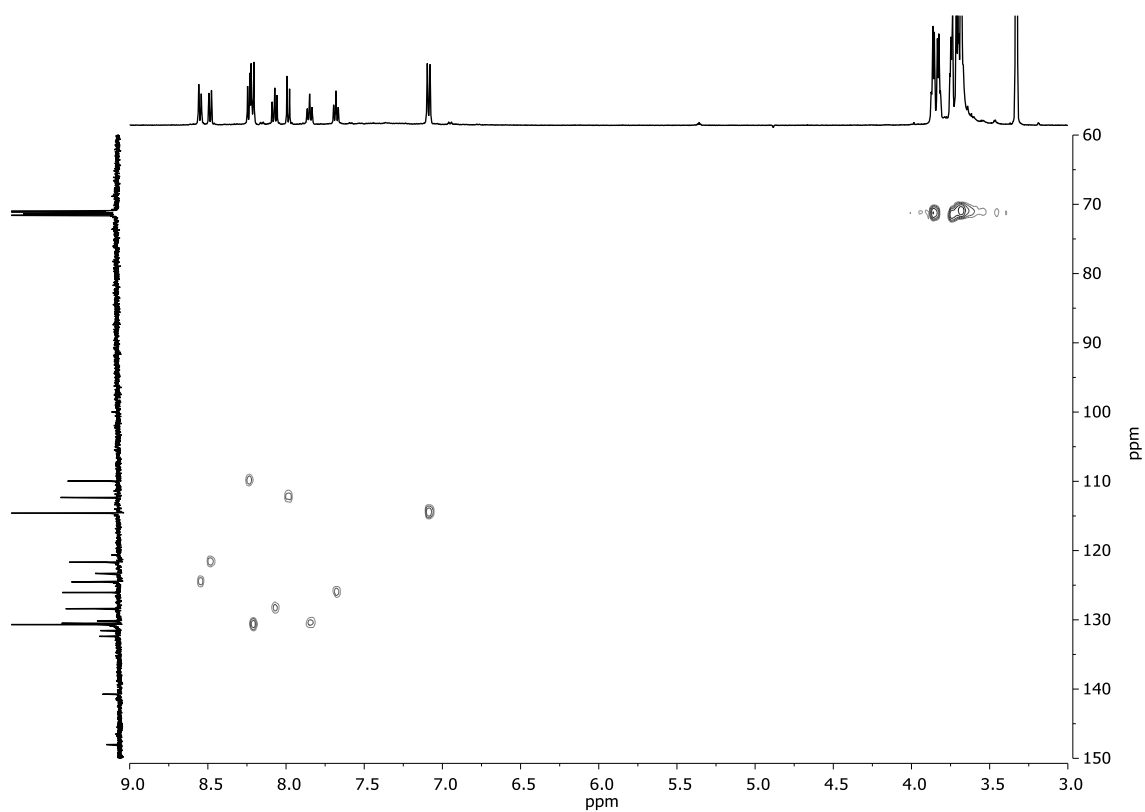
¹³C-NMR (CD₃OD)
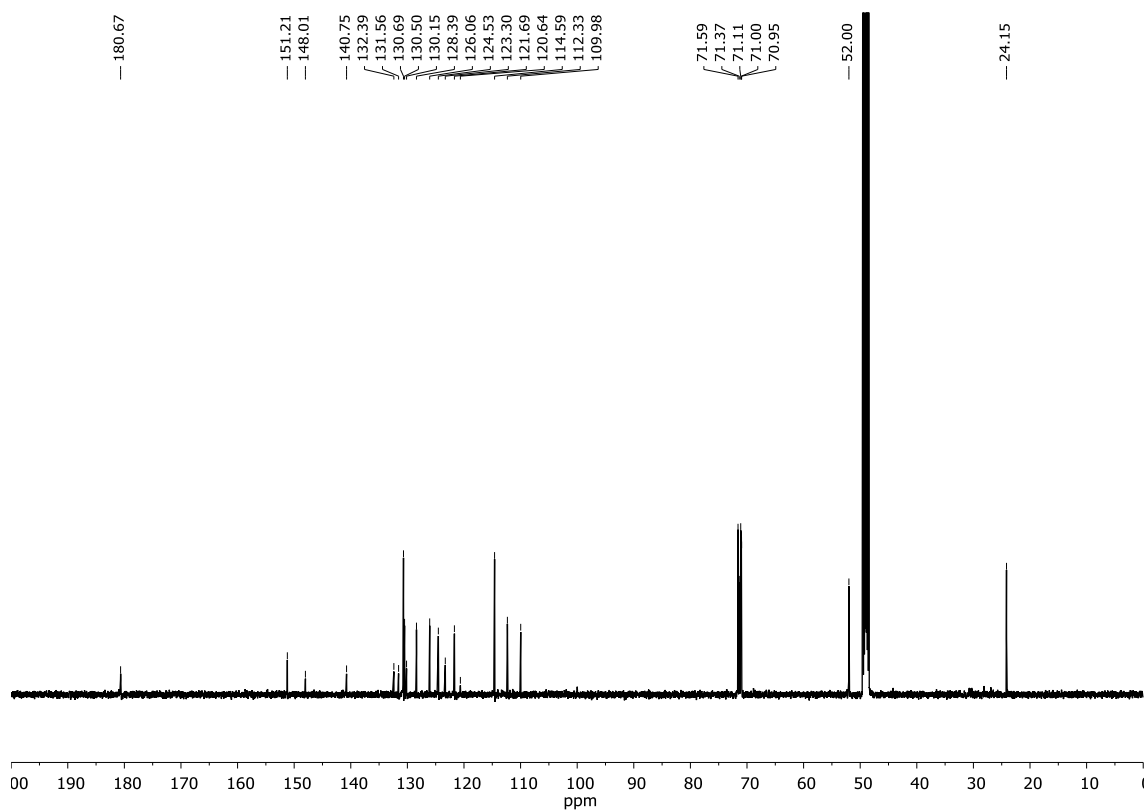
135-DEPT (CD₃OD)
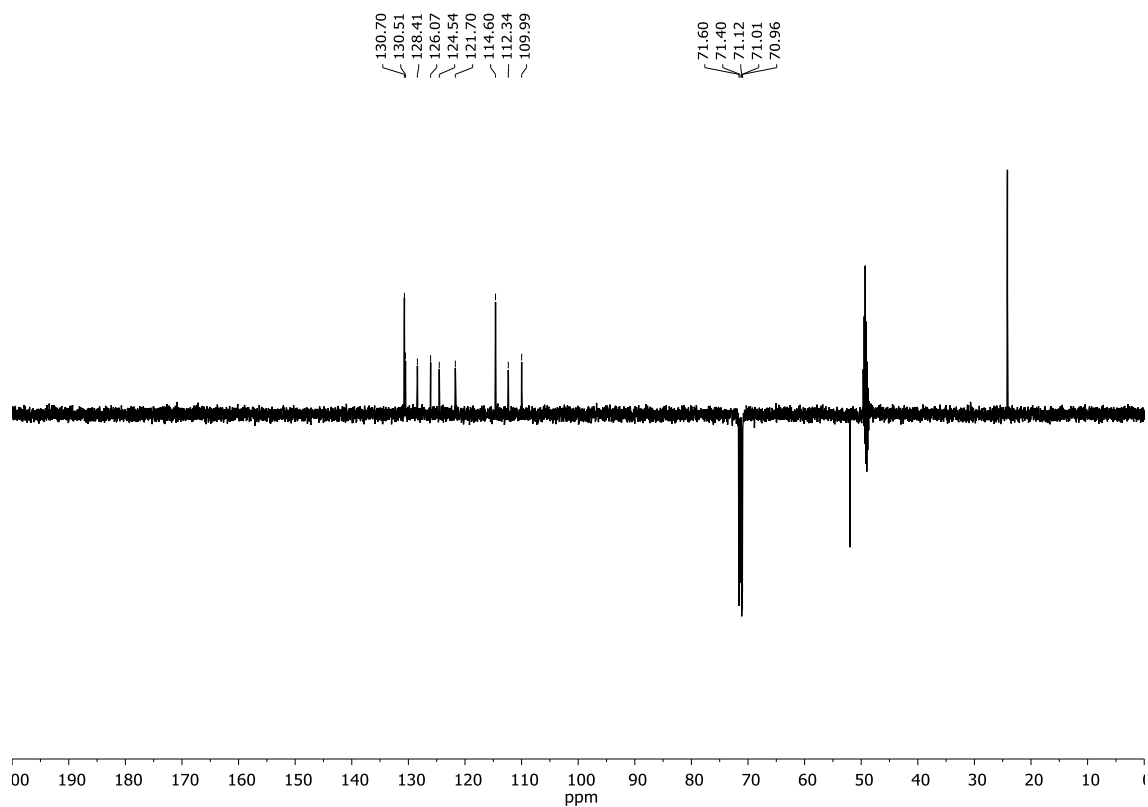
UV-VIS (a) and FS (b) (MeCN)
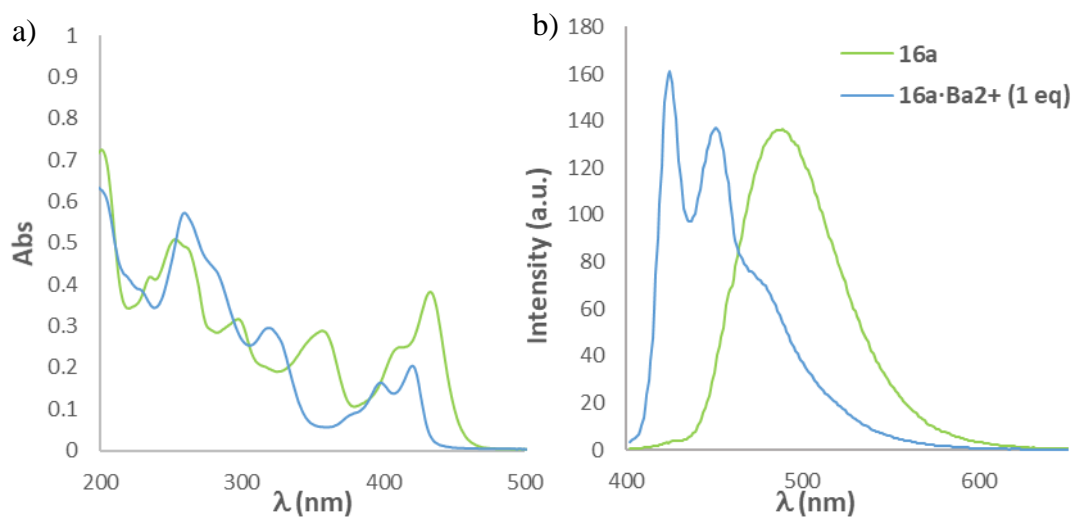
Figure 95.- a) Absorbance spectra for compound **16a** and **16a·Ba^{2+}** (1 eq), $5 \cdot 10^{-5}$ M in MeCN, r.t. b) Fluorescence spectra for compound **16a** and **16a·Ba^{2+}** (1 eq), $5 \cdot 10^{-5}$ M in MeCN, r.t., λ_{exc} = 252nm.

16-(4-(imidazo[5,1,2-cd]naphtho[2,3-a]indolizin-1-yl)phenyl)-1,4,7,10,13-pentaoxa-16-azacyclooctadecane, 16b

^{1}H-NMR (CDCl$_3$)
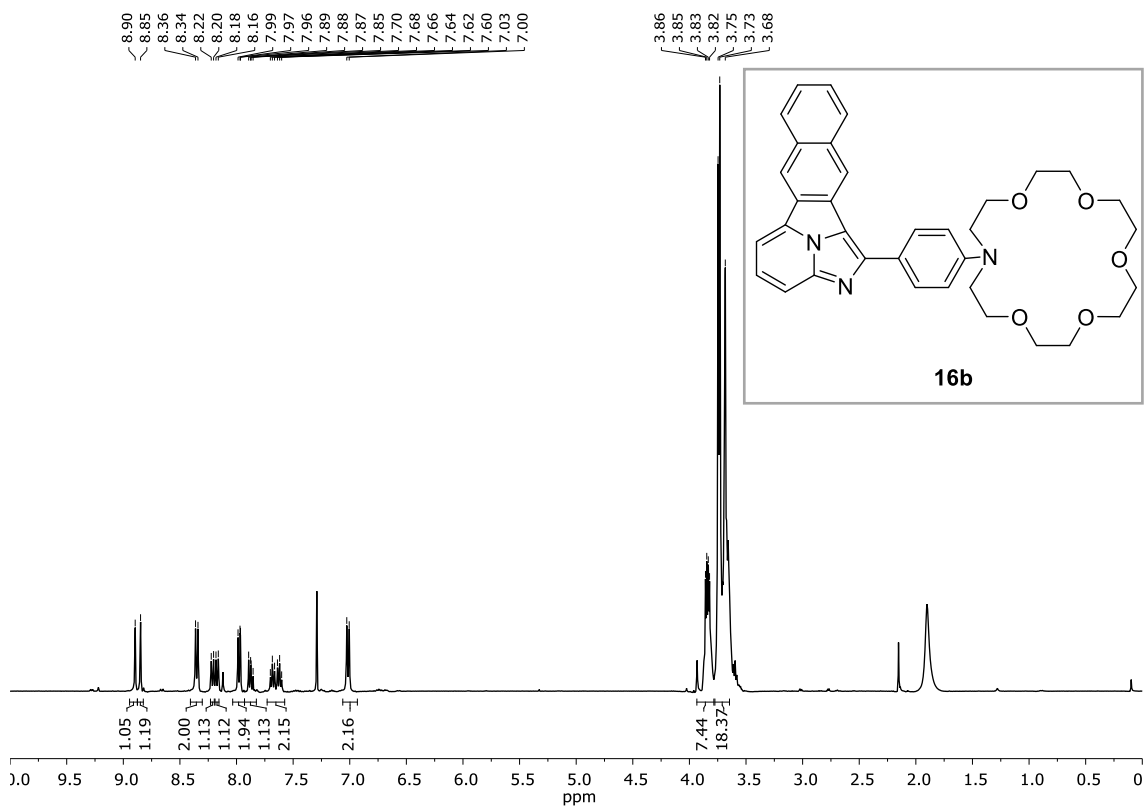
g-COSY (CDCl$_3$)
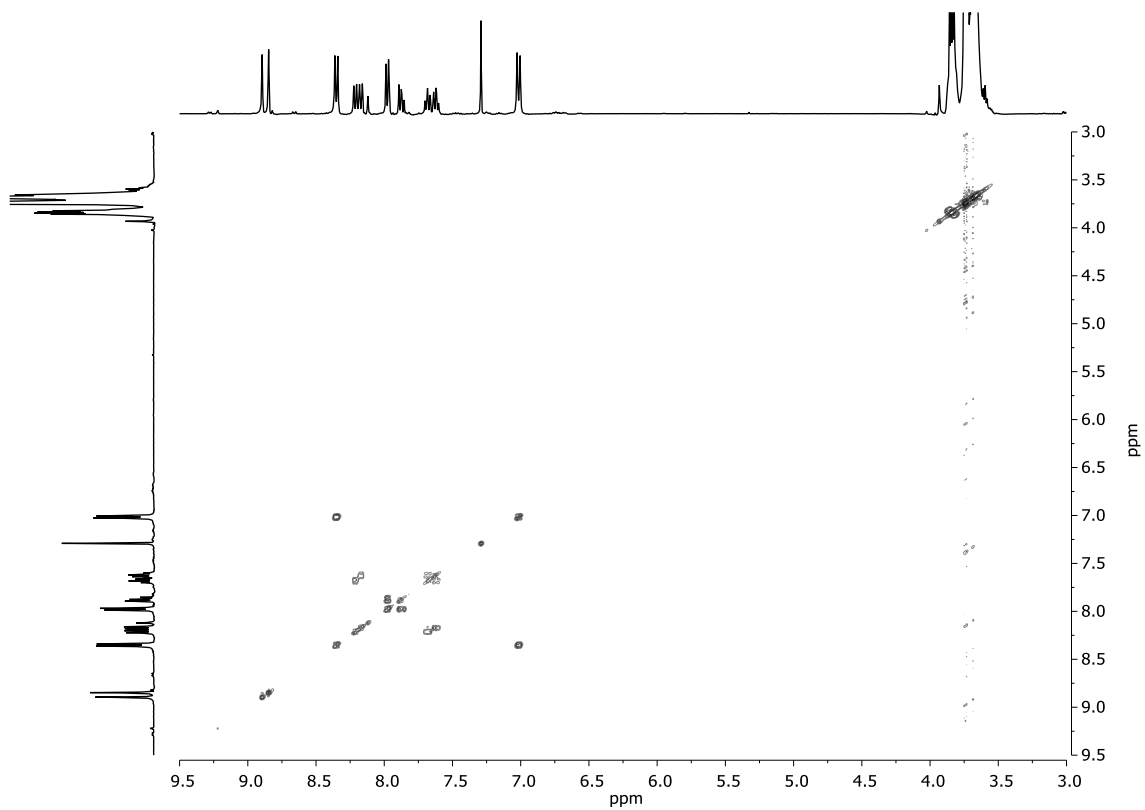
g-HSQC (CDCl₃)
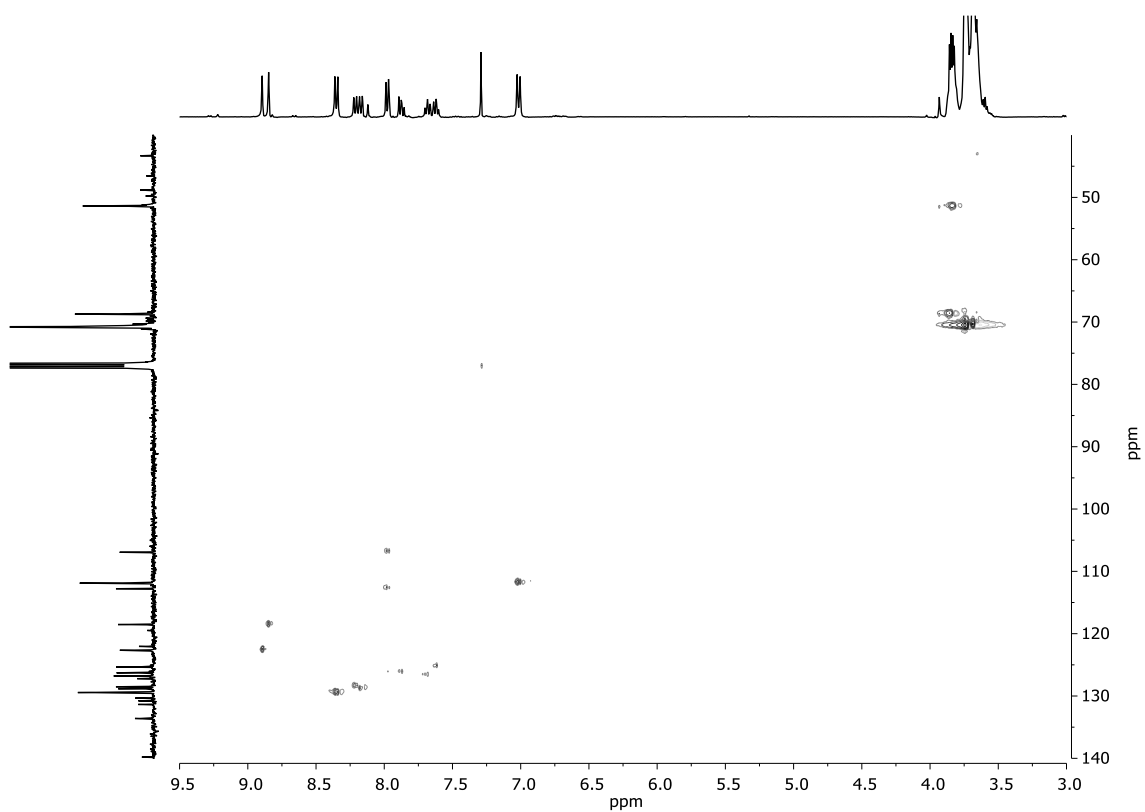
¹³C-NMR (CDCl₃)
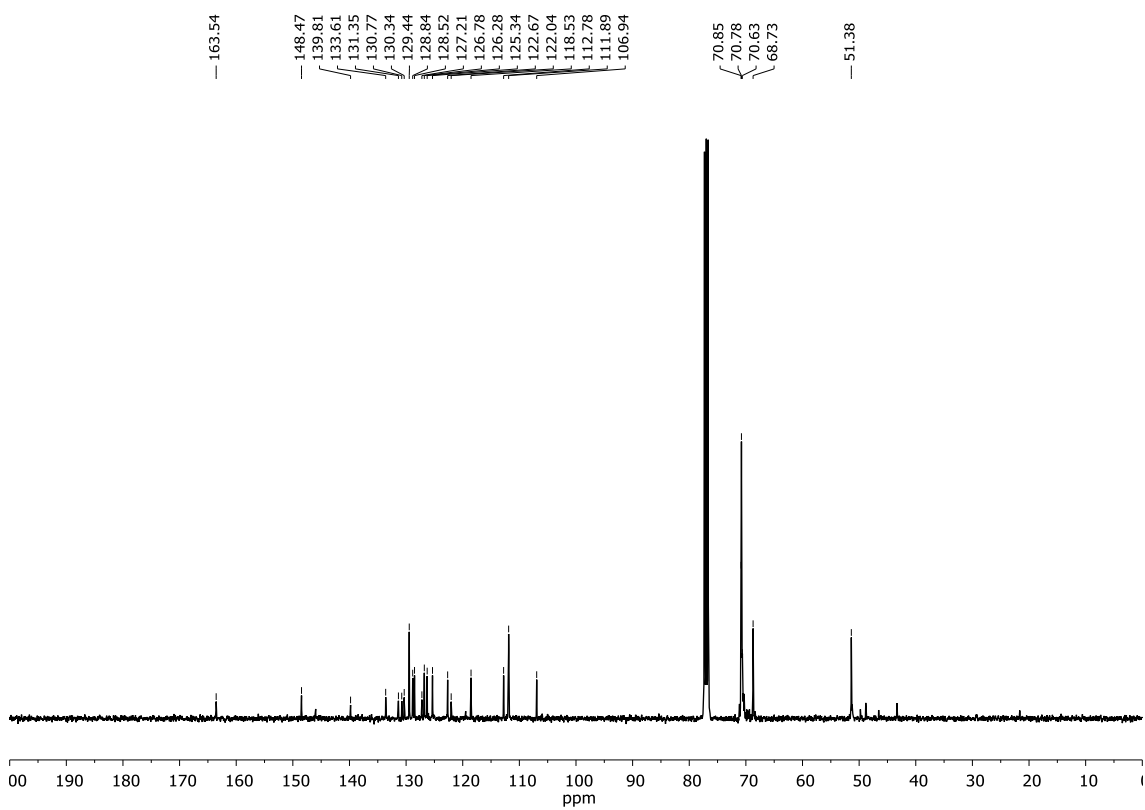
135-DEPT (CDCl₃)
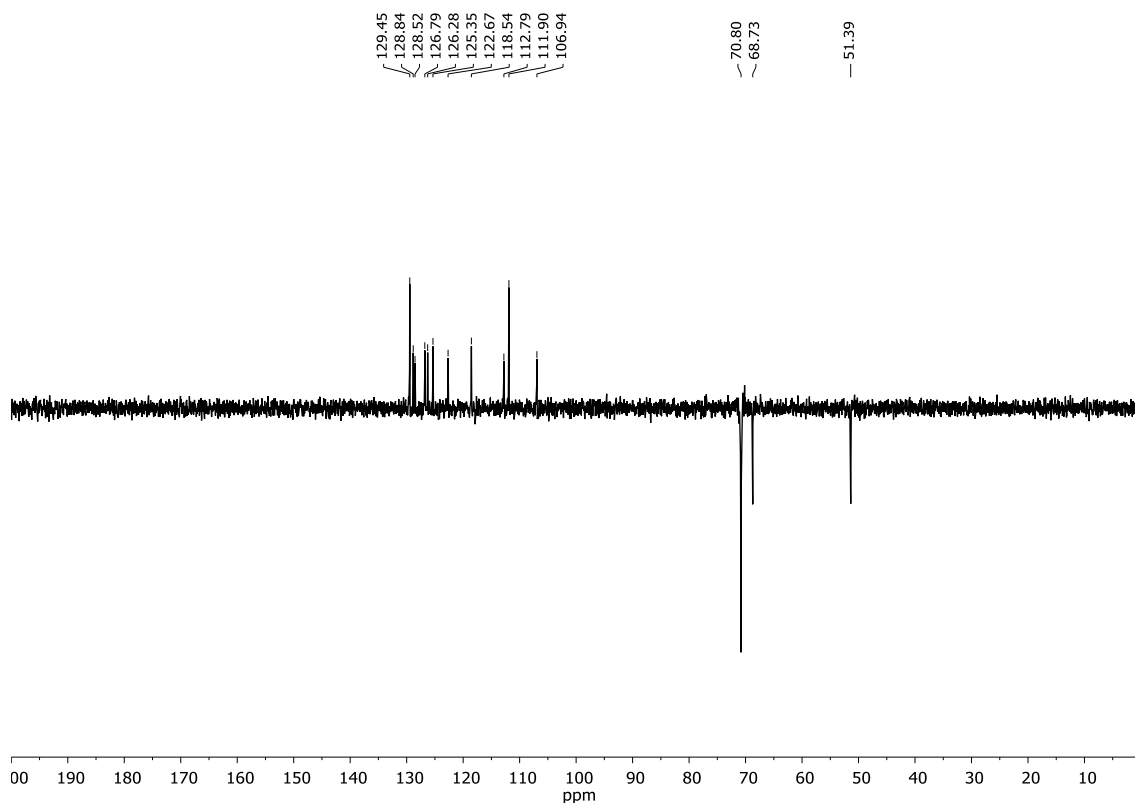
UV-VIS (a) and FS (b) (MeCN)
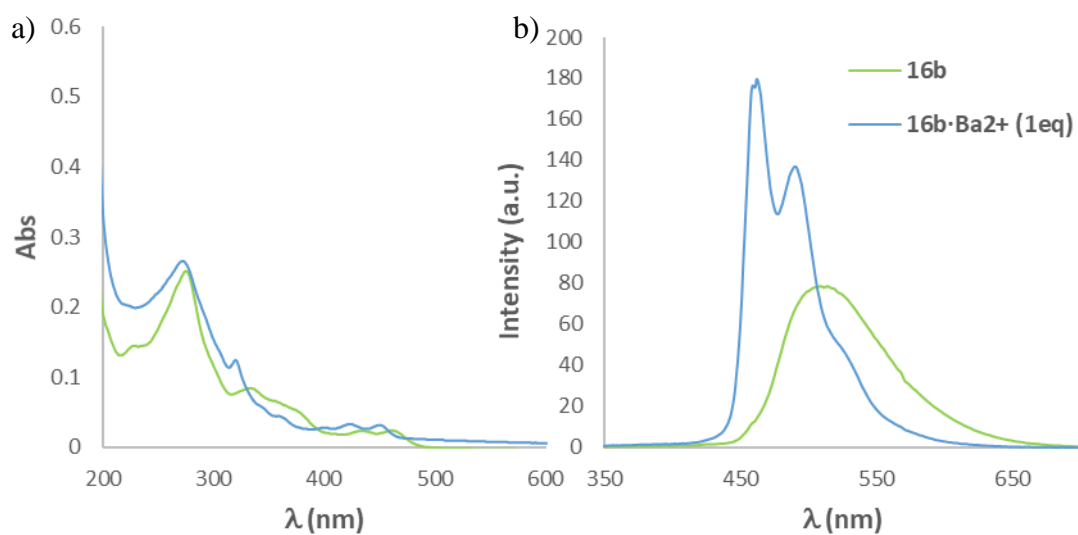
Figure 96.- a) Absorbance spectra for compound **16b** and **16b·Ba²⁺** (1 eq), $5 \cdot 10^{-5}$ M in MeCN, r.t. b) Fluorescence spectra for compound **16b** and **16b·Ba²⁺** (1 eq), $5 \cdot 10^{-5}$ M in MeCN, r.t., λ_{exc} = 252nm.

Methyl 1-(4-(1,4,7,10,13-pentaoxa-16-azacyclooctadecan-16-yl)phenyl)benzo[a]imidazo[5,1,2-cd]indolizine-4-carboxylate, 16c

^{1}H-NMR (CDCl$_3$)
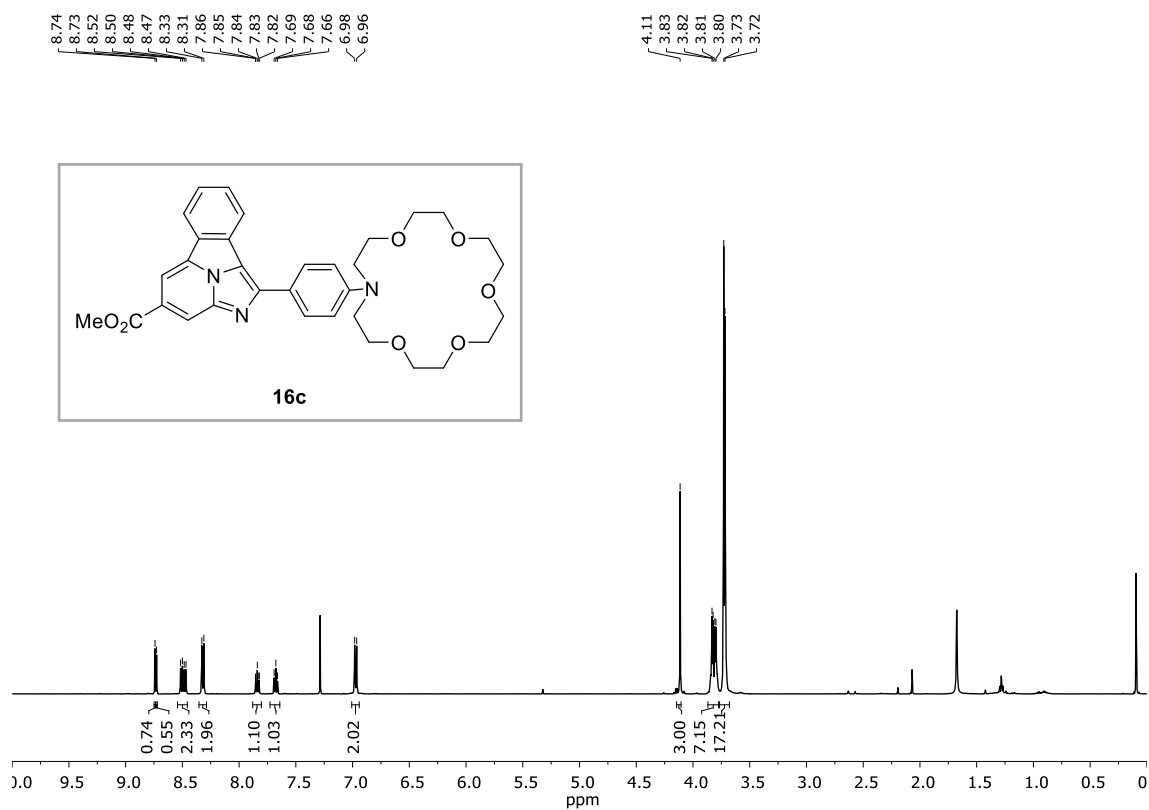
g-COSY (CDCl$_3$)
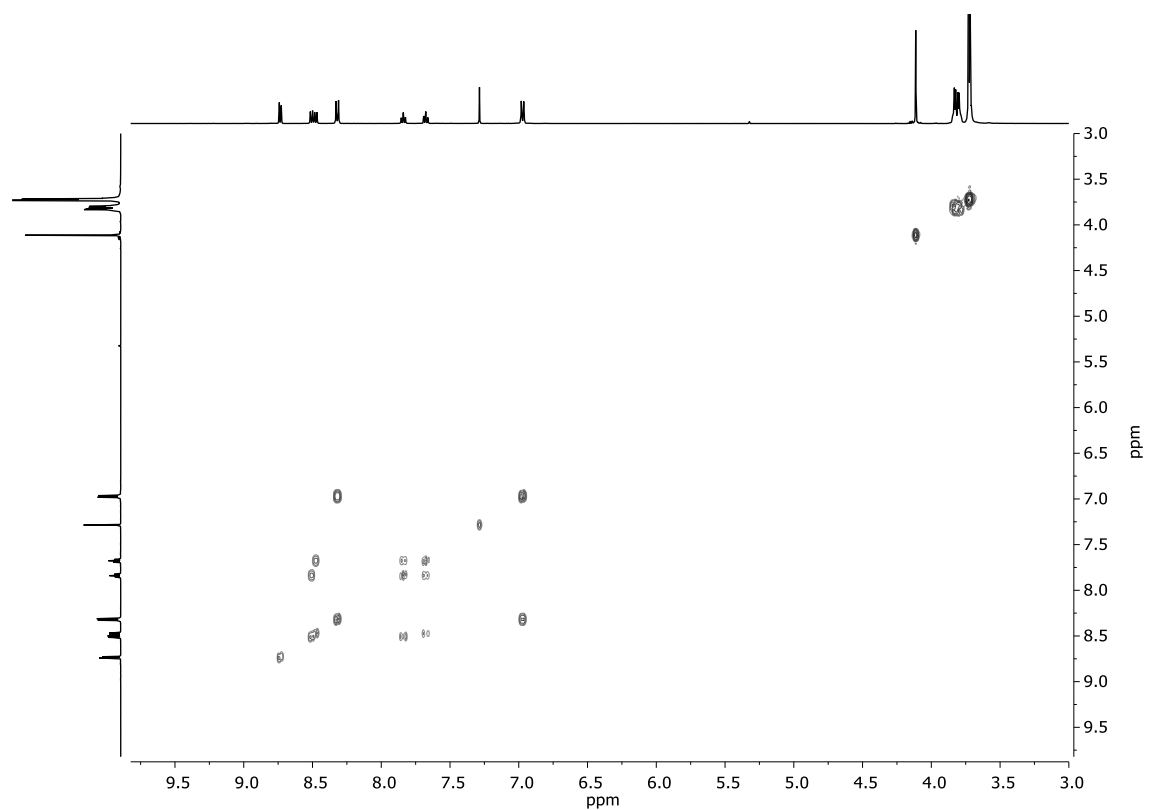
g-HSQC (CDCl₃)
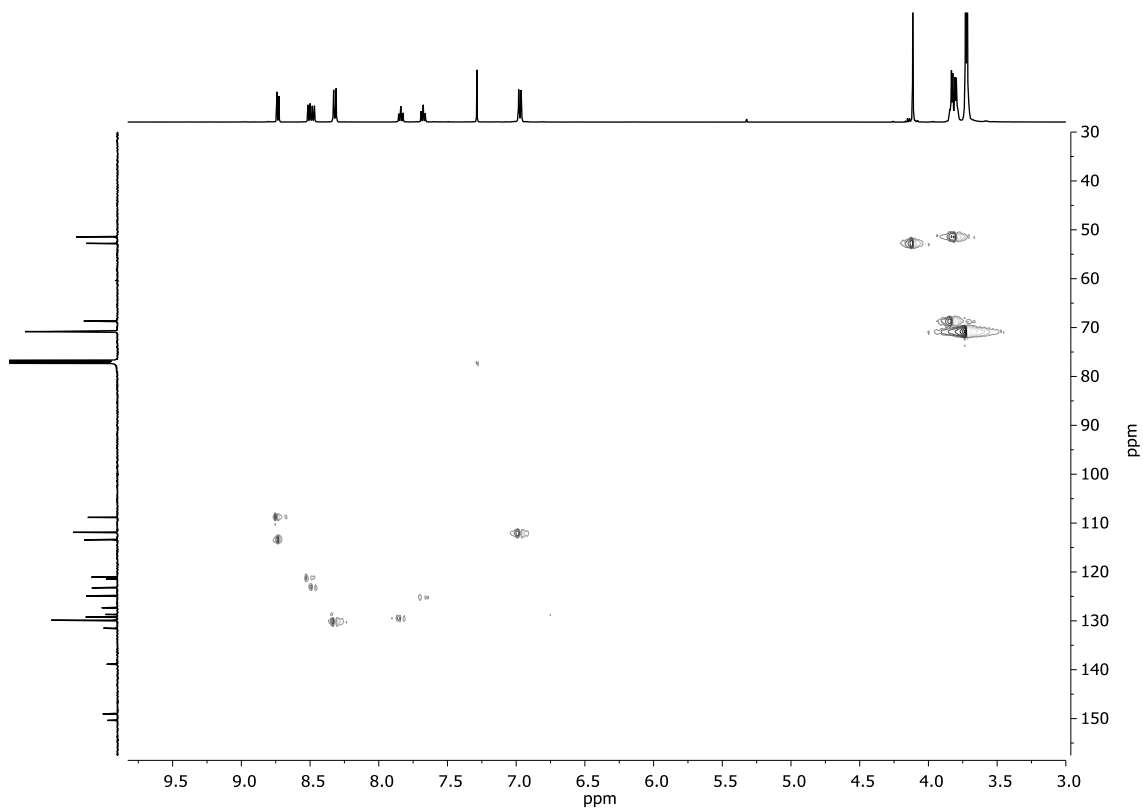
¹³C-NMR (CDCl₃)
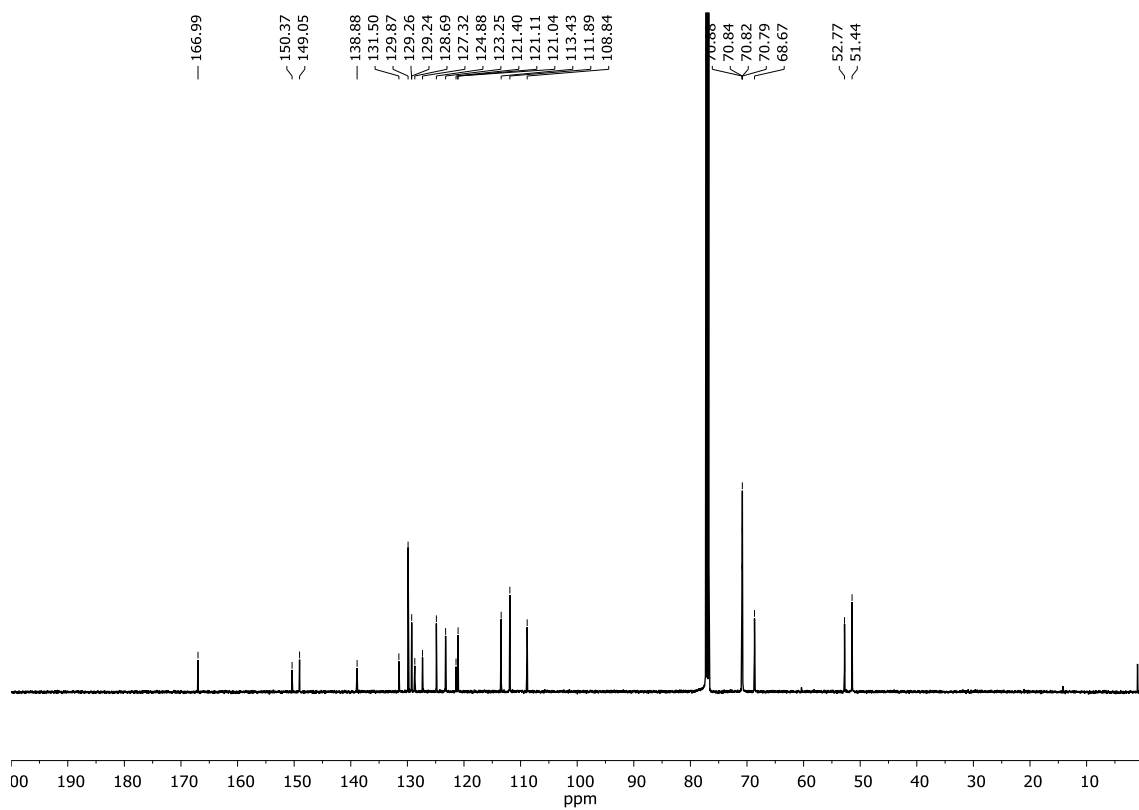
135-DEPT (CDCl₃)
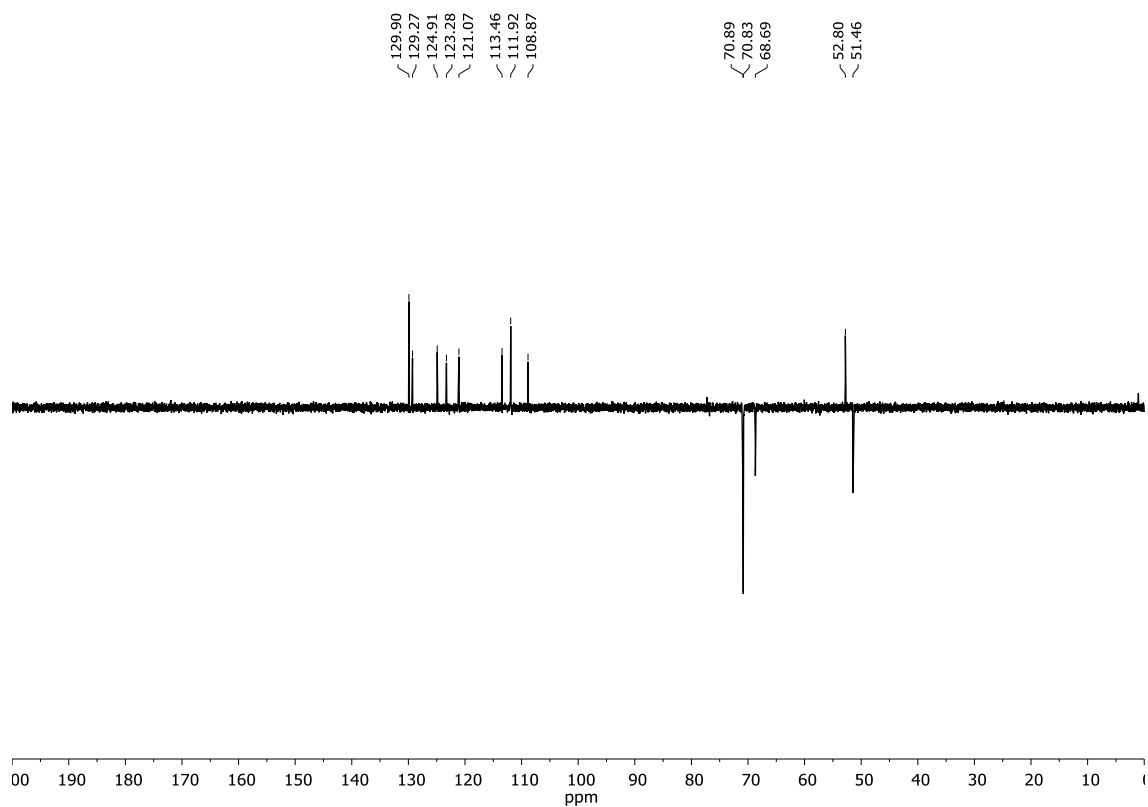
UV-VIS (a) and FS (b) (MeCN)
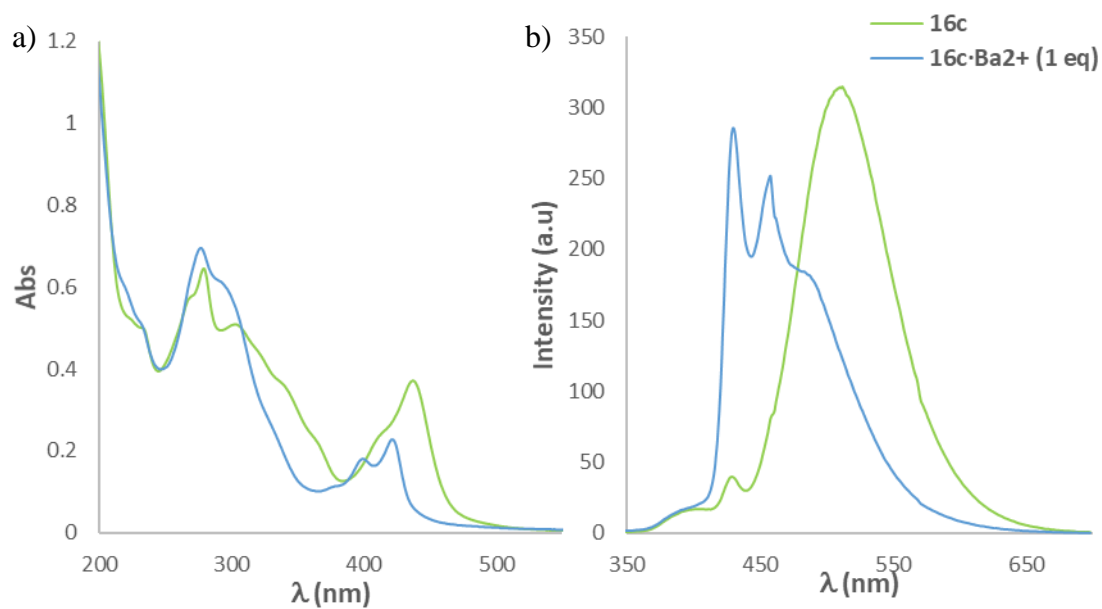
Figure 97.*-* a) Absorbance spectra for compound **16c** and **16c·Ba²⁺** (1 eq), $5 \cdot 10^{-5}$ M in MeCN, r.t. b) Fluorescence spectra for compound **16** and **16c·Ba²⁺** (1 eq), $5 \cdot 10^{-5}$ M in MeCN, r.t., $\lambda_{exc} = 252$nm.

16-(4-(2,2a1,3-triazacyclopenta[jk]fluoren-1-yl)phenyl)-1,4,7,10,13-pentaoxa-16-azacyclooctadecane, 16d

^{1}H-NMR (CDCl$_3$)

g-COSY (CDCl$_3$)

g-HSQC (CDCl₃)

¹³C-NMR (CDCl₃)

150.59
148.99
135.29
133.99
131.90
130.90
130.84
130.11
129.32
128.87
125.67
125.11
121.57
119.08
104.76

70.68
70.58
70.40
70.12

49.11
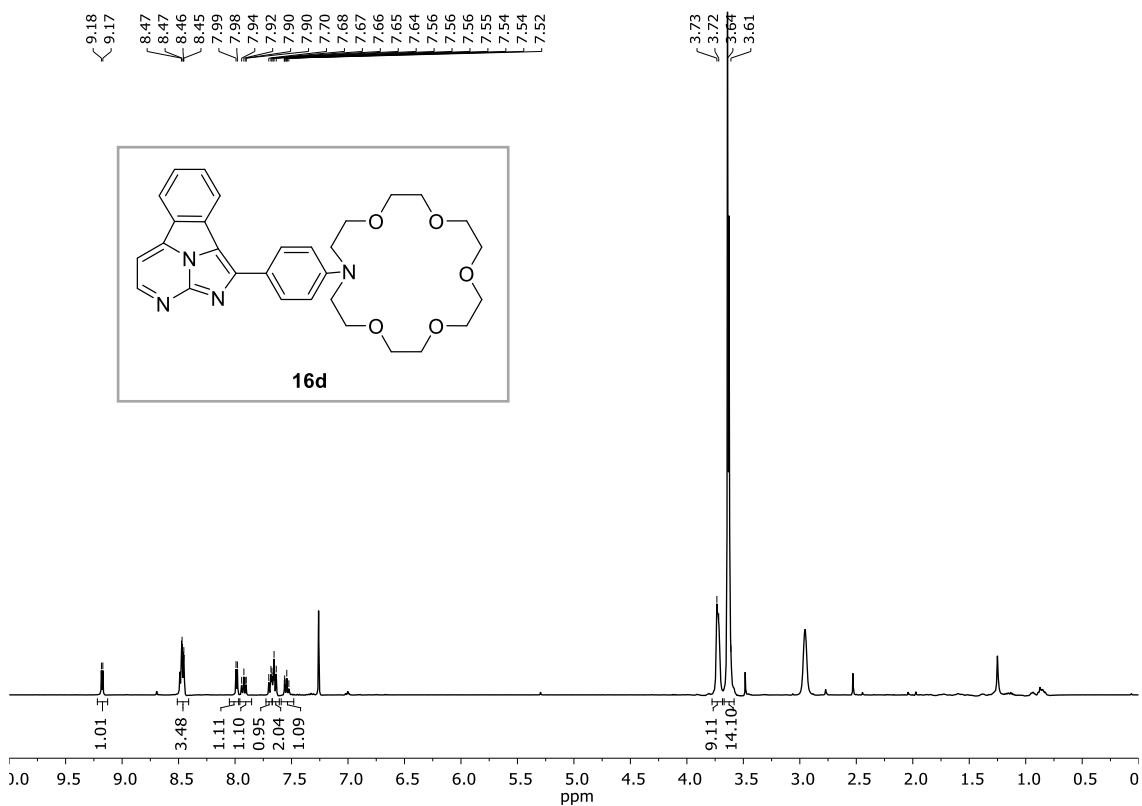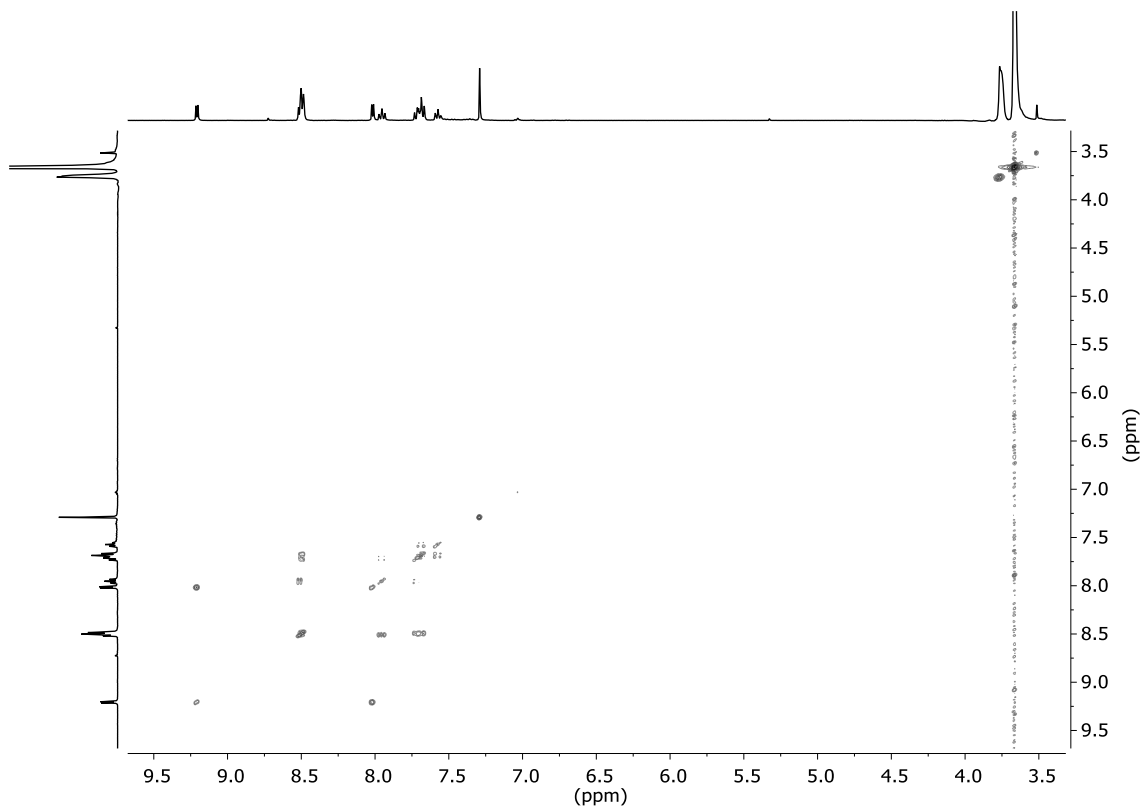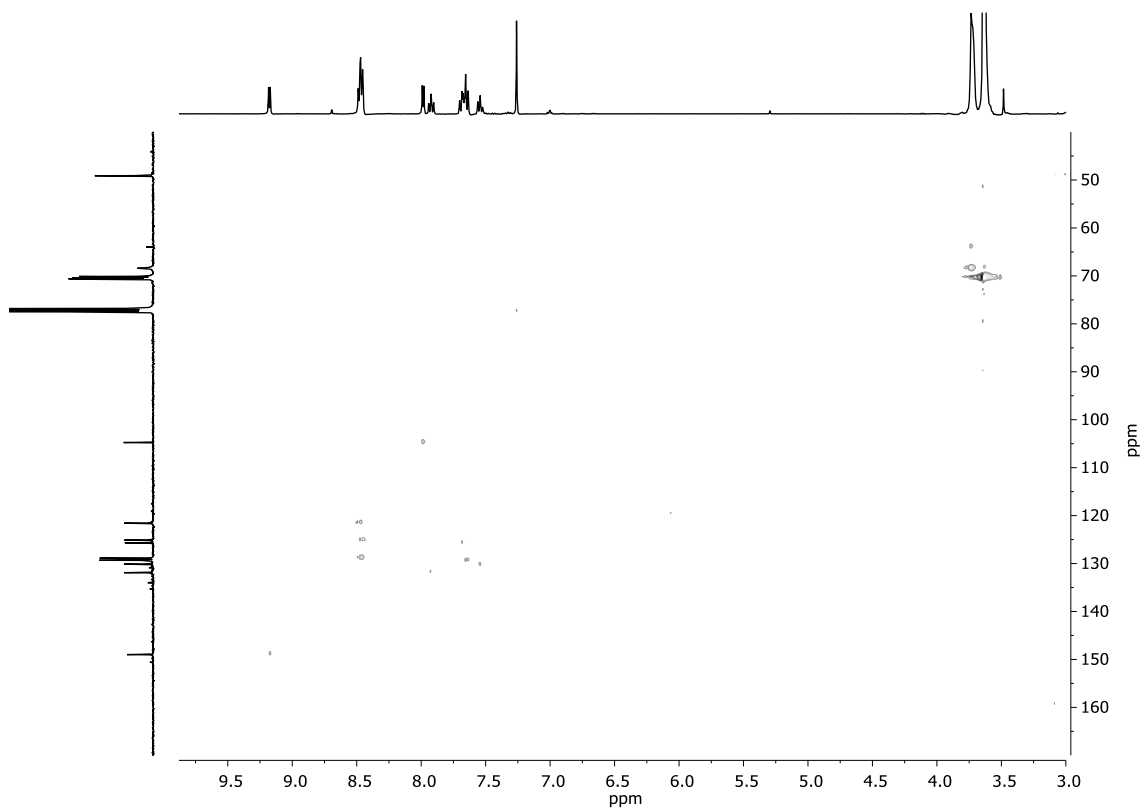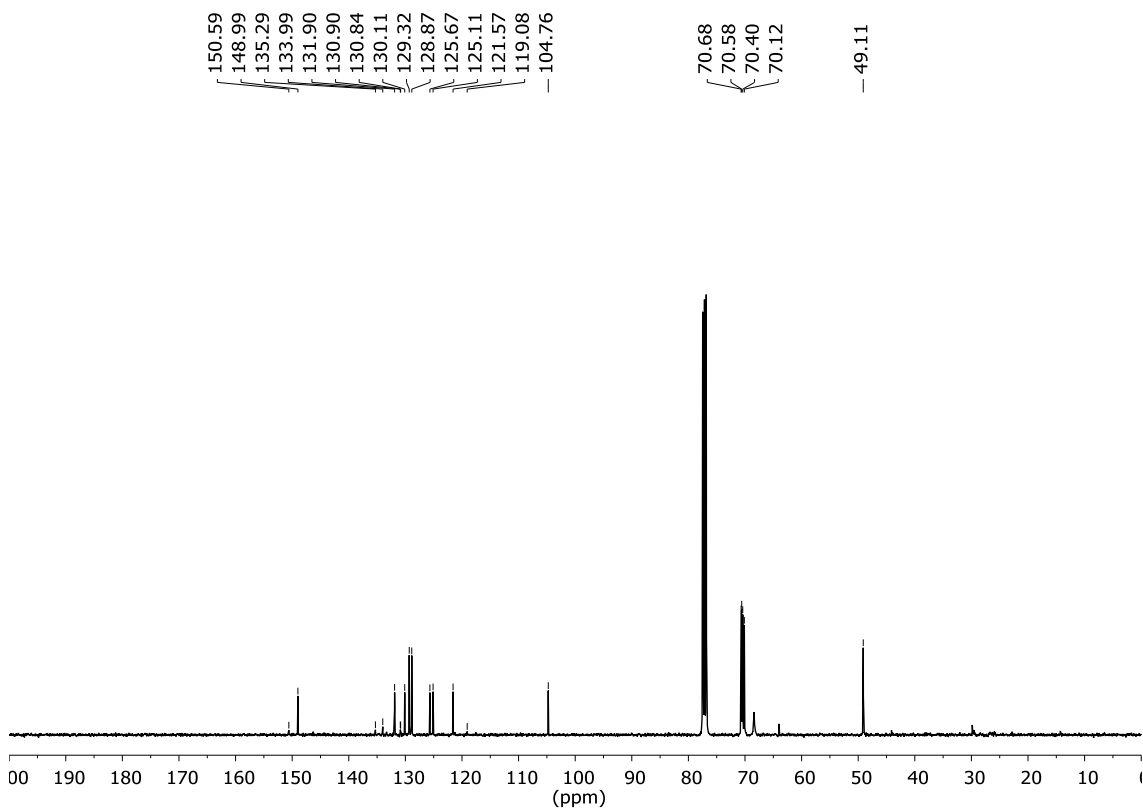
UV-VIS (a) and FS (b) (MeCN)

Figure 98.- a) Absorbance spectra for compound **16d** and **16d·Ba^{2+}** (1 eq), 5·10^{-5} M in MeCN, r.t. b) Fluorescence spectra for compound **16d** and **16d·Ba^{2+}** (1 eq), 5·10^{-5} M in MeCN, r.t., λ_{exc} = 252nm.

10-(4-(benzo[a]imidazo[5,1,2-cd]indolizin-1-yl)phenyl)-1,4,7-trioxa-10-azacyclododecane, 16e

^{1}H-NMR (CDCl$_3$)

g-COSY (CDCl₃)

g-HSQC (CDCl₃)

^{13}C-NMR (CDCl$_3$)

149.35, 147.87, 139.83, 130.80, 129.77, 129.49, 128.93, 128.82, 128.75, 128.68, 126.99, 125.83, 125.22, 124.07, 123.98, 123.02, 122.25, 120.73, 119.68, 117.02, 112.61, 112.45, 112.42, 112.17, 111.96, 111.91, 108.01, 106.38, 71.57, 69.90, 69.61, 52.62

135-DEPT (CDCl$_3$)

129.53, 128.79, 125.87, 124.11, 123.06, 120.77, 112.65, 111.99, 108.05, 71.61, 69.94, 69.64, 52.66
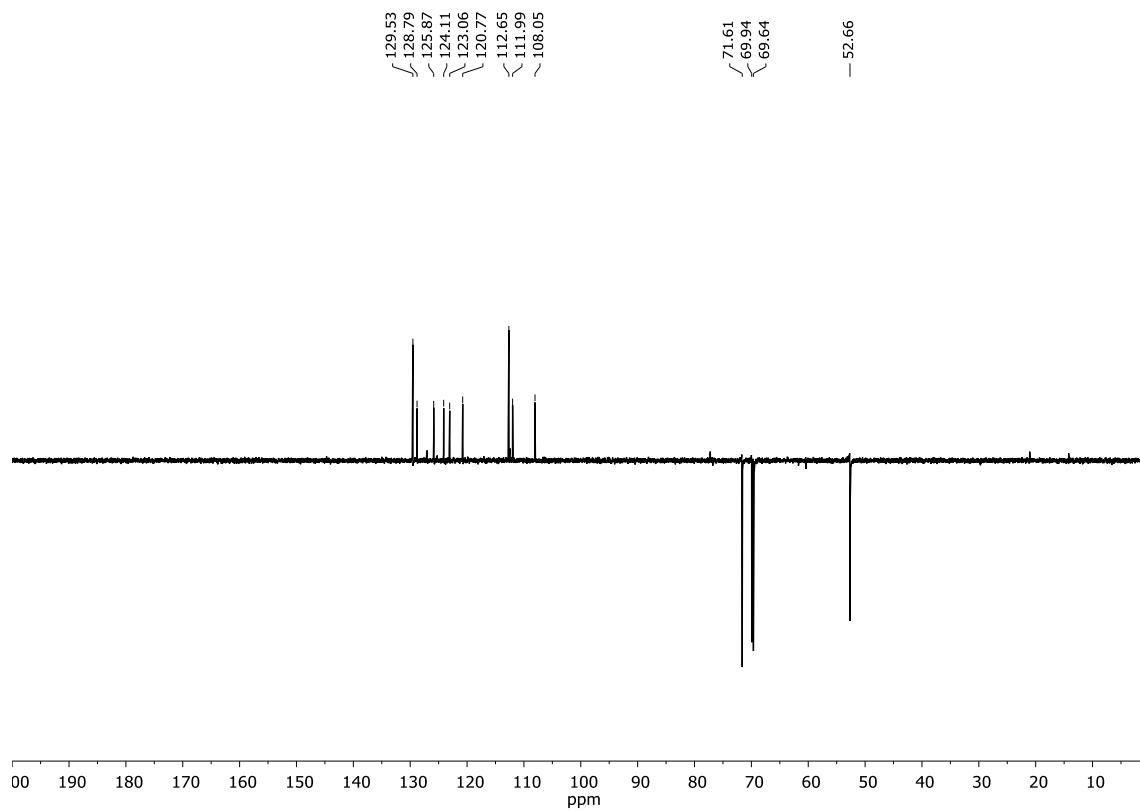
UV-VIS (a) and FS (b) (MeCN)

Figure 99.- a) Absorbance spectra for compound **16e** and **16e·Ba²⁺** (1 eq), 5·10⁻⁵ M in MeCN, r.t. b) Fluorescence spectra for compound **16e** and **16e·Ba²⁺** (1 eq), 5·10⁻⁵ M in MeCN, r.t., λ_{exc} = 252nm.
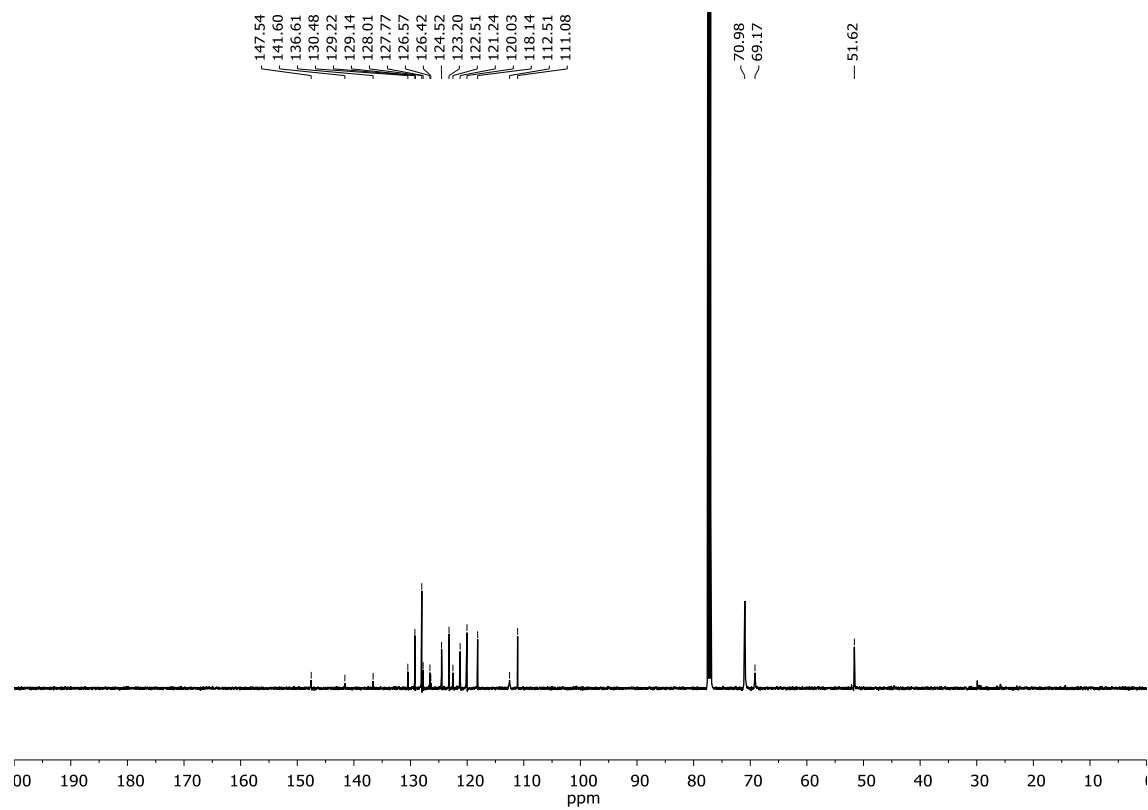
13-(4-(benzo[a]imidazo[5,1,2-cd]indolizin-1-yl)phenyl)-1,4,7,10-tetraoxa-13-azacyclopentadecane, 16f

¹H-NMR (CDCl₃)
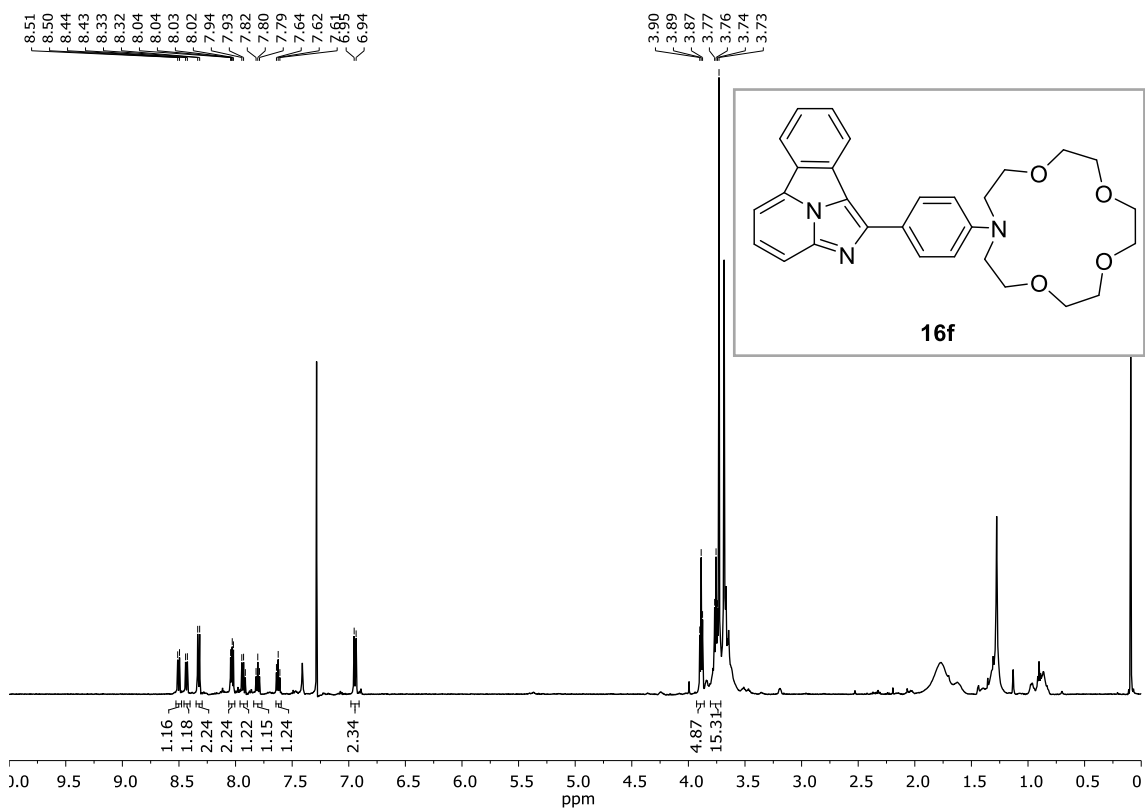
g-COSY (CDCl₃)
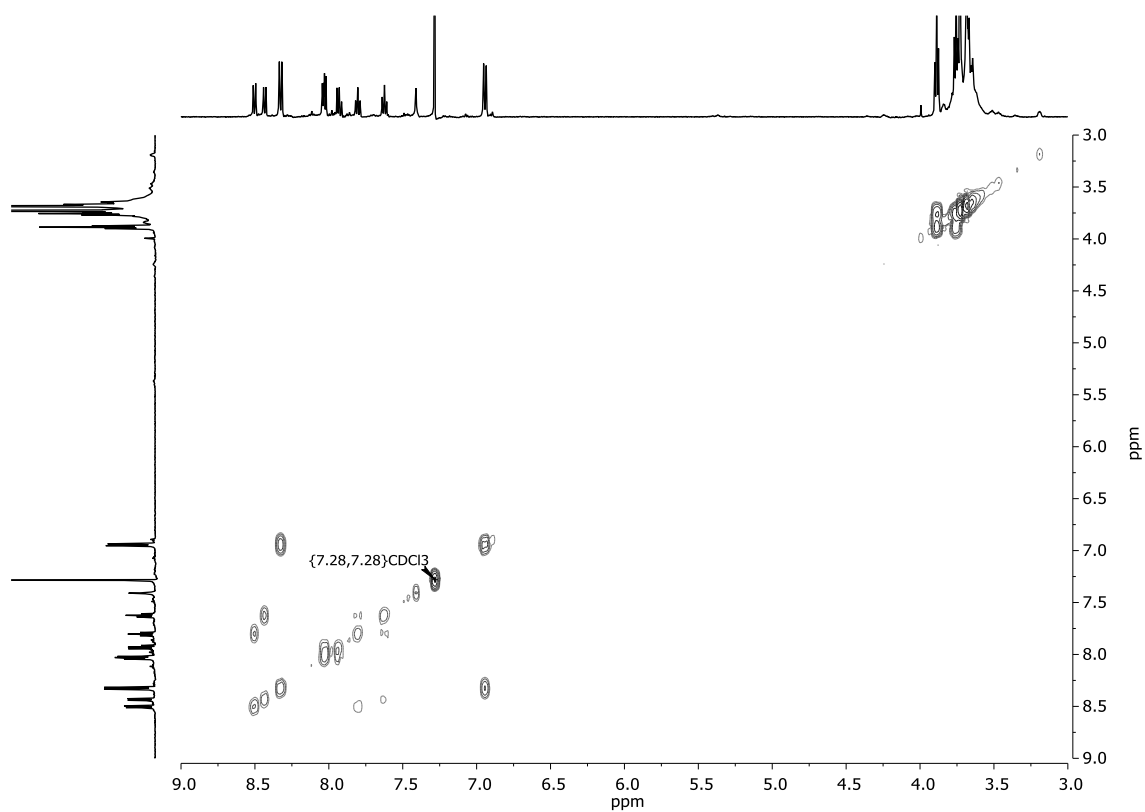
g-HSQC (CDCl₃)
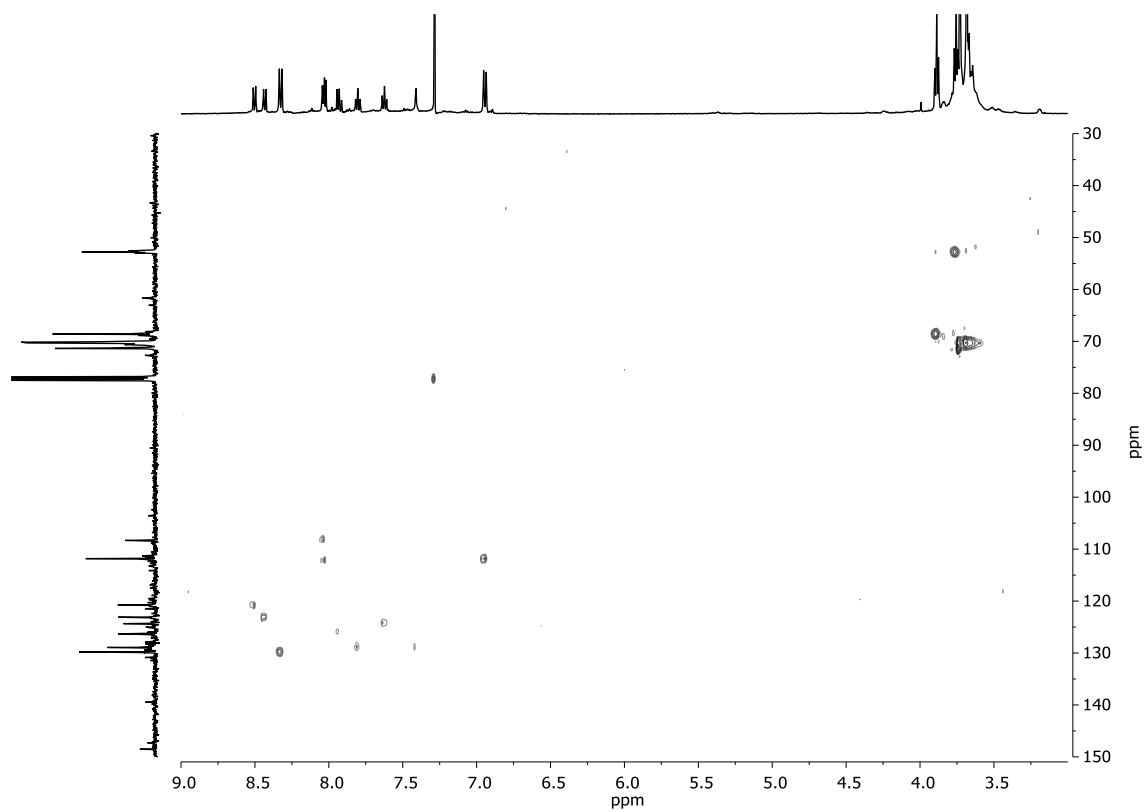
^{13}C-NMR (CDCl$_3$)
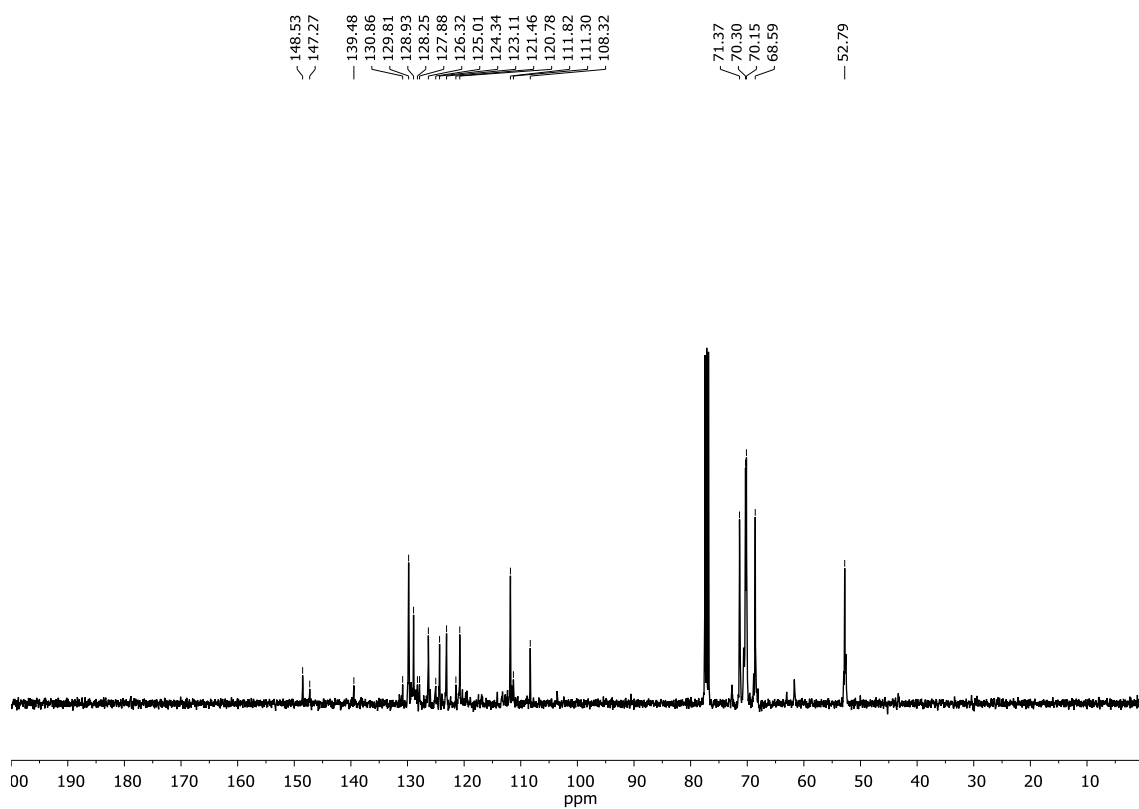
135-DEPT (CDCl$_3$)
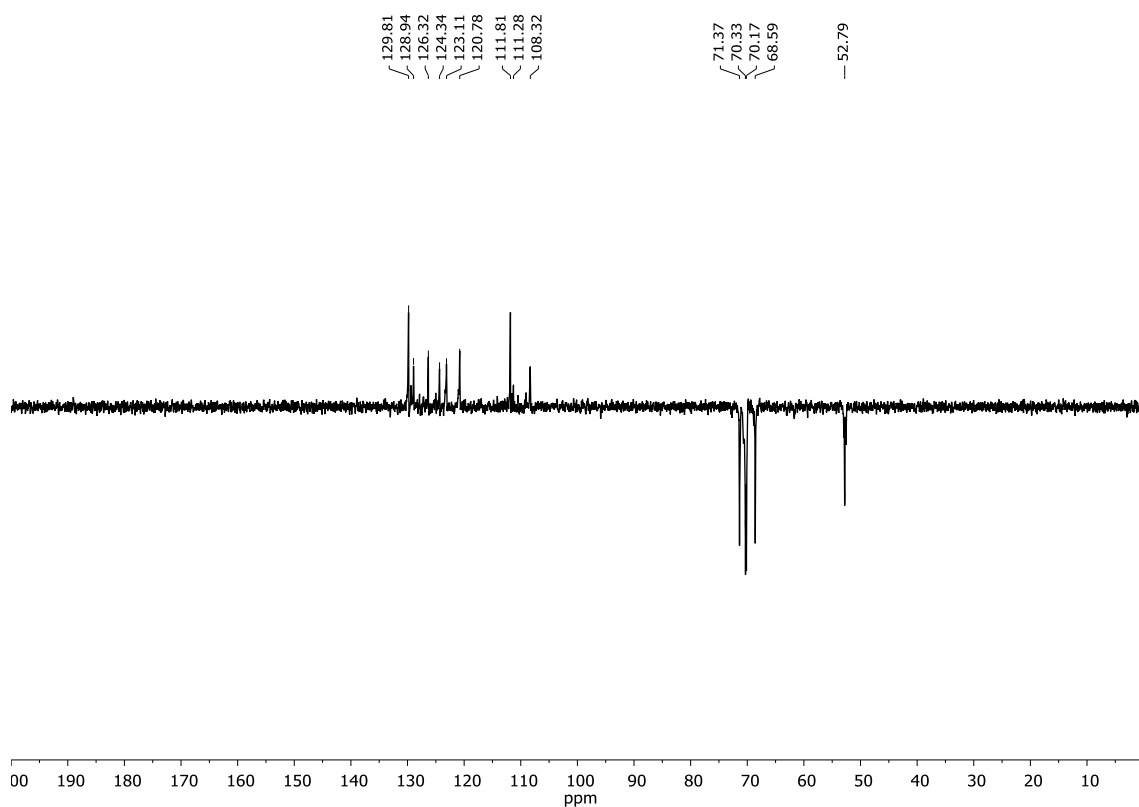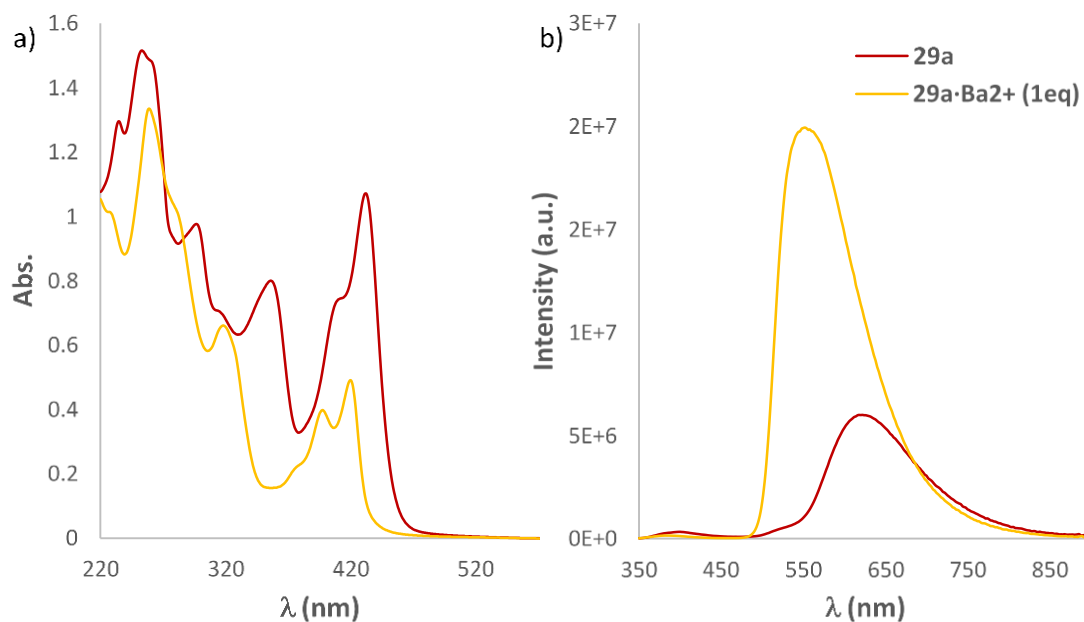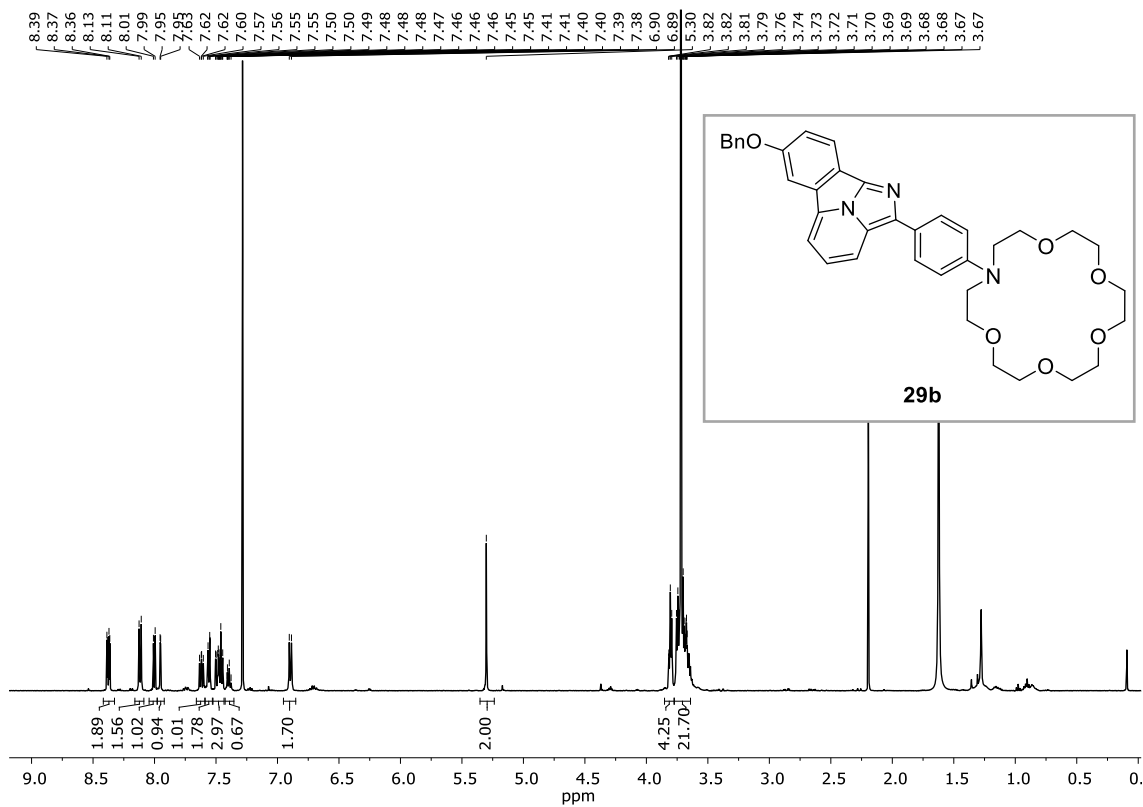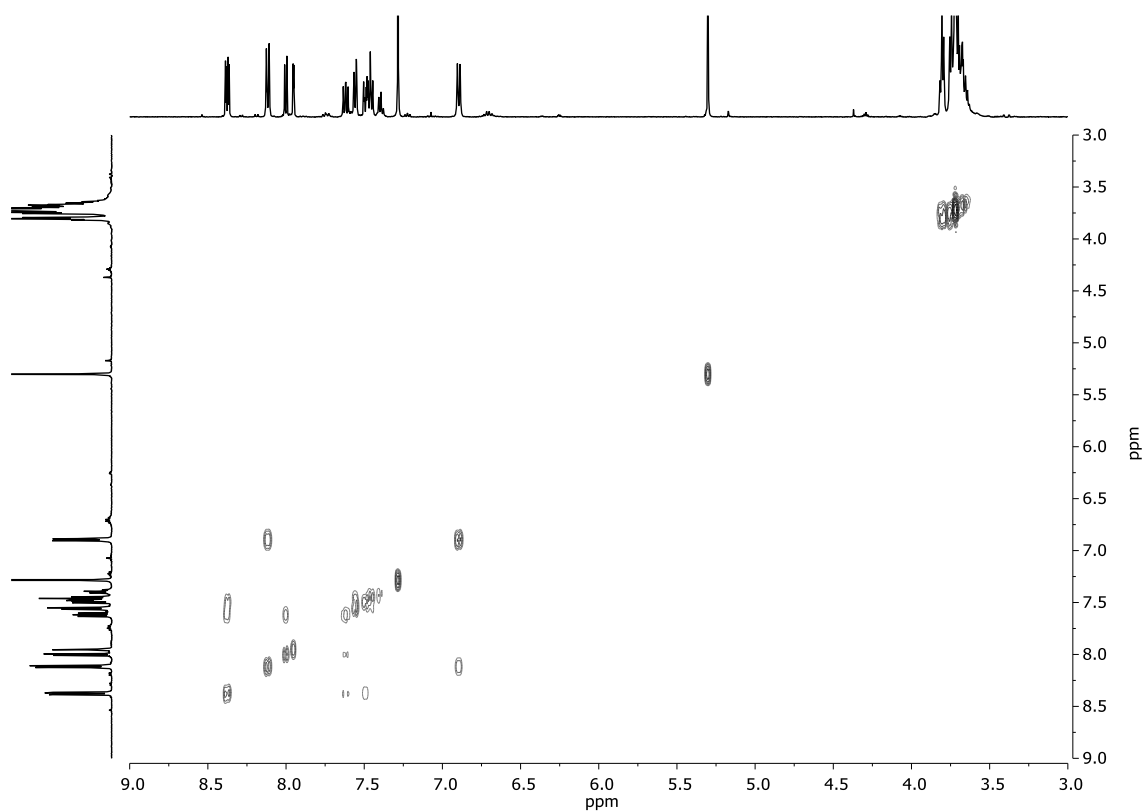
UV-VIS (a) and FS (b) (MeCN)
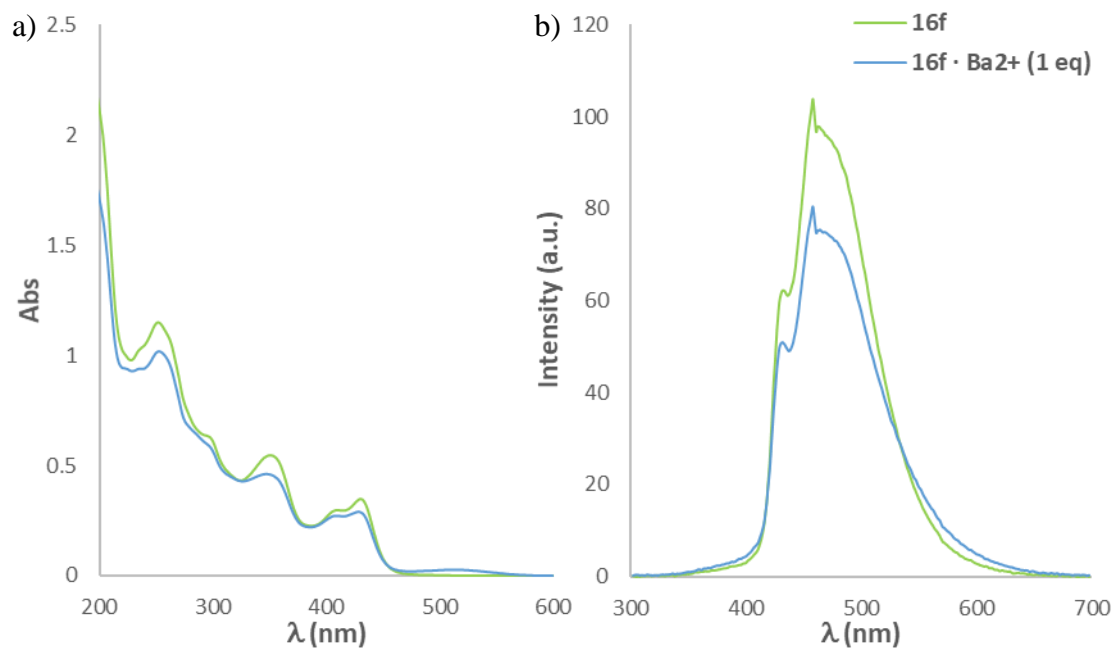
Figure 100.- *a)* Absorbance spectra for compound **16f** and **16f·Ba²⁺** (1 eq), $5 \cdot 10^{-5}$ M in MeCN, r.t. b) Fluorescence spectra for compound **16f** and **16f·Ba²⁺** (1 eq), $5 \cdot 10^{-5}$ M in MeCN, r.t., $\lambda_{exc} = 252$nm.
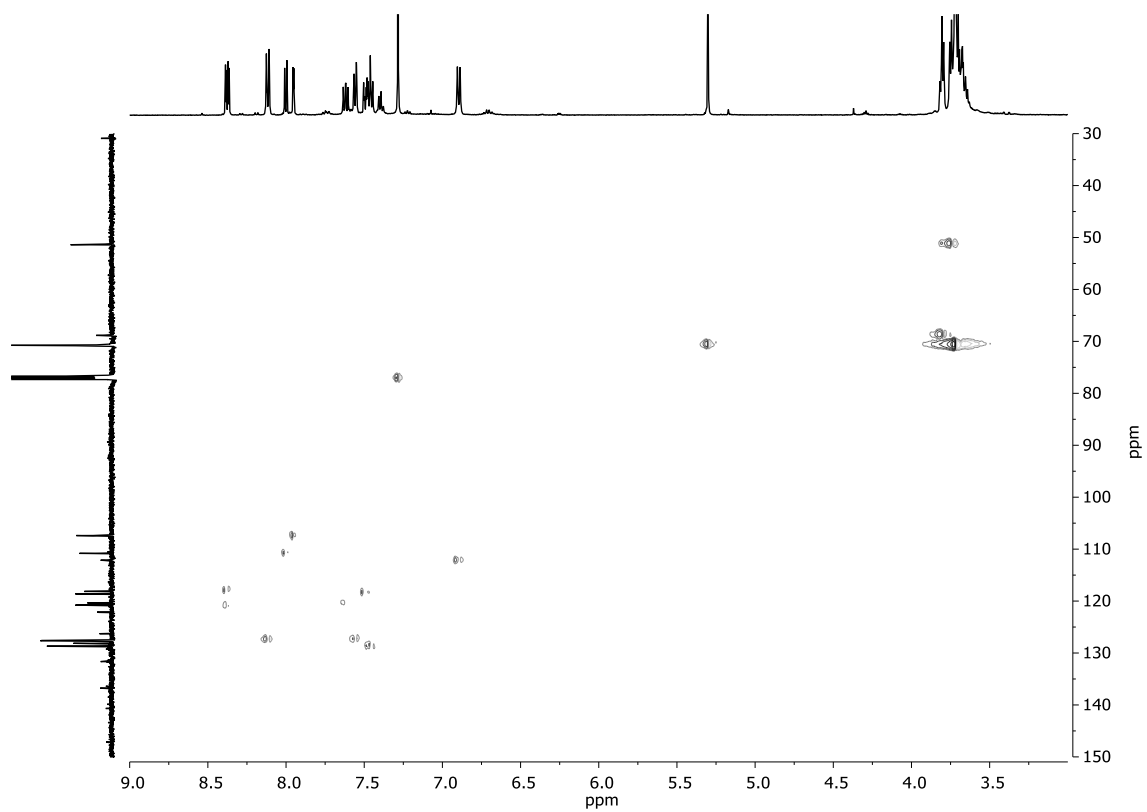
(E)-6-bromopicolinaldehyde oxime, 18

¹H-NMR (DMSO-d₆)
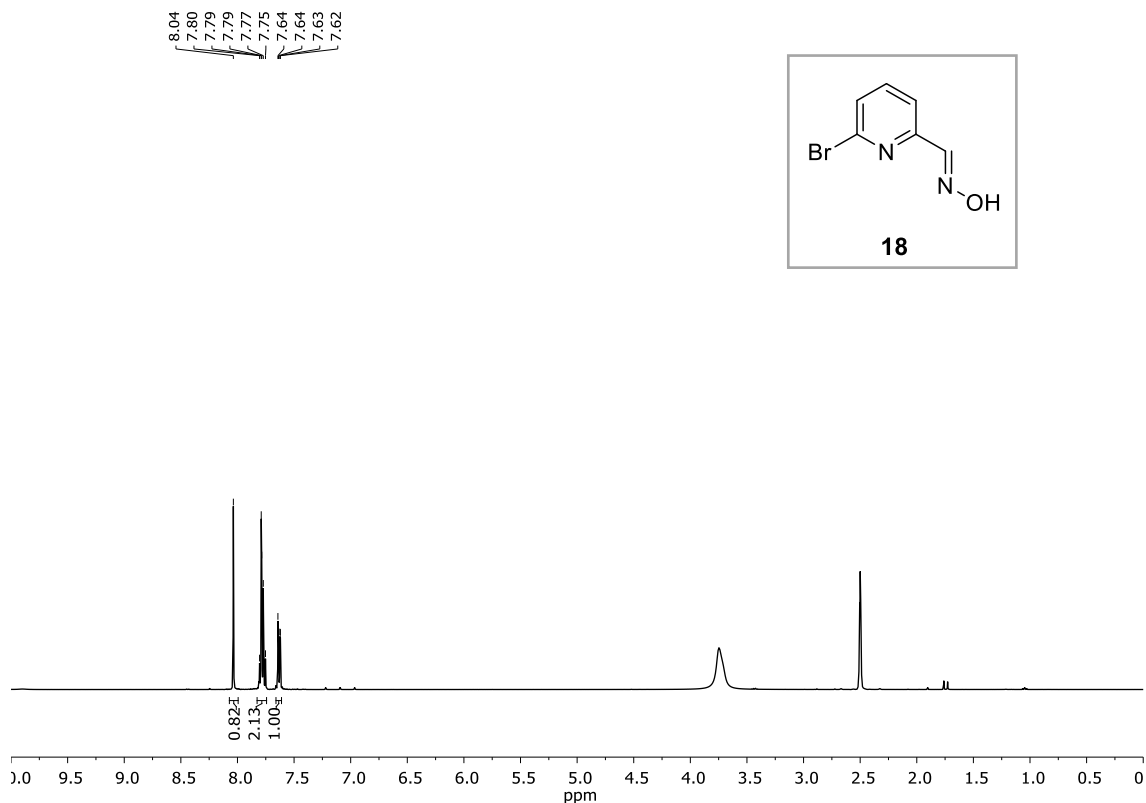
(6-bromopyridin-2-yl)methanammonium acetate, 19

^{1}H-NMR (CDCl$_3$)

7.61 7.59 7.57 7.45 7.43 7.31 7.29 7.29 — 4.22 — 1.96

1.00 0.90 1.10 1.84 5.94

).0 9.5 9.0 8.5 8.0 7.5 7.0 6.5 6.0 5.5 5.0 4.5 4.0 3.5 3.0 2.5 2.0 1.5 1.0 0.5 0
ppm
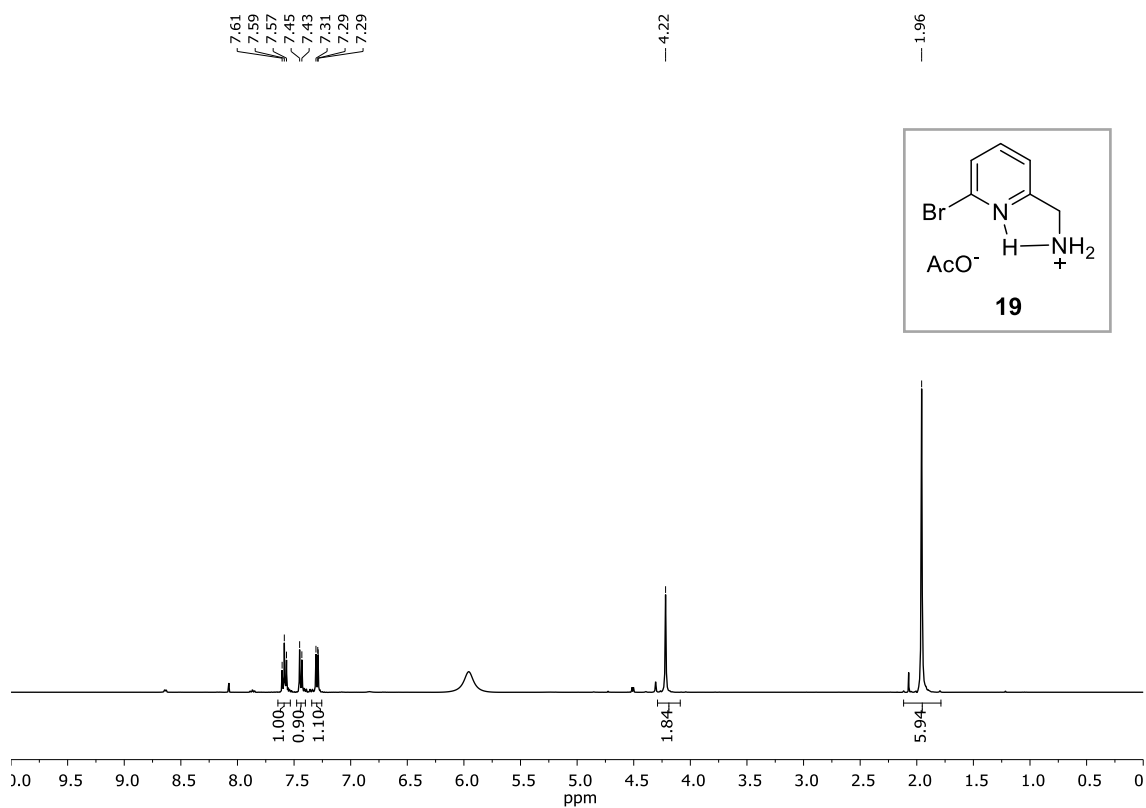
N-((6-bromopyridin-2-yl)methyl)benzamide, 20a

^{1}H-NMR (CDCl$_3$)

7.88 7.88 7.86 7.86 7.58 7.56 7.55 7.54 7.54 7.52 7.52 7.53 7.51 7.51 7.48 7.47 7.46 7.45 7.45 7.44 7.43 7.41 7.36 7.35 4.75 4.74

1.55 1.79 3.02 0.79 2.00

).0 9.5 9.0 8.5 8.0 7.5 7.0 6.5 6.0 5.5 5.0 4.5 4.0 3.5 3.0 2.5 2.0 1.5 1.0 0.5 0
ppm
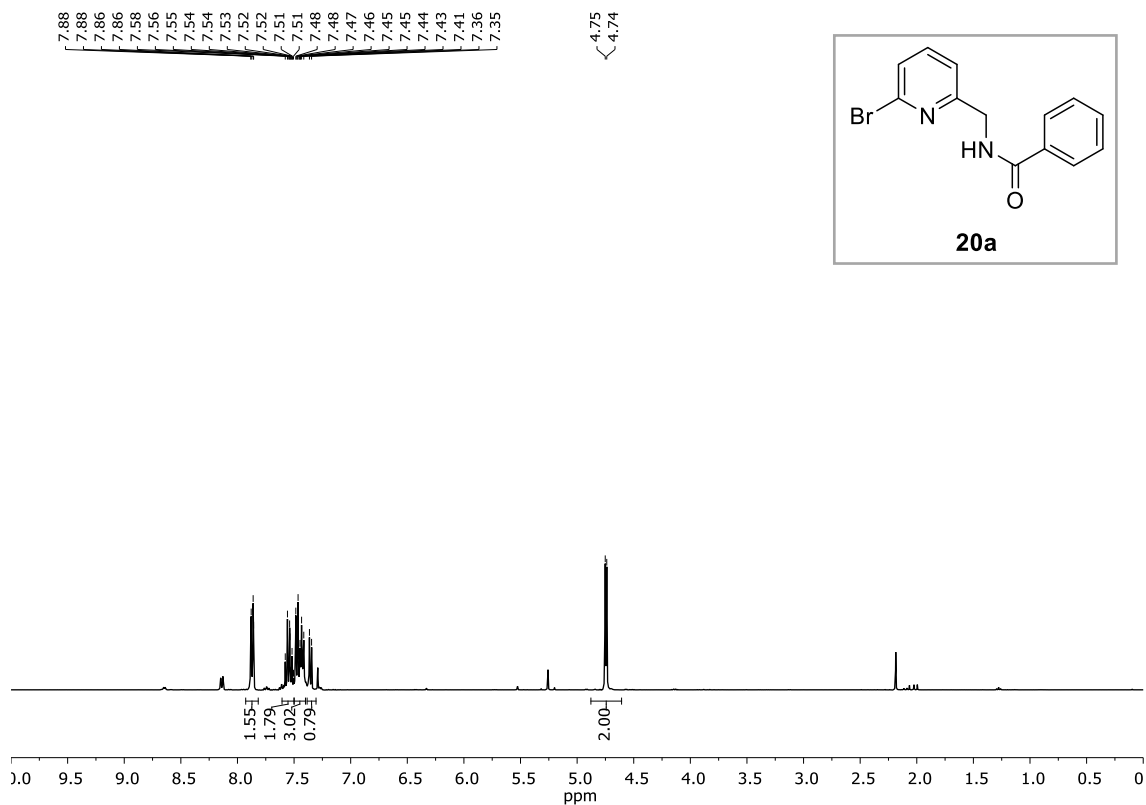
4-(benzyloxy)-N-((6-bromopyridin-2-yl)methyl)benzamide, 20b

¹H-NMR (CDCl₃)

5-bromo-3-phenylimidazo[1,5-a]pyridine, 21a

¹H-NMR (CDCl₃)
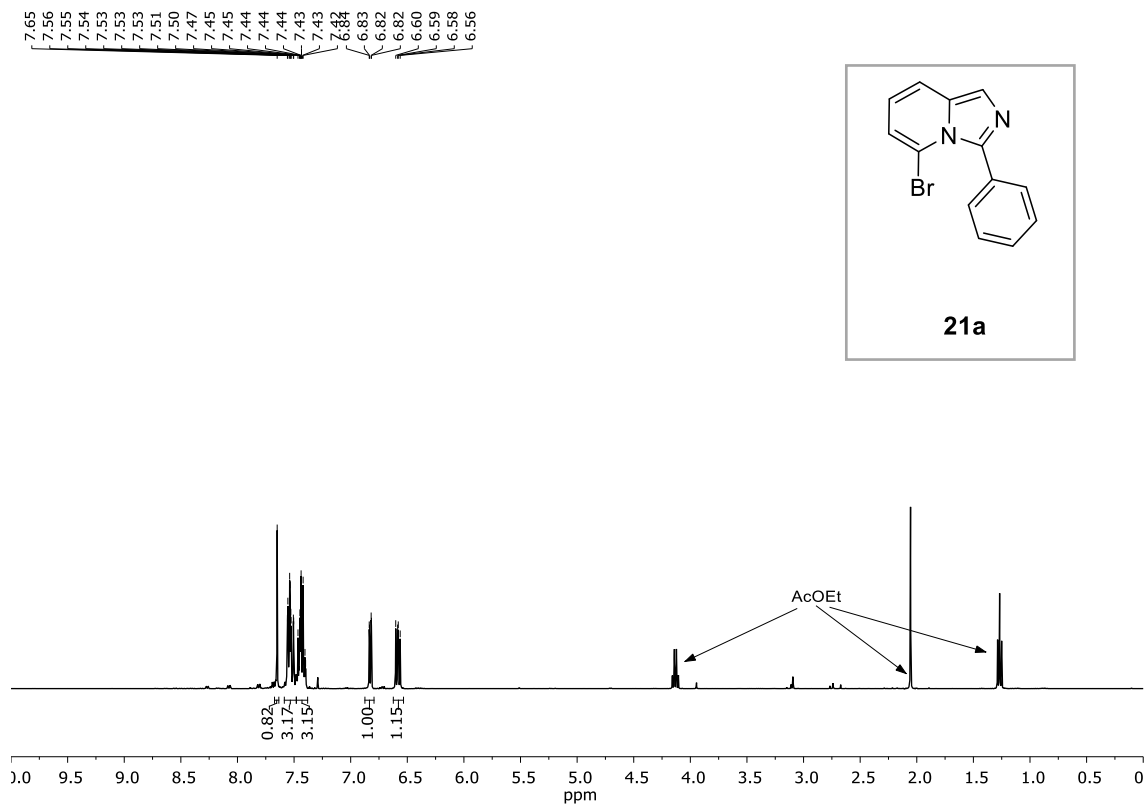
3-(4-(benzyloxy)phenyl)-5-bromoimidazo[1,5-a]pyridine, 21b

^{1}H-NMR (CDCl$_3$)
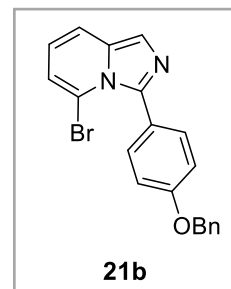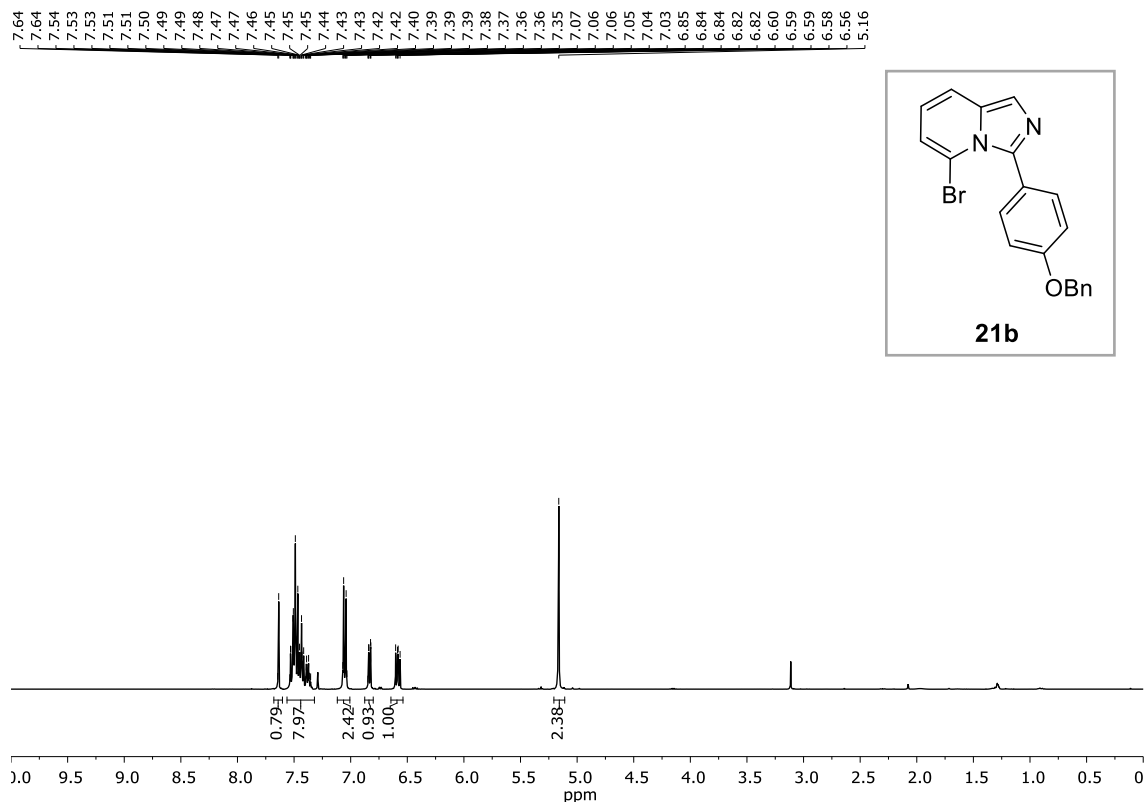
Benzo[a]imidazo[2,1,5-cd]indolizine, 22a

^{1}H-NMR (CDCl$_3$)
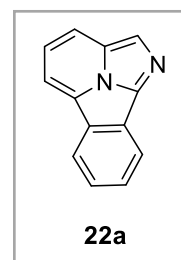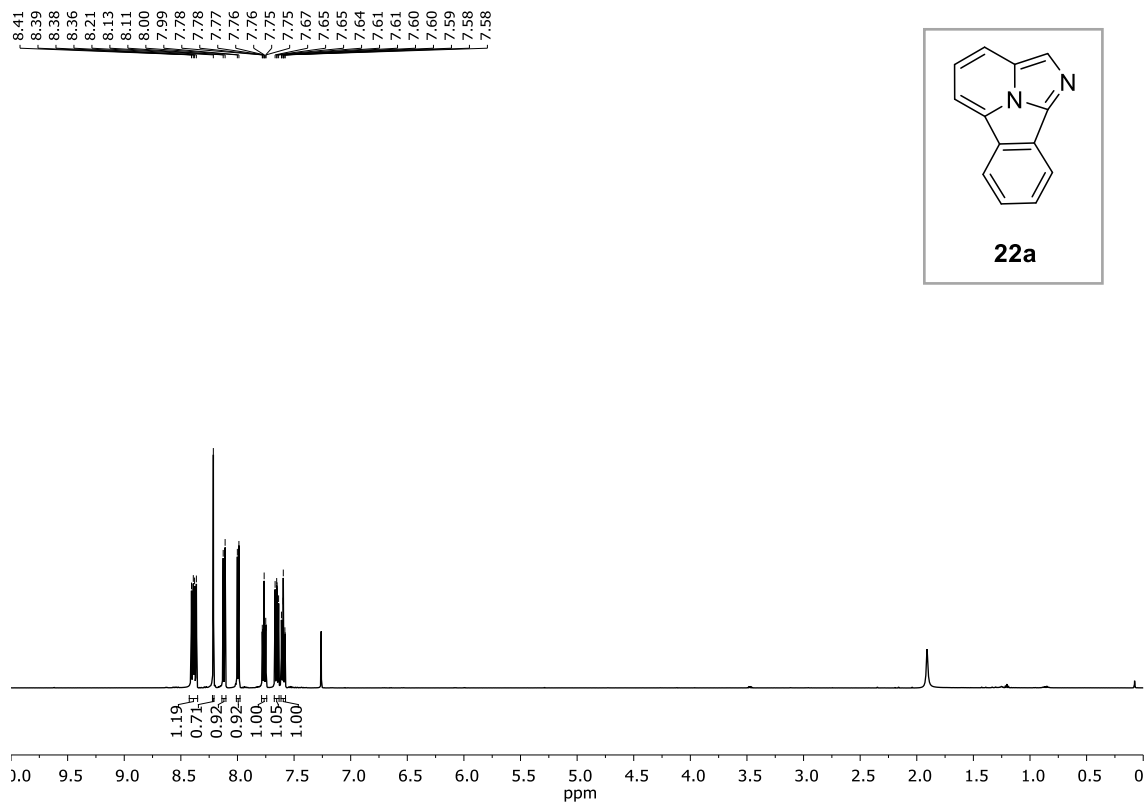
7-(benzyloxy)benzo[a]imidazo[2,1,5-cd]indolizine, 22b

¹H-NMR (CDCl₃)
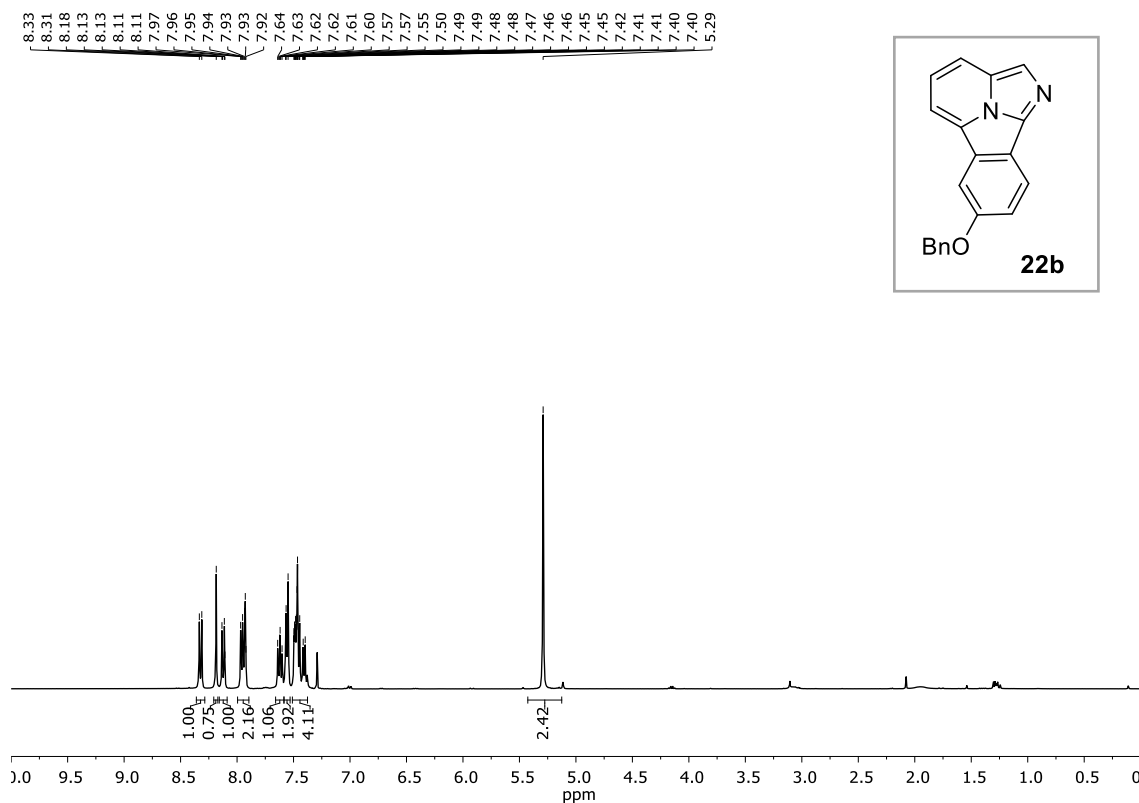
2-bromobenzo[a]imidazo[2,1,5-cd]indolizine, 23a

¹H-NMR (CDCl₃)
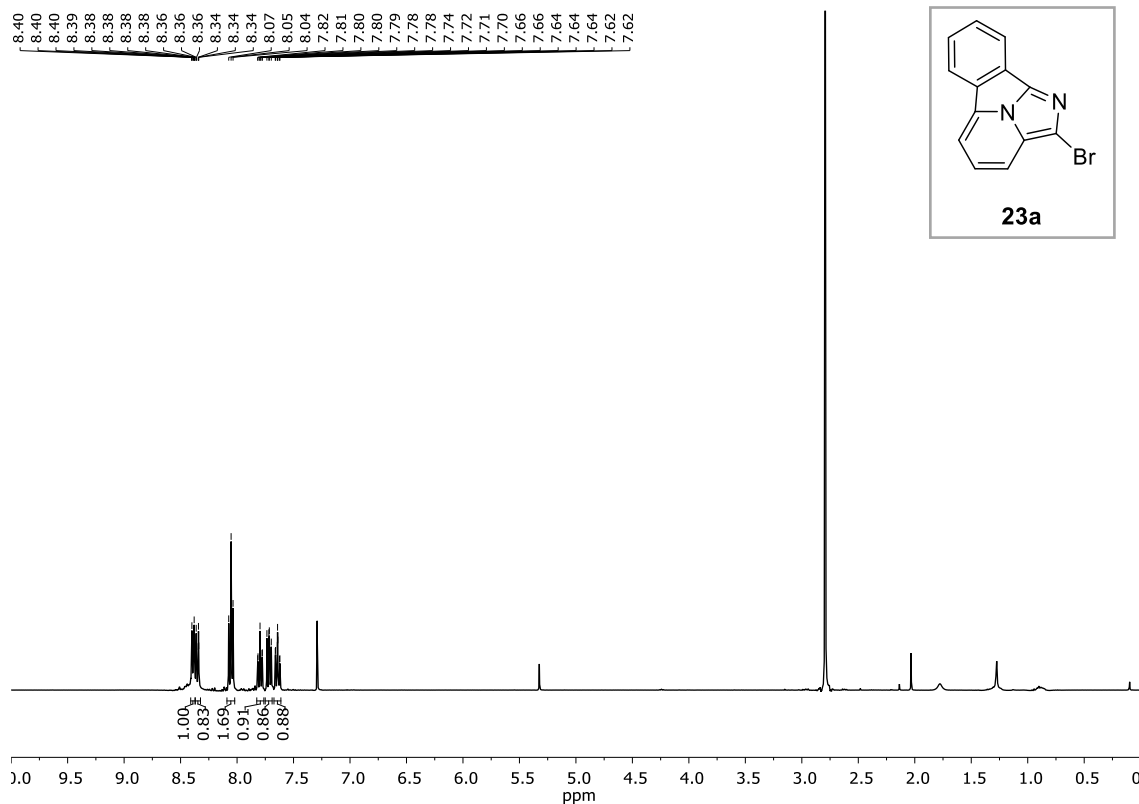
7-(benzyloxy)-2-bromobenzo[a]imidazo[2,1,5-cd]indolizine, 23b

¹H-NMR (CDCl₃)
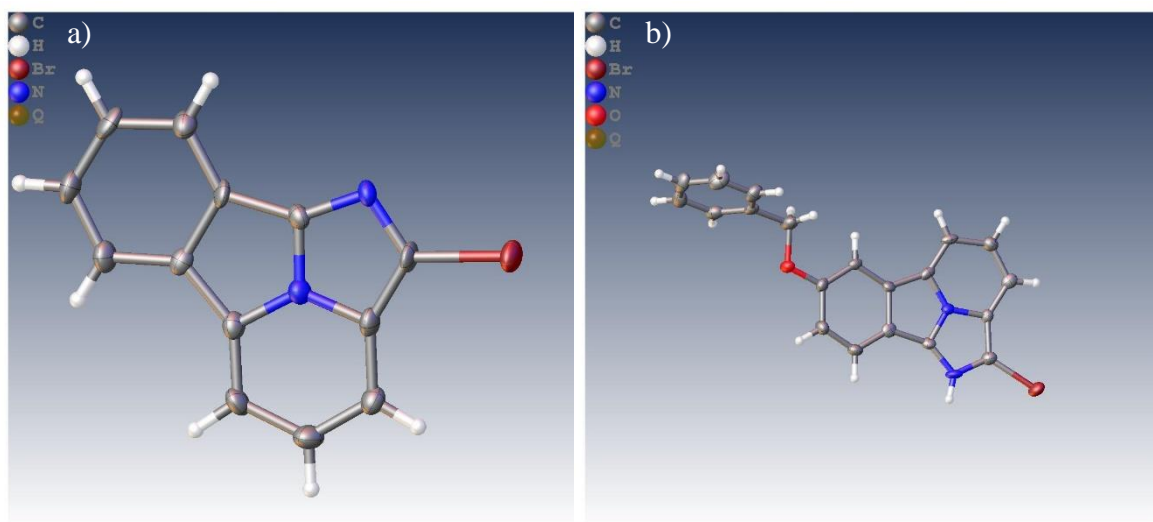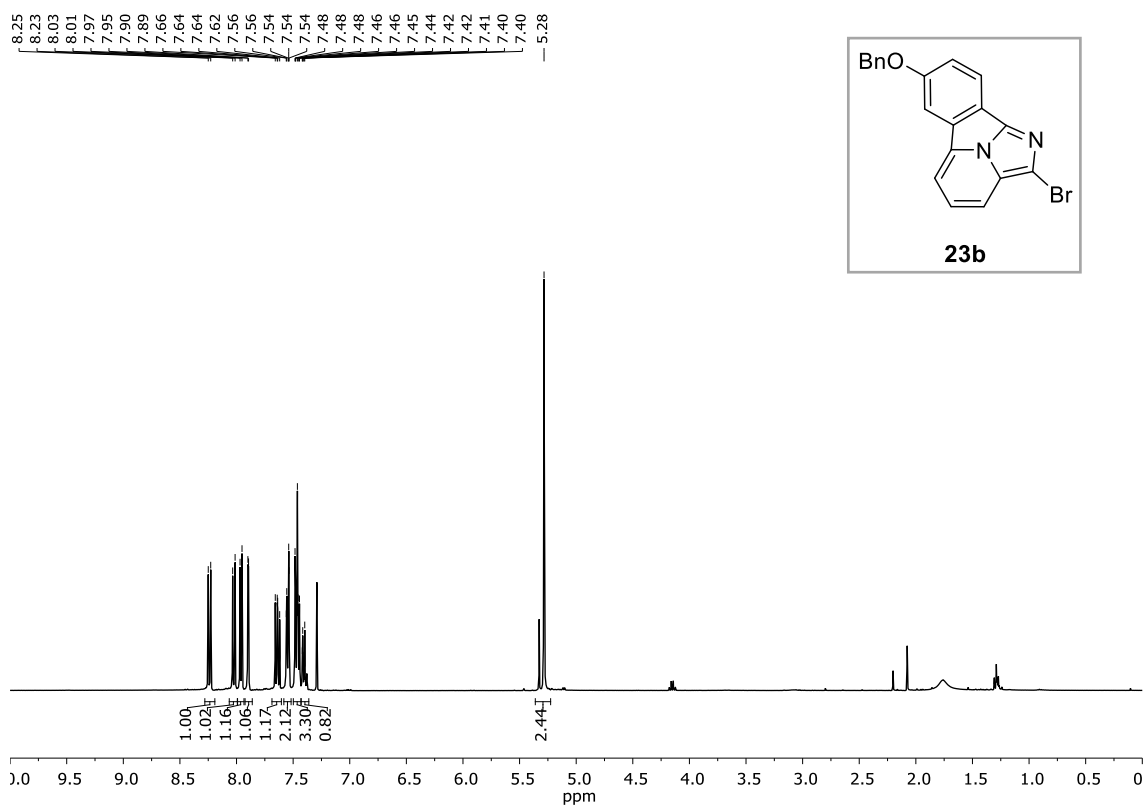
Figure 101.- X-ray diffraction structures of compounds a) **23a** and b) **23b**

16-phenyl-1,4,7,10,13-pentaoxa-16-azacyclooctadecane, 25

¹H-NMR (CDCl₃)
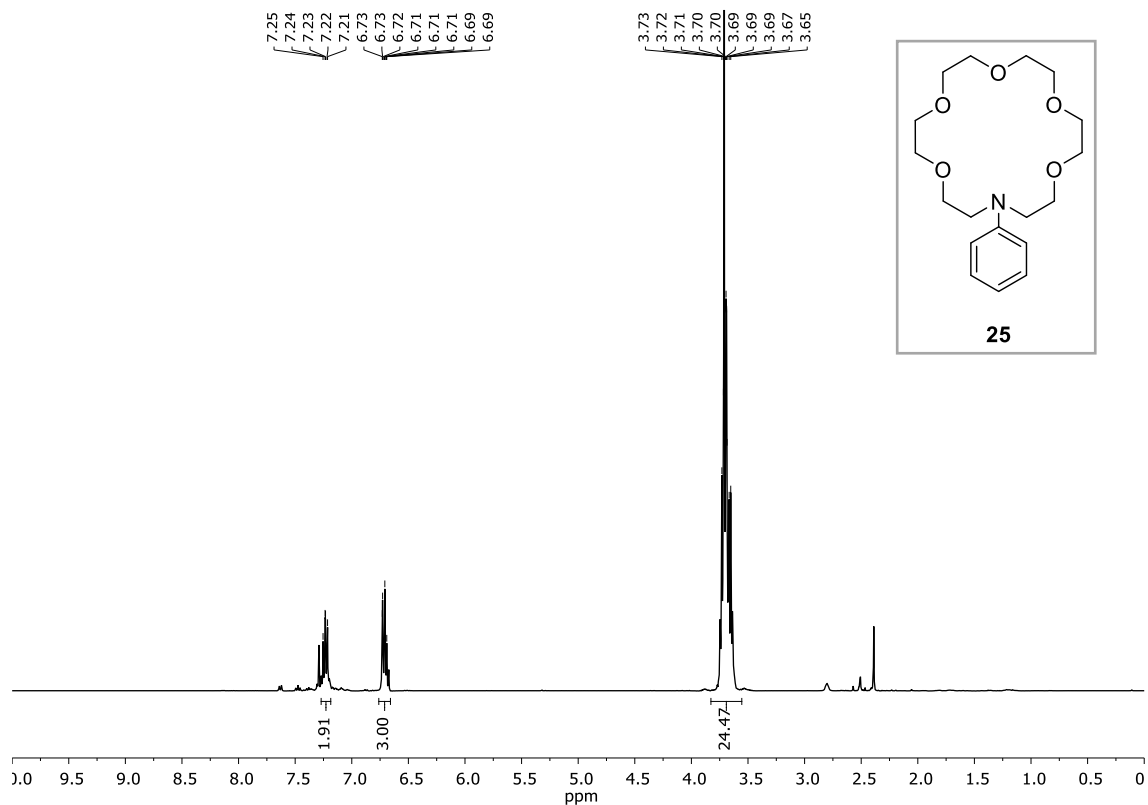
16-(4-iodophenyl)-1,4,7,10,13-pentaoxa-16-azacyclooctadecane, 26

¹H-NMR (CDCl₃)
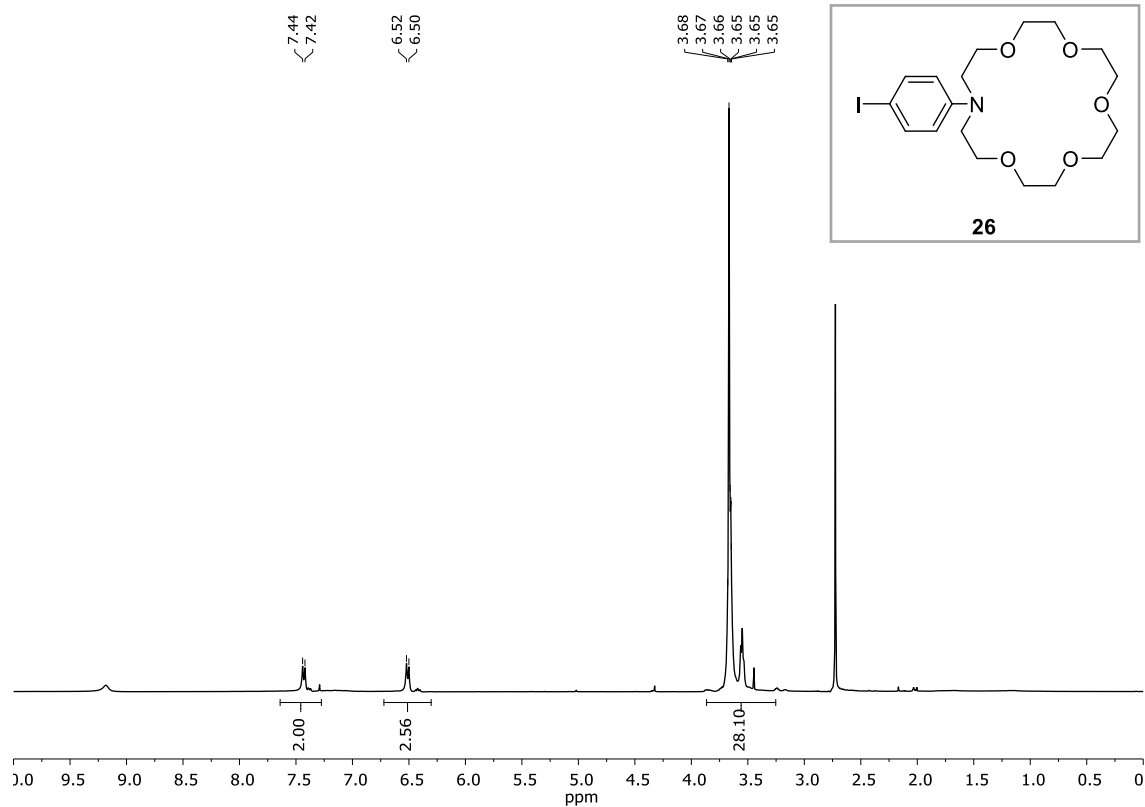
16-(4-(4,4,5,5-tetramethyl-1,3,2-dioxaborolan-2-yl)phenyl)-1,4,7,10,13-pentaoxa-16-azacyclooctadecane, 27
¹H-NMR (CDCl₃)
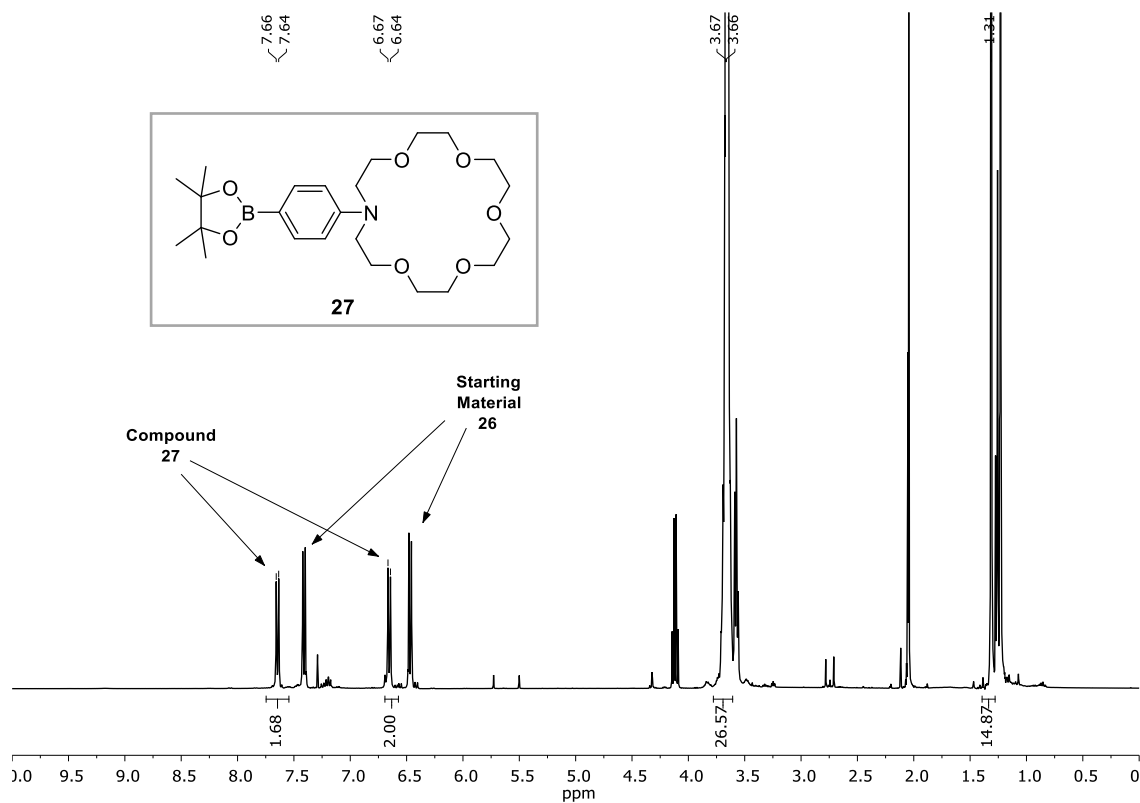
2-(4,4,5,5-tetramethyl-1,3,2-dioxaborolan-2-yl)benzo[a]imidazo[2,1,5-cd]indolizine, 28a
¹H-NMR (CDCl₃)
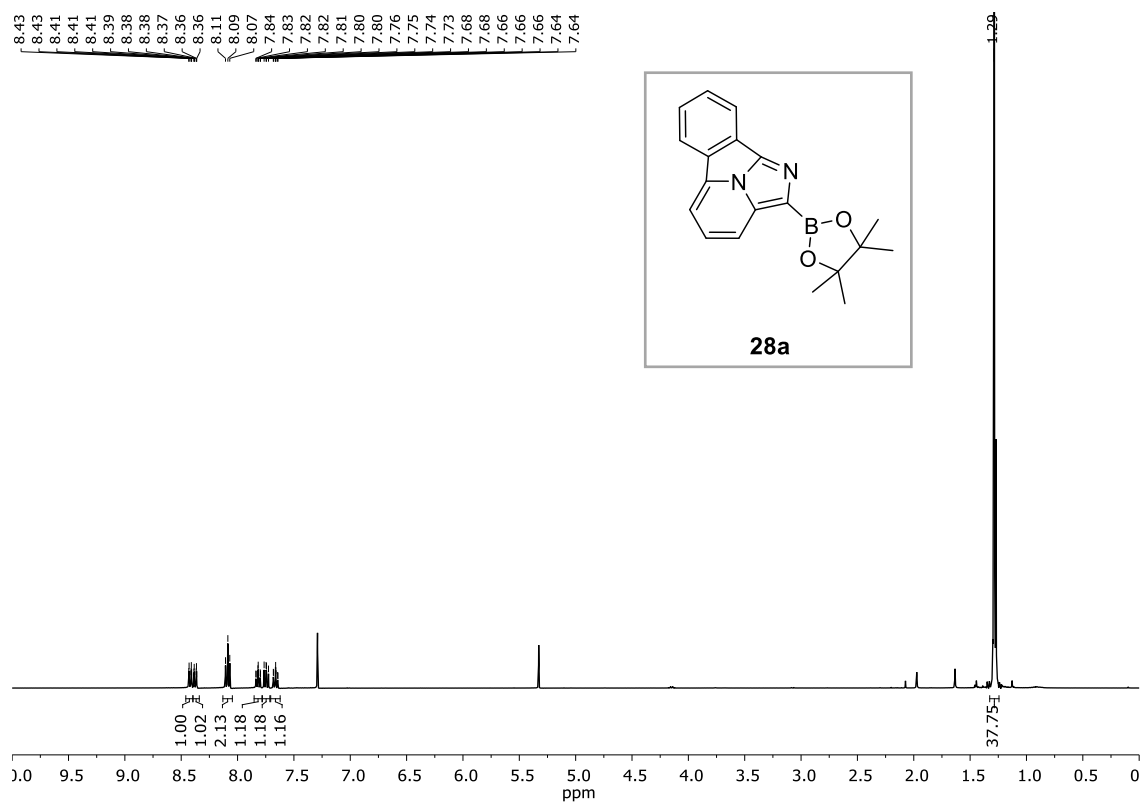
7-(benzyloxy)-2-(4,4,5,5-tetramethyl-1,3,2-dioxaborolan-2-yl)benzo[a]imidazo[2,1,5-cd]indolizine, 28b

^{1}H-NMR (CDCl$_3$)
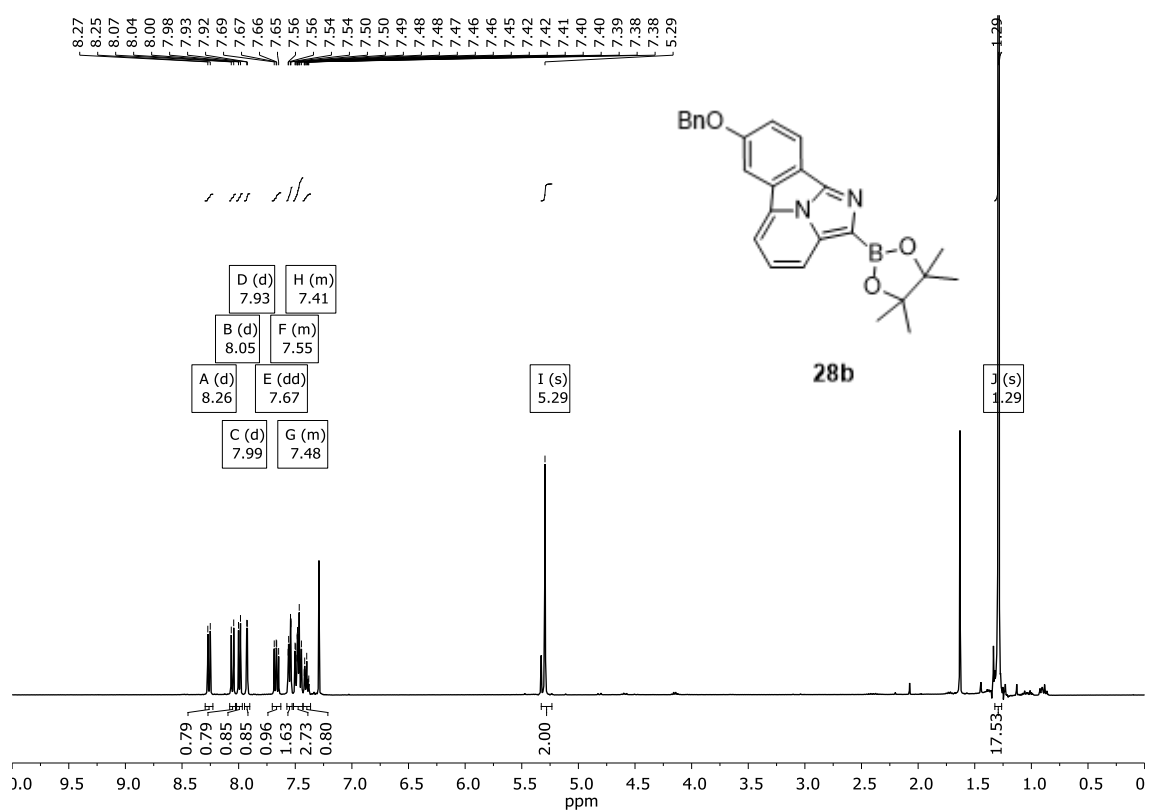
16-(4-(benzo[a]imidazo[2,1,5-cd]indolizin-2-yl)phenyl)-1,4,7,10,13-pentaoxa-16-azacyclooctadecane, 29a

^{1}H-NMR (CDCl$_3$)

g-COSY (CDCl$_3$)

g-HSQC (CDCl₃)

¹³C-NMR (CDCl₃)

147.54
141.60
136.61
130.48
129.22
129.14
128.01
127.77
126.57
126.42
124.52
123.20
122.51
121.24
120.03
118.14
112.51
111.08

70.98
69.17

51.62
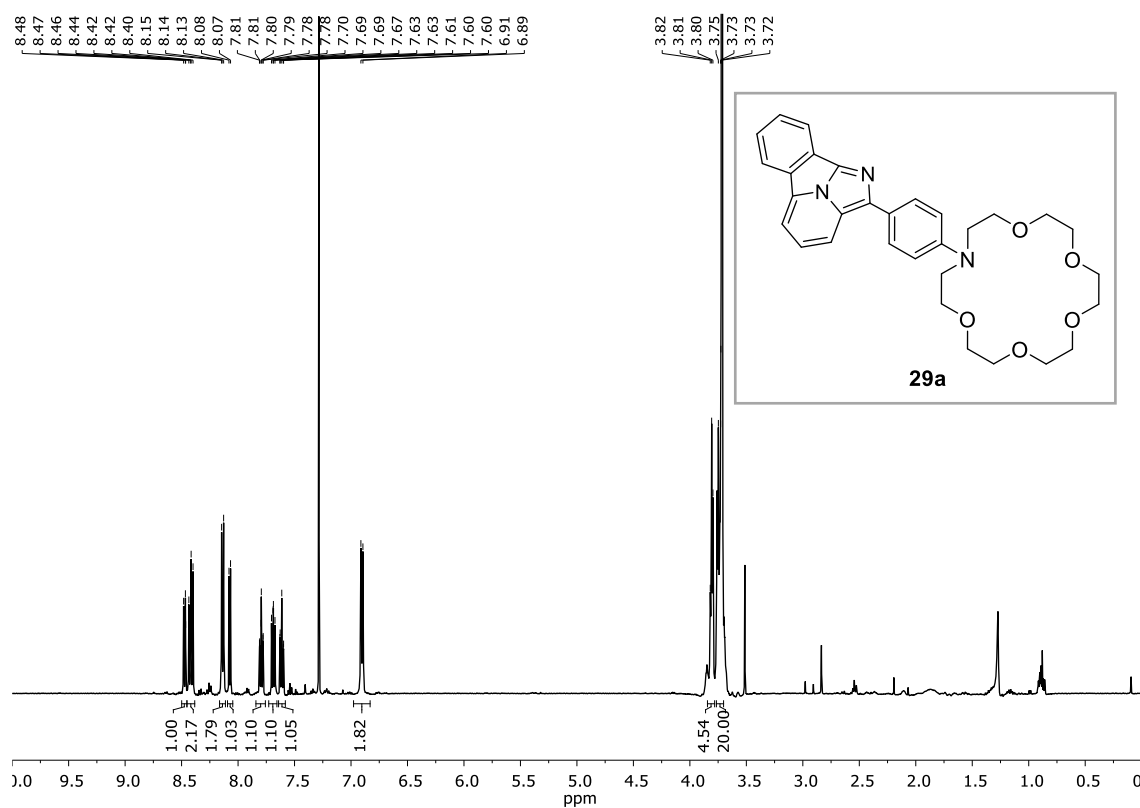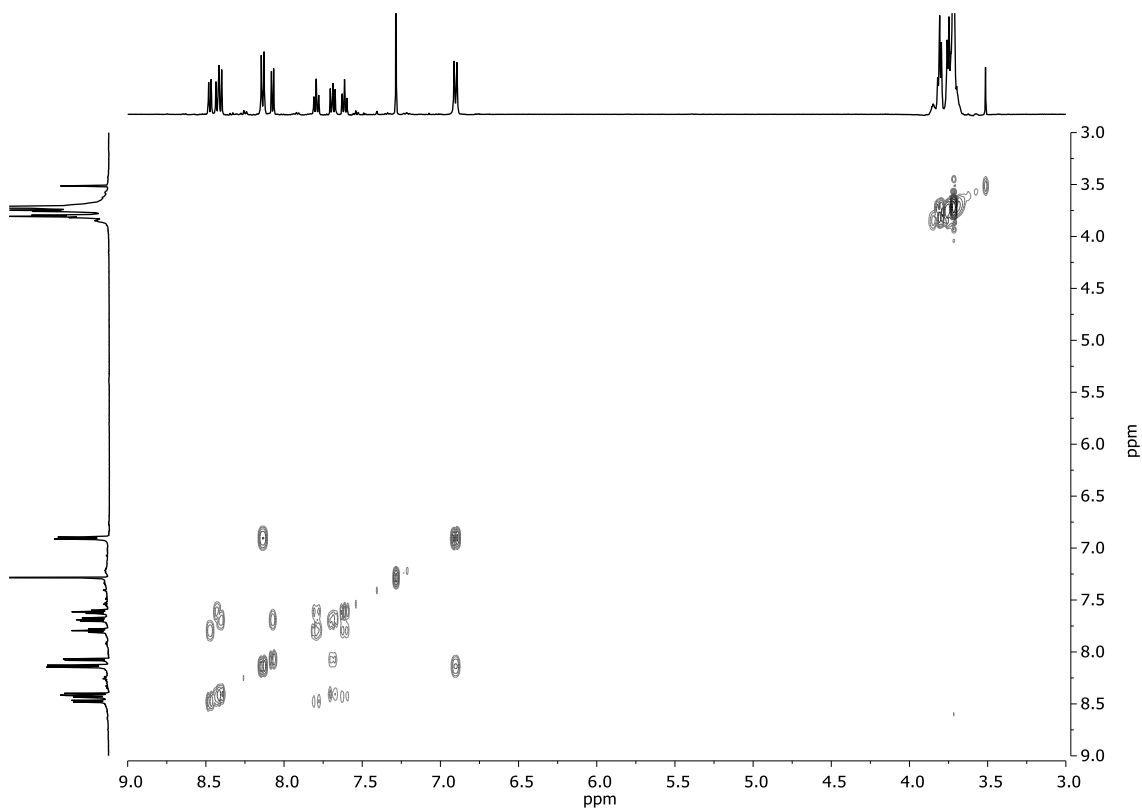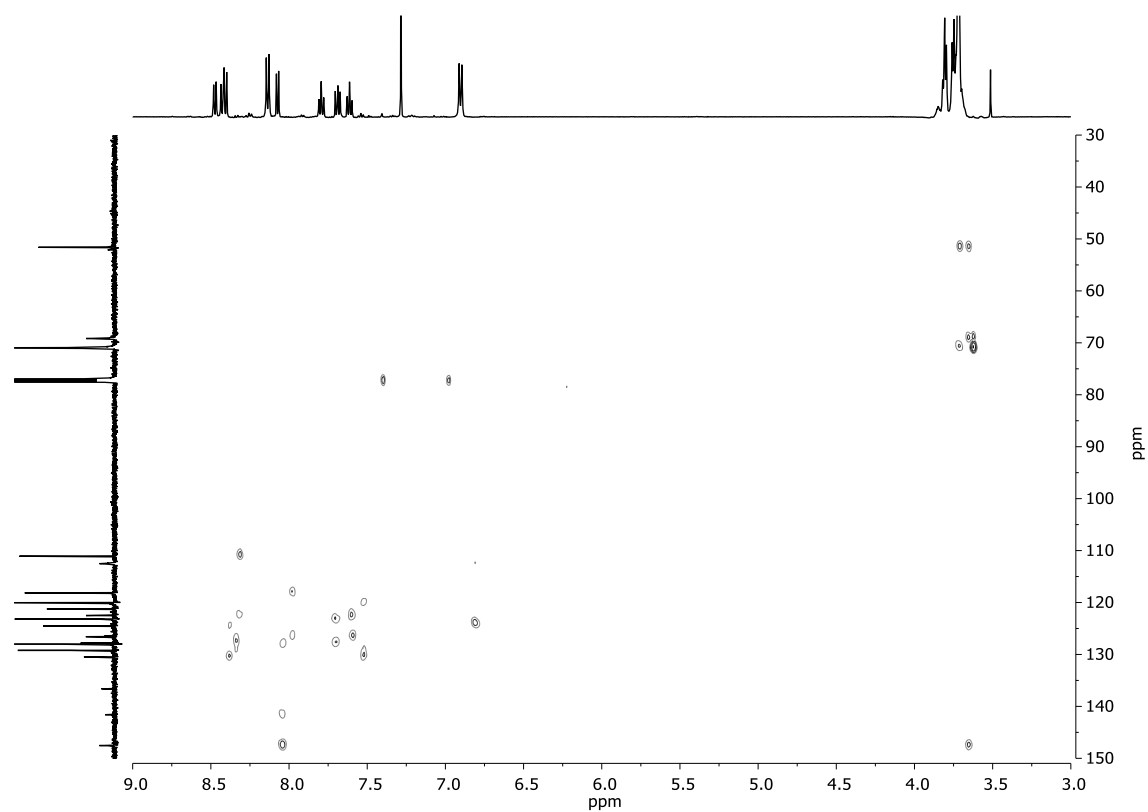
UV-VIS (a) and FS (b) (MeCN)

Figure 102.- a) Absorbance spectra for compound **29a** and **29a·Ba^{2+}** (1 eq), $5 \cdot 10^{-5}$ M in MeCN, r.t. b) Fluorescence spectra for compound **29a** and **29a·Ba^{2+}** (1 eq), $5 \cdot 10^{-5}$ M in MeCN, r.t., λ_{exc} = 325 nm.

16-(4-(7-(benzyloxy)benzo[a]imidazo[2,1,5-cd]indolizin-2-yl)phenyl)-1,4,7,10,13-pentaoxa-16-azacyclooctadecane, 29b

^{1}H-NMR (CDCl$_3$)
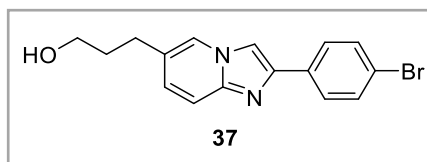
g-COSY (CDCl₃)

g-HSQC (CDCl₃)

^{13}C-NMR (CDCl$_3$)

156.60
147.14
140.68
139.88
136.78
136.40
131.65
128.69
128.14
127.65
127.58
126.28
122.19
122.11
120.78
120.35
118.61
118.14
112.14
110.82
107.38
70.75
68.85
51.38

135-DEPT (CDCl$_3$)

128.68
128.13
127.64
127.57
120.77
120.35
118.61
118.13
110.81
107.37
77.19
70.73
68.84
51.38
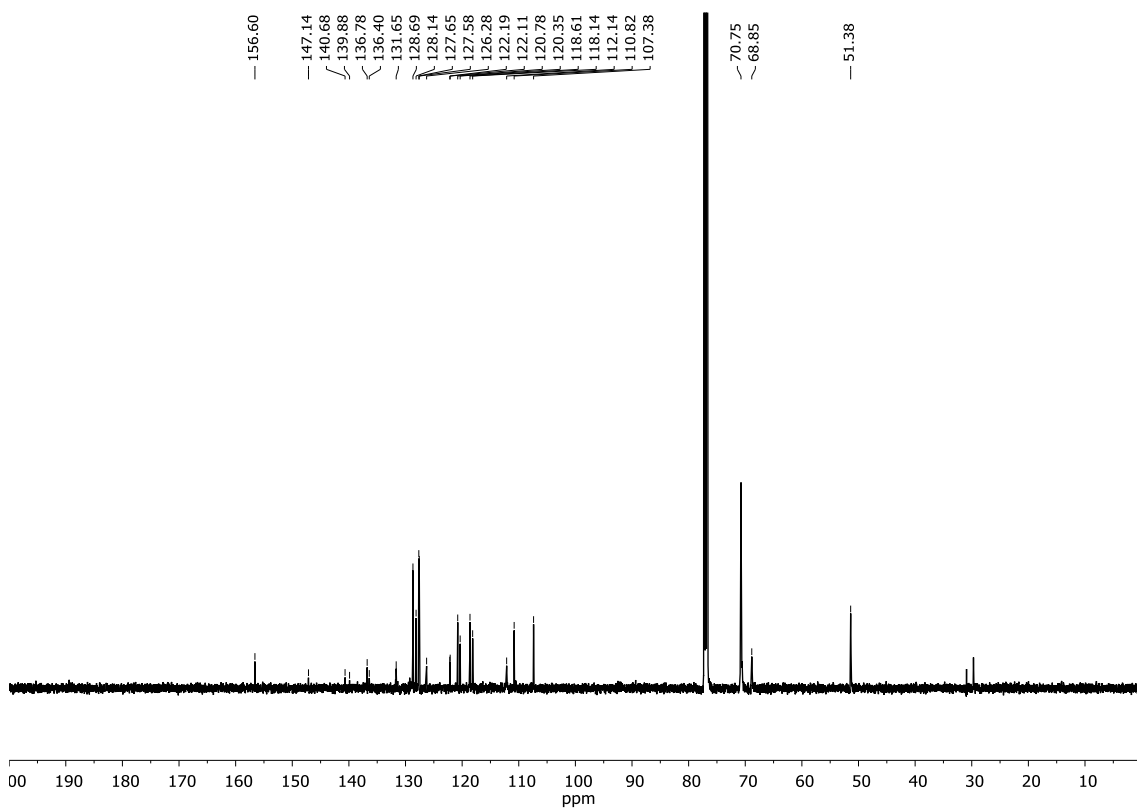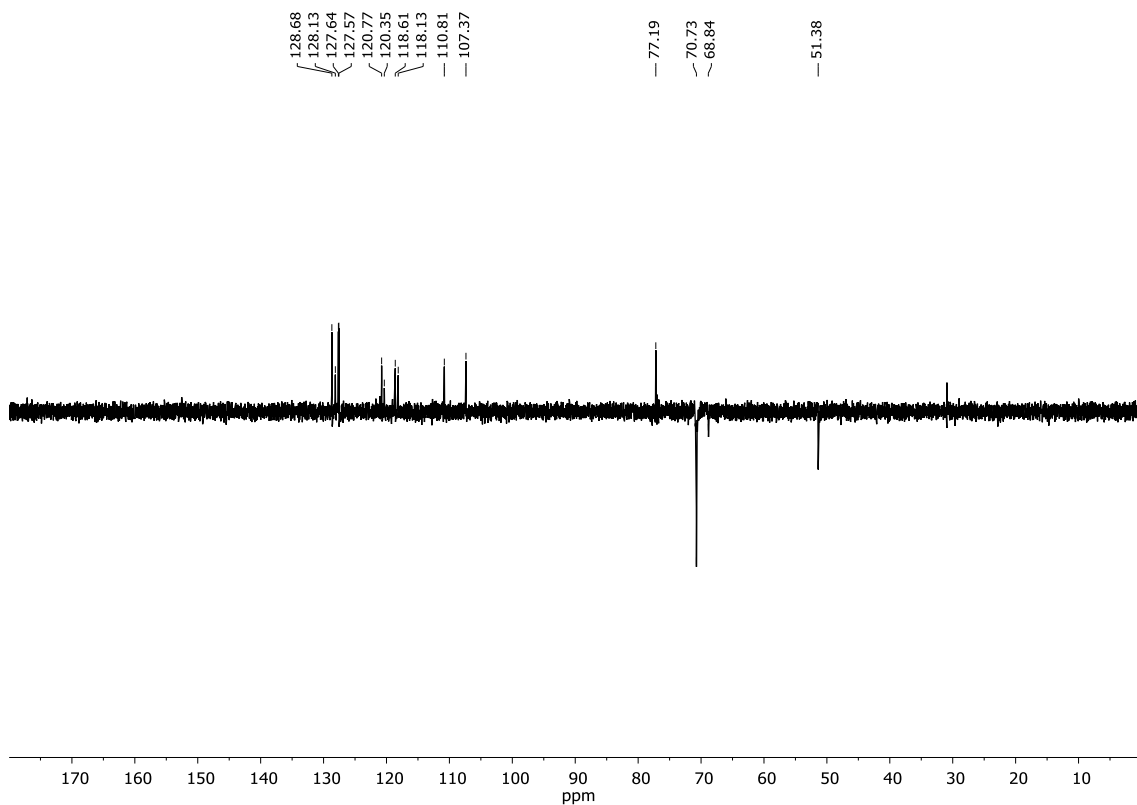
UV-VIS (a) and FS (b) (MeCN)
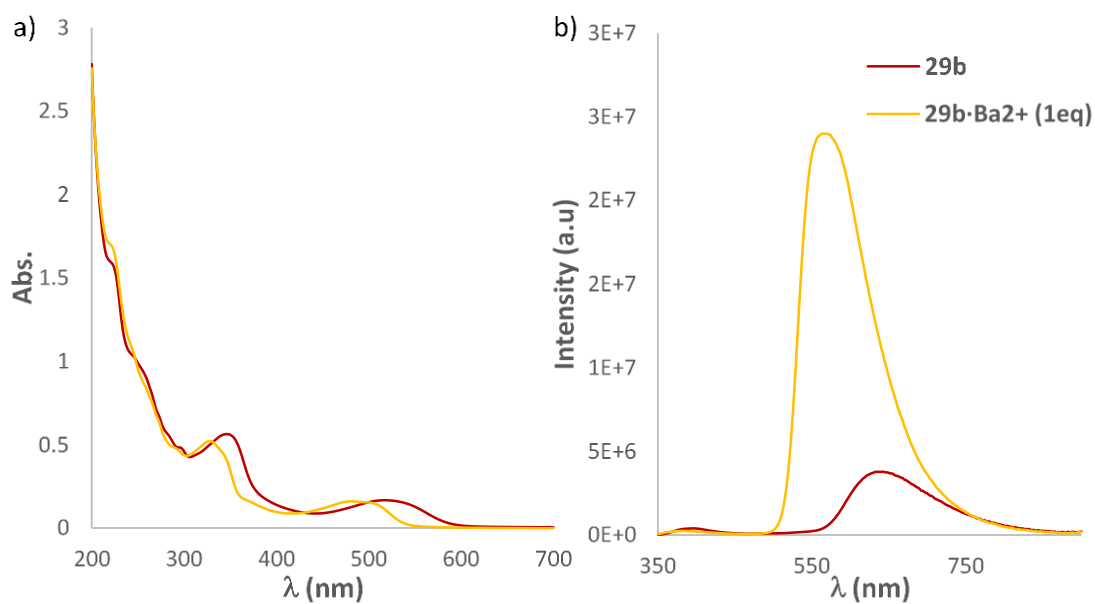
Figure 103.- a) Absorbance spectra for compound **29b** and **29b·Ba^{2+}** (1 eq), $5 \cdot 10^{-5}$ M in MeCN, r.t. b) Fluorescence spectra for compound **29b** and **29b·Ba^{2+}** (1 eq), $5 \cdot 10^{-5}$ M in MeCN, r.t., λ_{exc} = 325 nm.

(2-(4-(1,4,7,10,13-pentaoxa-16-azacyclooctadecan-16-yl)phenyl)imidazo[1,2-a]pyridin-7-yl)methanol, 30

^{1}H-NMR (CDCl$_3$)
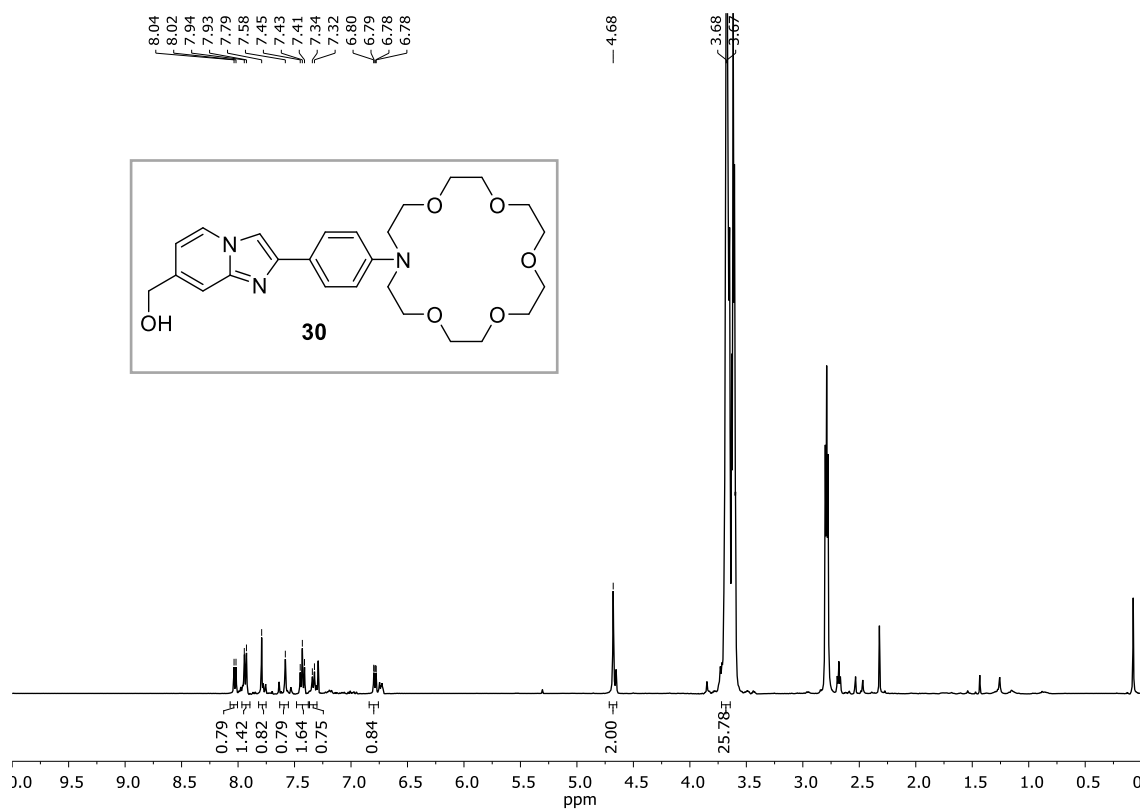
3-bromo-2-(4-bromophenyl)imidazo[1,2-a]pyridine, 31

^{1}H-NMR (CDCl$_3$)

8.21
8.19
8.05
8.05
8.04
8.03
7.68
7.66
7.66
7.65
7.64
7.63
7.62
7.33
7.32
7.31
7.31
7.30
7.28
7.00
6.99
6.98
6.98

0.77
2.00
0.91
2.21
1.00
1.13

).0 9.5 9.0 8.5 8.0 7.5 7.0 6.5 6.0 5.5 5.0 4.5 4.0 3.5 3.0 2.5 2.0 1.5 1.0 0.5 0
ppm
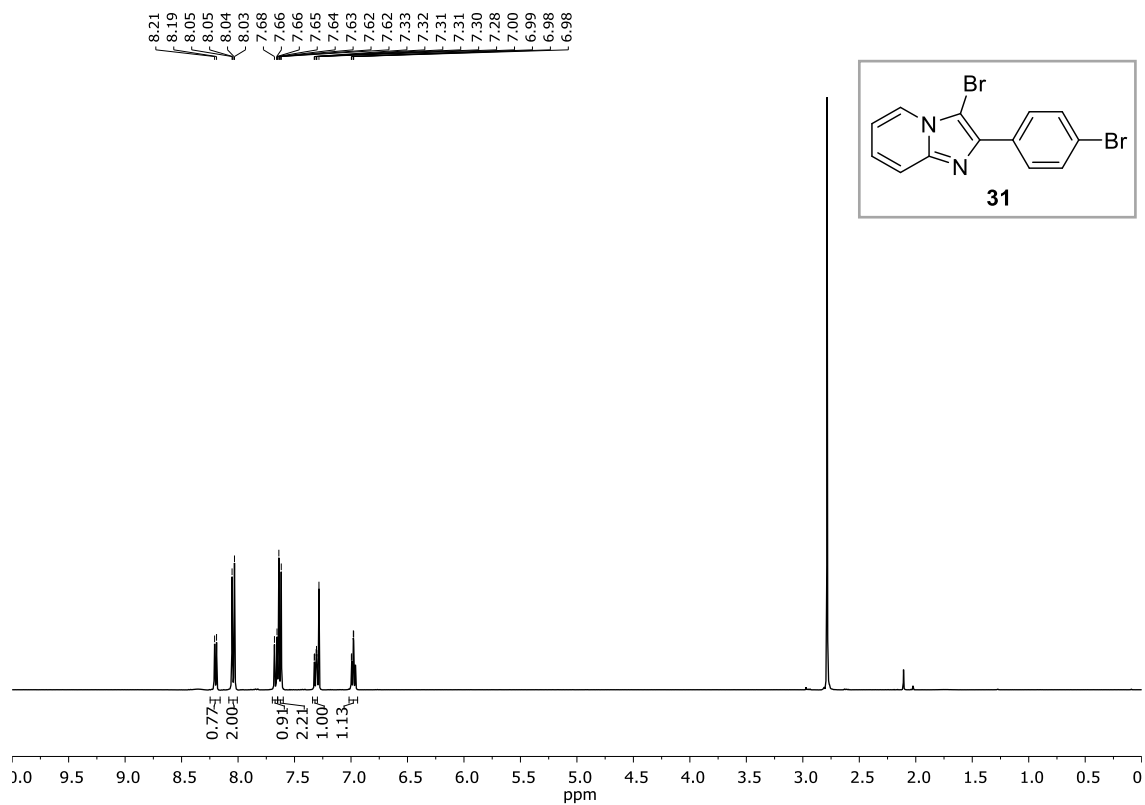
5-bromopyridin-2-amine, 32

^{1}H-NMR (CDCl$_3$)
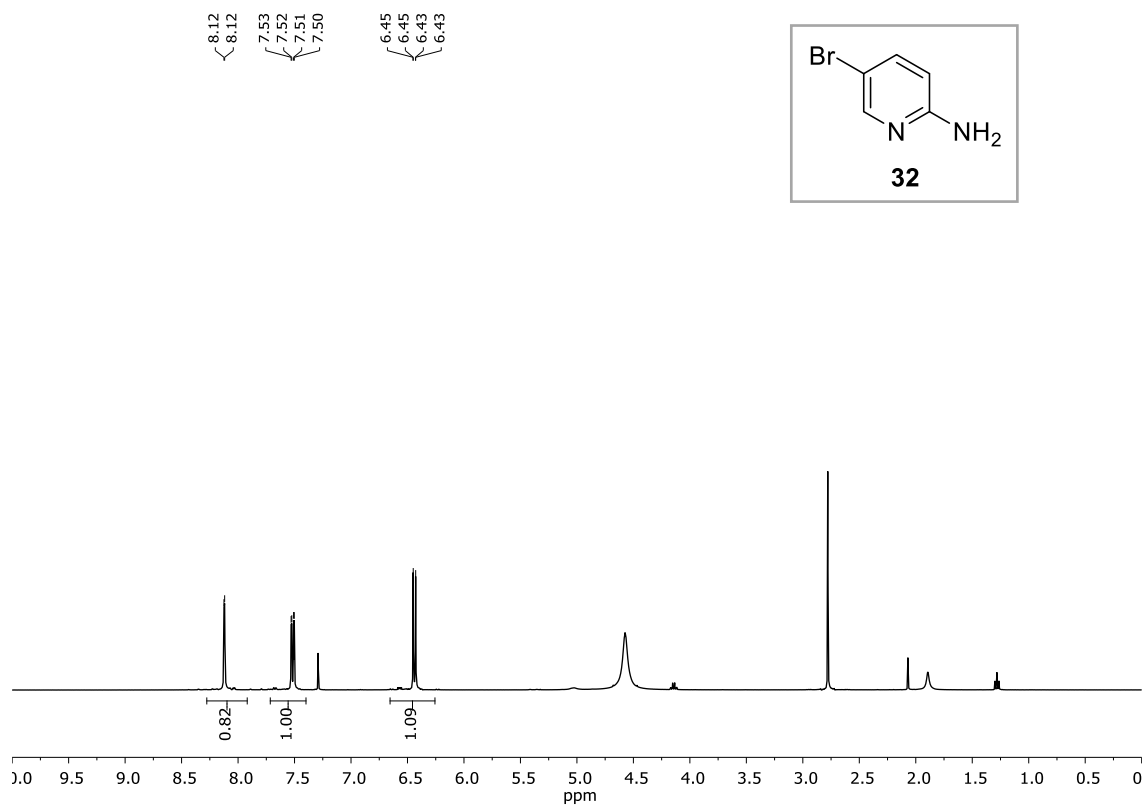
8.12
8.12
7.53
7.52
7.51
7.50
6.45
6.45
6.43
6.43

0.82
1.00
1.09

).0 9.5 9.0 8.5 8.0 7.5 7.0 6.5 6.0 5.5 5.0 4.5 4.0 3.5 3.0 2.5 2.0 1.5 1.0 0.5 0
ppm

16-(4-(4-bromoimidazo[5,1,2-cd]naphtho[2,3-a]indolizin-1-yl)phenyl)-1,4,7,10,13-pentaoxa-16-azacyclooctadecane, 33

^{1}H-NMR (CDCl$_3$)
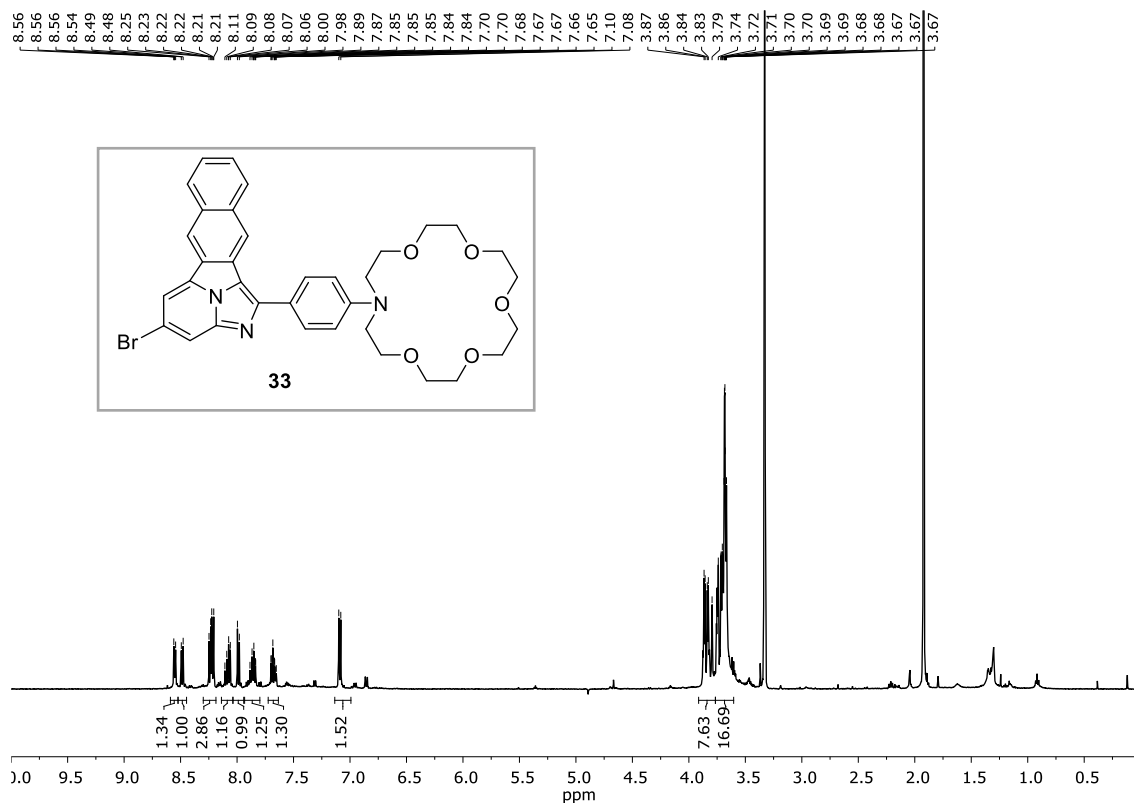
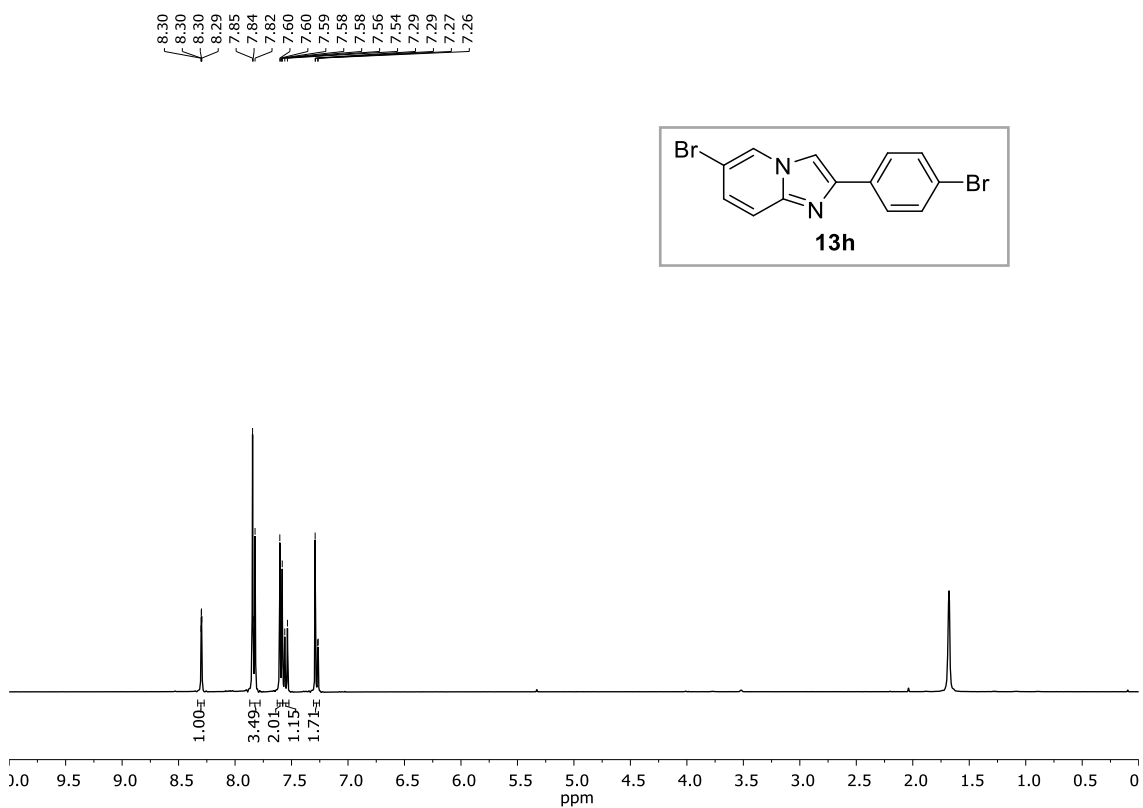

Methyl (E)-3-(6-aminopyridin-3-yl)acrylate, 36a

^{1}H-NMR (CDCl$_3$)
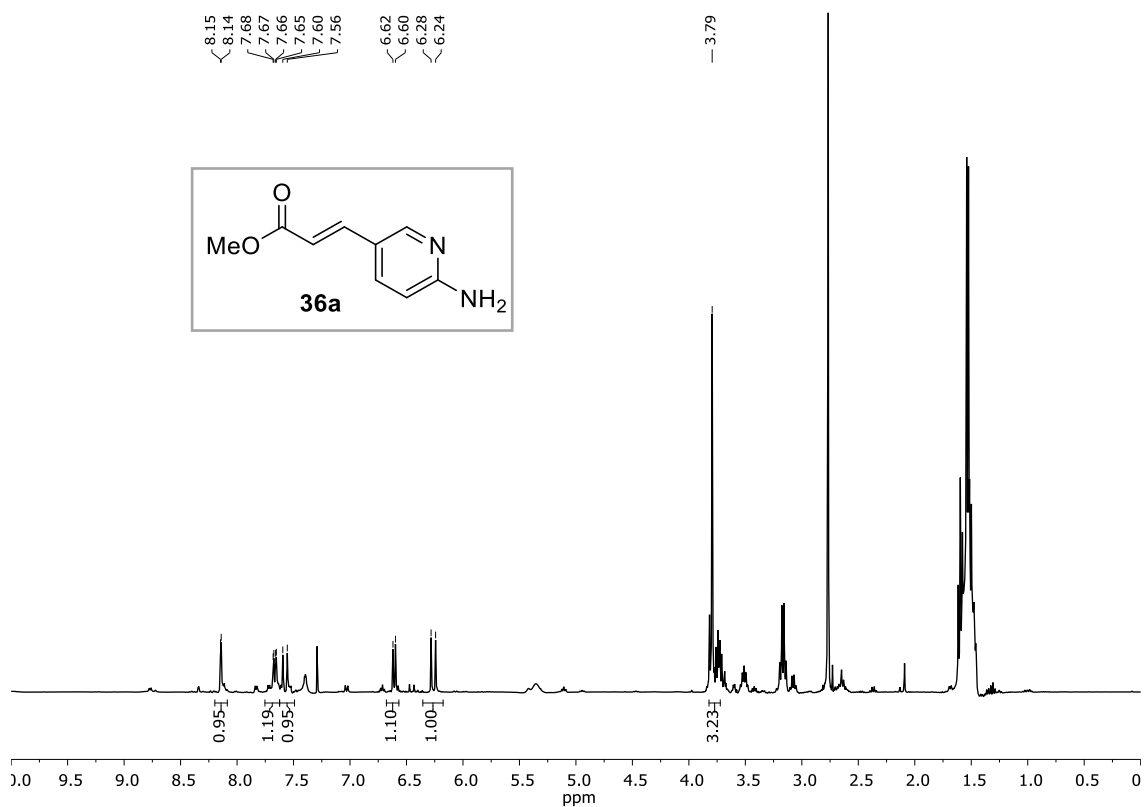
Methyl (E)-3-(2-(4-bromophenyl)imidazo[1,2-a]pyridin-6-yl)acrylate, 13d

^{1}H-NMR (CDCl$_3$)
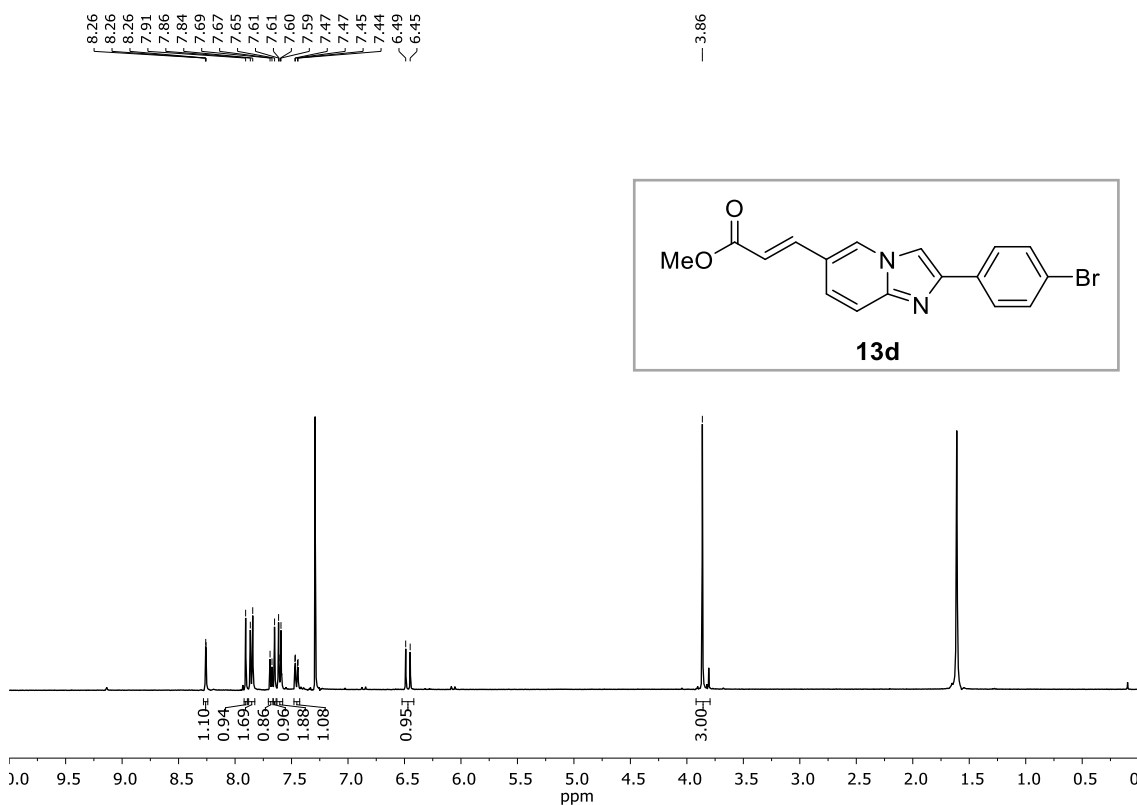
Methyl (E)-3-(2-aminopyridin-4-yl)acrylate, 36b

^{1}H-NMR (DMSO-d$_6$)
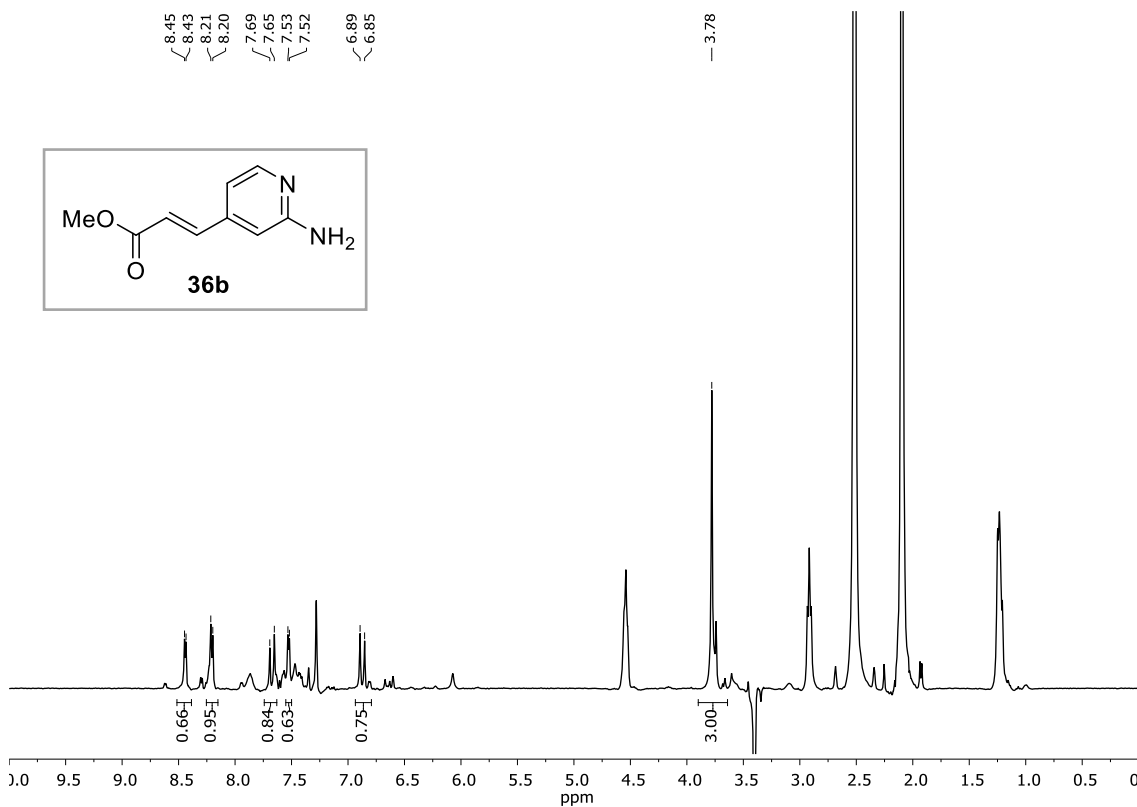
3-(2-(4-bromophenyl)imidazo[1,2-a]pyridin-6-yl)propan-1-ol, 37
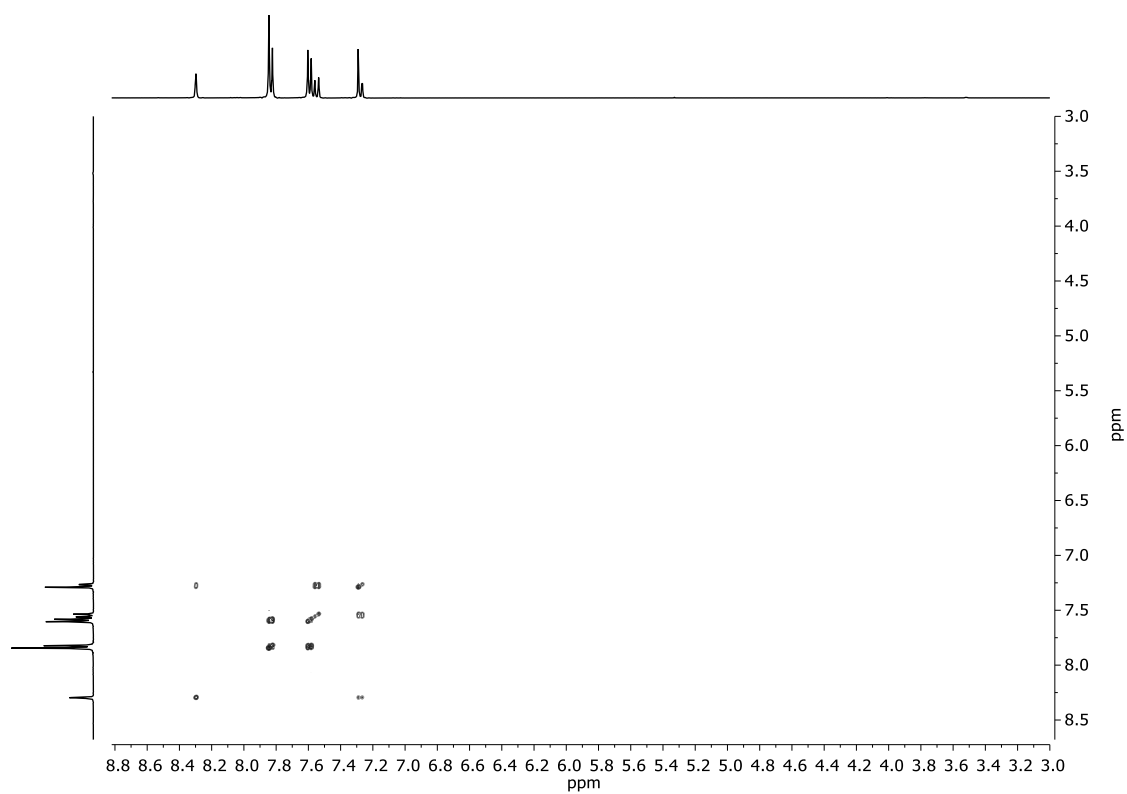
^{1}H-NMR (CDCl$_3$)
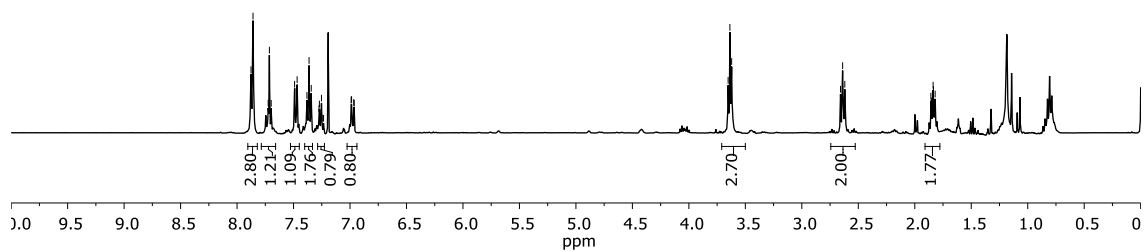
g-COSY (CDCl$_3$)
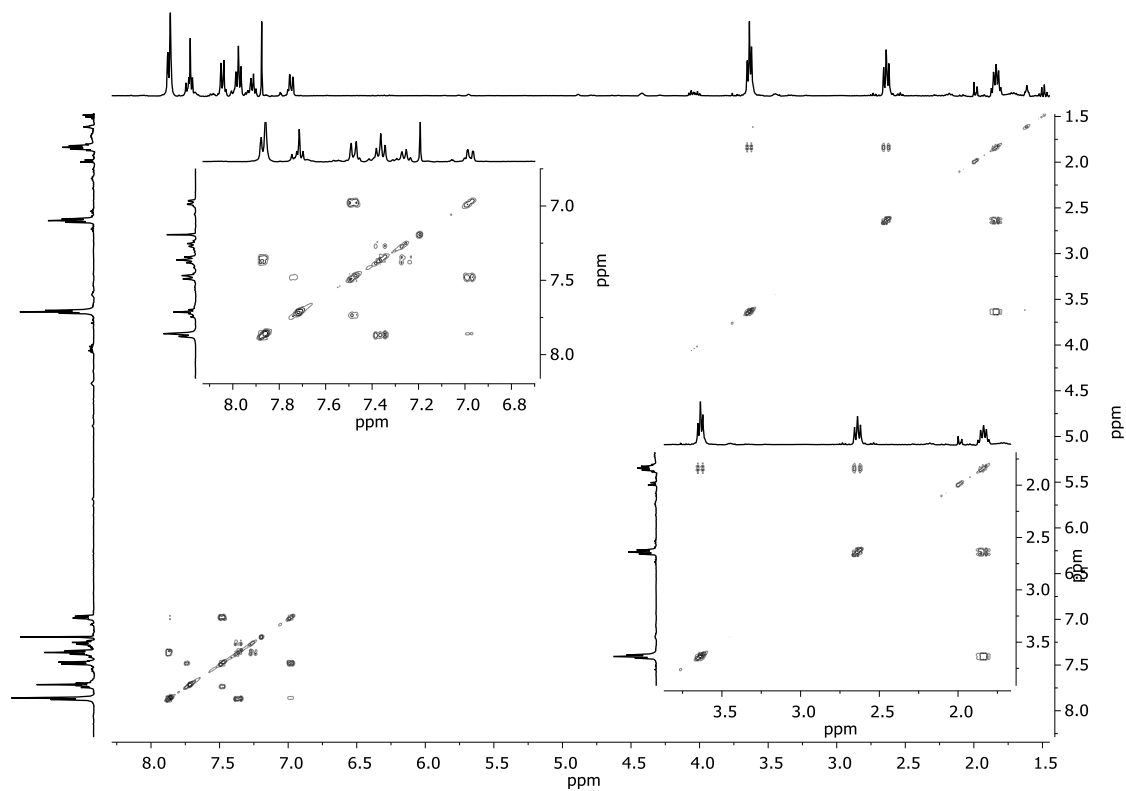
2-(4-bromophenyl)imidazo[1,2-a]pyridine-7-carboxylic acid, 13f

¹H-NMR (DMSO-d₆)

(2-(4-bromophenyl)imidazo[1,2-a]pyridin-7-yl)metanol, 13g

¹H-NMR (CDCl₃)

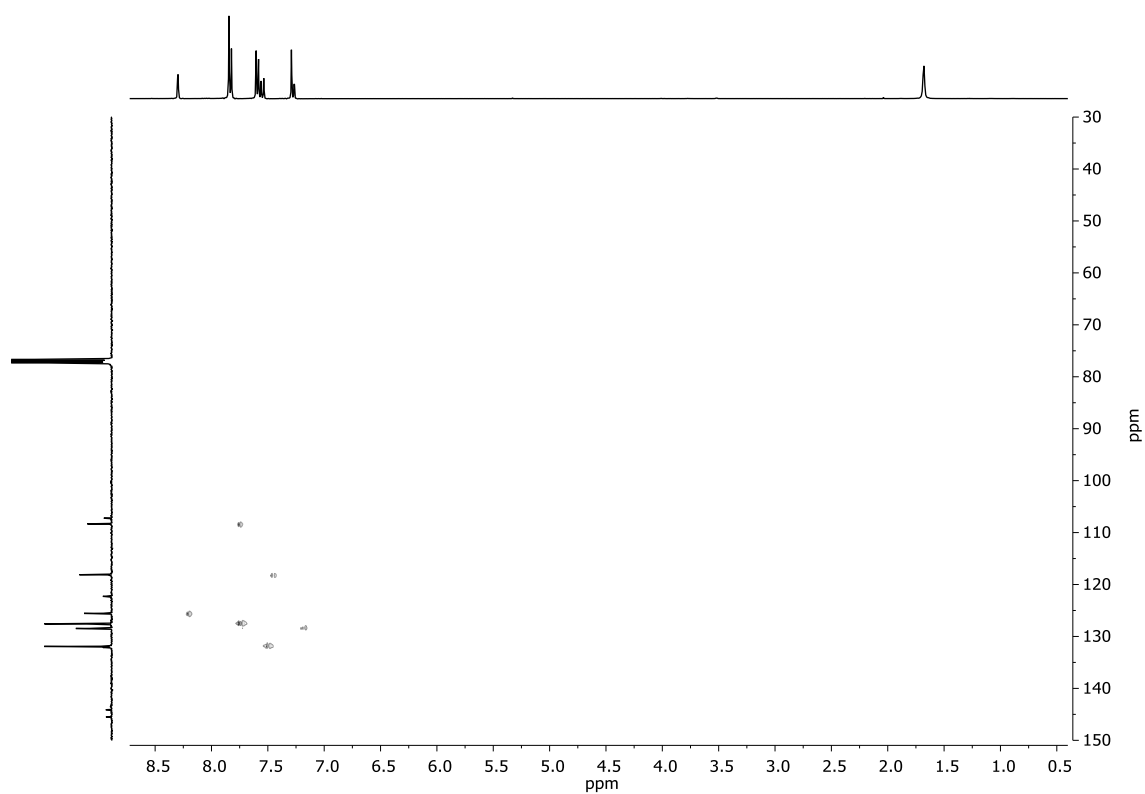## 6-bromo-2-(4-bromophenyl)imidazo[1,2-a]pyridine, 13h

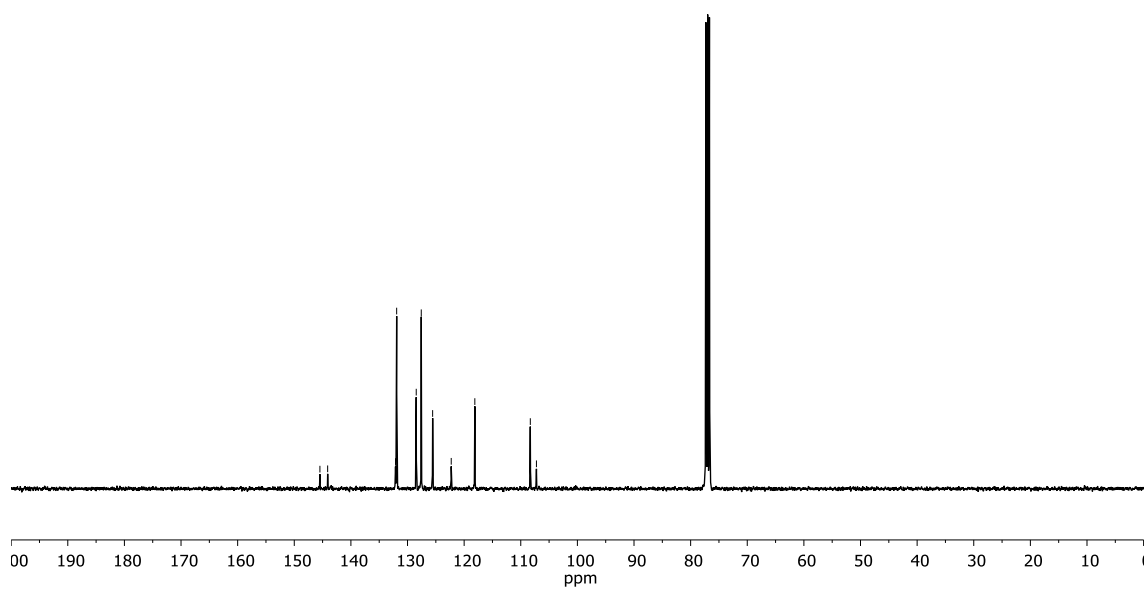### ¹H-NMR (CDCl₃)

g-COSY (CDCl₃)

_g_-HSQC (CDCl₃)

¹³C-NMR (CDCl₃)

135-DEPT (CDCl₃)